Force Sensing for Measuring Human Body Movement

ANTHONY JOHN MOLLOY

A Thesis Submitted to

THE UNIVERSITY OF ASTON IN BIRMINGHAM

as part of the requirements

for the degree of

DOCTOR OF PHILOSOPHY

Engineering Systems and Management

April, 2006

Summary

The research developed in this thesis explores the sensing and inference of human movement in a dynamic way, as opposed to conventional measurement systems, that are only concerned with discrete evaluations of stimuli in sequential time.

Typically, conventional approaches are used to infer the dynamic movement of the body; such as vision and motion tracking devices, with either a human diagnosis or complex image processing algorithm to classify the movement. This research is therefore the first of its kind to attempt and provide a movement classifying algorithm through the use of minimal sensing points, with the application for this novel system, to classify human movement during a golf swing.

There are two main categories of force sensing. Firstly, array-type systems consisting of many sensing elements, and are the most commonly researched and commercially available. Secondly, reduced force sensing element systems (RFSES) also known as distributive systems have only been recently exploited in the academic world.

The fundamental difference between these systems is that array systems handle the data captured from each sensor as unique outputs and suffer the effects of resolution. The effects of resolution, is the error in the load position measurement between sensing elements, as the output is quantized in terms of position. This can be compared to a reduced sensing element system that maximises the data received through the coupling of data from a distribution of sensing points to describe the output in discrete time. Also this can be extended to a coupling of transients in the time domain to describe an activity or dynamic movement. It is the RFSES that is to be examined and exploited in the commercial sector due to its advantages over array-based approaches such as reduced design, computational complexity and cost.

Acknowledgements

Special thanks must go to John Penny, Toby Norris and Dheeraj Bansal for their philosophical conversations relating to the ideas and concepts in the research.

David Saad, Ian Nabney, David Lowe and Geoff Carpenter, for giving me the time and permission to sit in on their lecture series relating to aspects of the research

Also I would like to thank Peter Brett and Steve Wheeler from Primasil for finding and providing the funding for the project.

On the practical side I would like to thank Alistair Davies and Mark Reed of the Belfry golf course for providing the real data for the project and for the donation of the golf driving mats. Also thank you to Robin Taylor and Mark Prince for providing me with the data acquisition and etching facilities to incorporate the hardware for the research.

And finally, to the technicians (Jim Jeffs, Paul Piezer, John Thurgood, Bill Curtis, Dave Farmer and Ian Murkett) for their constant favours and building support throughout the project.

Table of Contents

List of Figures

CHAPTER 2

CHAPTER 3

CHAPTER 4

APPENDIX B

APPENDIX C

APPENDIX D

List of Tables

CHAPTER 3

CHAPTER 4

Notation

α - Constant of proportionality, integral proportion (hysteresis), rejected region, and the weight decay coefficient

a - Number of harmonics in the x plane, numerator and auto regressive coefficients

$\mathbf{\Lambda}$ - Eigenvalue matrix

$\mathbf{A}$ - Captured data in matrix form

ADC – Analogue to Digital Converter

ARMA – Auto Regressive Moving Average

b - Number of harmonics in the y plane, the evaluated bias matrix, denominator and moving average coefficients

B - Backshift operator

C - Capacitance in Farads F

CCD – Charged Coupled Device

CNS – Central Nervous System

COM – Centre of Mass

COP – Centre of Pressure

∂p - Change in unit pressure in Pa

d - Distance between two capacitive plates in m and desired target value

D - Bending stiffness in Nm, diameter in m and deterministic time series

DFT – Discrete Fourier Transform

DOF – Degree of Freedom

e_0 - Permittivity of free space, given as 8.85×10^{-12} Fm^{-1}

e_r - Dielectric constant of the material used between the capacitive plates

E - Youngs Modulus in N/m^2, total error over all training patterns and expectation

Σ - Is an (m x n) diagonal matrix with positive or non-zero elements called singular values

f - Length of the rectangular plate in the y direction in m, evaluation of a function and frequency in Hz

FEA – Finite Element Analysis

FFT – Fast Fourier Transform

g - Position of the load in the x plane in m

GA – Genetic Algorithm

GLM – Generalised Linear Model

h - Position of the load in the y plane in m, step width and time series of length N

H_a, H_o - Alternative and null hypothesis respectively

i - i^{th} element in the vector

IRLS – Iterative Re-weighted Least Squares

j - j^{th} element in the vector

J - FFT Frequencies in Hz

k - One half of the weight decay coefficient η, spring constant and lag

K - Constant value, gain and also is a linear evaluation mapping matrix

l - Length of the capacitive plate, length of tube in m

L - Mass of loading in kg

μ - Mean

m - Magnitude, number of columns

M - Moments in Nm

MEC – Mathematical Extracted Coefficients

MEMS – Micro Electro Mechanical Systems

MLP – Multi-Layer Perceptron

n - Number of rows, samples, delay in time series

net - Calculated network output

N - Number of samples

p - Poles and probability

ρ - Density in kg m^{-3} and correlation coefficients

P - Total number of training patterns and pressure in Pa

PCA – Principal Component Analysis

PCB – Printed Circuit Board

PF – Polynomial Fitting

PVDF - Polyvinylidene Fluoride

Q - Flow rate in $m^3 s^{-1}$

r - Resistance in Ω, radius in m, rank, roots and cross correlation

RBF – Radial Basis Function

RC – Resistance, Capacitance

RF – Radio Frequency

RFSES – Reduced Force Sensing Element System

σ - Standard Deviation

s - Laplace transform

SLP – Single Layer Perceptron

SVD – Singular Value Decomposition

θ - Angle of swing in rad

t - Thickness of the surface in m, time in s, target evaluation and wall thickness

T - Transpose of a matrix and period of waveform in s

U - Depth of load area in m

U - Is an orthogonally rotated PCA consisting of regular eigenvectors columns of $\mathbf{AA}^{\mathbf{T}}$

USB – Universal Serial Bus

v - Poisson's ratio of the surface, width of load area in m and viscosity

V - Sensory output Voltage V and Volume in m^3

V - Eigenvector matrix and is also a unitary orthogonally rotated PCA consisting of eigenvectors of $\mathbf{A}^{\mathbf{T}}\mathbf{A}$

w - Deformation of surface in m, width of the capacitive plate in m, evaluated weighting matrix and frequency in rad s^{-1}

W - Applied loading on the surface in N

$\bar{x}$ - Mean evaluation

x - Sensory element position in the x direction, compression displacement in m, time series of length N and distance from the COM to the pivot in m

X - Input coefficient or input pattern matrix and also time series

y - Sensory element position in the y direction in m

Y - Output coefficient, or output pattern matrix

z - Z Transform, or z-test evaluation

Z - Principal component matrix

CHAPTER 1

Introduction

1.1 Initial declaration

The aim of this research is to develop a new force sensing system that possesses improvements over conventional force sensing methods. The new force sensing system is one that can be described as an information sensor capable of association and classification of various stimulating static and dynamic behaviours on a surface. The resultant output is information relating to the stimulus, such as the classification of movement or kinematic posture of a subject on a surface. Various functions are therefore required to provide this output information and are to be described in this thesis.

1.2 Objectives set by the requirements of the funding body for the system

The application for this novel force sensing system is to measure dynamic forces exerted by the feet on a two dimensional surface throughout a golf swing. The first intended output of the system is a recognition scheme, to discriminate between various swing types, swing parameters and common faults apparent in the golf swing. The second intended output of the system is to offer feedback and advice for improvement based upon the recognition results.

The objectives of this golf swing mat are initially defined by the group funding the project, for what they require to market and sell the system. The general requirements for the end user are: 1) the general aesthetics of the system; and 2) the feedback information given by the system to enhance any golf player's performance. The success or achievement in both categories will therefore drive the marketing capability of the product.

1.2.1 Required aesthetics of the golf mat

The requirements and objectives for the appearance of the system are given as follows:

1) Develop an alternative system to conventional approaches to provide similar feedback during or after the cost swing, reduce the installation complexity, and the cost of the system.
2) The sensing system, must be a thin structure that can be integrated within an existing golf driving mat, or be representative of a golf driving mat.
3) The sensing surface and Astroturf layer must be interchangeable, over a period of time to prevent surface fatigue, corrosion or damage.
4) The driving mat must be designed so that it can be easily assembled, installed, or repaired if needed
5) The driving mat must be computer driven (this can either be through a laptop or monitor with an integrated computer).
6) The connectivity between the processor and peripheral device can either be a serial RS232 or USB connection.
7) The driving mat can be either powered by AC or DC supply

1.2.2 The feedback information given by the system to enhance any golf player's performance

The golf mat must be able to provide various features that can be fed back to the golf player on the driving mat in either real time or in a post-swing analysis, defined as:

1) Real time feedback for the golfer to provide a balanced posture at the stance position.
2) Accuracies of output must be within 5% of actual evaluations, as to give generalised outputs, as opposed to discrete accurate output evaluations, which are of no real concern to the feedback in human movement error.

3) A post-swing analysis of the loading at the feet, throughout the entire swing.
4) A post analysis of the loading conditions of the feet at the critical points in the swing, i.e. Top swing, Mid down swing, Impact, and Follow through.
5) A comparable analysis of the captured force transients at the feet with that of the professional for a complete golf swing.
6) A personalised swing signature, (the movement of the COP against time)
7) Various swing parameters such as, the swing timing, swing consistency, velocity, and power in stroke.
8) A classification analysis of various flaws during the swing.
9) A database program to store swing improvements and weaknesses for individual golfers over time.

The research also is to investigate loading stimulating conditions apparent on a surface, which are:

1) Single load, constant magnitude, fixed position force
2) Multiple loads, constant magnitudes, fixed position forces.
3) Single load, changing magnitude, fixed position force
4) Multiple loads, changing magnitude, fixed position forces.
5) Single load, constant magnitude, varying position force.
6) Multiple loads, constant magnitude, varying position forces.
7) Single load, changing magnitude, varying position force
8) Multiple loads, changing magnitude, varying position forces

Categories 1 and 2 have been investigated for primarily fixed or static conditions on the distributive surface by Stone (1997) and Tongpadungrod (2002). However these types of loading conditions have limited application. This research starts at categories 3 and 4 for loading conditions applied to RFSES, which have greater potential for application. The applications for systems that can process and define these types of loading are wide and can be used, for example, in the analysis of the dynamics of the human body. The analysis of the dynamics of the human body is of great importance to sports and medical

fields that require thorough examination and interpretation of human activity; hence the RFSES must be able to evaluate loading conditions up to at least category 5 to infer the movement of a body.

1.3 Analysis of dynamics

There are two physical methods that can be used to analyse the dynamics of an object whilst in contact with a surface. These are tactile systems that are in contact with the body in some way and vision system. Typically, for a thorough comprehensive examination of the golf swing, the two systems are used simultaneously to maximise and correlate the data captured for the dynamics. For example, Hosea et al. (1990) analyses the effect of dynamic activity affecting the lumbar spine in professional and amateur golfers. To carry out this dynamic analysis, reflective markers were placed on selected segments on the spinal cord. Four synchronized cameras were then placed around the subject to allow a stereoscopic visualisation of all the data points.
Myoelectric activity of the golfers back was determined using a tactile electromyography (EMG) technique.

Foot pressure profiles have also been recorded throughout the golf swing. Wallace et al. (1994) used piezoelectric transducers to determine pressures at eleven positions under the foot, in conjunction with a three dimensional video capture technique. Also, Barrentine et al. (1994) used two force platforms covered with artificial grass to collect ground reaction forces for the left and right feet. In addition, high speed motion analysis was used to correlate the temporal aspects of the club swing with the force platform data.

If this force system can analyse and classify the collected data correctly and be correlated and verified by the collected data received by a vision system, then it is sufficient to suggest that the tactile system could be effective enough as a stand alone system to classify the dynamic correctly. If the tactile system is proved to be effective enough without the use of a vision system, then the synchronisation of the data capture,

complexity of image filtering and processing is eliminated from the capture and analysis of the dynamic activity. This elimination of a vision system would also improve portability and reduce complexity during the classification process.

The RFSES must be able to analyse the captured mechanical stimulations from the contact of the feet on the surface, recreate and determine the dynamic activity occurring on the surface without the use of a vision system. The processing and classifying stage, through pattern recognition, should be one that simulates the association techniques for classification by the human brain. This is so that there is a meaningful perception from the input. Assuming that an array-type force system is one which has a large number of input transients, then the brain would typically look for prominent features or transients to extract and use in the decision making process to what the feature means. In this case, only a few selected prominent transients would be regarded as decisive in the decision making process and the non-descriptive transients would be rejected. With this technique a filtering process would be used for an array approach.

Therefore, the research will only investigate the use of minimal sensing points that are optimally positioned to generate transients that possess the most prominent features that are descriptive to the dynamic activity. The RFSES technique is also known as 'the distributive tactile sensing method', which was first described by Stone and Brett (1996) They investigated the mechanical deformation of a surface and related this to a static loading configuration. This system operates on the basis that the continuum of the surface holds all of the information about its displacement due to the contacting stimulus and that the surface is highly responsive, i.e. it is assumed that the surface can return to its original structure instantaneously subsequent to loading. Minimal displacement sensing points are then positioned optimally in close proximity to the surface as to extract maximal information about the stimulus, despite a reduction in sensing elements. This information is then processed with the use of a mathematical algorithm from the coupled data set to interpret the static stimulus on the surface. This interpretation could be a classification of shape type, magnitude, position, orientation of an object, or whatever is required as an output to represent the stimulus.

The fundamental purpose of this research is to investigate the RFSES, with the addition of a characterisation and recognition of applied dynamic loading patterns at fixed positions in space. This type of analysis is common with most other dual systems described, such as the analysis of a golf swing. Secondly, a recognition and classification-processing algorithm is to be adopted to analyse the dynamics of an object on a surface, from the dynamics of the loading conditions of the feet that are fixed on a surface. The advantage for this type of classification is that more information exists in the dynamic time series as opposed to individual instantaneous time points, therefore the accuracy of the system should be enhanced for classification. Finally, a slow responsive force surface with impinging static and dynamic stimulations at fixed points is to be investigated, to complete the thesis as an advance in the force sensing field. Further investigations would advance from this point, such as a slow responsive surface, with dynamic loads with a changing contact position. This is assumed to develop a greater uniqueness to the richer structure in the dynamic signature of the output transient from the coupling of three dynamic components. This richer structure will therefore increase the information received by the system as to enhance the classification accuracy and maximise the number of possible classification groups relating to the complex stimulating input.

All current and conventional approaches into the monitoring of body efficacy during the golf swing are to be explored to determine the capabilities and limitations of these various monitoring systems. Specifically for the golf swing, much research has been carried out ((i) to (iv) are discussed in Appendices A.1 to A.4).

i) Video of biomechanical movement and movement of the club.
ii) Evaluation of the biomechanics of bodies using laser based systems.
iii) Evaluation of forces on the club.
iv) Evaluation of EMG and myoelectric voltages on the body.
v) Foot to ground force profiles.

1.3.1 Foot to ground pressure profiles during the golf swing

For the purpose of analysing foot to ground pressure patterns it has been found that recent studies have shown that proper biomechanics of the foot are necessary for the correct transfer of weight and swing efficiency. The first investigation into the ground reaction forces during the golf swing of a single elite golfer was performed by Carlsoo (1967). This measurement was recorded through the use of two force plates under the feet, with additional measurements of electromyography and cinematographic analysis. He identified a changing of force in the left foot before the back swing was complete. This led to the theory that the left foot initiated the back swing for right handed golf players. Cooper et al. (1974) quantified peak vertical forces throughout the entire golf swing and provided information on rotational moments. He recorded that the maximum vertical forces were greater than the body weight and attributed this to centrifugal forces caused by swinging the club. The recordings, taken through two force plates, found that at impact with a driving club, the golfer had 75% of body weight on the front foot close to the pin, which switched to almost 50% just after impact. Maximum vertical forces were recorded as being 150% of body weight whilst using the driving club and 133% for the 3-iron. His final conclusions were that the weight shift is not complete to the left leg at contact for right-handed golfers.

More interestingly, the studies by Williams and Cavanagh (1983) used force plates and three-dimensional cinematographic analysis to determine ground reaction forces and centre of pressures during the golf swing. The results of these experiments indicated that the right and left foot functioned differently from one another and showed no symmetry. Individuals possessed an ability to repeat identical foot force-production patterns for successive swings and that overall group variability was less for the highly skilled group than the less skilled group. Also skilled players have been found to transfer vertical force from the back to front foot at a higher rate. This conclusion was also found by Richards et al. (1985) who concluded that it is possible to discriminate between lesser and more skilled golfers on the basis of ground reaction patterns.

Kawashima (1987) found that skilled golfers always kept their weight within the stance, while the unskilled moved it out of the stance during the swing. In addition, the force volume (against the force plate) exerted on to the base in the swing reached 160% of body weight in men and 140% in women. Thus this research also coincides with similar findings from Cooper et al. (1974).

Pforringer et al. (1987) concluded that motion of various body parts trigger reactive forces from the shoe-ground interface, yielding useful information of the foot biomechanics in the golf swing. Recent studies by Barrentine (1994), Brown (2002), Kawashima (1994), Koenig (1994), Riltler (1987), Shippen (2002), Pietrocarlo (1996), Wallace (1990) and Wallace (1994), have also measured foot to ground reaction forces using force plates to study the force movement at the feet during the golf swing. Interestingly, research by Okuda (2002) who used a force platform concluded that delayed but rapid transfer of body weight from the rear foot to the front foot was critical for a successful swing.

The capture and measurement systems that have been deployed for such analysis have been mainly force plate based, piezo or force elements in proximity to the sole of the foot. The data capture from the force plate is in synchronisation with the picture capture from three or more motion cameras. However, the disadvantage of this type of research is that the analysis has only been concerned with laboratory-based findings as opposed to the actual game of golf, due to lighting restrictions. The artificial operating environment of the indoor golf station may affect the performance of the golfer and the outcome of the shot is not known.

1.4 Reduced Force Sensing Element System (RFSES)

There are no systems to date which monitor ground reaction forces over a selected time frame and then use the information to define classifications of movement. In addition to this, the interpretation of the RFSES can therefore monitor activities that are representative of a vision method. The advantages of these types of systems are that

complex image processing, light dependencies and complex association techniques are not required to determine the classification of movement. The application for this technology is a system that can replicate the performance of a load platform, to determine the location of the feet on the surface at the golf stance, interpret the loading magnitudes of the feet throughout the golf swing and finally to characterise and classify the type of swing. Other applications to be explored for this RFSES include:

1) Loading distribution exposed on a seat to determine seating posture.
2) A sway table that can determine the magnitude, velocity and, acceleration of the centre of pressure in real time.

CHAPTER 2

Human and Machine Force Sensing Systems

This chapter reviews the current state of the art in force sensing and its application in academic and commercial fields. It will also demonstrate a novel type of force sensing and its relation to the human system that has evolved to be optimally integrated for maximum sensitivity and performance. The system will therefore simulate the synthesis of the human system into a mechanical one through the strong integration and optimisation between functions. The functions in this case are the loading condition, the surface, the sensors, the processor and output. This is to be described for a preliminary validation of the previous research and more specifically, its relation to human measurement.

2.1 Human tactile sensing system

The human skin is aroused through the use of receptors embodied within it. The area served by a receptor is known as its receptive field. A receptive field tends to be circular in shape due to the formation of the peripheral branches on the sensory fibres. For a grouping of receptors the receptive fields are of the same dimensions, thus if receptors are densely packed then there is a probability that the fields will overlap. Overlapping receptive fields provide a basis for complex analysis and integration of the sensory unit's input because the stimuli impinging on the receptive field of one unit will also elicit impulses in the adjacent units, although to different degrees.

The neural basis of differential tactile sensitivity and discrimination lies in part on the number of sensory units and branches per unit area of skin. A simple test can be carried out to determine the spatial resolution or density of receptors in the skin. The test is known as the two-point discrimination test in which the tips of calliper arms are placed on the skin and the distance between the arms reduced until only a single point is felt. The smaller the distance the higher the discrimination and number of receptive fields. Weinstein (1968) carried out a two-point discrimination threshold experiment to determine the sensory density in the skin and found that in the fingertips the threshold distance is (2-3mm), thus concluding that the receptive fields are small and degree of

overlap is high. The opposite is true for the back (39mm) or legs (42-45mm). Therefore in the fingertips, even two closely applied stimuli are likely to activate two different sensory units, since one point impinges on the receptive field of one unit and the second point on an adjacent receptive field. As long as the CNS neuron receives messages from two separate sensory units, two points can be distinguished. If both point stimuli fall in the receptive field of one unit, only one point will be perceived.

For the example of Pacinian receptors, one corpuscle is served by any FAII (Fast Adapting II) myelinated nerve fibre and is responsible for the sensitivity over a large area of skin, such as a whole digit or part of the palmer skin see paper (Moss-Salentijn 1992). The nerve fibre FAII, associated with touch and pressure, possesses a relatively large diameter and shows low thresholds of simulation and high sensitivity in relation to other nerve fibres in the body. It is classified into type I_b (A_α) fibres with a diameter of 22μm and with an action potential conduction velocity of around 120m/sec. The action potential generated from the Pacinian corpuscle in the myelinated fibre is propagated in a discontinuous fashion, jumping from one node of the Ranvier to the next.

Myelinated fibres release neurotransmitters called glutamate at their terminal endings, which synapse in the dorsal root ganglion just outside the spinal cord on the dorsal side. Sensory information is then entered into the spinal cord through sensory fibres of the dorsal column pathway, which ascend towards the medulla oblongata part of the brain. Synapses are formed with neurons in the dorsal column nuclei and become part of the medial lemniscal pathway. These fibres reach the thalamus on the opposite side of the brain, which triggers the ventral posterior lateral nucleus that receives somatic sensory information. Synapses are again formed which in turn extends to the neocortex where the coded data is then "decoded" into a perception of touch. It is interesting to be aware that a congenitally blind child, able to see for the first time in late childhood, could not name objects seen and would require to be taught the meaning of the visual world although the child is processing data on what it sees. There is therefore no natural connection between the stimulus and the sensation which it arouses, Wyburn (1960). This implies that a learning phase is required to characterise and relate a stimulus response to a sensation

through an association from memory in the brain. A more detailed description of the receptive cells in the skin is given in Appendix B.1

2.2 View of current Mechanical tactile system in relation to the human system

Over the last few centuries, as discussed in (Section 2.1), humans have discovered the physiological and biological formation of the human body in great detail. However, it has only been over the last few decades that humans have developed the resources and technology to couple the human physiology concept with that of the technology available. The ability to replicate a human being has been a concept of mass investment and interest in a wide range of fields such as industrial, medical, military, agriculture, space exploration and construction industries to simulate the sensation of human touch for measurement and analysis. There are many advantages listed, such as: flexibility, operational time, running cost, size/shape of required tactile surface and accuracy of measurement. Pennywitt (1986) and others have stated that a tactile sensor should have the same properties as human skin. To mimic human skin tactile sensors should strive to have high sensitivity, fast response and a continually variable output.

We typically define a tactile sensor as a device or system that can measure a given property of an object or contact event through physical contact between the sensor and object. However, some previous definitions have assumed that tactile properties must involve force and a number of early tactile sensors were based on strain gauges or other force sensing arrangements for normal and/or shear stresses. It is only recently that tactile sensing can be described as a device that can determine the shape of an object Caiti (1995), texture Dargahi (1998), Mayol-Cuevas (1998) and temperature Banim (R.S. 2003), etc.

It is important to be aware of how mechanical tactile sensing has evolved to date to be able to make good judgement for the design of a close human mimicking tactile sensor. One of the first records published on mechanical tactile devices was one by Brugler et al.

(1969) and was a direct-translation reading aid for the blind, using integrated electronics. The device translates images using a 144-element monolithic phototransistor array into a tactile output array of vibratory piezoelectric reeds, so that the subject could interpret a picture through a tactile medium.

However, one of the first tactile devices to be used as a sensing device was one by Johnson (1974), who developed a tactile prosthetic device for a person with impaired sensory nerves. The device produces a tone whose pitch increases with increasing pressure on transducers worn on the thumb and index finger. The transducers used were constructed on the principal of conductance proportional to contact area which increases with pressure and is an example of a single-point tactile sensor.

Typical mechanical tactile replications of the human system tactile system have to date mainly been single-point, array, multiple point, smart RFSES and for singular to multiple dimensional applications. All of these types of devices are to be examined in detail in this chapter and to be compared with that of the physiological system.

2.2.1 Single-point sensors

The first technological methods that have been applied endeavour to mimic the physiological force measurement sensation of a human to release the potential benefits of the technology have been single-point sensors coupled with a control mechanism that responds to the output characteristic of the sensing element. An example of this would be a thermostat in an air conditioning system. The thermostat constantly records data on only the temperature of the environment around it. This can be assumed to replicate a temperature dependant receptor in a physiological system such as the free nerve endings. The results of this element are passed to a control system through a communication mechanism such as cables/wires or a transmission device such as variable wavelengths in frequency i.e. Radio Frequency RF, which replicate the Central Nervous System (CNS). This input data is decoded and discriminated, so that the operating system can make an intelligent decision, such as operating a heating or cooling mechanism upon the discrimination of the input. This stage is said to replicate the function of the brain as to discriminate an input and classify it, so that an intelligent prognosis can occur.

Temperature and force elements are typically single-point devices that can be described as tri-axial tactile systems as they can record temperature in a three dimensional space. These devices are normally ideal for simplistic applications, such as a thermostat in a temperature control system for example. However, their complexity of operation and control is far from the ideal of a physiological system. The main difference between the two systems is that a single-point device tends to react to only one sensing element response, as opposed to multiple responses in a physiological system. Failure in a single-point system is very high, which can lead to inaccuracies in the decision making process upon the data it is receiving from possibly an inaccurate measuring element. Redundancy in a single-point system would therefore make the whole system fail, as opposed to a physiological system that can allow for redundancy to discriminate the sensation with a only a reduced level of accuracy due to the high compensation of other operational sensing elements.

Such a system is demonstrated by Harrison (1994), who investigated foot to ground pressure profiles for the diagnosis of post-fracture osteoporosis using simply an air pressure transducer coupled with an air filled silicone tube inserted in the side of a shoe. Pressure differential measurements were then amplified and logged by a data logging device when the subject was both active and inactive during the day. Only the total magnitude of the pressure measurement could be recorded for each foot.

Single-point sensing can operate on micro scales, as demonstrated by Yoshinobu Murayama (2003) who developed a micro-mechanical sensing platform for an accurate characterization of the elastic properties of the ovum via one dimensional measurement. The tactile sensor was fabricated having piezoelectric material into a needle shaped 20um transduction point.

2.2.2 Array tactile sensing

Array systems are designed to be more informative and accurate than single-point sensors. The main difference between the two systems is that array tactile systems can measure multiple point and differential stimulations over a selected area. The functionality of the array system mimics the human tactile system closer than that of a single-point sensor because the human tactile system can also discriminate between multiple point sensations with different stimulating magnitudes.

To provide this functionality large numbers of sensing elements with large numbers of multiplexing and electrical connections are required to capture the full extent of the stimulus over a selected surface range. The pitching of elements are either linear or rectangular arrays like image processing techniques applied to computer vision. Spatial resolution or tactile element density over the sensing area is therefore critical for the resolution changes over small distances. Thus, a low number of elements over an area will give a poor output or image resolution of the stimulus on the surface and the opposite is true for a high element density. These array devices are designed to infer impinging

stimulations in close proximity to each individual sensing element and are only concerned with producing their own unique pixel or tactels (tactile element space, the area in which an element is stimulated) coordinate information about the stimulus. The reason for constructing a high-density device is because it does not know where the stimulus may occur and so must sense in all possible places on the surface where the stimulus may be; low levels of utilisation are apparent for these devices.

The array sensing method is similar to that of the human system in the way it adopts many sensing elements to capture the full extent of the stimulation. However, the human tactile systems performance is not dependant upon the density of the sensing elements under the skin or the pattern of pitching under the surface like an array system. The density of sensing elements in an array tactile system is typically in the order of one sensor per 0.4 - 1.0cm^2 from Wallace (1990) and Rittler (1994) respectively, compared with one receptor per 4.5cm^2 of leg skin Weinstein (1968). These conclusions indicate that array force sensing can typically have a density of sensing element up to ten times that of a human tactile system. Sensing receptors tend to be located in groups at certain locations and at different depths in the skin unlike an equal pitched array set-up.

The processing and discrimination of the stimulus on the tactile surface in the array set up is similar to that of the single-point sensing system and consists of simply a transformation of the stimulus into an electrical signal at each sensory coordinate. Hence, the only processing that is required for an array system is the real time electrical signal interpretation into direct information about the stimulus. This transformation differs somewhat to that of a human system that facilitates a complex interpretation from the coupling of sensory inputs, a characterisation and a classification process to interpret the stimulus. However, array devices are appropriate for cases where high degrees of accuracy are required to measure loading stimulations on the surface.

Array devices are conventionally the most popular for the measurement of loading profiles of various objects from the macro to micro scales. An example of one of the first type of array devices was one demonstrated by Hillis (1982) who described a dexterous

robot manipulator able to feel what it is doing. A high-resolution array tactile sensor was applied with hundreds of pressure sensors in a space the size of a fingertip. The device was built as a demonstrator to distinguish between elements such as nuts, bolts, washers, dowel pins etc, using simple pattern-recognition techniques to interpret the developed output image from the array.

The most common form of commercial array sensing tends to be integrated for the use of force plates applied in the measurement of feet loading profiles for sport and medical applications for example Shippen (2002), who used a AMTI model OR6-5 force plate for the analysis of lumped mass accelerations while moving for various medical applications and Koenig (1994) who used a Kistler™ Force plate for the analysis of foot to ground pressure profiles during the golf swing.

Currently, the art of array tactile sensing has expanded to micro scales for the use in cell measurement and to achieve higher levels of sensitivity and output resolution. Liqun (2003) and Engel (2003) present a polyimide-based two-dimensional membrane based tactile sensing array. Micromachined thin-film metal strain gauges were then positioned on the edges of the machined polyimide membranes. When normal forces were applied then the resistance of the strain gauges changes giving rise to a characteristic loading condition at that specific element for output image processing.

2.2.3 Smart and information sensing

The most significant aspect of any force sensing approach is that of signal processing. Such processing can provide system flexibility and more accurate responses compared with other methods. Rather than having individual sensors, together with individual interfaces and interconnections, it may be possible to develop a complete sensing system that is capable of self diagnostics, calibration and testing. The complete sensing system will allow signal processing to be brought as close as possible to the sensor itself or integrated with the sensor. Such sensors are generally termed smart sensors.

Information devices can be described as devices that can generate information relating to the stimulus. These can be classifications relating to features that are not in direct contact with the surface but have a link to the surface in some way. For example in the classification of various golf swings, such as the angle of club take away, tempo of the swing, or alignment of the body at address are all indirectly related to the loading on the surface. Therefore, these are uncharacteristic of conventional sensing systems as information sensors can produce information about an activity on the force surface, as well as direct loading profiles.

Currently research in the tactile field is extending to these types of devices. Since they add various features, such as a reduction in the required number of sensing elements, and allowance for redundancy in the system. They also mitigate several disadvantages of conventional systems, such as self calibration, and self diagnosis. In order to achieve these benefits, system intelligence is therefore required, to handle and optimise the input data more efficiently, as opposed to more conventional linear translation approaches.

System intelligence can therefore be derived through digital means, such as artificial intelligence or pattern analysis, applied in computer programs or directly embedded onto microchips.

There are only a few commercial products available that make use of the processing capability of a neural network, such as artificial intelligent washing machines. This is on the basis that if the robustness of the algorithm is to fail then such a device would not be as great an issue as opposed to a medical tool that relied upon a neural network algorithm. Other associated problems with these systems are in transferring the technology involved from the research, such as the robustness of the neural networks from laboratories into industry. In all tactile sensors there is a major problem of information processing and interconnection. An array has n^2 connections and individual wires and any reduction in interconnection requirement is welcomed due to ease of construction and increased reliability. This therefore drives the selection and interest for a smart sensing RFSES approach. The smart sensing approach therefore allows for

flexibility in the manufacturing process through the appliance of self calibration techniques which allows for the transfer of research between the laboratory and manufacturing environment to become possible.

2.2.4 Reduced Force Sensing Element Systems

These devices can be termed smart sensors for their system integration capabilities and tend to capture more information about the applied stimulus than single-point sensors. They tend to be associated more closely with array-type devices however they can be differentiated in the way that RFSES are intelligent devices that can self calibrate, filter and process the data accordingly to the applied stimulus.

RFSES sets are most similar to human sets in the way that it can globally use the information retrieved from the sensing elements to describe a force sensation. Firstly, from the number and distribution of the sensing elements required which are vastly reduced as opposed to array-type devices. An example of the number and pitching of elements in a two dimensional tactile skin is described in Section 3.4.9 and defines the optimal number and location of sensing elements to provide balanced and maximal sensitivity amongst elements for stimulus interpretation. The fundamental differences are:

1) RFSES and human systems do not require sensing elements at every location where the load can possibly be like array devices
2) RFSES and human systems do not have equally pitched sensing elements like an array-type devices.

Secondly, human systems do not attain the high level of measurement accuracy of array-type systems, as the brain will give a result based upon a known association to the input stimulus, which will not be of high measurement accuracy.

Thirdly, the human system globally uses all of the captured data from all of the receptors to characterise and classify the stimulus through a coupling of the receptor signals across the continuum of the surface. For example, in the human system, assume that you are holding something that is circular in shape, and without using any visual perception it is possible to infer the shape of the object that is being held. This implies that a grouping of all receptors stimulated will give rise to a classification from memory, so that the shape can be inferred. This is also similar to the operation of a RFSES that uses the strong coupling between elements. The information received by the processor can infer what the stimulus is, through a classification process, based upon the capture of all the element responses.

The main difference between the RFSES and the conventional array approach is that an array device holds each elements response as a separate entity regardless of any other receptors response. Therefore, the information received by the processor is not maximised through the analysis of the differences between elements.

Finally, RFSES and human systems are intelligent enough to accommodate redundancy in the system from the death of a receptor or element and can retain classification or association accuracies for instantaneous or dynamic stimuli over a period of time. For example, a keyboard can be classed as an array device. If one of the keys fails then that key can no longer be used. However, a RFSES or human system can be trained or evolved to accommodate such a failure if one of its elements fails in the system, as the processor/brain along with the other elements can compensate for the loss of the element.

RFSES are mainly new novel devices and can be used for various applications that do not require detailed stimulus location accuracy. For example, in a RFSES by Tongpadungrod (2002), describes a distributive tactile sensing system using a classificatory neural network. The developed system was trained to discriminate between circles and squares, but would not be able to classify a shape that was unknown to it and would then classify the shape closest to one of the shapes it knows.

There are examples of preliminary RFSES with applied neural networks, or signal coupling as far back as the 1980's. However, they are seldom researched and documented in any of the literature. The first one to name is by Worth (1989) who provided tactile sensing for a loading contact problem. The system described can be classified as a RFSES as it facilitates an array of sensing elements providing inputs for a single layered back propagation trained neural network. In this way all of the inputs from the elements are handled as a vector so that the back propagation algorithm maximises the input information through the use of differences between the magnitudes in the input data. The resultant response of this single layered linear algorithm was used for a local closed-loop gripping mechanism able to recognise the angle of contact between the object and the cylindrical finger with the embedded tactile sensing array.

A regressive RFSES is one which can give a result based upon an interpolation of the predictions it knows and is described by Caiti (1995) who investigated the inverse elastic contact problem through the analysis of loading contours of objects. Objects with different loading profiles were used as test subjects positioned on a distributive tactile surface and measured strain relating to the input loading on the surface. The system provided a regressive output relating to the static loading condition through an analysis of a Radial Basis Function (RBF) and Multi Layered Perceptron (MLP) method, which are two different network interpretation algorithms. Again this approach applies a method of maximising information received through a determination of the differences between inputs. These differences are to be used in the analysis of a regressive output value on or between possible values that have been trained in the range. This is also indicative of a human system that can describe sensations that it is accustomed to. However, it can also interpolate between known classifications, for example, describing the quantity of sugar remaining in a bag. If the human knows that one-kilogram is the weight of a bag of sugar then it is possesses interpolator techniques to estimate the quantity of the loading if it is other than the known weight association.

Other RFSES can include simply a system comprising of a four load cells positioned near the corners of a load bearing plate. The centre of pressure on the load-bearing surface can

therefore be determined through a linear triangulation transformation algorithm between the measured load cell magnitudes. The operation of the determination of the centre of pressure on a surface is useful for the analysis of the movement or sway of a human that can be directly related to the severity of a balancing disorder. Dargahi (2000) used only three Polyvinylidene Fluoride (PVDF) sensing elements using a triangulation. He concluded that this type of system could be miniaturised and then be integrated into an endoscopic grasper or prosthetic finger.

Even though the mentioned benefits of RFSES are great in comparison to other force sensing methods, research into RFSES is relatively small in relation to conventional array approaches. This point can be demonstrated by a literature survey that was carried out on the two main systems. Several subject databases were searched and all abstracts of the published papers on array and RFSES approaches were listed, so that they could be divided into array and RFSES. The results in figure 2.1 illustrate the numbers of publications by year on array and RFSES.

The array concept was first introduced in 1969 and then the potential of the concept could be exploited in the mid 80's due to an upturn in computer processing capability and the introduction of robotics. The capacity of this concept was then pushed again in the early to mid 90's when these methods were being strongly applied to robotics, by which time the concept of the RFSES was being introduced. Research on RFSES methods has then taken steady but low level of interest from this point to date. However, array methods had then taken another boom when the array concept could then be applied to Micro Electrical Mechanical Systems (MEMS) for the analysis of particles and cells on micro-scales.

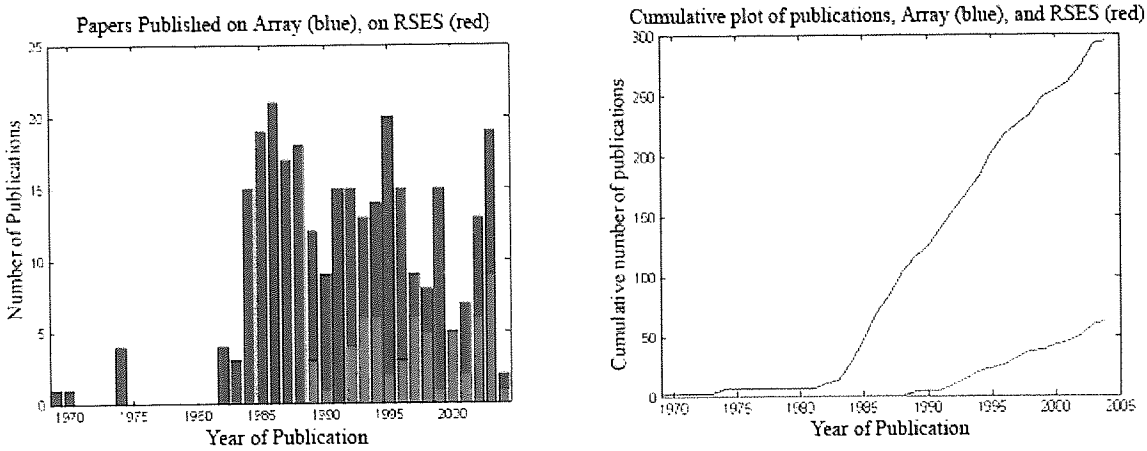

Figure 2.1 - Publications of force sensing. (left) - Number of publications of array and RFSES to date. (right) - Cumulative plot of the numbers of publications.

Figure 2.1 shows current research in RFSES is dwarfed by research on array-based systems. If the two theories were combined then it would be possible to provide an interpolation of a loading condition between sensing elements in the matrix. This could then be used on micro scales that are limited to maximal resolutions from the possible packing density of the sensing elements. Accuracies of loading or edge shape on this level could be enhanced further than other conventional methods.

CHAPTER 3

Proposed Reduced Force Sensing Element System

This chapter demonstrates a novel-type force sensing system that has been evolved to be optimally integrated for maximum sensitivity and performance. The system is to therefore simulate the synthesis of the human system into a mechanical one through the strong integration and optimisation between functions. The functions in this case are the loading condition, the surface, the sensors, the processor and output. This is to be described for a preliminary validation to the previous research and its relation, more specifically to human measurement. The results from this chapter show that it is possible to use a (RFSES) to interpret the accuracy to within 0.5% for multiple load magnitudes and 5.2% for multiple load positional accuracy.

3.1 The RFSES and its strong integration between functions.

The accuracy of the RFSES is related to the optimal integration between sensory functions, similar to the way that the human system is evolved to provide an accurate classification and association sense of touch. The integrated schematic of functions of the RFSES is illustrated in figure 3.1, which represents the integration between the stimuli, the surface, the sensors, the processor and the output.

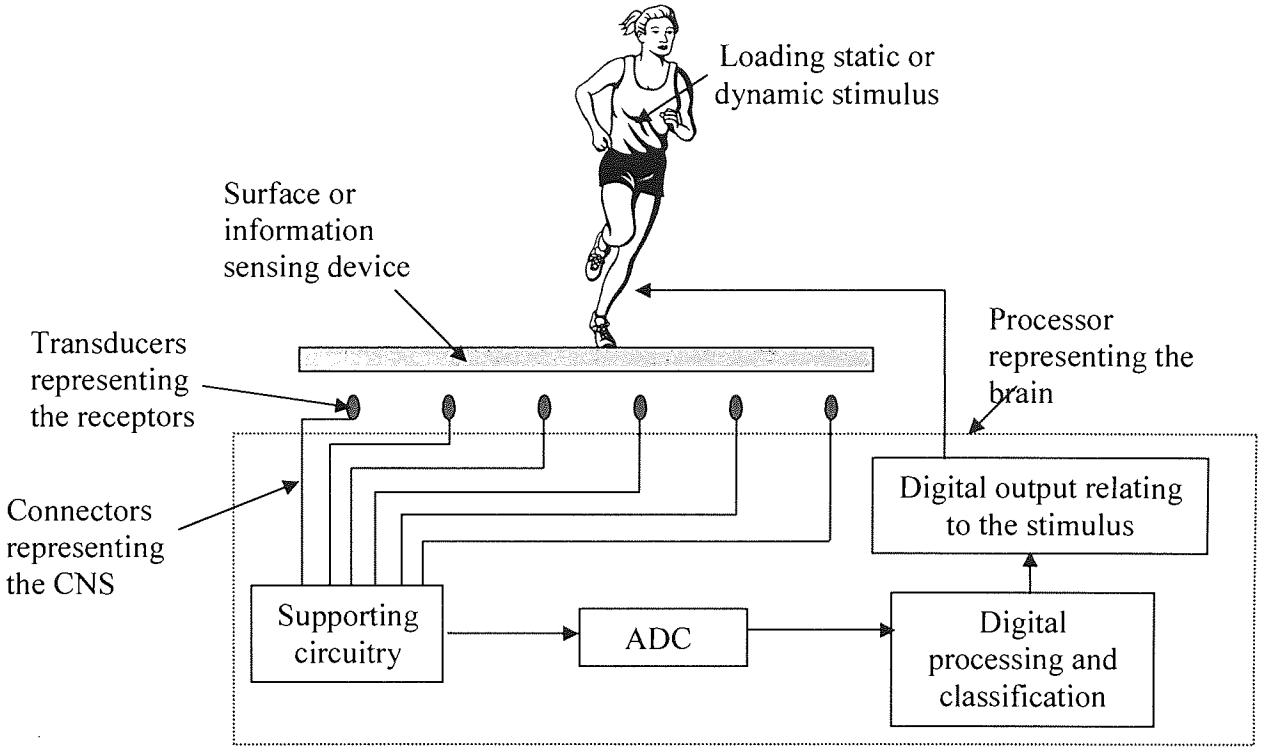

Figure 3.1 - A schematic of the RFSES and comparing its functionality with the human tactile system.

3.2 Surface or information sensing device

The functionality of the RFSES system depends strongly on the coupling effect between sensing elements in order to maximise information received by the processor. However, to provide this coupling effect a medium must be applied to bring all sensing elements into a communication in some way. Most of the described RFSES use a homogeneous surface material that provides not only a coupling effect between sensing elements but also as a structure to hold all of the information about the load and to harness the load from being in direct contact with the sensing elements. The coupling between elements conventionally takes the form of a surface that can elastically deform upon loading. This type of surface allows for differential deformations to occur across the continuum of the surface upon loading. This can then provide a coupling effect between sensing elements due to the decaying magnitude of the deformation propagating from the loading stimulus across the elements under the surface, figure 3.2.

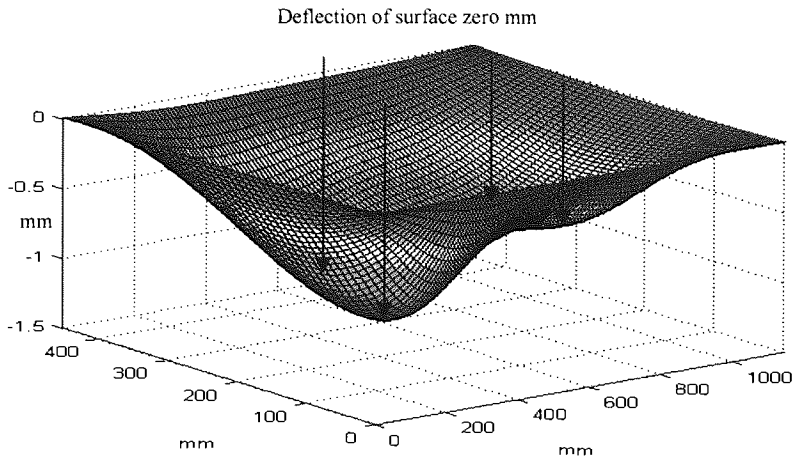

Figure 3.2 - Deformation magnitudes of a surface in bending developed from equation (3.22), under a stimulation of four discrete point loads shown as arrows on the figure.

The figure illustrates the coupling effect apparent with an elastic surface. The loadings are positioned at the peak deformations described as the arrows in the figure. However, deforming disturbances can be observed at other places on the surface removed from the loading positions. It is the measurement of disturbances at various points under the surface that can be used to describe the underlying profile of the surface and loading stimulus through a coupling of all of the deformations that are measured and known. The properties of the surface are to be investigated as it forms an integral part of the system to function optimally and within the set limitations of the other integral functions.

The diagram in figure 3.2 has been derived from a mathematical expression for the deformation of a plate simply supported at the edges. Any homogenous elastic surface can be modelled to show how it deforms across the continuum when loaded. This was first described by Navier (1820) found in Timoshenko (1959), who provided a double trigonometric series expression for the deformation of a thin plate when subjected to loading. The derivation of the model can be described by a differential expression for the deformation in both x and y planes (fully described in Appendix C.1) and is given in the form:

$$w(x,y)=\frac{4W}{\pi^4 e.f.D}\sum_{a=1}^{\infty}\sum_{b=1}^{\infty}\frac{\sin\left(\frac{a.\pi.g}{e}\right).\sin\left(\frac{b.\pi.h}{f}\right)}{\left(\frac{a^2}{e^2}+\frac{b^2}{f^2}\right)^2}.\sin\left(\frac{a.\pi.x}{e}\right).\sin\left(\frac{b.\pi.y}{f}\right) \tag{3.22}$$

Where D the bending stress which can be obtained through an integration of the bending moments to give (3.23), where t, is the surface thickness, v is the Poisson's ratio, and E is the Young's Modulus of the material :

$$D=\frac{t^3E}{12\left(1-v^2\right)} \tag{3.23}$$

The series in (3.22) converges rapidly and therefore discrete values can be given for the limits of the coefficients of a and b, so that sufficient accuracy can be determined through the first few terms of the series. The value of the coefficients of a and b determine the number of terms in the formulation of the deformation and hence the accuracy, albeit the values of a and b must be odd integers, as if even terms are used the expression inside the summation can be equated to the value of zero (see figure 3.4). From this it is possible to evaluate the odd coefficients of a and b to give an accuracy to within 10μm, which is equivalent to a step change of 7mV for the sensing element selected, with the acquisition card selected reading changes as small as 5mV (see sections 3.3.8 & 4.3). If the series in (3.22) is to be computed to give a result, then large values of a and b can require high levels of processing due to the numbers of terms that have to be evaluated and this can be time consuming. A trade off between accuracy and processing capacity needs to be examined to determine the maximum number of coefficients.

A plot of the deflection evaluation against the number of series in the Navier expression (3.22) for a and b coefficients is presented in figure 3.3. A load of 80kg is positioned at loading coordinates of 10x10mm the corner steel plate with a Young's Modulus of 200GPa, Poisson's ratio of 0.3, and dimensions of 790x540x4mm at. The deformation evaluation at the corner of the plate is to be determined through a varying number of a and b coefficient to give.

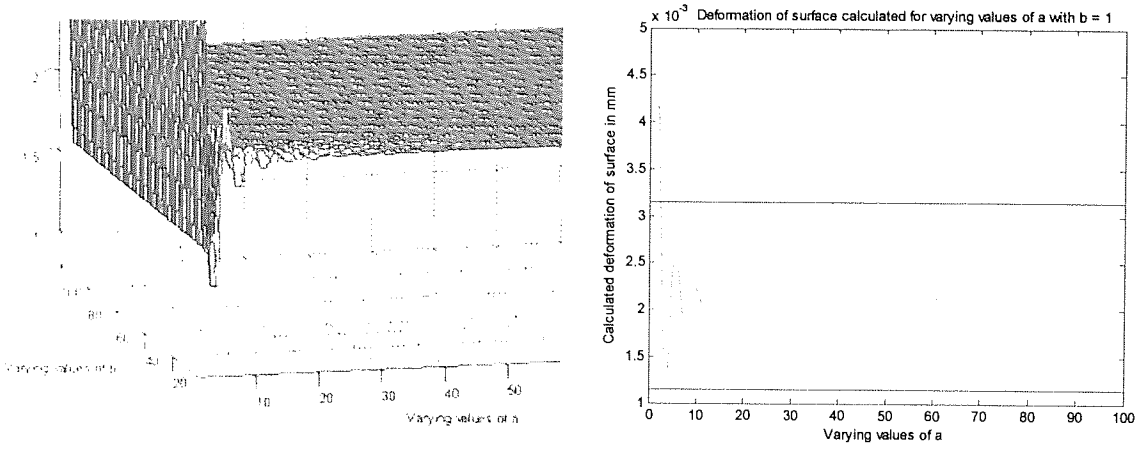

Figure 3.3 (left) - Calculated deformations by the Navier's expression for varying values of a and b for minimal deformation. (right) - A cross section of the figure on the left, for a varying value of a and when b is set to a value of 1.

In figure 3.3 it can be seen that when the value of a or b equals 1 or small numbers, then this gives large oscillatory inaccuracies in the calculation. Hence, more terms need to be used to describe the deformation. The actual value of the deformation is at a value of 0.0021mm, this is when a and b are equal to infinity or 100 respectively shown in the figure. However, the required accuracy is set to be to 10μm, which in this case gives the calculation accuracy between the ranges of x $\pm$ 0.005mm for the solution. The minimum a and b value needs to be determined to give these required accuracies.

Looking at the profile on the right in the figure, when b = 1, the result is oscillatory for small values of a. However, it can be observed that a settles within the range (under the line for the required accuracy) when a = 5 to give an accuracy of 10 microns when the calculation is given in mm. This means that only five summation terms are required to perform the level of accuracy required.

However, it is the maximum loading conditions that need to be examined to give the maximum values of the coefficients required to give a required degree of accuracy. This is due to the fact that the calculation of small deformations gives rise to small inaccuracies and hence small values for a and b. Maximum conditions need to be evaluated as they result in large deflections with higher levels of accuracy resolution and

can be determined under the same plate conditions as before; however the load and point of interest must be at the centre of the plate. The calculated deformation at infinity for a and b gives 2.9610mm. This can be represented in figure 3.4 and shows the evaluation of the deformation through changing values of a and b, ranging from 1 to 10000 summation terms to give the maximum deformation evaluation.

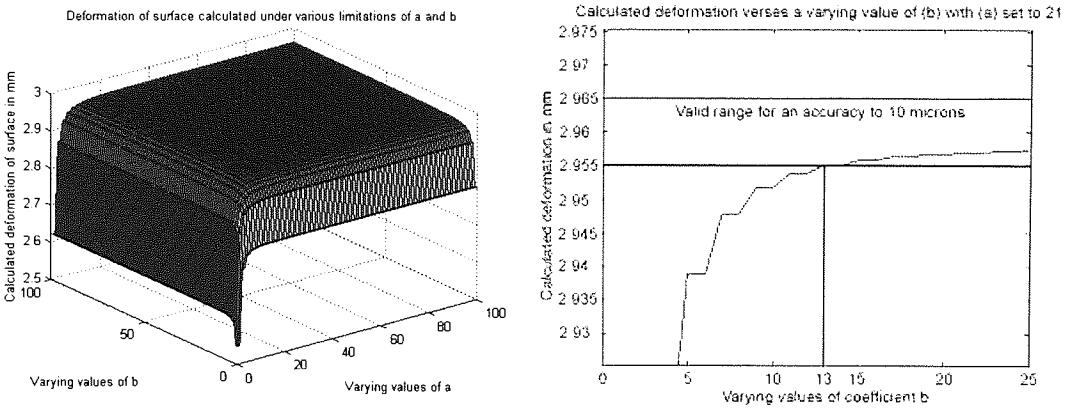

Figure 3.4 (left) - Calculated deformations by the Navier expression for varying values of a and b for a maximal deformation. (right) - The lowest values of a and b to give the required accuracy of the result.

Figure 3.4 shows how the accuracy of the resolution changes with respect to a varying number of coefficients of a and b, with a point of interest and a load of 80kg positioned at the centre of the plate with coordinates of 395mm and 270mm in the x and y plane respectively. It can be seen that in the figure on the left low values of a and b lead to the highest inaccuracies in the calculated result; however it has been found that the values of a and b are to be 21 and 13 respectively from the figure on the right. This is so that the calculated result can fall within the required accuracy range of 2.96 ± 0.005mm. From these evaluated values it suggests that a minimum of 273 terms is required in the representative series. Also this is to be expected as the length: 0.79m (a = 21) is longer than the width: 0.54m (b = 13), meaning that more harmonics are required to represent the longer length than the width. Although, if the length is equal to the width then the odd values for a and b would be equivalent.

From this it is possible to suggest that the larger of the two values of a and b need to selected in the two analyses so that the model can determine the deformation of the

surface to within an accuracy of 10 microns for any expected loading conditions anywhere on the surface.

3.2.1 The selection of elastic properties and dimensions for the surface

It has been decided that the surface and structure have to be integrated within an existing golf mat, so that the theoretical analysis and laboratory findings can be easily integrated into a device that a golf player is accustomed to. This gives various limitations to the dimensions, durability and composition of the required surface. A standard golf mat is to be used as the structure and can be observed in figure 3.5.

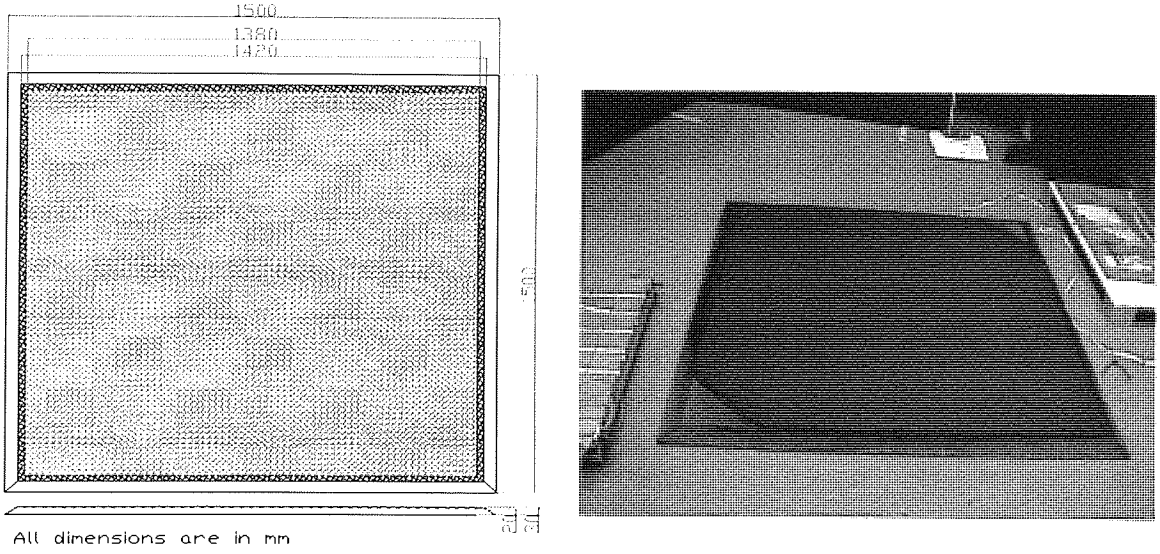

Figure 3.5 - Dimensions of a conventional driving mat.

Figure 3.5 indicates the dimensions of a standard golf driving mat. The dimensions indicate the limitations of the force surface as (1380x1380)mm. The thickness of the force system is also important as this gives limitations to the dimensions of the sensing element, the sensing range, the material thickness and supporting surface, which in this case is 20mm (from the lower part of the left figure 3.5), the Astroturf on the surface consumes a further 10mm of the thickness of the mat.

The surface also needs to be designed in order to comply with the expected anthropometrics and loading of the human body. The posture of the human body at a standing position typically takes a stance that is equivalent to the shoulder width of the subject and within the range of the golfers feet size. The surface length and width must therefore be at a minimum or greater than the 95^{th} percentile (male) for a bideltoid shoulder breadth of 510mm and foot size of 285mm, (data taken from Pheasant 1998).

The stiffness and thickness of the surface needs to be designed to deform elastically within the sensory range of the element and to handle the expected loading conditions. The weight of the body in the 95^{th} percentile (male) is 94kg, (Pheasant 1998) however the surface also needs to be able to cope with dynamic loading conditions imposed by the body.

Kawashima (1987) found that the peak force (against the force plate) exerted on to the base during the swing reached a peak of 160% of the mass of the individual. From this it can be found that the maximum force on the surface would be 150kg during any swing up to the 95^{th} percentile of individuals.

3.2.2 An investigation of various surfaces as a coupling medium between elements under design constraints

A wooden chipboard material was first selected to investigate the principle of a distributive approach. The material selected was 1000x419x18mm to comply with the limitations of the anthropometrics and dimensions of the golf mat.

The stiffness of the wooden surface has been calculated through expression (3.22), by the use of measured deformations at various points under the surface. The results show that the surface was non homogeneous, as the minimum Young's modulus was calculated at $9.1x10^8$ Pa at one element point and a maximum of $1.5x10^9$ Pa at another sensing point, this is also supported by the stress relaxation profile in figure 3.7.

An aluminium surface was also investigated. The aluminium surface selected was Toplate C250, 5083 (NP8) alloy and the dimensions were 800x600mm so that it could comply with the required anthropometrics in Section 3.3.1 and the limitations of an existing driving mat. The Young's Modulus and Poisson's ratio of the selected aluminium was found to be 70.3×10^9 Pa and 0.33 respectively.

Using a material that has a greater Young's modulus will consequently reduce the thickness required of the surface. Reducing the thickness of the material allows for a weight reduction in the system and dimensional flexibility for design within the dimensional constraints. In this case, a steel surface (S275-43A) was analysed to possess a greater bending stiffness than the other materials with the value of 200GPa and Poisson's ratio of 0.3. The dimensions were again selected to suit the limitations of the driving mat and anthropometrics, in Section 3.3.1 and given as 790x540mm.

Assuming that the maximum deformation of the surface was to be no greater than 5mm under a maximum loading of 150kg at the centre of the plate an expression for the thickness of the either the aluminium or steel plate could be derived from (3.22) and (3.23) to give:

$$t = \left(\sqrt[3]{\left(\frac{\sum_{a=1}^{21} \sum_{b=1}^{13} \sin\left(\frac{a.\pi.g}{e}\right).\sin\left(\frac{b.\pi.g}{f}\right).\sin\left(\frac{a.\pi.x}{e}\right).\sin\left(\frac{b.\pi.y}{f}\right)}{\left(\frac{a^2}{e^2}+\frac{b^2}{f^2}\right)^2} \right)} \right) . \frac{48W\left(1-v^2\right)}{\pi^4.e.f.E.w(x,y)} \qquad (3.24)$$

From this expression it is possible to provide a plot for the stiffness of the plate E verses the thickness of the plate t for various Poisson's ratios v (0.3: metals - 0.7: plastics), if all other constants in the expression are known. In this case the plot of expression (3.24) gives (left) the thickness for an aluminium surface and (right) for the steel surface:

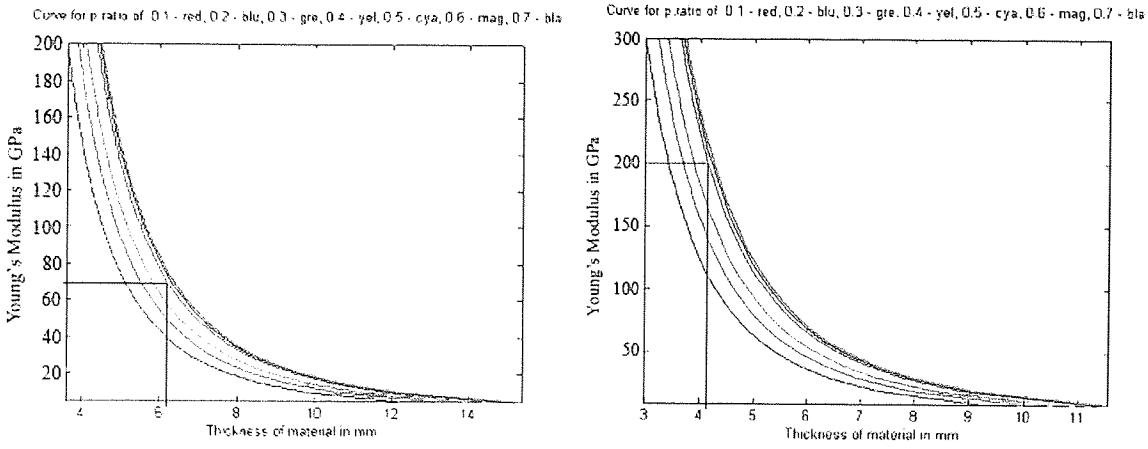

Figure 3.6 - Shows the threshold material properties that will give a maximal deformation of 5mm when loaded at the centre of the plate with a stimulus of 150kg. (left) - An aluminium plate with dimensions of 800x600mm. (right) - A steel surface with dimensions of 790x540mm.

For the case of the aluminium plate, the Young's Modulus is given as 70.3GPa with a Poisons ratio of 0.33 (shown as the green curve in figure 3.6 on the left). The vertical black line illustrates the minimum thickness threshold value for this material to give a 5mm deformation. However, any values taken above the green curve are also acceptable to give deformations less than the maximum 5mm.

From the figure on the left the minimum value of the thickness is calculated as 6.1mm, however, it has been decided that a preferred thickness value of 7mm is to be used in this case, which will give a maximum acceptable deformation of 3.4mm from (3.24).

Similarly, the figure on the right illustrates that the minimum steel surface thickness for a 5mm deformation is 4.14mm. However, a preferred thickness of 4mm has been selected to give a total deformation of 5.54mm.

To keep the structure within the Navier model for a simply supported surface, the plate was supported on a 30mm mild steel frame right around the edge of the plate to simulate a condition close to a simply supported surface.

3.2.3 Investigation of loading

The loading repeatability was examined to determine the integral proportion of hysteresis and permanent deformation of the material between loading and relaxing. Two optical sensors were placed in proximity to the surface in question which was then incrementally loaded on a steel loading hook and circular plate of radius 20mm in steps of 1kg from 0kg up to a load of 40.0kg.

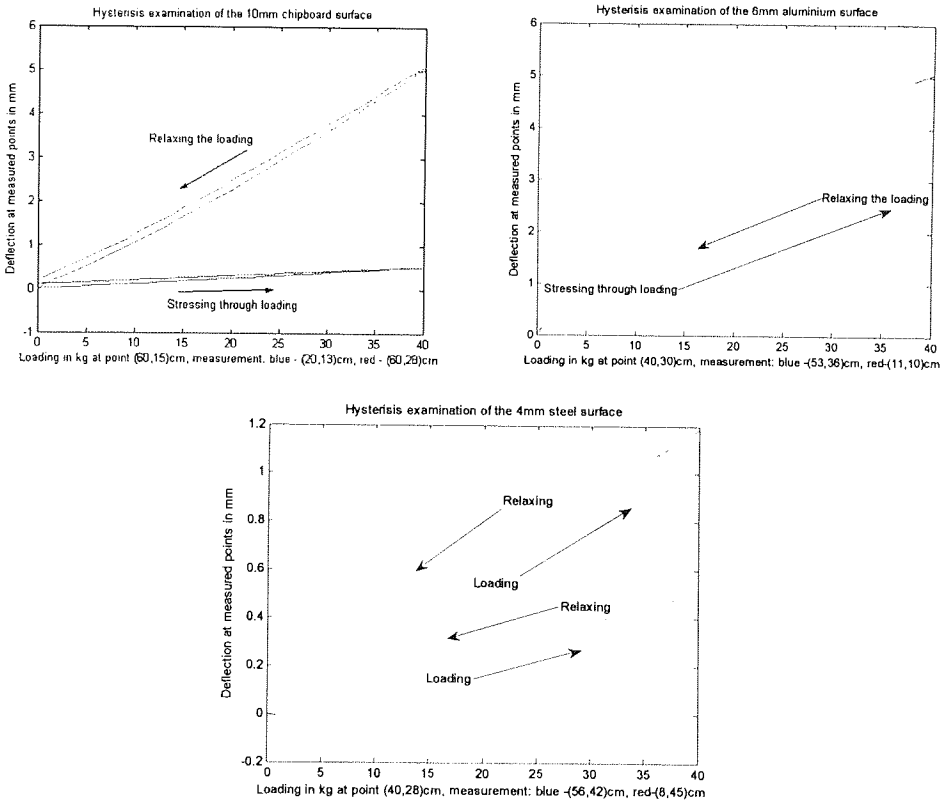

Figure 3.7 (top left) - Recorded deformations at two points on a wooden chip board. (top right) – Aluminium surface. (bottom) - Steel surface, all subjected to a point loading and relaxation.

The results in figure 3.7 are expected from the theory of the Navier model, which is a proportional linear relationship between the deformation and the applied loading. The top left figure represents the stress relaxation profile of a wooden chip board surface. Point loading with the loading hook on the surface at coordinates of (50, 15)cm was incrementally applied in a stressing time of 5 minutes, which was the time taken to record and load the weights up to a value of 40kg. The loads were then incrementally reduced in a relaxing time of 5.3 minutes in total for removing and recording the deformations. Two

optical sensors were used to record the deformation of the material using the relative calibration curve for the sensor. The wooden chipboard was examined at coordinates of (20, 13)cm shown as the blue curve and (60, 28)cm as the red curve in the above figure, through a stressing and relaxing of the surface.

The top right figure represents a similar investigation for the aluminium surface. Deformations were recorded at points (25, 36)cm and (67, 13)cm, from a point loading at coordinates (40, 40)cm. The data was captured during a stressing time of 6.3 minutes and a relaxing period of 5.3 minutes.

Similarly, the bottom figure represents the stress relaxation profile for the steel surface, under similar testing conditions in the two prior investigations. Deformations were recorded at points of interest (20, 13)cm and (60, 25)cm. Point loading was applied at point (49, 18)cm and stressed during a period of 4.1minutes and relaxed during a period of 4.8 minutes.

Through the use of integrals it is possible to calculate an evaluation of the hysteresis through a proportionality relationship between the work done by the surface during stressing and the work done in relaxing the surface. This can be described as:

$$\alpha = \frac{\int_0^{Max(L)} f(\text{deformation from stressing}).dL}{\int_0^{Max(L)} f(\text{deformation from relaxing}).dL} \tag{3.25}$$

where L is the load applied.

The integrals in (3.25) can be evaluated numerically through the use of Simpson's rule in (3.26).

$$\int_a^b f(L)dL = \frac{1}{3}h[f_0 + 4(f_1 + f_3 + \ldots + f_{b-1}) + 2(f_2 + f_4 + \ldots + f_{b-2}) + f_b] \tag{3.26}$$

Through the use of expression in (3.26) and (3.25) the hysteresis proportionality of the points can be calculated and given in Table 3.1 as:

	Hysteresis at point 1 (%)	Hysteresis at point 2 (%)
Wooden surface	19.44	6.59
Aluminium surface	3.73	3.34
Steel surface	3.56	3.8

Table 3.1- Varying hysteresis between materials, indicating repeatability.

With regard to the wooden chip board surface, large recorded permanent deformations may be due to the variability of glue content in the chip board mixture, thus creating variability in the bending stiffness across the material. The elasticity of the material in this case is dependent upon the glue mixture; hence if the material is subjected to a large loading, it can fall outside the limit of elasticity and induce permanent deformation.

The results also show that large levels of hysteresis occur in the wooden chip board due to the permanent deformation of the material under applied loading at both points. Figure 3.7 shows that a permanent deformation of around 0.1mm occurs at both points on the surface and hence it can be suggested that this propagates itself across the continuum of the surface under loading and can therefore create problems of elastic repeatability that is required of the surface.

It has also been found that the hysteresis in the steel surface is similar to that of the aluminium surface. Relatively small levels of hysteresis were recorded in both the aluminium and steel surface which demonstrate elastic qualities that would be acceptable as a possible working solution for a repeatable force sensing surface. Density and cost must therefore play contributing factors in the selection of the proposed surface.

3.2.4 Other suggested materials as coupling mediums between elements

It was decided that a material with a low mass was to be investigated in order to increase the mobility of the system. To accomplish this, a PVC material was selected with a Young's Modulus of 10GPa and poisons ratio of 0.3, could be moulded into a structure with increased stiffness. Due to the complexity of the structure a direct mathematical formulation would be difficult to derive, hence a finite element analysis is to be used to define the stress, strain and maximum deformation for different surface structures. The mesh of the surface was defined with 21152 triangular prism elements and 7519 nodes, to fully capture the deformation of the modelled system.

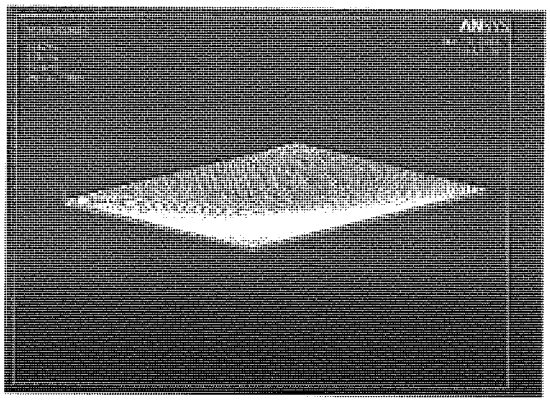

Figure 3.8 - Representation of a PVC surface modelled using a FEA approach.
The above diagram represents the Material properties and dimensions
with a loading of 150kg in the centre of the surface.

The surface dimensions in figure 3.8 have been defined as 0.85m in x, 0.60m in y and with a depth of 8mm. The maximum deformation of the surface using this FEA approach has been calculated as 38mm with a loading of 150 kg placed at the centre of the surface.

The calculated deformation in this case is too great for it to be a viable solution. However, it is possible to strengthen the structure to increase stiffness of the material to reduce the maximum deformation. Ribbing the surface may reduce the maximum deformation and increase stiffness adequately. Equilateral triangular ribs with each side of length 10mm have been used in this case to reduce the deformation of the surface to within 5mm. The modelled representation of the PVC surface with ribs can be observed in figure 3.9.

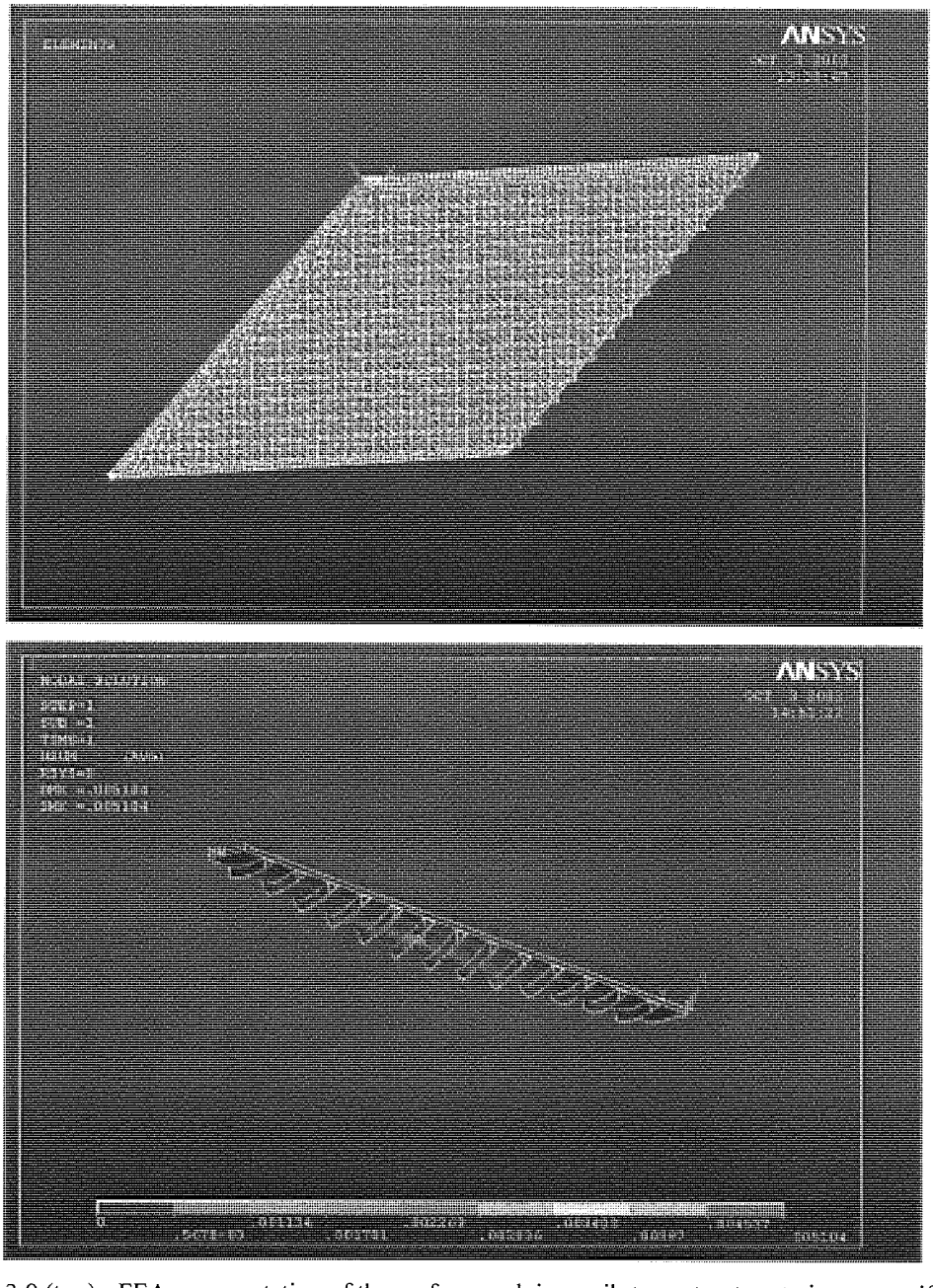

Figure 3.9 (top) - FEA representation of the surface applying a rib-type structure to increase stiffness. (bottom) - Deformation of the surface subjected to a 150kg load at the centre of the plate.

Figure 3.9 shows an FEA representation of how the structure will appear with a rib-type strengthening structure. Note: that the application of ribs does not stretch to the very edge of the surface. Therefore, the structure could be integrated on a supporting framework to house the sensing elements under the surface.

On the appliance of a 150kg loading at the centre of the surface it can be observed from the right figure in 3.9 the deformation lies within the respective requirement. In this case the maximum deformation of the surface is given as 5.1mm. This therefore could be a working solution, but would require a large surface thickness of 16.66mm to give the required stiffness, compared with 4mm for a steel plate. An alternative solution would be to simply select a solid PVC surface with a thickness of 16.66mm, which may improve the cost and efficiency in the manufacturing process. However this would also be unacceptable as a solution to fit within the design limitations of the surface and structure.

A fibreglass surface was also investigated, but to generate the required stiffness a thickness of 12.69mm would be required consisting of 29 unidirectional layers of E glass fabric material with a stiffness of only 6.9GPa. Other problems exist with this solution in the manufacturing process only half of this thickness can be cured at any one time due to the limitations of the processing machines. The quality of the material could also be a costly solution, i.e. this solution would cost 100 times that of a steel sheet.

3.2.5 Harmonic responses of the selected surface and structure

A surface needs to be selected with a fundamental frequency greater than the highest possible frequency present in the working load. Dujardin (1997) analysed a smoothing technique for data capture in human gait analysis. The analysis applied a frequency filter with a cut off at 10Hz to eliminate any external noise. From this it is suggested that most human movement for gait will occur in the 0-10Hz bandwidth. For the purpose of surface design the natural frequency of the material must be largely different from this bandwidth to prevent surface resonance.

A simple test is to be carried out to determine what the natural response is of the working surface and structure, through a frequency tap test. Sensing elements are positioned under the surface to record the mechanical deformation of the surface under an instantaneous impact. In this case a wooden mallet is used to provide the instantaneous impact on the

surface. However, a wooden mallet is not a point load and will also have its own natural frequency there will be a time delay between the impact and vibration, such that the natural response of the surface is unaffected by the use of the mallet. Figure 3.10 shows the response of the wooden surface and supporting aluminium frame around the surface. The examined position of the resonant frequency is from a sensing element at the position of (60, 27)cm and is in proximity to the centre of the surface and impact force applied to the surface. The selection of these coordinates is so that the magnitudes of vibration are greater and so the reacting effects are more observable.

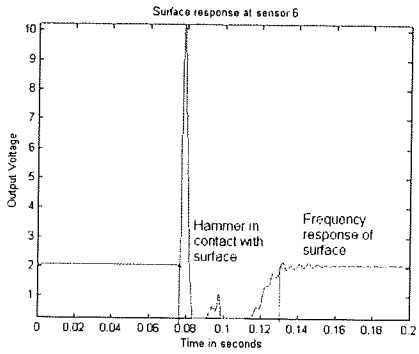

Figure 3.10 - Frequency tap test of the wooden surface.

The output voltage from a reflective optical sensing element is displayed in figure 3.10, verses the time, which is in contrast to the magnitude. Although, the test shows that the element reads 0V after impact, this implies that the surface is touching the head of the element, albeit the only characteristics of interest, is the frequency and signal decay shown in the right of the figure. This is opposed to the magnitude of deformation of the surface at the sensor point. However the output voltage in this case is directly proportional to the magnitude of deformation and is given as $\mathbf{V}(t) = \alpha . \mathbf{w}(t)$. Thus the change in voltage can be assumed to be equal to a proportional change in deformation of the surface at the sensing point.

The resonant harmonic responses are taken from all examined surfaces, using a National Instruments USB data acquisition card with a capture rate of 10000 Hz, to prevent aliasing of the captured data. The responses are then analysed through an FFT to determine the numeric value of the fundamental or resonant frequency, in figure 3.11.

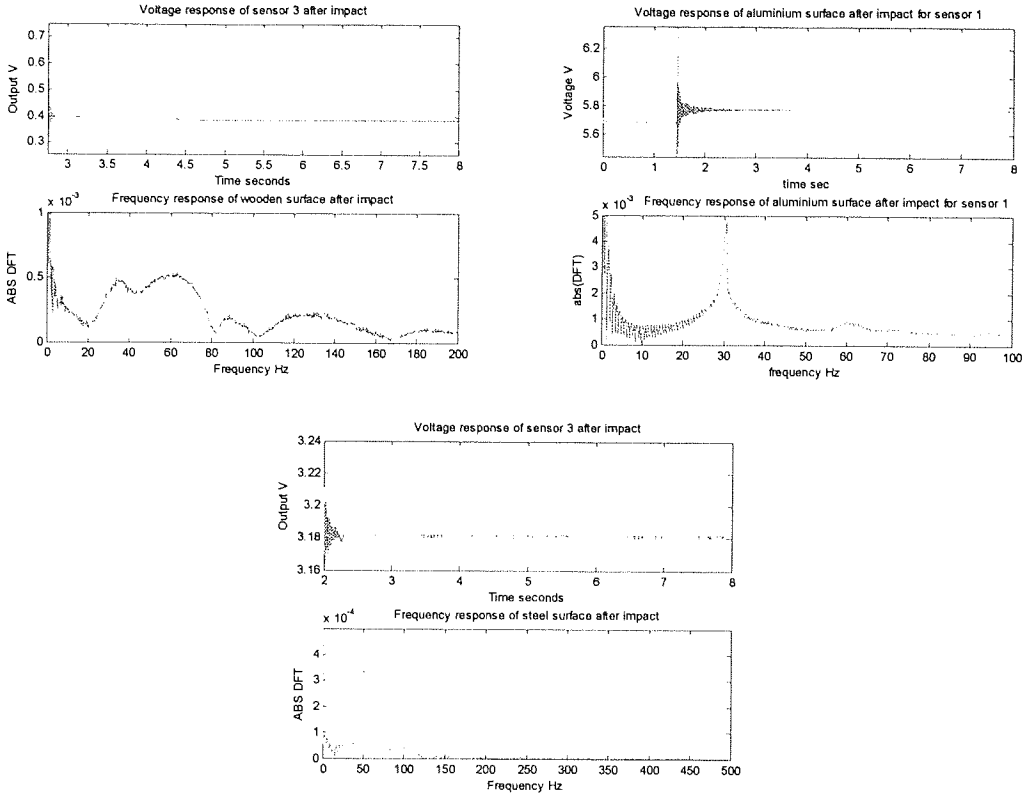

Figure 3.11 – (top left, top plot) - Is the response of a proximity sensor positioned under the surface for a wooden surface supported around the edge subject to a sudden impact. (top left, bottom plot) - Is a frequency plot (DFT) of the proximity sensors response, that represents the harmonic response of the wooden surface following a sudden impact.

(top right, top plot) - Is the response of a proximity sensor positioned under the surface for an aluminium surface supported around the edge subject to a sudden impact. (top right, bottom plot) - Is a frequency plot (DFT) of the proximity sensor under the aluminium surface, following impact.

(bottom, top plot) - Is the response of a proximity sensor positioned under the surface for a steel surface supported around the edge subject to a sudden impact. (bottom, bottom plot) - Is a frequency plot (DFT) of the proximity sensor under the steel surface, following impact.

Figure 3.11 (top left, bottom) illustrates the resonant frequency for the wooden surface is at around 20-70Hz when the whole system vibrates until rest after a sudden impact. These smeared frequency responses indicate that the wooden surface is either an amalgamation, or a composite material with resonant frequencies in the range, as there is no definitive resonant spike. This is indicative of the actual material as the wooden surface is a chipboard material being made up from an amalgamation of woodchip and glue.

The aluminium surface structure under examination gave a resonant frequency of around 30Hz. This is close to the possible loading frequency of the body which can affect the response of the surface in conjunction to the loading. Also it is to be noted that the aluminium surface was only supported by ten points around the edge of the surface and that visual and audible rattle occurred at the edge of the surface after the testing impact. This indicated that this structure has poor damping qualities for the absorption of loading impacts.

In the bottom plot in the figure 3.11 for a 4mm steel surface supported around the edge, shows a possible working solution. In this case the resonant frequency has been determined to be at around 50Hz which would be suitable for the expected loading frequencies of the body.

3.3 Sensory elements required to measure the deformation of the surface under an applied load

The sensing elements are incorporated to provide inputs to the information system. Sensing elements can be classified as being either static or dynamic devices. Sensing elements avoid the effects of aliasing, if the frequency of the working load is within the frequency response of the element. Such elements can give steady state responses, as opposed to dynamic elements that tend to be differential devices that only respond to changes in the condition of the contact. Dynamic elements can be assimilated to being similar to that of the Fast Adapting (FA) mechanoreceptors in the hand that can determine conditions such as slippage and vibration.

Tactile sensing in general tries to determine properties such as force, proximity, contact and is usually inferred through the measurement of a deformation or strain of a known material. Various static devices can provide such required functions and are to be discussed in detail in this section with the case for and against to aid in the selection process for an appropriate device to be used in this research.

3.3.1 Capacitive devices

Capacitive devices are used to measure or relate proximity to potential electric charge between two conductive surfaces. This can be described by:

$$C = \frac{\varepsilon_0 \varepsilon_r .l.w}{d} \tag{3.27}$$

Where C is the capacitance of the device in farads (F), ε_r is the dielectric constant of the material which is used as an elastomer between the two plates of the capacitor, ε_0 is the permittivity of free space given as the value of 8.85×10^{-12} Fm^{-1}, the length of the plates l and width of the plates w are multiplied to give the cross sectional area of overlap between the two plates in (m^2) and d is the distance between the two plates in (m). A capacitive touch sensor relies on the applied force either changing the distance between the plates or the effective surface area of the capacitor as either a function of:

$$C=f(K/d) \text{ or } C=f(K.(l \text{ or } w)) \tag{3.28}$$

Or in a resonant LC circuit a change of capacitance or inductance will give a change in resonant frequency through:

$$f_r = \frac{1}{2\pi\sqrt{LC}} \tag{3.29}$$

Where f_r in (3.29) will inevitably change through the capacitance variances given in (3.27). However, these devices require amplification circuitry as the output range of these devices is very small with respect to a small change in capacitance. These devices also need to be heavily screened, as stray capacitance from the human body can give poor resolution. Such noise can also change the resonant frequency responses through an LC circuit, thus changing the electrical potential. These devices are also limited to applications with limited loading conditions that give small deflections. From (3.27) it can be noted that a large capacitance of the device is given by a thin dielectric or gap between the two plates d. Thus, relatively small deflections of the capacitive plate give large changes in capacitance and hence a greater output potential. However, if the device

is to be used to determine high loading magnitudes, then the distance d needs to be increased to accommodate the subjected large magnitudes of deformation. Hence the resultant capacitance and output potential of the device will inevitably be reduced. For example; Fearing (1990) only applied a loading stimulus in the order of 50-100 grams on the capacitive surface.

Capacitive approaches were first integrated as displacement sensors by Spencer (1984) who applied a component capacitance measurement system for component identification through a sorting robot. Other successful uses of capacitive sensors have been demonstrated by Jayawant (1985), Peine (1994), Chen (1998) who applied capacitive methods to MEMS systems and interestingly Fearing (1990) who applied an array of 96 capacitive sensing elements in a robotic finger to describe the localisation of forces to within an accuracy of 0.2 tactels and a measurement of the total and tangential force to within an accuracy of 20%.

3.3.2 Conductive and resistive devices

The uses of compliant materials that have defined force-resistance characteristics have received considerable attention in touch and tactile sensor research. The output of the sensor can be in the measurement of the resistance of a conductive elastomer or foam between two points. The majority of the sensors use an elastomer that consists of a carbon doped rubber that can convert force information into an electrical resistance change through an alteration of particle density. In general, resistance r of the conductive elastomer per unit area for a constant temperature is given as:

$$r = kp^{-n} \tag{3.30}$$

where k is the constant of the elastomer, p is the applied pressure and n is the sensitivity factor for pressure. Furthermore, this type of sensing device is also sensitive to changes in temperature, as the volume of the sheet changes with respect to a change in temperature. If the resistance measurement is taken between opposing surfaces of the elastomer, the

upper contacts have to be made using a flexible printed circuit, to allow movement under the applied force. The output of which can then be simply conditioned through a voltage divider network to provide the required output for further processing and can be easily constructed to produce a tactile image with a high resolution. However, these types of sensors suffer from a number of significant disadvantages:

- Elastomer-based sensors are highly non-linear. In addition the time constant of the elastomer, when force is applied, is different from the time constant when the applied force is removed.
- The force-resistance characteristic of elastomer based sensors are highly non-linear, requiring the use of signal processing algorithms.
- Due to the cyclic application of forces experienced by the tactile sensor, the resistive medium within the elastomer will migrate over a period of time.
- Additionally, the elastomer will become permanently deformed and fatigued leading to permanent deformation of the sensor. This will give the sensor a poor long-term stability and will require replacement after an extended period of use.

However, even with these disadvantages, the devices are widely used commercially due to their simple design and interfacing capabilities with robotic devices. One of the first examples of this applied approach was one by Johnson (1974), who developed a tactile prosthetic device to indicate the magnitude of an applied pressure. Other devices that have been successfully developed have been ones by Larcombe (1981), Yuji (2000), Russell (1990) and commercially by Tekscan (2000) who utilised conductive and semi-conductive inks for elements positioned in to a matrix of electrically conductive rows and columns to form a sensory surface.

3.3.3 Magnetic and inductive devices

There are two approaches to the design of touch or tactile sensors based on magnetic transduction. The electrons in a conductor are deflected by a magnetic field generated by an applied force on a permanent magnet perpendicular to the applied electric current resulting in a change of flux. Firstly, the flux measurement can be made by either a Hall effect or a magnetoresistive device. Or secondly, the core of the transformer or inductor can be manufactured from a magnetoelastic material. This can deform under pressure and cause the magnetic coupling between transformer windings, or a coil's inductance to change. A magnetoresistive or magnetoelastic material is one whose magnetic characteristics are modified when it is subjected to changes in externally applied physical forces. The magnetorestrictive or magnetoelastic sensor has a number of advantages that include high sensitivity and dynamic range, no measurable mechanical hysteresis, a linear response and physical robustness.

This was demonstrated by Checinski (1985), who developed a magnetoelastic device that could measure forces linearly in the 1-100g range, through an amplification and filtration process and suggests that hysterisis, repeatability and temperature error for this type of device is estimated to be less than 1%, 5% and 1% per 10^0C respectively. However, disadvantages exist for Hall effect devices as the e.m.f.s produced are only a few micro-volts and the effect is strongly temperature dependant. This is so that the outputs obtained are low and require amplification. Also a great associated problem is the magnetic screening, particularly if an elastic and thin sensor is to be constructed.

One of the first Hall effect devices was used by Kinoshita (1983), who applied elements in a robotic finger to determine a cross sectional pattern of an object applied to the contacting area. Other similar devices include Kinoshita (1984) and Leaver (1998) who also applied these devices for robotic applications.

3.3.4 Optic, photoelasticity and fibre optic devices

The rapid expansion of optical technology in recent years has led to the development of a wide range of displacement sensors. The operating principles of optical-based sensors are well known and fall into two classes:

Intrinsic, where the optical phase, intensity, or polarization of transmitted light are modulated without interrupting the optical path
Extrinsic, where the physical stimulus interacts externally with the primary light path.
Intrinsic and extrinsic optical sensors can be used for touch, torque and force sensing.

For industrial applications, the most suitable will be the ones which require the least optical processing. For example, the detection of phase shift using interferometry is not considered a practical option for robotic touch and force sensors. For robotic touch and force-sensing applications, the extrinsic sensor based on intensity measurement is the most widely used due to its simplicity of construction and the subsequent information processing. The potential benefits of optical sensors can be summarized as follows:

- Immunity to external electromagnetic or capacitive interference
- The use of optical fibre allows the sensor to be located some distance from the optical source and receiver.
- The use of reflective optical sensors allow for large sensing ranges and can be positioned in proximity to the force surface
- Low weight and volume

Modulating the intensity of light by moving an obstruction into the light path can change the light intensity received and hence give a representative change in resistance through a silicon phototransistor or CCD (charged coupled device). This change in resistance can give a change in output potential through a simple potential divider configuration. The force sensitivity is determined by the spring coefficient in the tactile material or

elastomer. Alternatively, reflective sensors can be constructed with source-receiver fibre pairs embedded into a solid elastomer structure.

When applying a load to a tactile surface this causes the surface to deform by creating either an obstacle to the light path or moving in such a way that the light intensity changes in relation to the deformation of the material. These devices are designed with an Infra Red (IR) transmitter receiver pair situated in close proximity to each other and are facing in the same direction. The transmitter projects an IR sphere around the transmitting device when powered by a direct current and the receiver responds when the IR from the transmitting device is reflected back in to it. The distance between the transmitter to reflective surface and back to the receiver is therefore a function of the light intensity captured by the receiver. The light intensity entering the receiver causes the internal resistance of the receiving device to rise or fall and acts like a variable resistor. Hence, an output potential response can be configured into what is required through the use of a voltage divider circuit, or through the properties of the surface or reflective object. One of the first examples of these devices was used by Rebman (1983) and has been used in the tactile sensing field by authors such as Brett (2000), Begej (1988), Fischer (1996),

Photoelasticity is the phenomena where stress or strain causes birefringence in optically transparent materials. It relies on a phase shift introduced into a beam of polarized light. This is generated from a difference in the refractive indices along different optical axes with the sensing material and hence the intensity of the light at the detector (CCD) changes as a function of the applied force.

This type of sensing device has been used as a force sensor to measure pressure profiles on the soles of the feet during human gait (Maalej 1988) and is of considerable importance in the measurement of slip, so as stresses parallel to the sensing surface can be detected using this approach (Eghtedari 1989). Other examples of the application of this device have been documented by, Cameron (1988), Relmer et al. (1999), Howard (2001) and Mott et al. (1986).

Optical fibres were first used solely for the transmission of light to and from a light transmitting sensor. However, it is possible to construct tactile sensors from the fibre itself. A suitable design can be based on internal-state microbending of optical fibres and is the process of light attenuation in the core of the fibre when a mechanical bend or Bragg grating (of the order of few microns) is applied to the outer surface of the fibre. The degree of attenuation also depends on the fibre parameters, such as the radius of curvature and spatial wavelength of the bend.

Current research has suggested the feasibility of this approach and was first demonstrated for the application in robotic end effectors by Crosnier (1985). He applied a matrix of 64 fibre optic cables with light photo detectors to respond to normal forces applied to the structure. Other such examples of this approach have been composed by Schoenwald (1987), King and White (1985) and Taine (1985).

3.4.5 Piezoelectric and Polyvinylidene Fluoride (PVDF) Devices

Piezoelectric devices have been found to be the most common devices used in force sensing to date and were first discovered in crystals like quartz. A mechanical stress applied to the crystal lattice leads to a concentration of charges on the surface that can be measured. Piezoelectric crystals are ridged and therefore the displacements of the crystals are almost negligible; however they inherently feature excellent linearity over a wide amplitude range and possess good signal to noise ratio factors in the order of 120dB. These devices are classified as dynamic devices and are only highly responsive for the measurement of changing loading condition due to the signal decay when the impinging load condition remains constant.

These devices are usually manufactured through the use of polymeric materials such as Polyvinylidene Fluoride (PVDF) that exhibit piezoelectric properties. Polyvinylidene Fluoride is not piezoelectric in its raw state, but can be made piezoelectric by heating the PVDF within an electric field. A thin layer of metalization is applied to both sides of the

thin PVDF to collect the charge and permit electrical connections being made. One of the first examples of PVDF being used as a piezoelectric force sensor was one by Plander (1987), who describes the application of the system to robotics. Other such systems apply this approach for robotic gripping mechanisms for force (Pirolo 1989) and slippage determination are ones by Dargahi (2000) and Canepa (1998).

3.3.6 Piezoresistive and strain devices

A strain gauge is a resistive sensor and when attached to a surface will detect the change in length of the material as it is subjected to external forces. The strain gauge is manufactured from either resistive elements (foil, wire, or resistive ink) or from a semiconducting material. A typical resistive gauge consists of the resistive grid being bonded to an epoxy backing film. If the strain gauge is pre-stressed prior to the application of the backing medium, it is possible to measure both tensile and compressive stresses. The semi-conducting strain gauge is fabricated from a suitable doped piece of silicon and shows a relationship between the electrical resistances to mechanical stresses and is known as the piezoresistive effect.

Pressure transducers operate on the basis of resistive or capacitive sensing methods. The devices are usually configured with a bridge configuration of strain elements and a pressure sensitive element to deform under load. The most common is the diaphragm pressure sensor that consists of a thin stretched membrane, whose deflection is usually measured through strain gauges. However, the disadvantages of these sensing elements are their relatively small elasticity, small resistance changes and the fact that they need to be integrated in or on the sensing surface that can generate problems for surface replacement. From this only small deformations can be monitored and on the collection of data the output response needs to be amplified.

These devices have been applied to many applications. Russell (1993) applied piezoresistive devices to a robotic grasping mechanism so that a surface contact profile

could be determined for the manipulation of the contacting object. Other piezoresistive tactile devices that are mainly used for robotics are ones by Fiorillo (1997), Leung (1996), Hillis (1982), Russell (1993), Fearing (1990) and for foot pressure profiles by Rittler (1988).

3.3.7 Ultrasonic devices

These sensors use electrostatic material, such as piezoelectric crystals. When excited by a high voltage, the crystal bends and vibrates to send sound pressure waves out from the sensor to a range between 0.5 to 30 feet. These sound waves are in the 50 kHz range, making the sensor insensitive to surrounding noise that occurs in the audible (100 Hz to 20 kHz) range. A timer is started when the 50 kHz sound wave is sent out. The same electrostatic element then acts as a receiver, deforming when struck by sound waves. The circuit accompanying the sensor contains a tone decoder and acts as a band pass filter, ignoring all sound except that in the 50 kHz range. When a 50 kHz signal is received, the timer is stopped and a voltage proportional to the time of flight is calculated. The sensor must wait for the sound wave to return from a maximum distance of 30 feet and therefore has a maximum sampling rate of around 20 Hz. These devices are reported to record displacements from the element from as little as 30mm.

Ultrasonic sensors are very stable when measuring distances of surfaces that are either parallel or cylindrical to the source and should be used when accuracy is needed in these situations. They tend to become less reliable when the surface of interest is skewed relative to the sensor. This has to do with the reflective nature of sound waves and the sensor's 15° angle of view. Other associated problems exist such as interference from air movement from heating or air conditioning systems, hissing from pipes or from road drills and telephone rings. All of these stimuli can create noise near or in the ultrasonic range and affect the devices response.

However, there are several authors who have described displacement sensing devices using this approach, namely Ando (2001) who designed a system with a 2x2 matrix of ultrasonic transmitters and receivers. From this a model of the gradients from the ultrasonic wavefronts was used to obtain the precise location of the emission source to derive the three rotational and translational components of the object. The results show that linearity and independence of each component were good, giving accuracies of within 5μm in a measurable range of 2mm and 0.06^0, in a measurable range of 5^0. Other such systems include ones by Komatsubara et al. (1993) and Shinoda (1994) who used ultrasonic methods for quick detection and localization of touching, sensation of texture under movement, quick detection and localization of slip and detection of precursors of slip.

3.3.8 Selection of appropriate sensing element

An appropriate sensing element must possess various desired characteristics. A sensing element must:

1. possess unique output responses for a sensing ranges between 0 and 5mm;
2. possess minimal supporting circuitry;
3. possess high levels of repeatability;
4. possess a high level of sensory response;
5. possess small dimensions as to increase flexibility in the design;
6. the sensory responses must be non or minimally effected by outside interference;
7. be relatively inexpensive on the market at the current time of application;
8. give changing responses at static and dynamic conditions;

Using this criterion it is possible to select the most appropriate sensing element for the required application, however, all elements could be used to provide adequate deformation measurement. It is possible to examine all elements against this criterion to determine the most appropriate device: see table 3.2

Criterion\Element	Capac.	Condu.	Magne.	Optic.	Piezo	Resis.	Ult.Son.
1		√	√	√	√	√	
2				√			√
3	√		√	√	√		√
4	√	√	√	√	√	√	√
5	√	√	√	√	√	√	
6		√		√	√	√	
7	√			√	√	√	
8	√	√	√	√		√	√
Total Points	**5**	**5**	**5**	**8**	**6**	**6**	**4**

Table 3.2 - Indication of adherence to the desired criterion for all possible sensing elements.

The results show that reflective optical devices are the most suited for this application, as they satisfy all the criteria. The selected optical device is to be a reflective optical element (SY-CR102) (figure 3.12 with its respective response characteristics). Fall and rise times tend to be within 1ms which is adequate for the operation. However, these devices are primarily designed as counting devices and for the discrimination of rotation speeds, but can be very useful for the measurement of proximity.

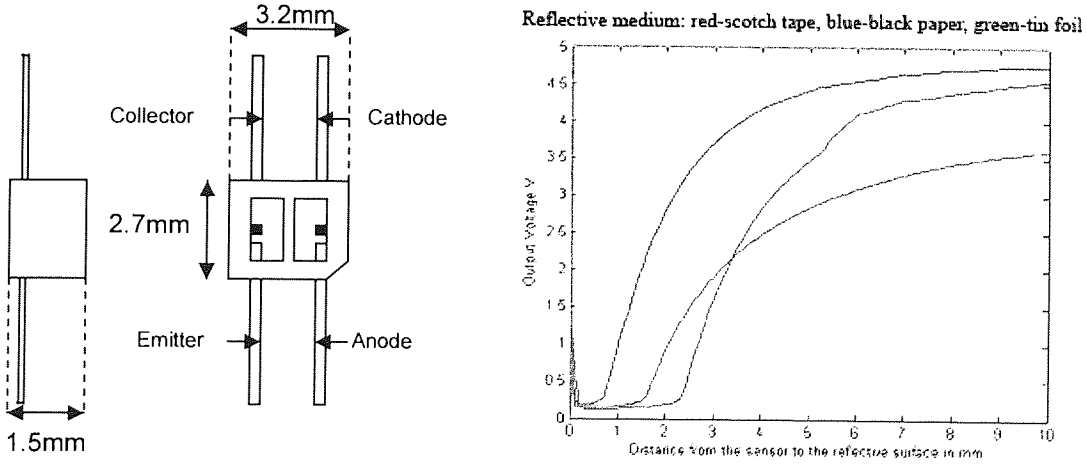

Figure 3.12 (left) - The dimensions of the device. (right) - The characteristic response of the device.

Figure 3.12 illustrates three important design features for the integration in the sensing system. The figure on the left illustrates the dimensions of the selected device and that on the right indicates the sensing range of the element with the proposed reflective material.

This plot was developed through the use of a travelling microscope, in a darkened room, so as to simulate conditions expected under the surface. The microscope surface was

covered with the relevant reflective material, and was initially positioned at the tip of the element. The output of the element through the divider network was then recorded at the initial condition. Subsequent voltages were then similarly recorded at 0.1mm increments up to a distance of 10mm. Although the surface in bending will provide a slight angle to the sensing point, the angle of bend is considered to be so small, that the reflective surface can be assumed to be almost parallel to the element. Based upon this assumption the reflective surface was always positioned parallel to the tip of the element to provide the sensor characteristic curves shown.

The working sensing range is to be through the decay of the light intensity as a function of $1/r^2$. When the surface is moved away from the element, then a highly reflective medium is required to elongate the sensing range. In this case scotch tape has been found to be highly reflective and hence give an acceptable sensing range. However, the opposite is true if the working sensing range is to be in the range where the surface is too close to the sensing element, thus an absorbing material would be required. From these recorded calibrations, it can be taken that the surface must be positioned 7mm from the sensing element, so that a deformation of the required 5mm falls into the curved sensing range.

The sensing device and PCB mounting surface measure a thickness of 3mm, thus the gap between the deforming surface and sensory supporting surface is 10mm, indicating the dimensions of the supporting framework required.

The supporting circuitry of the element can be a potential divider network configuration with no need for amplification. This is due to the fact the resistance of the receiver in the element can vary between 0 to 5KΩ dependant upon the received light intensity. From this configuration it is possible to generate a direct output voltage response between 0 to 5V. The required voltage and current for the photodiode are 1.7V and 20mA respectively hence, the potential that must be dissipated through a supporting resistor is 3.3V if the supply to the device is 5V. From this the supporting value of the resistor can be calculated as (3.3/20mA) Ω, or 165Ω. The preferred value of this dissipating resistor is therefore 181Ω. The receiver requires 5V and 1mA operating current to operate hence the

resistance of the receiver can be calculated as (5/1mA) Ω, or 5KΩ. The set-up configuration can therefore be drawn in figure 3.13 of the element, with dimensional integration into the structure and golf mat.

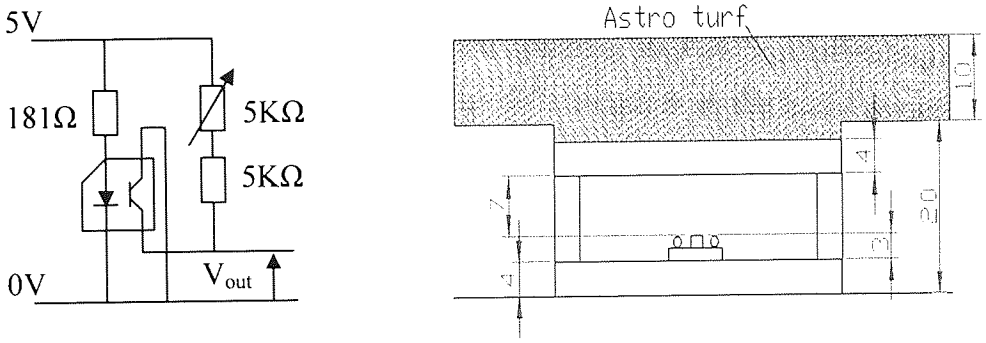

Figure 3.13 (left) - A schematic of the supporting circuitry for the sensing element. (right) - The dimensions of the structure, sensor and sensing range.

Figure 3.13 shows the schematic of the sensor with proposed supporting potential divider network. The output voltage or sensory response is taken directly as a voltage drop across the receiver when the resistance of the device changes. This is coupled with a variable resistor, so that the output characteristics can be changed to accommodate an optimal sensing range. This proposed method represents a simple and inexpensive solution to acquire voltage responses relating to the proximity.

The integration of elements into the structure within the golf mat is also given in figure 3.13. The figure indicates that the given constraints of the current golf mat have been adhered to, with the facilitation of the full force sensing system. The proposed system comprises of a sensory supporting steel surface 4mm and force surface ranging from 4-6mm. The force sensing surface has been designed to deform to within 5mm under the exposure of a 150kg load placed at the centre of the surface, however the system is designed handle deformations up to 7mm as a safety precaution to prevent damage of sensing elements. The proximity sensory element modules have also been designed so that they are as thin as possible (3mm), to allow for flexibility and minimisation in the design of the system.

Changing environmental factors can affect the performance of the sensory system. From this the response magnitudes of the elements can not be taken as direct descriptors. However it is possible to calibrate the elements to the surrounding conditions, through the analysis of the differences between initial and current responses. The initial sensing element's data acquisition defines the current operating state of the surrounding condition and then sequential acquisitions are taken as differentials from the initial responses. This is such that the sensing system can be robust against power noise, humidity and temperature changes.

3.3.9 Quantity of sensing elements required

This section describes the limitations and optimal quantity of elements that can be used under the surface to describe a desired stimulus. The first section analyses the quantity of sensing elements required, as to maximise the amount of information received by the system to describe the stimulus. The second section describes the limiting effect of the required number of sensing elements, as a function of the system accuracy. The third section describes a constraining evaluation of the number of sensing elements, as to enhance maximum and equal sensitivity between elements.

3.3.9.1 The advantages of using high numbers of sensing elements

The optimal number of sensors can be formulated from an analysis of varying numbers of sensing elements under the surface. The greater number of coupled sensing elements, the greater the number of differences that exist between sensing elements.

For example 4 sensing elements produces 6 possible differences between elements, 8 sensing elements, gives 28 possible differences and 12 sensing elements gives 66 possible differences between values. From permutation theory the number of differences y, is given as:

$$y = \frac{x(x-1)}{2} \tag{3.31}$$

It can therefore be noted that the greater the number of sensing elements (x), then the greater the number of differences (y) that can be used as information describing the stimulus on the surface.

Comparing the quantities of possible information received by a processor to handle the input information to describe the applied stimulus, between a RFSES and an Array system can be viewed in figure 3.14.

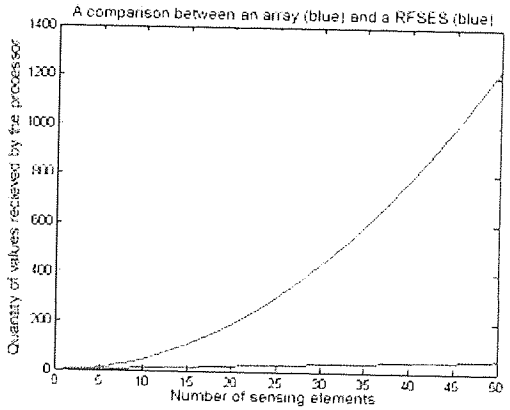

Figure 3.14 - Information received verses the number of sensing elements used to describe the stimulus. Blue curve is an Array system, Red curve is a RFSES.

Figure 3.14 shows that using a RFSES to predict a loading stimulus is more effective than that of an array method, for example the determination of load position, or magnitude.
A greater number of sensing elements in a RFSES maximises the possible describing values received by the processor, through a correlating function between elements to produce a transformation of the output relating to the applied stimulus. This can be compared with a linear function relating the number of sensing elements to the quantity of values received by the transformation algorithm in an array system. However, this is only true in this case for a number of elements greater than three.

The transformation of the presented values in a RFSES can either be a linear or non-linear approach, such as a matrix inversion, or neural network method respectively to

provide the association between sensing elements. This can be compared to an array method that only facilitates a straight forward transformation of the measured values at a particular sensing point, to be represented as a singular value or representative picture element of the stimulus on a monitor or screen.

3.3.9.2 Limitations on the number of sensing elements

The number of sensing elements required can also be limited, to be enough to give the accuracy required to interpret the loading condition. A test can be undertaken to determine the system accuracy with respect to the number of sensing elements used.

To provide this analysis, empirical sensory data is collected into a matrix, from 16 elements positioned in an equal pitched 4x4 matrix formation under the surface. A 4mm steel surface with dimensions of 790x540mm, supported on an unconstrained frame around the edge of the plate, was used to provide the testing surface and structure. A singular loading hook with circular base plate of radius 20mm and mass of 0.5kg was then placed in the centre of the plate. Loads ranging from 0 to 40kg, in steps of 1kg were incrementally loaded and unloaded, for which to provide the changing electrical voltages based upon 91 different loading conditions.

The voltages collected with respect to the loading applied were stored in an input and output matrix respectively, whereby each sensing elements data corresponds to a singular vertical vector in the input matrix. These vectors can therefore be randomly or selectively removed from the input matrix and a linear inversion method and system accuracy can then be recalculated from a reduction in the selected element. On the basis of this, the input matrix can change dimensionally; hence a simple matrix inverse is not possible for non square matrices.

However, the Moore-Penrose matrix inverse, also known as a generalised inverse or pseudo-inverse was first investigated by Moore (1920) and then Penrose (1955) and can be used with non square matrices. Given that X K = Y, the result is shown in the form:

$$K = (\mathbf{X}^T X)^{-1} X^T Y \tag{3.32}$$

Where **Y** is the required output or target of the system relating to the collected input patterns **X**. **K** is therefore a matrix of linear coefficients that provides the mapping between input and output matrices X and Y. Further empirical data is then collected **X''** and measured output **Y''** to test the accuracy of the developed mapping **K** from the trained samples **X** and **Y** from:

$$\text{error} = \frac{1}{N}\sum_{i=1}^{N}\sqrt{((\mathbf{Y}^C{}_i - \mathbf{Y}_i'')^2)} \tag{3.33}$$

Where **Y''** is the target and $\mathbf{Y}^C$ is the calculated value through the determination of pseudo-inverse method **K**. The test carried out captured 100 voltage data sets from all sixteen elements under the surface positioned in a matrix configuration with its respective measured load magnitude at the centre of the plate. From this a linear mapping **K** of input to output data can be formulated and then tested a further 14 times with sensory data unknown to the mapping evaluation. The regressive result of which can then be compared to the actual loading on the surface to generate the system accuracy for load determination.

The data value given by one of the elements in the matrix is then randomly eliminated from the training and testing input data samples and then the linear mapping **K** is then recalculated. This is then evaluated for accuracy from the testing data samples with the respective elements data removed. This process is then repeated until only one element remains under the surface giving an accuracy verses sensor number result. This whole analysis is then carried out a further 3 times to determine how the removal pattern of sensing elements affects the accuracy in the system with the remaining elements under the surface. The results can be seen in figure 3.15.

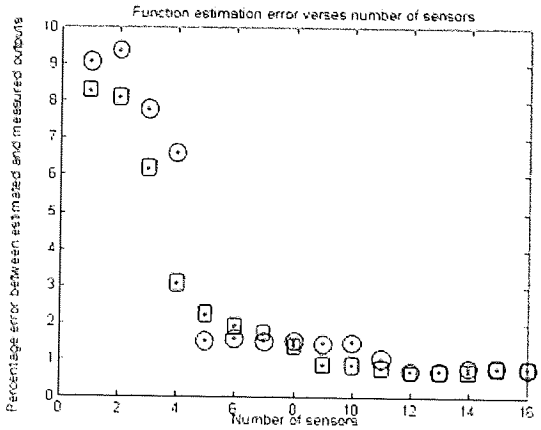

Figure 3.15 - How random removal of various sensing elements affects the system accuracy of load determination. Squares represent a random removal of elements for the 1st cycle and circles represent the system accuracy for a 2nd random removal of sensing elements in the matrix.

From the results in figure 3.15, it can be seen that there is variability in the accuracy between tests when the sensors have been randomly removed. This implies that a reduction in some sensing elements at set positions gives little rise to changes in accuracy (green circle trend: removal of five random sensing elements from 10 to 5 has little effect on system accuracy) where others will have a large effect (blue square trend: removal of 5 random sensing elements from 10 to 5). This suggests that some elements are more dominant than others and some elements are recessive at the set positions in the sensing array. From these results, the average reduction in error is given in figure 3.16, from an analysis of 100 sensor decay pattern orders as:

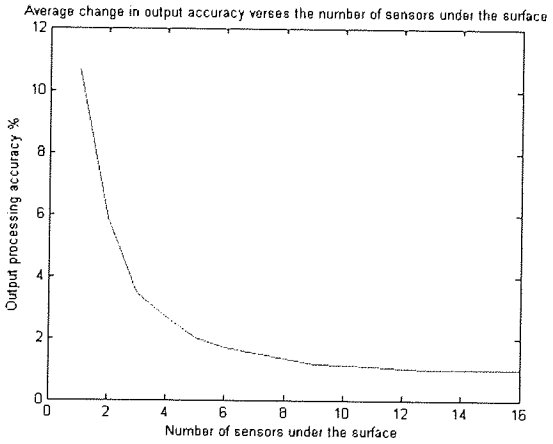

Figure 3.16 – Average accuracy of the system related to number of sensing elements.

It can be seen that only eight sensing elements are required to give output accuracies similar to that of 12 or greater sensing elements. At this point, the graph starts to converge; hence, increasing the number of sensing elements under the surface, will have little or no effect to large changes in accuracy of the system. The results and conclusion from this experiment are derived through the use of the pseudo-inverse computation of the voltage matrix, as opposed to alternative neural methods.

3.3.9.3 Optimal positioning of sensing elements

It is important to optimise the location of the sensing elements, such that all sensing elements have equal and maximal contribution as inputs into the information processor. Tongpadungrod (2003) optimised sensory locations in a one and two dimensional space. This was accomplished through an optimisation algorithm to maximise the principal components from the possible output classifications from the simulated sensory input deformations. However, the method discussed here shows an alternative and more specific regressive approach applied to the mathematical interpretation of the two dimensional surface in deformation.

In this case we assume that once the golfer has mounted the surface, the feet remain in stance position during the golf swing. For simplicity of the calculation, the load distribution of the feet we take as four main points. It is assumed that the forces of the feet act mainly at the heel and hallux areas of each foot. In reality the forces act at four main areas on each foot, these are the ball (digitus minimus areas), heel (calcaneous areas), metatarsals and hallux. However; over 82% of the force is carried by only the heel and hallux areas during a quasi-static stance (Kawishima 1999), thus making the assumption valid.

Based on the 95th percentile for males, the stance width is fixed in this case at 0.5m and the distance between the balls of the toes and heels is 0.24m. The coordinates of stance in this case has been selected to be equally positioned on the surface as: (0.145,0.39)m for

the left ball of the toe, (0.145,0.15)m for the left ball of the heel, (0.645,0.39)m for the right ball of the toe and (0.645,0.15)m for the right ball of the heel.

The optimal position of the eight sensing elements from figure 3.16 can be evaluated through a manipulation of Navier's model (3.22) for thin plate deformation. It is assumed that the surface is simply supported around the edge. The full expression for the deformation at any point of interest, i.e. at sensor point one (x_1,y_1), is described as the loading at the point (g_1,h_1) with a magnitude of W_1, plus the loading at point (g_2,h_2) with a magnitude of W_2, plus the loading at point (g_3,h_3) with a magnitude of W_3 and plus the loading at point (g_4,h_4) with a magnitude of W_4. This is a superposition of all of the loading conditions on the surface to derive the deformation at the point of interest (x_1,y_1). The full expression given as a derivation of (3.22) gives:

$$
\begin{aligned}
w(x_1,y_1) = &\left(\sum_{a=1}^{21}\sum_{b=1}^{13} \left(\frac{\sin\left(\frac{a.\pi.x_1}{e}\right).\sin\left(\frac{b.\pi.y_1}{f}\right).\sin\left(\frac{a.\pi.g_1}{e}\right).\sin\left(\frac{b.\pi.h_1}{f}\right)}{\left(\left(\frac{a^2}{e^2}\right)+\left(\frac{b^2}{f^2}\right)\right)^2} \right) \right) \cdot \left(\frac{48W_1\left(1-v^2\right)}{\pi^4.e.f.t^3.E} \right) \\
&+ \left(\sum_{a=1}^{21}\sum_{b=1}^{13} \left(\frac{\sin\left(\frac{a.\pi.x_1}{e}\right).\sin\left(\frac{b.\pi.y_1}{f}\right).\sin\left(\frac{a.\pi.g_2}{e}\right).\sin\left(\frac{b.\pi.h_2}{f}\right)}{\left(\left(\frac{a^2}{e^2}\right)+\left(\frac{b^2}{f^2}\right)\right)^2} \right) \right) \cdot \left(\frac{48W_2\left(1-v^2\right)}{\pi^4.e.f.t^3.E} \right) \\
&+ \left(\sum_{a=1}^{21}\sum_{b=1}^{13} \left(\frac{\sin\left(\frac{a.\pi.x_1}{e}\right).\sin\left(\frac{b.\pi.y_1}{f}\right).\sin\left(\frac{a.\pi.g_3}{e}\right).\sin\left(\frac{b.\pi.h_3}{f}\right)}{\left(\left(\frac{a^2}{e^2}\right)+\left(\frac{b^2}{f^2}\right)\right)^2} \right) \right) \cdot \left(\frac{48W_3\left(1-v^2\right)}{\pi^4.e.f.t^3.E} \right) \\
&+ \left(\sum_{a=1}^{21}\sum_{b=1}^{13} \left(\frac{\sin\left(\frac{a.\pi.x_1}{e}\right).\sin\left(\frac{b.\pi.y_1}{f}\right).\sin\left(\frac{a.\pi.g_4}{e}\right).\sin\left(\frac{b.\pi.h_4}{f}\right)}{\left(\left(\frac{a^2}{e^2}\right)+\left(\frac{b^2}{f^2}\right)\right)^2} \right) \right) \cdot \left(\frac{48W_4\left(1-v^2\right)}{\pi^4.e.f.t^3.E} \right)
\end{aligned}
\tag{3.34}
$$

It is assumed that the deformation w of the surface, can be measured by the sensor at (x_1,y_1), the positions of the loads are known, the material dimensions and properties of the

surface are known and that the only variables that remains unknown are the magnitudes of the four loads that represent the loading profile of the golfer on the surface, where: W_1 is the load on the left toe, W_2 is the load on the right toe, W_3 is the load on the left heel and W_4 is the load on the right heel).

The expression (3.34) can therefore be reduced down due to the calculable constants *A*, *B*, *C* and *D* to give:

$$w_1(x_1, y_1) = A_1W_1 + B_1W_2 + C_1W_3 + D_1W_4 \tag{3.35}$$

This can also be extended to the other elements, which in this case are seven more positions and measurements of sensing elements under the surface. This will therefore generate eight equations with the four unknown loads, based upon the finding illustrated in figure 3.16 for the selection of 8 sensing elements. This can be represented in matrix form to give:

$$\begin{bmatrix} w_1 \\ w_2 \\ : \\ w_8 \end{bmatrix} = \begin{bmatrix} A_1 & B_1 & C_1 & D_1 \\ A_2 & B_2 & C_2 & D_2 \\ : & : & : & : \\ A_8 & B_8 & C_8 & D_8 \end{bmatrix} \cdot \begin{bmatrix} W_1 \\ W_2 \\ W_3 \\ W_4 \end{bmatrix} \tag{3.36}$$

The loads $W_1 - W_4$ can be derived through a pseudo-inverse of the constants in the multiplying matrix, times by the measured deformations *w* at the all of the sensing points. It is the condition of this pseudo-inverse that is of most interest. The condition of a matrix is the ratio between the largest and smallest singular value in the matrix and measures the sensitivity of the solution of a system of linear equations to errors in the data. It gives an indication of the accuracy of the results from matrix inversion and the linear equation solution. Values of the condition of the inverted matrix in this case close to 1 indicate a well-conditioned matrix and larger ratio values indicate poorly conditioned matrix similar to that of a Hilbert matrix, (Penny & Lindfield 2000).

This (condition number) benchmarking approach is one which can be derived from a theoretical evaluation, based upon the position of the sensing elements. Although other benchmarks, such as the derivation of the system accuracy for the position of such elements, can only be accomplished through physical measurement and movement of the elements under the surface. This method although arguably more informative, would be unacceptable as a working solution. This is due to the time required to collect training data for a number of loading conditions for every possible sensor location.

As the matrix in question is derived from mainly the selected positions of the elements, then a low condition number will indicate that there are no positions of elements that are more or less sensitive than the other elements in the system. If a high condition number is apparent then this will indicate that 'some elements' positions are more sensitive or dominant than other recessive elements. If the positions of the sensing elements move then this will inevitably change the configuration of the pseudo-inverse matrix and hence its final condition evaluation. It is therefore important to search for sensory locations that are of a low condition number, which indicates a maximum and equal sensitivity of the solution for cross a multiplication of the measured deformations.

To search and locate for the optimal positions with minimal condition numbers, a genetic algorithm (GA) has been applied to minimise this condition or cost function. This searching algorithm has been selected due to the non-linearity of the condition number algorithm available. The (GA's) are non-linear optimisation methods that function on the result of the output evaluation, generated from the selected input variables. However, the Conjugate Gradient Method (CGM) can be used as an alternative non-linear optimisation method, which is one of the principal algorithms used in an MLP network. Using the (CGM) as an optimisation algorithm, would require the (CGM) to be trained with many possible positions to condition numbers to determine the underlying function of the model as a set of weights and biases. The algorithm would then have to be tested with low condition number values to give optimal sensory positions, although these positions may be outside the limitations of the surface. So needs to be tested and checked for

infinite condition number evaluations. However, the (GA) will give solutions inside the defined limitations due to the maximum and minimum conditions applied to the GA.

The GA is modelled on the genetic evolution of any species, through a process of 'survival of the fittest'. To represent this evolutionary process, the positions of the sensing elements under the surface are to be held as a binary representation of the elements in the x and y directions, thus defining the limitations of the surface. The resolution in the x direction is to be held as a ten bit binary representation and a nine bit resolution in the y direction, due to the dimensional difference of the directions.

Initially, the eight sensing element positions are randomised, each generating its own binary representation of the coordinates of the position. All coordinate binary strings are then combined to give a chromosome or individual. The chromosome in this case is of 152 bits in length, with a breed ratio set to 50%. This ratio indicates the number of selected chromosomes that are to breed and the number of chromosomes that are carried forward to the next generation. A minimisation of the condition numbers are required for our application, however the GA searches for maximum conditions. But this can be resolved by looking for the reciprocal of the condition number. This is so that the condition number is maximised, in order to search for the true minimum condition number

The selection process takes place on the basis of the weighting of the cost values. Chromosome cost functions are then calculated to give percentages of the total summation of all of the cost function values. A random number generator is applied to select n number of chromosomes between 1 and 100 inclusive. This number will then select the chromosomes that are to be selected. If one chromosome holds a large percentage of the total value of the cost functions then it has a better chance of survival or having better odds for selection. A random 50% (breed ratio) of chromosomes carry forward to the next generation and the other chromosomes cross breed randomly to form new chromosomes. A cross breed in this case is also initially set as six genetic splices.

The first splice is a random number between 1 and 152. This will indicate where the splice is to be made. Assume a value of 10 is randomly generated then a swapping occurs between the chromosomes in individuals after this bit position.

Before splice:

Chromosome #1: 1101100011**0101010000100010011110**...152 bit length (coordinates x,y)

Chromosome #2: 0101011010***1001010101010110001101***...152 bit length (coordinates x,y)

After the splice the new chromosomes become:

New chromosome #1: 1101100011***1001010101010110001101***.....152 bit length

New chromosome #2: 0101011010**0101010000100010011110**.....152 bit length

This splicing is then carried out a further five times to generate two possible unique chromosomes. Splicing; also then occurs in the same way amongst the other breeding chromosomes and is then carried forward into the next generation.

A mutation is then applied to all of the bits in all of the chromosomes in the new generation, at a rate of 0.1% initially set in this case. A random number is then generated between 1 and 1000 inclusive. If this random number then equals the value of 1, then that representative bit is inverted from a 1 to a 0 or from a 0 to a 1, otherwise the possible mutation process then moves on to the next bit in the sequence and the random the process continues in a similar way.

Once the new generation is formulated then the cost functional values are re-calculated for all new and carried over populations and the process continues as before, until the minimum value of the cost function is determined. A comprehensive analysis requires an optimisation of the selected parameters. This will take the form of keeping all the possible parameters constant throughout the test and changing only one of the variables. This will therefore define the optimisation for that specific parameter. This is similar to the way the parameters are selected in an MLP network.

As mentioned earlier, the parameters that remain constant, for the first analysis are; the breed ratio set to 50%, the mutation rate set to 0.1%, the number of generations set to 100 and the number of splices set to 6. The parameter that is varied initially is the size of population selected, and is varied from 10 to 400 in increments of 10.

The test determines the condition numbers from all the final chromosomes, and then locates the minimum from the population of chromosomes. The test is the repeated a further 9 times, in order to evaluate the true minimum and mean condition result for that specific set of parameters, across all tests. Figure 3.17 illustrates the mean condition number from the test for all of the various population sizes.

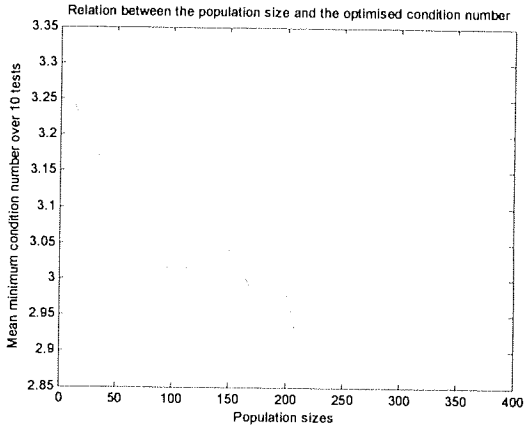

Figure 3.17 – Mean condition number plotted against population size.

The above figure illustrates that the mean condition numbers for the test is converging at around 2.9. The peaks and troughs on the curve are representative of the random selection process within the algorithm. However, the curve would become far smoother if several more examinations were taken using the mean of the condition number. It illustrates that a starting population size of around 200 or greater would be adequate in locating a minimum condition solution. If too large a population is selected, then this results in the requirement for large processing time and capacity.

Taking 280 chromosomes as a near convergence optimum or constant, then the number of generations are now varied for which to determine its own convergence minimum, the results of which are illustrated in figure 3.18.

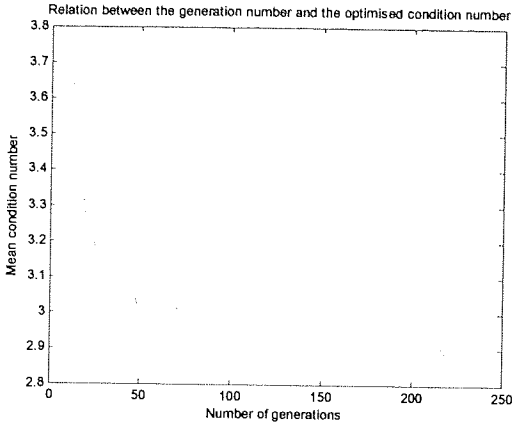

Figure 3.18 - The effect on the averaged minimum condition number over a varying number of generations, for 10 repeated experiments.

The results of figure 3.18, indicate that the convergence of the minimum for the number of generations fall within generations 120 or greater. Again the test is now repeated to evaluate the optimal breed ratio. The size of population is taken as 280, the numbers of generations are taken to be 130, the numbers of splices are taken to be 6, and the mutation rate is set at 0.1%. The breed ratio is to vary between 5% and 100% in increments of 5%. Again the test is repeated 30 times for which to evaluate the averaging of the minimum condition numbers.

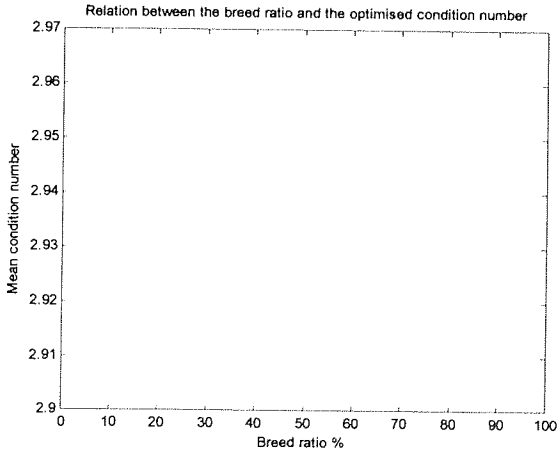

Figure 3.19 - Averaged minimum condition number for varying breed ratios

The above figure illustrates that the optimal condition number converges after a breed ratio of around 40%, however a value of 75% will be selected as a convergence minimum in this case. The number of splices required is now to be investigated, whereby the

maximum possible number of splices is equal to 152, which is the length of the binary string, representing the sensor locations.

This analysis investigates the number of splices taken between 4 and 152 in increments of 4 splices. The breed ratio is now set at 75%, the number of generations is given as 130, the population size is given as 280, and the mutation rate is given as 0.1%. The results from the average minimum condition over 30 tests are given as:

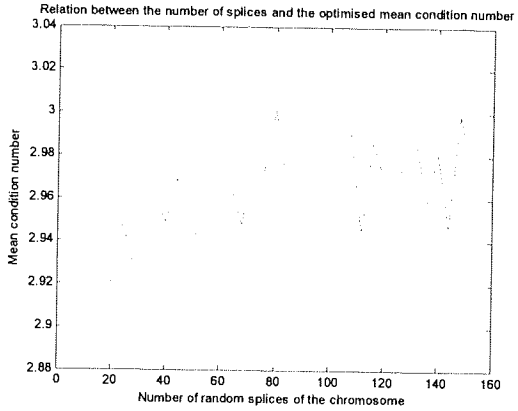

Figure 3.20 - Averaged minimum condition number for varying numbers of random chromosome splices over 30 repeated tests

Observing figure 3.20, it can be shown that an optimal number of splices of the chromosome, should be at around eight. The averaged trend appears to largely increase after this point, until a convergence is noted at around 70 random splices taken during the test. Finally, the optimal mutation rate value is to be investigated. The test constrains the optimal parameters of the algorithm, to a breed ratio of 75%, 130 generations, 280 populations and 8 randomised splices. However, the mutation rate is to be varied between 0.1 - 10% in increments of 0.1%, and is repeated 10 times, to generalise the optimal of the test result. An upper limit of 10% is selected, due to the fact that only small percentage values are required, to aid in the release of the iterative process if stuck in a local minimum. Figure 3.21, clearly shows that only low mutation rates are required for optimal performance, in this case the mutation rate is optimal at a mutation rate of 0.2%.

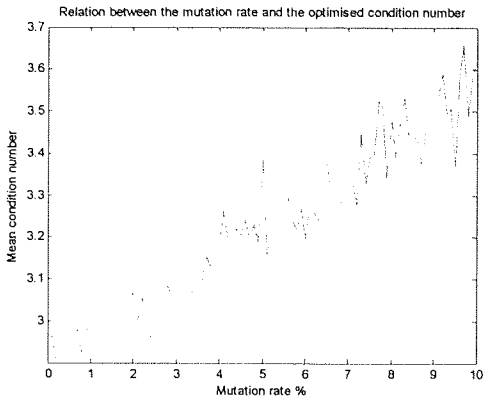

Figure 3.21 - Averaged minimum condition numbers over 10 tests for varying mutation values

Using these defined optimal parameters, the test to locate the optimal sensory locations is repeated 20 times to determine a close true optimal solution. An example of the propagation of the chromosomes, representing sensing element position over the generations is illustrated below from the optimal parameters in steps of 20 generations.

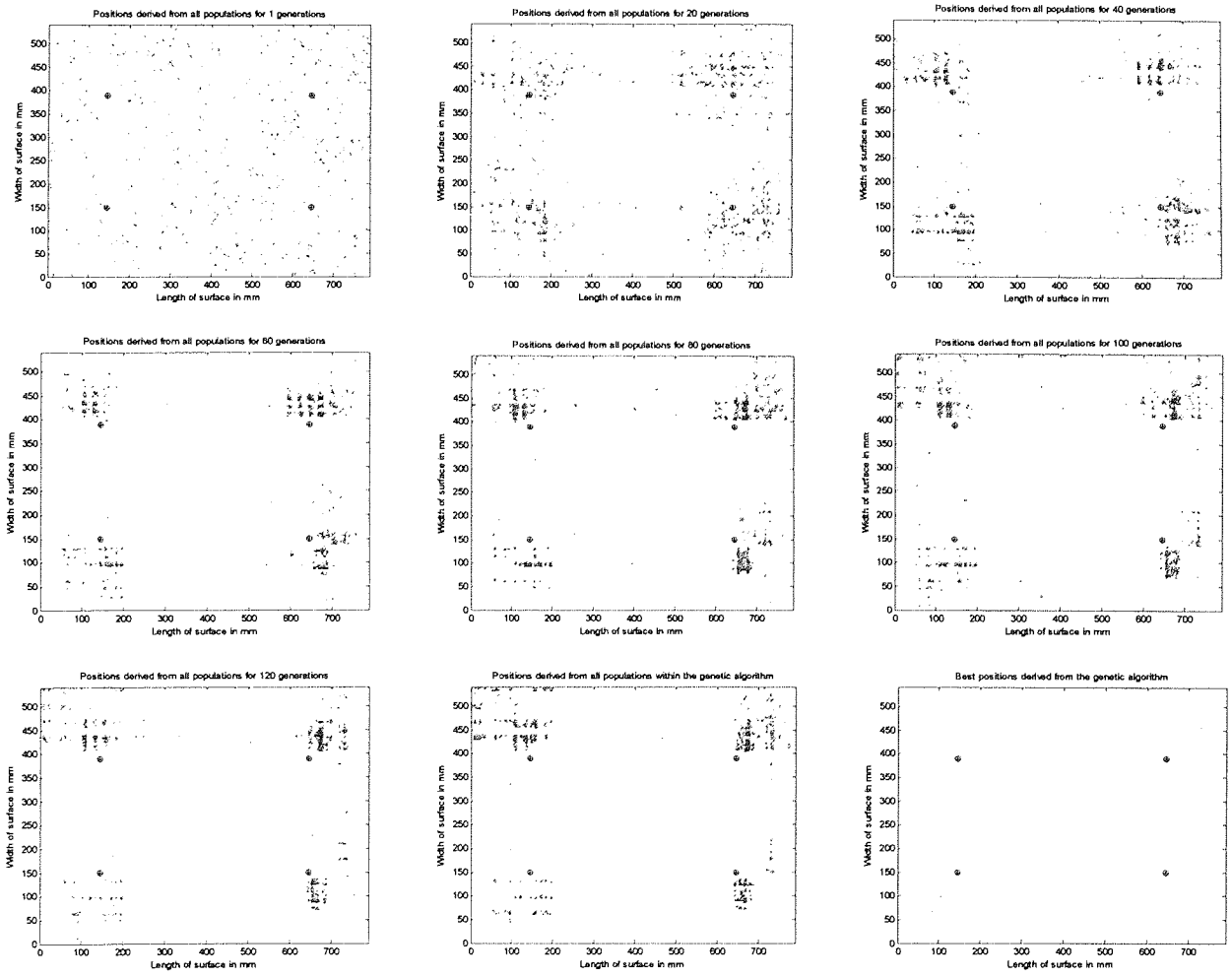

Figure 3.22 - Propagation of the optimal sensing element positions over 130 generations, in steps of 20 generations. The black circle with a star in the middle shown is the loading positions of the feet on all of the graphs, and each coloured cross illustrates a sensor number. The final plot illustrates the best location for the elements over all of the chromosomes and generations.

The above figures illustrate how the optimal sensing positions propagate towards the expected loading positions of the feet. This is due to larger deformations occurring at the positions of the feet, and hence larger sensitivities at these positions. This can be represented in figure 2.23, which possesses the minimum condition number of 2.75 over the 20 tests of the optimal parameters.

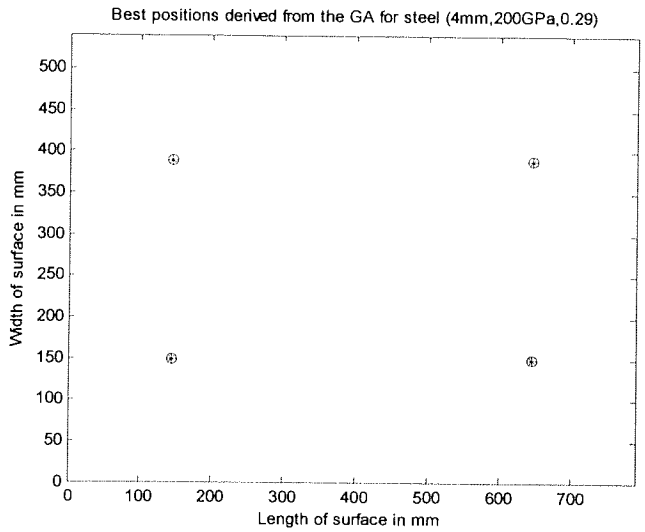

Figure 3.23 - The best possible sensory locations for a minimal condition number.
x represents the optimised sensory locations and o is the loading points of the feet.

Figure 3.23, shows the optimal sensory locations derived move towards the loading points and can be observed that two elements propagate towards each loading position. This movement and pitching of the elements also appears to give a greater balance to the sensitivity between elements. It also shows that the optimal positions are non-equally pitched like array-type devices. This is indicative of the non symmetry of the system, thus providing a greater uniqueness in the differences between sensing elements. It is also more representative towards a human system as opposed to an array configuration of sensing elements.

This GA analysis has been extended and run to derive the minimum condition numbers for a range of sensing elements between 4 to 100 sensing elements under the surface. The condition evaluation of array devices has also been investigated for equal pitched positions analysis is indicated in figure 3.24

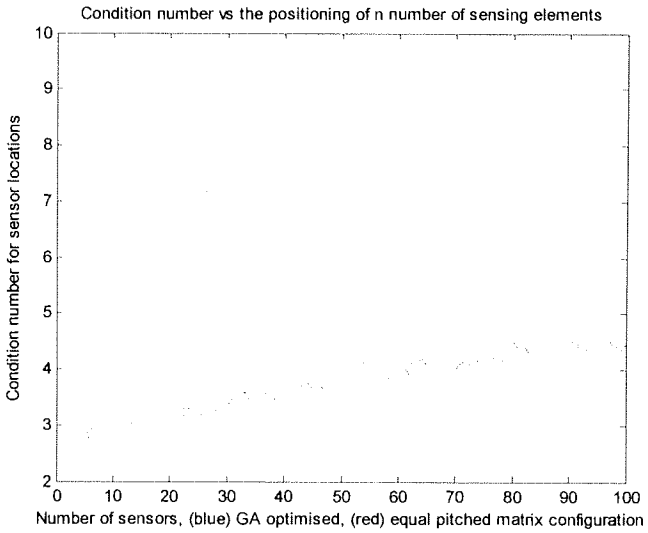

Figure 3.24 - Condition of the positioning of sensory elements in an array and RFSES that apply the presented sensory condition calculation method.

Figure 3.24 represents the condition numbers for different numbers of sensing elements and hence the sensitivity of the elements in the system. It can be observed that positioning elements in the presented way (blue diamonds) is more effective for providing a maximal equal sensitivity than elements positioned in an array or matrix formation (red diamonds).

The reason for the increase in condition number verses the number of sensing elements, is due to the fact that the greater the number of sensing elements that is applied, then the more difficult it is to find positions for elements to all possess equal and maximum sensitivity. However the lower the number of sensing elements applied in the system then the more sensitive and equally sensitive they become as information for the processor.

This supports the reason for a reduction in sensing elements required, namely in this case the condition of the sensitivity at eight sensor elements from figure 3.24, which is comparability at a minimum value compared with other volumes of sensing elements.

A theoretical example of this is to be illustrated. Assume that a weight shift from the left to right feet and back is to occur on the surface, following a sinusoidal movement. This is demonstrated as:

Force on left foot = $\frac{1}{2}\, mg\, sin\, (wt + \frac{1}{2}\, \pi) + \frac{1}{2}\, mg$, and
Force on right foot = $\frac{1}{2}\, mg\, (1 - sin\, (wt + \frac{1}{2}\pi))$, where the weight of the subject is 70kg, the frequency of sway to be given as 1Hz, thus, $w = 2\pi$. Also assume that the loading on the heels of both feet are 70% of the total load on either foot throughout the movement. The loading on the four points is therefore given as:

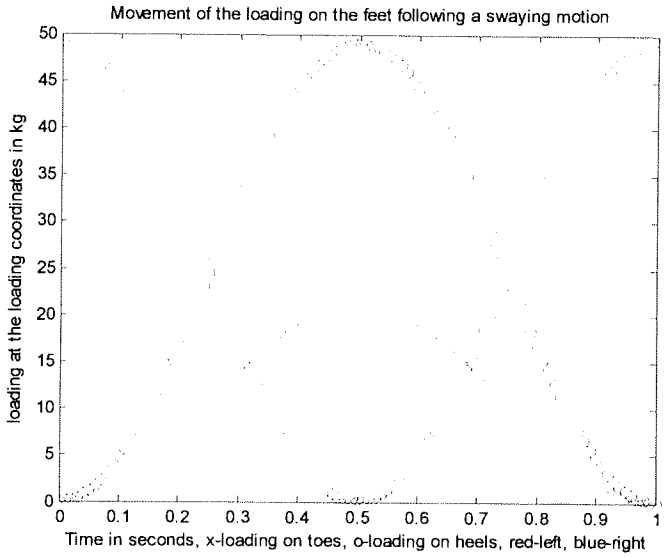

Figure 3.25 – A calculation of four loads moving on the surface at the set loading points, for a sway of the body from left to right and back, at the constant frequency of 1Hz. Where the blue curves represent the right foot, and the red curves are the left foot, where x is representing the toes and o is representing the heels of the feet.

Simulating the expected deformations at all eight optimised points with a condition number of 2.75 under the steel surface, using the loading data in figure 3.25, and equation 3.34 gives:

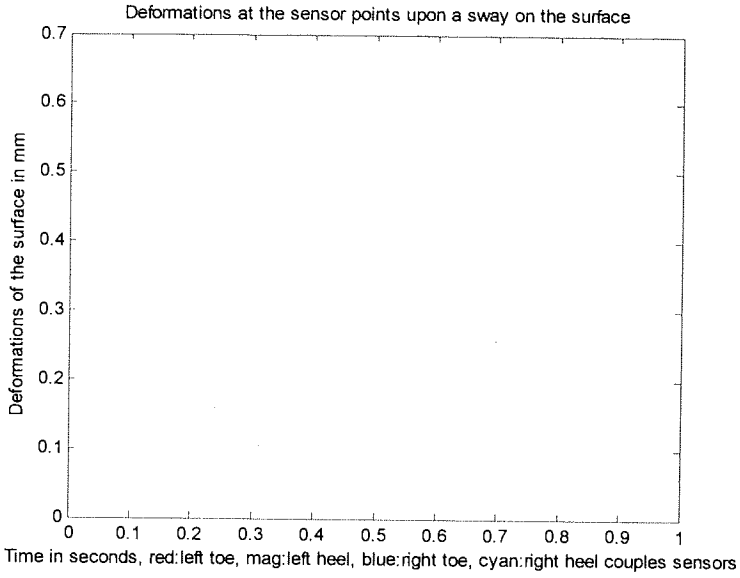

Figure 3.26 – Calculated changing deformations of the 4mm steel surface at the eight calculated optimal sensing locations, through the loading conditions given in figure 3.25.

The above diagram is very interesting and highlights the theory behind the findings. The first is that even though sensors have been found to be distributed as four pairs of elements, the difference in deformation between pairs is large. This is noticeable when the loading condition is at a maximum near the element pairing, hence highlights a good optimised position of elements by the GA. i.e. the elements are more responsive to larger loading magnitudes.

It can be viewed that at the given distribution of elements, each one shows deformation uniqueness with regards to any other element throughout the loading condition. This implies that the greater number of elements then the greater the uniqueness, hence information received by the system. Although there will be a ceiling limit on the total number of elements required to enhance system accuracy, this can be seen in figure 3.16.

Analysing the effect of the condition number with fewer elements, for example the examination of four sensing elements at each loading point, as opposed to four pairs of elements as calculated as optimal, is an interesting question. The result in the condition number using one element at each loading point gives a condition number of 3.5788. This

shows that even elements situated at the maximum loading conditions on the surface gives a poorer result to the one 2.75 found by the GA for eight elements. Considering figures 3.17-3.21 it shows that the difference is significant in terms of the minimum condition number. Also such a distribution of four elements gives symmetry, and hence generates linear relationships between captured data from the elements, thus reducing uniqueness of the dataset.

Testing the robustness in the position of elements can be determined by slightly moving the optimal positions of the elements and recalculating the condition number. This is useful to determine the robustness and non linearity of the algorithm. This is also indicative of the robustness of the assembly process through the manual positioning of the elements under the surface.

It is initially assumed that only moving the sensing locations by a small amount will affect the condition number of the multiplying matrix. This is due to the fact that the calculation of eigenvalues and eigenvectors is in general numerically unstable. Thus an empirical evaluation is necessary. Although, all of the eight elements have converged to a minimum to give similar sensitivities through the GA, then a small change in the position of one element should not strongly affect the condition of the matrix, as opposed to a poorly conditioned and random positioning of elements.

The optimal positioning of the elements found by the GA (as in figure 2.23) is:

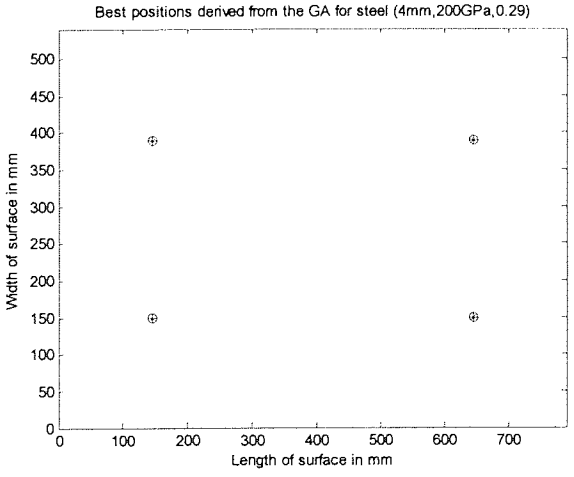

x1 = 670.42 y1 = 467.23
x2 = 699.74 y2 = 83.32
x3 = 712.08 y3 = 95.98
x4 = 109.55 y4 = 91.76
x5 = 62.49 y5 = 90.70
x6 = 689.71 y6 = 469.34
x7 = 89.49 y7 = 474.61
x8 = 97.21 y8 = 451.41

giving an optimised condition number of 2.75, from a condition of the multiplying matrix of:

$$M = \begin{bmatrix} -51.49 & -33.91 & -34.6 & -323.05 & -195.5 & -47.79 & 632.34 & 891.15 \\ -36.66 & -51.4 & -52.45 & 863.4 & 523.76 & -32.07 & -243.83 & -336.6 \\ 791.54 & -286.67 & -276.61 & -42.67 & -27.62 & 683.19 & -46.22 & -65.63 \\ -297.37 & 757.55 & 747.26 & -53.71 & -36.36 & -260.39 & -26.47 & -37.15 \end{bmatrix}$$

Moving one sensing point for example element 2 by -10mm in the x direction changes the condition number to 2.77 from 2.75, from a multiplying matrix of coefficients of:

$$M = \begin{bmatrix} -51.47 & -33.45 & -32.05 & -322.99 & -195.48 & -47.79 & 632.36 & 891.19 \\ -36.63 & -50.62 & -48.67 & 863.49 & 523.79 & -32.07 & -243.8 & -336.55 \\ 791.7 & -285.04 & -252.56 & -42.12 & -27.46 & 683.15 & -46 & -65.29 \\ -297.78 & 753.88 & 682.98 & -55.16 & -36.79 & -260.3 & -27.03 & -38.05 \end{bmatrix}$$

Firstly, if the positioning of the elements is slightly different to the ones that have been calculated as optimal, then this will only give a small change in the optimal performance for equal sensitivities between elements. This is indicated by an increase in the condition number of only 0.02, indicating algorithm and assembly robustness for the positioning of elements.

Secondly, comparing the two matrices it can be seen that only through a small change in one of the input parameters, then this effects all of the coefficients held within the multiplying matrix. The reason for this is due to the cross multiplication of the co-factors through by the new calculated determinant of the matrix used in generating a matrix inverse.

This relationship shows that final position of all of the elements depends upon each of the elements uniquely, and that each element's position shows a relationship with other elements to provide a minimum conditioning number.

It may be possible to locate dominant and recessive sensory locations in the inverse matrix or through a redundancy process through the application of empirical data to

provide various weightings to sensory elements. If it is possible to define weighting values for sensing elements then this can enhance maximum and equal sensitivity for both array and RFSES.

From the dynamic changing of loads on the surface in figure 3.26, it can be observed that the magnitudes of deformation between left and right feet are similar at t = 0 and t = 0.5seconds, indicating an equal sensitivity between points, for a sway at the left or right positions. However these are shown to be non symmetric indicating that the system possesses uniqueness when the body is in either the left or right position.

As this movement is symmetric about the y axis on the surface, the elements show a non symmetric output. This implies that the system will have uniqueness for all symmetric and non symmetric movements on the surface and across any axis. This is extremely useful when taking the magnitudes or differences in the data to describe a movement that has a unique describing character, albeit the sensing elements are responsive enough to the magnitudes of the loading condition.

The advantage of this type of approach is that sensing elements and system complexity are reduced, subsequently reducing the cost for such a system. I.e. A standard Force plate from Bertec Inc. (4060 series), with dimensions of 600x400x25mm aluminium surface, with a matrix of strain gauge sensing elements will cost in the region of £13,467. However, additional devices are also required in conjunction to use the device such as the AM 6071 digital amplifier, for the multiplex of strain gauge elements also costing in the region of £4,970 (Section 3.5.8).

This can be compared to the production cost of one RFSES costing in the region of £110. The construction cost of the steel surface and base plate cost at around £65, the sensing elements and supporting circuitry costs at around £8, or £1/sensing point (63p for the element, 16p for the resistors, 10p for the circuit board, and assembly of the board). The circuit board with the USB data acquisition costs around £15, and the supporting frame (30x10mm) around the edge costs at around £20.

3.4 Data acquisition devices

The system uses digital data for the sensory information. However, the responses of the sensing elements are predominantly analogue. An Analogue to Digital Converter (ADC) is to be used to provide this function between the analogue elements and the digital processor. The ADC works on the basis of quantising a discrete analogue sample taken over a period of time into a digital value. The length and accuracy of the described digital value is therefore dependant upon the resolution or bit size of the device. The sampling rate also defines the quantisation of the describing analogue signal in the time domain, and high sampling rates generate more digital values to describe the analogue signal, hence average quantisation evaluations over the time sampling period are also reduced.

The requirements for the device are at least an eight channel ADC, with a high bit resolution, and high sampling capabilities. Various off-the-shelf ADC devices are available; however these tend to be modular systems that possess poor flexibility for integration.

However, a Microchip™ unit has been employed with closely matching specifications. The PIC18F2320 possesses 9 analogue input channels, a 10 bit resolution giving a magnitude quantisation of 0.0049V and a maximum sampling rate of 1250 samples per second giving a time quantisation of 0.0008 seconds. The chip is interfaced with a serial communication device (MAX232CPE) operating at 115200bits/second with a capacity of transferring 1440 digital samples for the eight elements per second. The configuration of the elements of one set of optimal positions with supporting circuitry and structure in figure 3.13 is configured with this device and is demonstrated in figure 3.27.

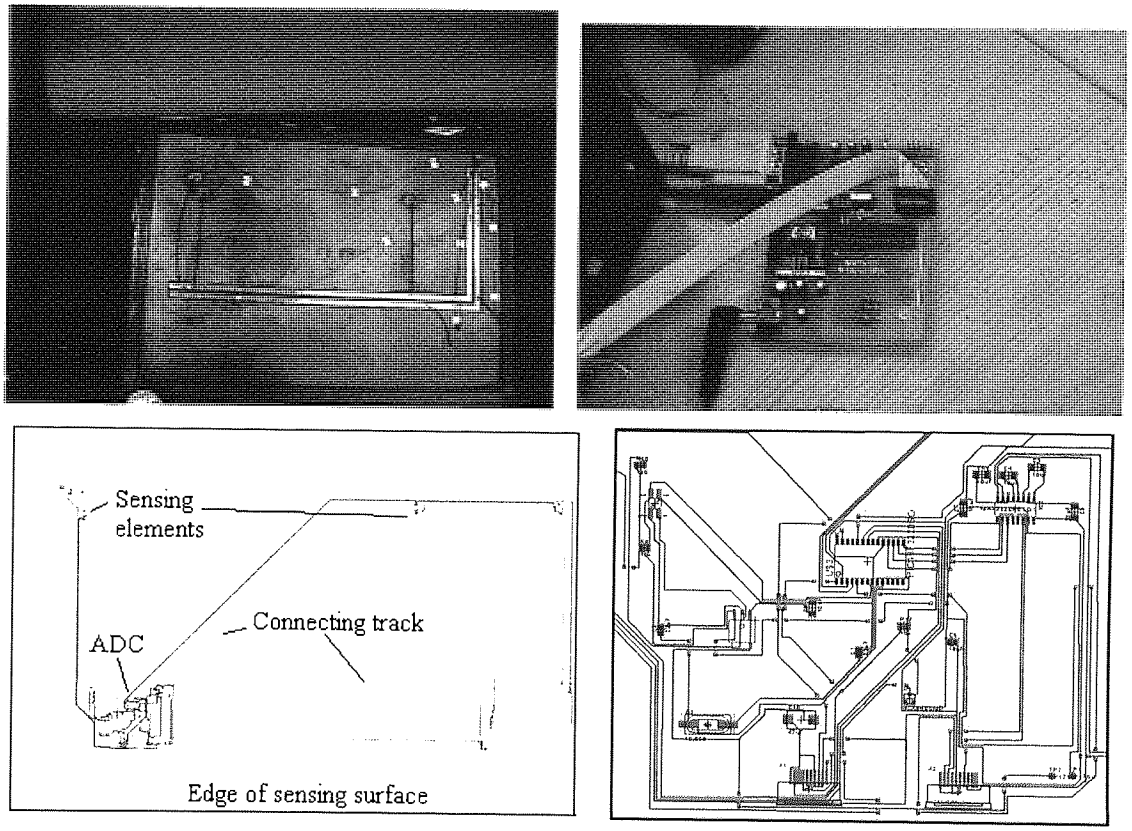

Figure 3.27 (top left) - First golf mat prototype of the sensing elements under the surface. (top right) - Designed serial ADC. (bottom left) - Final integrated design of the elements and ADC. (bottom right) - Close up of the surface mount ADC device in the design.

Figure 3.27 indicates the design of the complete sensing and acquisition system. The design has been developed all on a top layer of PCB or flexible circuit with surface mount components, such that the complexity and cost of the manufacturing process is reduced. A USB2.0 microchip (Package: PIC18F2455 / PIC18F4455) will be used to provide the device connections in the manufactured system, as they are more common than serial ports on current computers. The USB cable can be used as a power supply to the circuit, taken directly from the machine holding the processing algorithm, hence eliminating the requirements for an individual power supply. Other supporting images can be seen in Appendix C.2.

Also the current speed of the serial device is limited due to the baud rate and causes a bottleneck in the serial cable; however a USB device can speed up the communication rate from 115kbit/sec to 11Mbit/sec.

3.5 Real time data processing for linear regressive outputs

Once the coupled digital data set has been acquired from the proximity sensors, it is possible to extract information about the state of the surface under loading. Real time information from an instantaneous data set can give information about the loading and can either be load magnitude, position, shape, or slip. Output evaluation can either be regressive or classifying (see section 4.8).

Classification techniques tend to possess greater accuracy; however this comes as result of reduced output range and introduces system output resolution. Alternatively, regressive techniques are continuous digital outputs across the full output range; however suffer greater inaccuracies than classification-type systems. Classification-type systems are primarily based upon the response of regressive models, with additional classification algorithms. The choice of an appropriate interpretation method must therefore be selected upon the output requirement of the system.

For example a system by Caiti (1995) demonstrates two different regressive models (MLP & RBF) for the application of a reconstruction of object shape placed on a force surface as a continuous function. The main regressive interpretation models can either be inverse closed loop mathematical models, empirical inverse methods and Single Layer Perceptron approaches (SLP), empirical Multi Layered Perceptron (MLP) models, Radial Basis Functions (RBF), or Mixture Density Networks (MDN).

3.5.1 Linear Regression Inverse Closed Loop Mathematical Models for load magnitude

These methods are direct mathematical functions that relate the input stimulus to the required output represented through control theory as:

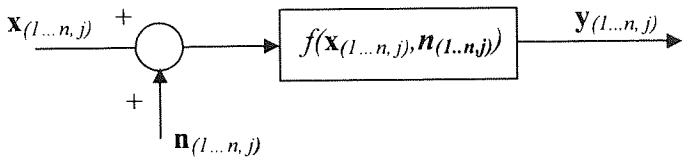

Figure 3.28 - Interpretation algorithm for a mapping
of the input with additional noise to the required output response.

Figure 3.28 demonstrates the inputs from the sensing elements with external noise to be processed by the simulated system function to predict an output based upon the input. Mathematical models are simulation models based upon assumptions that closely represent the system in question. These tend to be complex interpretations of how the system in question will respond towards the applied stimulus. These approaches are simple and effective ways of determining the output response without the use for real acquired data from the system. For example, in the representation of load magnitude on a surface, it is possible to derive the interpretation function through various assumptions.

The captured inputs in this case are electrical voltages subjected to external noise. From the sensory characteristic curves in question in figure 3.29 it is possible to convert the output sensory voltages into proximities and hence into deformations.

This can be developed through a polynomial representation of the calibration data such that the algorithm can generate a continuous proximity response to any discrete voltage. This can be represented by an n^{th} order polynomial representation found using a least squares approach. Figure 3.29 represents the measured and polynomial expression, given from: proximity (P) and acquired voltage (V) as:

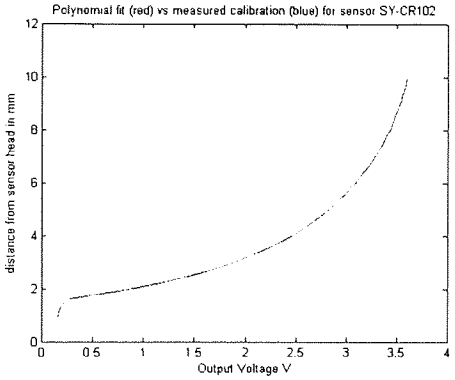

Figure 3.29 - Polynomial representation of measured sensory calibration.

$$P = -0.0530V^{10} + 1.0870V^{9} - 9.6146V^{8} + 48.1102V^{7} - 149.9392V^{6} + 301.9080V^{5} - 394.0906V^{4} + 325.5020V^{3} - 160.2460V^{2} + 42.2118V - 2.7868$$

Recording the proximity at initial conditions (i) from the above function, i.e. when the surface is un-stimulated, it is possible to calculate the deformation w of the surface at any point (n), from (3.37). This approach gives a direct calibration of the system, through a description of the differences in the deformations from initial conditions and not from the deformation magnitudes.

$$w_n = \begin{pmatrix} -0.0530V_{in}^{10} + 1.0870V_{in}^{9} - 9.6146V_{in}^{8} + 48.1102V_{in}^{7} \\ -149.9392V_{in}^{6} + 301.9080V_{in}^{5} - 394.0906V_{in}^{4} + 325.5020V_{in}^{3} \\ -160.2460V_{in}^{2} + 42.2118V_{in} - 2.7868 \end{pmatrix} - \begin{pmatrix} -0.0530V_{n}^{10} + 1.0870V_{n}^{9} - 9.6146V_{n}^{8} + 48.1102V_{n}^{7} \\ -149.9392V_{n}^{6} + 301.9080V_{n}^{5} - 394.0906V_{n}^{4} + 325.5020V_{n}^{3} \\ -160.2460V_{n}^{2} + 42.2118V_{n} - 2.7868 \end{pmatrix} \quad (3.37)$$

Once the deformations are known at all of the sensing points it is possible to calculate the loading magnitudes on the surface if all other known parameters are known about the surface and loading positions. The loading magnitude can therefore be calculated from expression (3.36), from a pseudo-inverse of the constant matrix, multiplied by the deformations at all sensing points in vector w (3.37). Thus the output response of this mathematical approach is in real time for a load interpretation. The result of this closed loop mathematical model at four loading points from real captured data is illustrated in figure 3.30, on being randomly loaded sixteen times at the set positions, to develop the testing input voltages that are to be applied to the model.

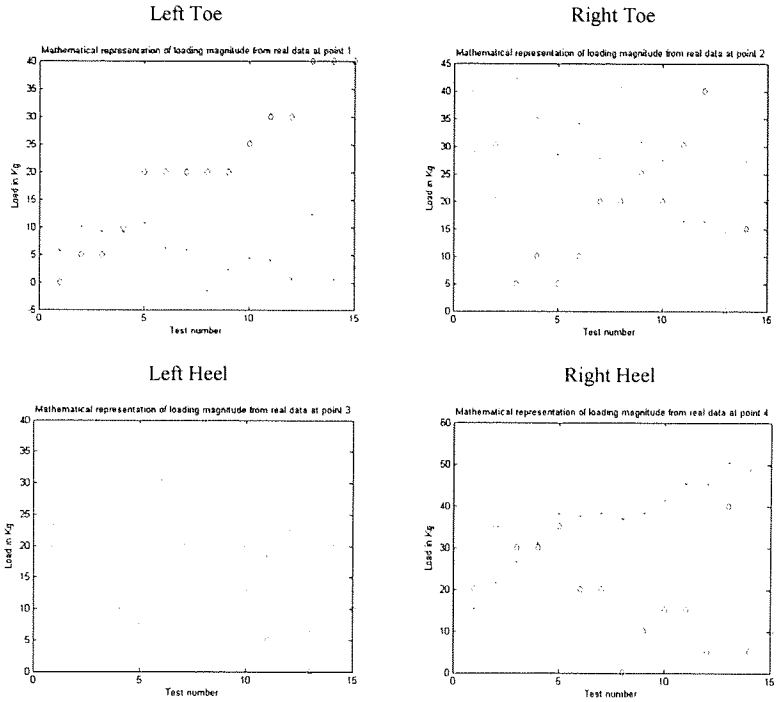

Figure 3.30 - Mathematical representations of the loading magnitudes on the surface.
The diamonds (◇) represent measured and crosses (x) calculated loading magnitudes in kg.

The results show average errors of 18.22kg or 22.78% at position (14.5,39)cm, 15.71kg or 19.64% at position (64.5,39)cm, 13.36kg or 16.7% at position (14.5,15)cm and 21.04kg or 26.3% at position (64.5,15)cm. The results illustrated suggest that a closed loop generalisation would be inappropriate as an accurate interpretation method. However; if the input deformations w are simulated by the model in (3.36), then the output evaluations of the loads W from the same model gives 100% accuracy. This implies that, if a mathematical generalisation was an exact representation to the actual system then these accuracies would be apparent. Finally, it is important to note that the model to predict load magnitude in 3.34 and 3.34 is a linear model, hence linear or non-linear interpretation methods can be used to predict load magnitude quite accurately.

The errors associated with this solution are due to the fact that the measured deformations are different to the ones expected by the model. This can arise due to continuity deficiencies in either thickness or stiffness of the surface, quantisation of the ADC, noise, electrical tolerances on elements and components, or environmental factors that can

physically deform the surface unlike that of the theoretical expression. The quality of the mathematical representation of the real system is therefore directly related to the calculated inaccuracies of the system output.

3.5.2 Linear Regression Inverse Closed Loop Mathematical Models for load position

This inverse mathematical approach can also be applied to determine load position; however a different manipulation of the surface representation equation (3.22) & (3.23) needs to be performed to determine loading coordinates g and h.

From the Navier model it can be assumed that the variables that are known in (3.22) are collected as constant terms, so that the expression becomes:

$$q = \sum_{a=1}^{21}\sum_{b=1}^{13} \sin(\mu_a.g).\sin(\varphi_b.h).\beta_{ab} \tag{3.38}$$

where,

$$q = \frac{w(x,y).E.\pi^4.t^3.e.f}{48W.(1-\nu^2)},\ \mu_a = \frac{a.\pi}{e},\ \varphi_b = \frac{b.\pi}{f},\ \beta_{ab} = \frac{\sin\left(\frac{a.\pi.x}{e}\right).\sin\left(\frac{b.\pi.y}{f}\right)}{\left(\frac{a^2}{e^2}+\frac{b^2}{f^2}\right)^2}$$

The system also assumes that eight sensing points are known then eight equations exist to solve for values of g and h. Expression (3.38) can then be expanded and represented as a set of linear equations, that can be written in matrix form expression (3.39) as:

$$\begin{bmatrix} q_1 \\ q_2 \\ \vdots \\ q_{16} \end{bmatrix} = \left[\sin(\mu_1 g).\sin(\varphi_1 h) \quad \sin(\mu_1 g).\sin(\varphi_2 h) \quad \ldots \quad \sin(\mu_{21} g).\sin(\varphi_{13} h)\right] \bullet \begin{bmatrix} \beta_{11}^1 & \beta_{11}^2 & \ldots & \beta_{11}^{16} \\ \beta_{12}^1 & & & \downarrow \\ \vdots & & & \vdots \\ \beta_{2113}^1 & \ldots & \ldots & \beta_{2113}^{16} \end{bmatrix}$$

Taking a pseudo-inverse of matrix β and multiplying by matrix q this will generate a matrix of new values (V) that is equivalent to the central matrix with unknown variables

g and h. This matrix form can then be translated back into a set of linear equations so that the values can be solved for the unknowns as:

$$\begin{aligned} V_1 &= \sin(\mu_1 g).\sin(\varphi_1 h) \\ V_2 &= \sin(\mu_1 g).\sin(\varphi_2 h) \\ &\vdots \\ V_{273} &= \sin(\mu_{21} g).\sin(\varphi_{13} h) \end{aligned} \tag{3.40}$$

Since equations 1 to 13, 14 to 26 and the following incremental batches of 13 equations up to equation 273 possess equivalent values of $\sin(\mu_n g)$ and can be substituted between equations in the batch to solve for one the variables, i.e. h as:

$\sin(\mu_1 g) = \dfrac{V_1}{\sin(\varphi_1 h)}$ and can be substituted into equation (3.40) to give:

$V_2 = \dfrac{V_1}{\sin(\varphi_1 h)}.\sin(\varphi_2 h)$ or algebraically for all samples as: $\dfrac{V_{n+1}}{V_n} = \dfrac{\sin(\varphi_{n+1} h)}{\sin(\varphi_n h)}$ (3.41)

up to equations at the end of the batch for equivalent values of $\sin(\mu_n g)$. Equation (3.41) can be solved graphically to find solutions for h within the limitations of the surface, albeit this method of finding a solution for h will be time consuming and impractical.

However the solution can be solved algebraically due to the fact that the term $\dfrac{\sin(\varphi_{n+1} h)}{\sin(\varphi_n h)}$ can be expressed as a Taylor series expansion to transform the function into polynomial expression. This is such that solving the roots of the polynomial will give rise to finding possible values for h. Expression (3.41) then becomes:

$$\frac{V_{n+1}}{V_n} = \frac{\varphi_{n+1} h - \dfrac{\varphi_{n+1}^3 h^3}{3!} + \dfrac{\varphi_{n+1}^5 h^5}{5!} - \dfrac{\varphi_{n+1}^7 h^7}{7!} \ldots + \dfrac{\varphi_{n+1}^{149} h^{149}}{149!}}{\varphi\ h - \dfrac{\varphi^3 h^3}{3!} + \dfrac{\varphi^5 h^5}{5!} - \dfrac{\varphi^7 h^7}{7!} \ldots + \dfrac{\varphi^{149} h^{149}}{149!}} \tag{3.42}$$

The reason why the term is required to be evaluated up to a term to the power of 149 is due to the fact that a large value of φ will induce a large frequency component in the evaluation due to a large value of b i.e. 13, hence a large number of terms are required to accurately represent the high frequency of the sigmoid. This can be represented graphically in figure 3.31 as:

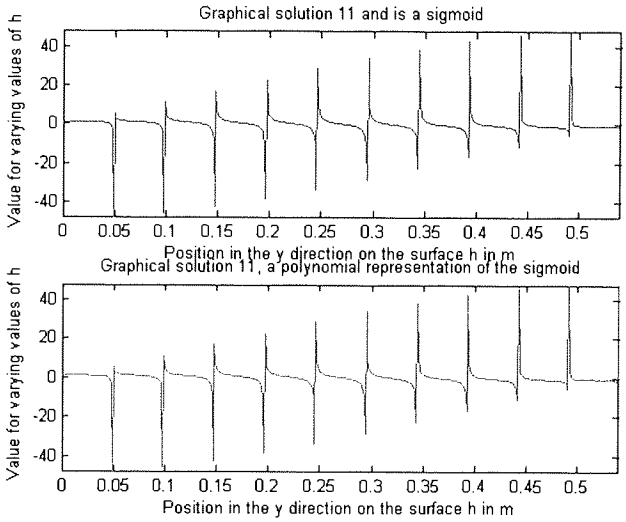

Figure 3.31 (top) - Expression using the sigmoid function in (3.41) and (bottom) - Taylor series expansion function (3.42), to evaluate varying values h.

Figure 3.31 shows a graphical representation of the solution for all possible values of h. In this case the equating value for a possible solution is given as: 0.073, thus when the curve crosses this point then a possible solution is found for h. These solutions can be derived through a manipulation of (3.41) & (3.42) to give expression (3.43) as:

$$0 = \frac{\left(\varphi_{n+1}h - \frac{\varphi_{n+1}^3 h^3}{3!} + \frac{\varphi_{n+1}^5 h^5}{5!} - \frac{\varphi_{n+1}^7 h^7}{7!} \ldots + \frac{\varphi_{n+1}^{149} h^{149}}{149!}\right) - \left(\left(\frac{V_{n+1}}{V_n}\right)\left(\varphi\, h - \frac{\varphi^3 h^3}{3!} + \frac{\varphi^5 h^5}{5!} - \frac{\varphi^7 h^7}{7!} \ldots + \frac{\varphi^{149} h^{149}}{149!}\right)\right)}{\varphi\, h - \frac{\varphi^3 h^3}{3!} + \frac{\varphi^5 h^5}{5!} - \frac{\varphi^7 h^7}{7!} \ldots + \frac{\varphi^{149} h^{149}}{149!}}$$

Solutions for equation (3.43) are when the numerator polynomial equals 0 and can be determined by taking the roots of the top polynomial. An example of this gives a graphical solution in figure 3.32 as:

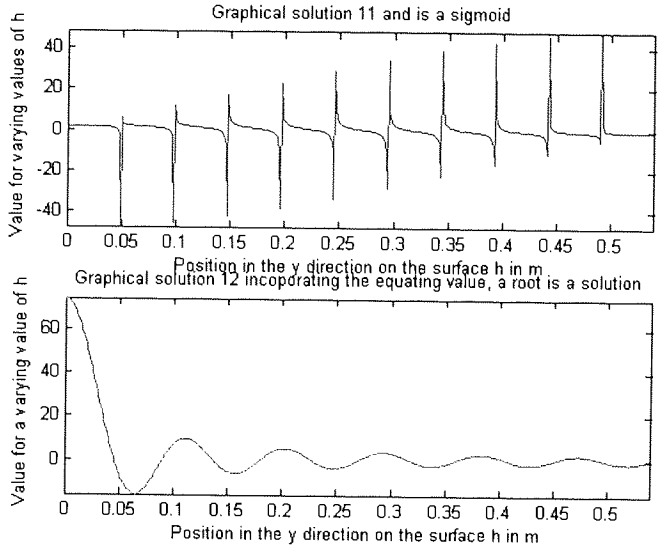

Figure 3.32 - Possible solutions for h from equation (3.43) for the 11^{th} expression.

Figure 3.32 shows the possible solutions to the 11^{th} expression in the first batch of equations when a=1. Note that there are many solutions due to the high order of the polynomial. Variable g can also be calculated from equations (3.40) down to (3.43), where expression $\sin(\varphi_n h)$ can be substituted out in all expressions where a similar term appears between all of the 273 given equations. From this a histogram can be derived for all derived solutions of g and h to give figure 3.33, all of which could be feasible with the correct corresponding evaluation in the other perpendicular plane:

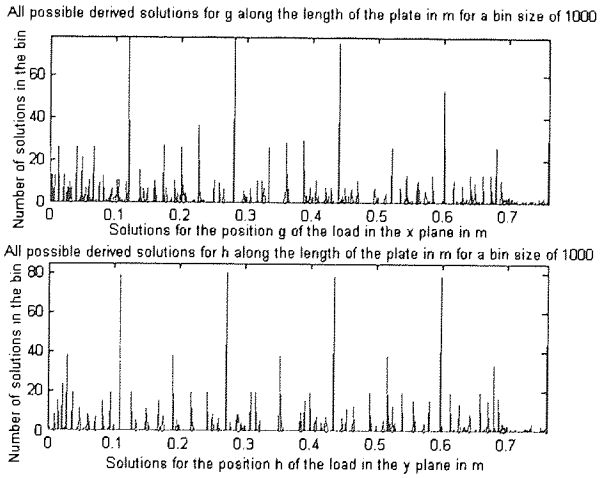

Figure 3.33 - Derived solutions of the position of the load in both the x and y plane for a fine length bin size.

As there are many possible solutions for that solution through all of the evaluated expressions, a histogram shows where the solutions lie across the axis visually. As it is not clear on the exact solution using this finite bin size, a coarser bin size will provide a more general solution, although at the expense of reduced model resolution. This is demonstrated in figure 3.34.

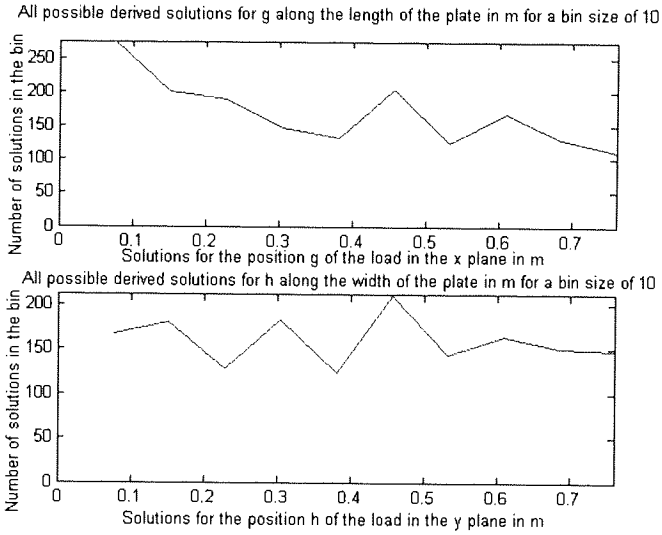

Figure 3.34 - a course bin size to define the probability of the derived values for g and h

It can be noted that in figure 3.34 the solution for the value for g and h can be observed as 0.076 m with 276 solutions near this value for g in the x direction and 0.456m with 211 given solutions near this value for h in the y direction. This can be compared with the position of the load at position 0.1 m in x and 0.45 m in y from the simulated data for the deformation at the sensing points at the given coordinates under the surface taken from the Navier's double trigonometric series.

The accuracy of this solution for generated simulated deformations for various loading positions was found to give an accuracy of: 0.3m or 39.5% error in the x direction and 0.1928m or 25.4% in the y direction, over the full range of positions for 14 tested simulated positions.

The advantage of this load coordinate interpretation system is that a mathematical function has been derived to describe the underlying system function with some degree of accuracy. However, the main problem with this closed loop load interpretation system is mainly the accuracy and is due to the assumptions made by the model and its similarity to a physical system. Secondly, using these models to determine load position specifically it is only possible to calculate the position of a single-point load on the surface. Thirdly, the time taken to derive a solution is time consuming for the processor and is on average 65.2 seconds to generate a solution for the position of the load and cannot be used for this application to provide evaluations instantaneously or in real time.

Finally, it also highlights that such a model is non-linear to predict load position, hence indicating that the input-to-output pattern will posses a non linear relationship. This will therefore imply that linear regression methods will not perform as well as non linear methods in the interpretation of load position.

3.5.3 Linear Regression Inverse Methods

As with mathematical approaches it can be determined that unknown variations in a unique system can directly affect the performance of these methods, along with the variable representing the stimulus. Through the direct analysis of a unique system, it is possible to derive parameters that represent the underlying system function more closely and hence system accuracy is greatly increased. These approaches are simple benchmarking tools for systems that behave linearly; however they require a substantial collected data set to construct the representative system parameters. To generate a direct mapping of these parameters, the responses of the sensing elements are informative of the loading stimulus on the surface need to be known along with the variable representing the stimulus.

A simple inverse method assumes that the system function can be represented by a set of weightings or multiplying constants. This can be assumed on the basis that the system

remains constant throughout. However, problems can arise from physical changes to any of the various functions in the system. This indicates that system repeatability is of most importance when constructing accurate representing system coefficients.

Assume that the inputs ($\mathbf{X}_n$) are eight and that the outputs ($\mathbf{Y}_n$) are four dimensional respectively for the n^{th} acquired data vector. The system coefficients (A...H) can be defined through a set of linear equations as:

$$\begin{aligned}
\mathbf{Y}_n^1 &= A_1\mathbf{X}_n^1 + B_1\mathbf{X}_n^2 + C_1\mathbf{X}_n^3 + D_1\mathbf{X}_n^4 + E_1\mathbf{X}_n^5 + F_1\mathbf{X}_n^6 + G_1\mathbf{X}_n^7 + H_1\mathbf{X}_n^8 \\
\mathbf{Y}_n^2 &= A_2\mathbf{X}_n^1 + B_2\mathbf{X}_n^2 + C_2\mathbf{X}_n^3 + D_2\mathbf{X}_n^4 + E_2\mathbf{X}_n^5 + F_2\mathbf{X}_n^6 + G_2\mathbf{X}_n^7 + H_2\mathbf{X}_n^8 \\
\mathbf{Y}_n^3 &= A_3\mathbf{X}_n^1 + B_3\mathbf{X}_n^2 + C_3\mathbf{X}_n^3 + D_3\mathbf{X}_n^4 + E_3\mathbf{X}_n^5 + F_3\mathbf{X}_n^6 + G_3\mathbf{X}_n^7 + H_3\mathbf{X}_n^8 \\
\mathbf{Y}_n^4 &= A_4\mathbf{X}_n^1 + B_4\mathbf{X}_n^2 + C_4\mathbf{X}_n^3 + D_4\mathbf{X}_n^4 + E_4\mathbf{X}_n^5 + F_4\mathbf{X}_n^6 + G_4\mathbf{X}_n^7 + H_4\mathbf{X}_n^8
\end{aligned} \tag{3.44}$$

Alternatively, these sets of linear equations in (3.44) can we written in matrix form as:

$$\begin{bmatrix} \mathbf{Y}_n^1 \\ \mathbf{Y}_n^2 \\ \mathbf{Y}_n^3 \\ \mathbf{Y}_n^4 \end{bmatrix} = \begin{bmatrix} A_1 & B_1 & C_1 & D_1 & E_1 & F_1 & G_1 & H_1 \\ A_2 & B_2 & C_2 & D_2 & E_2 & F_2 & G_2 & H_2 \\ A_3 & B_3 & C_3 & D_3 & E_3 & F_3 & G_3 & H_3 \\ A_4 & B_4 & C_4 & D_4 & E_4 & F_4 & G_4 & H_4 \end{bmatrix} \cdot \begin{bmatrix} \mathbf{X}_n^1 \\ \mathbf{X}_n^2 \\ \mathbf{X}_n^3 \\ \mathbf{X}_n^4 \\ \mathbf{X}_n^5 \\ \mathbf{X}_n^6 \\ \mathbf{X}_n^7 \\ \mathbf{X}_n^8 \end{bmatrix} \tag{3.45}$$

The application of a known stimulus $\mathbf{Y}_n$ on the surface will result in input responses $\mathbf{X}_n$ for a training pattern n. It is therefore possible to accumulate input and output training patterns across the possible output range, to determine the unknown system coefficients. This can be achieved through a pseudo-inverse of the collected input responses multiplied by the known output responses. However; in this example the bias term (which is equated to the errors in the system) has not been added for a simplistic and quick analysis of the method.

An example of the application of this method is the discrimination of load magnitude in both linear and non-linear systems and load position in a predominantly non-linear system. An aluminium surface with surface dimensions of 800x600x7mm was tested with 8 linear sensing elements (OPB 704), and four loading positions, each of an accumulating loading magnitude of 86.9kg. 165 training input patterns were collected, each with its corresponding loading pattern, along with a further 33 testing inputs and corresponding loading patterns, to examine the accuracy of the system mapping for the determined coefficients. The accuracy of the system shows that the average error for the calculated loading magnitudes is given as: 1.24kg or 1.43% for load 1 at coordinate (20,41.5)cm, 1.19kg or 1.34% for load 2 at coordinate (20,27)cm, 0.89kg or 1.02% for load 3 at coordinate (60,41.5)cm and 0.95kg or 1.1% for load 4 at coordinate (60,27) demonstrated in figure 3.35

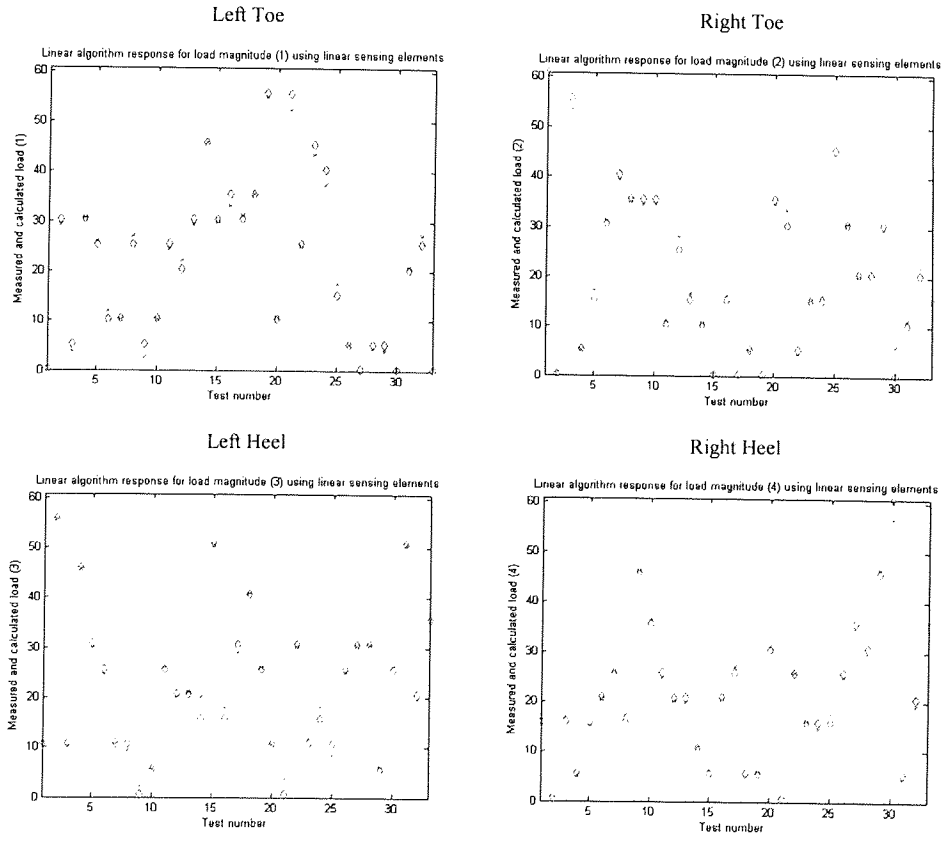

Figure 3.35 - Calculated responses from the derived coefficients verses the measured outputs. The diamonds (◇) represent measured and crosses (x) calculated loading magnitudes in kg.

The same linear inverse method was also applied to the steel surface with the non-linear optical sensors (SY-CR102). 154 training samples with respective outputs all summing to 82 kg were acquired to determine linear coefficients that represent the systems hidden function. 31 testing patterns were used to test the accuracy of this linear representation. It was found that the error for load 1 was given as 0.91kg or 1.11% at coordinates (14.5,39)cm, the error for load 2 is 2.62kg or 3.19% at coordinates (64.5,39)cm, the error for load 3 is 0.83kg or 1% at coordinates (14.5,15)cm and the error for load 4 was 2.63kg or 3.21% at coordinates (64.5,15)cm. These results are demonstrated in figure 3.36.

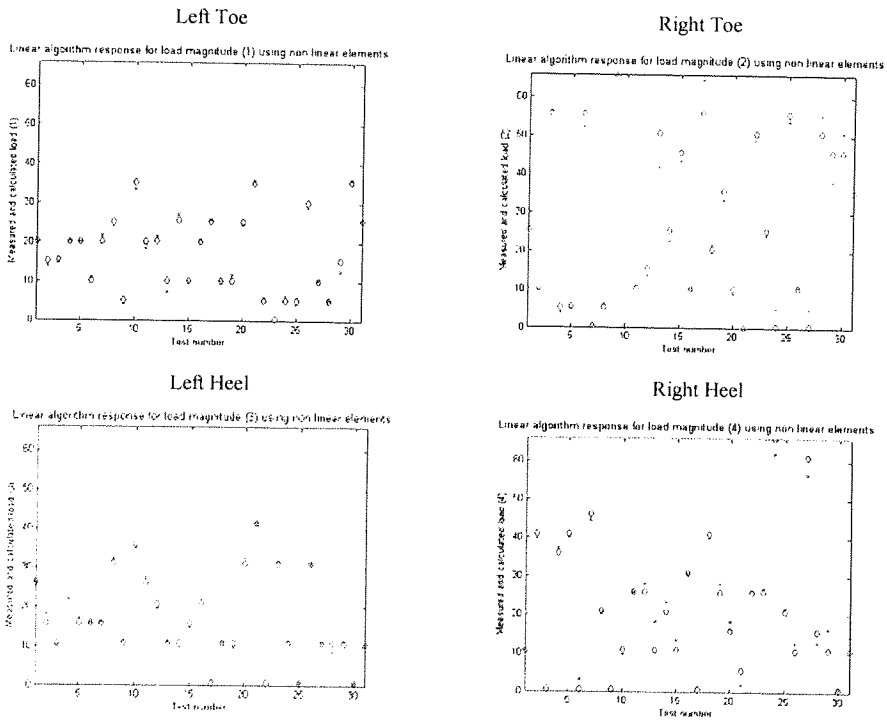

Figure 3.36 - Regressive output response of the linear inversion method for the steel surface with non-linear sensing elements.
The diamonds (◇) represent measured and crosses (x) calculated loading magnitudes in kg.

Observing the results between examinations under similar testing conditions it has been found that the average error for the linear interpretation method for the aluminium system with linear sensing elements is 1.22%. The error for the steel surface using non-linear elements under this interpretation method was found to give 2.13%. The errors between tests appear to be similar; however accuracies appear to be slightly greater in the system

with linear sensing elements; this is due to the fact that the system with the linear elements behaves more linearly thus a linear approach is more suited to this type of system. In the case of high accuracies being obtained using both types of sensing elements; this can be assumed to be due to small changes in loading, hence small changes in sensory response. Small changes on the sensory curve will appear to behave linearly or tangential to the characteristic curve of the element; however, a large output loading range will assume large deflections; hence give non-linear responses between the input responses. Data to the extremes of the output range will therefore behave non-linearly to the data in the linear range of the curve.

Position can also be assumed to be a representative characteristic of a loading stimulus on the surface. The movement of a constant loading on the surface will induce a large range of possible deformations at all sensing points. Inevitably, in the system with non-linear sensing elements, this will induce a set of non-linear training patterns at all possible loading coordinates. This can be supported through an examination of this method in the interpretation of a single-point load of 10kg on a steel surface of dimensions 760x760x2mm, facilitating 16 non-linear elements. The average error was given as 47.9% and 32.42% in the x and y directions respectively, from 192 training and 64 testing patterns.

For the interpretation of two loads of 10kg on the surface, 9560 input training patterns were used to train the linear model. A further 1912 patterns were then used to test the validity of the method, which gave errors of 19.74% and 14.62% in the x and y directions for load 1. The errors for load 2 were also given as 19.96% and 20.07% in the x and y directions. These results show that the relationship between the input responses and output coordinates is strictly non-linear. This can be due to the curved input to output relationship mentioned earlier.

3.5.4 Linear Regression Single Layered Perceptron (SLP) Approaches

There are two main forms of neural networks: function-based and memory-based. Back propagation-trained algorithms such as SLP and Multiple Layered Perceptrons (MLP), and linear inverse methods described above can be described as being function-based networks. These methods are inherently slow to train as they must compress the data into a generalised functional format created by the network topology. However; they possess very fast recall speeds, due to the simple feed forward of the input pattern through the generalised function to produce an associated output.

This can be compared with Memory based networks, such as the Cerebellar Model Articulation (CMAC), nearest-neighbour interpolation, probabilistic neural networks, and Kohonen Learning Vector Quantization. Rather than learn a generalising function of the data, these methods store examples of the training data in memory. When presented with a new input training pattern, nearby training patterns are recalled from memory and the output is a function of these patterns (e.g. a linear interpolation among the 5 nearest neighbours). Memory-based approaches learn very quickly as they simply remember each training input, but the recall can be much slower, since the nearest neighbours must be found, and then an interpolation performed to produce an output.

For the application, it is important to note that output speeds upon captured data should be as fast as possible for the aesthetics of the user system. More flexibility is offered to train the algorithm prior to an installation of the system, since the training of the algorithm is a one-off, then the time taken to train it is not a crucial issue as opposed to the time taken to create results. This indicates that only function based approaches will be explored for the nature of the application.

The forward model of SLP is identical to linear regression and possesses a bias term in it. This is applied as to give more control in the selection of appropriate weightings and so to achieve a better fit of input to output variables. These additional coefficients are often termed slack or surplus variables or in neural network theory, the bias terms. The

weighting and bias variables can be calculated using the pseudo-inverse method, assuming that the weighting of the bias term is set to +1 and the value of the bias is the error between the input and output variable equation, as explained in section 3.6.3. Alternatively, the Delta rule can be used determine the values of the weightings and the biases.

The Delta rule is a simple learning rule that states the weights should be adjusted by the difference between the desired output and the actual output. The error function E is the mean squared error over all of the training patterns and is expressed as:

$$E = \frac{1}{P}\sum_{p=1}^{P} e_p \tag{3.46}$$

Expression (3.46) represents the sum of the errors (e_p) across all of the training patterns P, divided by the number of training patterns to generate the mean error E. ($\mathbf{e}_p$) is calculated as:

$$\mathbf{e}_p = \left(\mathbf{d}_p - \mathbf{net}_p\right)^2 \tag{3.47}$$

Equation (3.47) expresses the squared error term, from the difference between the target output ($\mathbf{d}_p$) and the network calculated output ($\mathbf{net}_p$) for the output pattern in question. The network output ($\mathbf{net}_p$) is the result of the algorithm and is formed by summing the product of the derived weightings (w) and the input ($\mathbf{X}$) as:

$$\mathbf{net}_p = \sum_{i=0}^{n} \left(\mathbf{w}_i \mathbf{X}_i\right)_p \tag{3.48}$$

The output ($\mathbf{net}_p$) is derived from the same method to that of the feed forward function using the linear inverse method to formulate the optimal weighting values. Initially the weighting coefficients are randomised and then are changed in magnitude to converge to

a minimum error in (3.46). The learning rule is to define a change in weights for a converging minimisation through a method of steepest descent, for example:

$$\Delta \mathbf{w}_i = -k \frac{\partial E}{\partial \mathbf{w}_i} \tag{3.49}$$

Equation (3.49) can be evaluated by substituting equation (3.46) to give:

$$\frac{\partial E}{\partial \mathbf{w}_i} = \frac{1}{P} \sum_{p=0}^{P} \frac{\partial \mathbf{e}_p}{\partial \mathbf{w}_i} = \frac{1}{P} \sum_{p=0}^{P} \frac{\partial \mathbf{e}_p}{\partial \mathbf{net}_p} \times \frac{\partial \mathbf{net}_p}{\partial \mathbf{w}_{ip}} \tag{3.50}$$

Further, substituting equation (3.47) in to (3.50) and followed by partial differentiation with respect to $\partial \mathbf{net}_p$ expression (3.50) becomes:

$$\frac{\partial E}{\partial \mathbf{w}_i} = \frac{1}{P} \sum_{p=0}^{P} -2\left(\mathbf{d}_p - \mathbf{net}_p\right) \times \frac{\partial \mathbf{net}_p}{\partial \mathbf{w}_{ip}} \tag{3.51}$$

by differentiating $\frac{\partial \mathbf{net}_p}{\partial \mathbf{w}_{ip}}$ from equation (3.48), with respect to $\partial \mathbf{w}_{ip}$ gives the input $\mathbf{X}_{ip}$.

Substituting this and $-k$ from equation (3.49) and taking the constant factor -2 out of the summation yields from equation (3.51):

$$\Delta \mathbf{w}_i = \frac{2k}{P} \sum_{p=1}^{P} \left(\mathbf{d}_p - \mathbf{net}_p\right) \mathbf{X}_{ip} \tag{3.52}$$

The term 2k in equation (3.52) is often expressed as the learning rate η. Equation (3.52) shows the change in weight values using the steepest descent approach at a rate of the average squared error magnitude. Equation (3.48) calculates the network output which is substituted into equation (3.52). This equation therefore determines the change of the weight values required from a least mean squares sense and is then iterated many times to bring the average error towards a minimum. As a result this changes the weight values in the single layer.

3.5.5 Search Methods

Other search methods that can be used are conjugate and scaled conjugate gradient search methods. These methods are computationally more efficient that the method of steepest descent, due to its slow convergence. The steepest descent method, when searching, has to take right angles or be orthogonal to the line search direction after each step, and consequently it may search in the same direction as in previous steps.

The methods of conjugate gradients are an attempt to fix this problem through a 'learning from experience' approach. The difference between the two is within the choice of the next search direction from the minimum point. However; the conjugate gradient method converges quicker, because the search space is modified, or stretched along the eigenvector axes, so that the elliptical contours of the search space become circular. In this stretched space, the direction appears to be at a tangent to the now circular contours at the optimal point. Since the next search direction is constrained to be Q-orthogonal to the previous, they will appear perpendicular in this modified space. Hence, this will go directly to the minimum point of the quadratic function $f(x)$.

But, the less similar $f(x)$ is to a quadratic function, the more quickly the search directions lose conjugacy, and the method may not converge at all, athough, it is generally to be preferred over the Steepest Descent method.

The Scaled Conjugate Gradient Method (SCG) belongs to the class of Conjugate gradient methods, which show superlinear convergence on most problems. Moller's scaled conjugate training algorithm provides a way of calculating 'nearly' conjugate search directions without performing a time consuming line search or Hessian matrix for every learning iteration. Practical experiments have shown that it can outperform both conjugate gradient, and quasi-Newton algorithms (Nabney, 2002), and hence shall be used as the training algorithm for all following applications investigated.

3.5.6 Multi-Layer Perceptron (MLP)

The MLP is probably the most widely used neural network architecture for practical applications. The MLP usually consists of two layers, provides connectivity between the inputs to hidden units and following hidden units to outputs. It has the capability of providing any arbitrary mapping between input and output units for any continuous function, providing that the hidden weightings and bias units are selected appropriately. In general, provided that there is enough data to estimate the system parameters then the MLP can estimate any smooth function.

Minimising the error function along a direction d_k can be achieved through a numerical line search for a given step size λ_k or through numerical differentiation. Analysis of such algorithms often examines their behaviour when the error function is truly quadratic. The conjugate gradients algorithm is an iterative and efficient method for choosing mutually conjugate search directions. The search direction is selected in such a way that at each iteratively selected parameter value w_j, the current gradient g_k is orthogonal to all previous search directions. Hence at any given step in the iteration, the error surface has a direction of steepest descent that is orthogonal to the linear subspace of parameters spanned by the prior search directions.

Supposing that H is a symmetric positive-definite matrix, and two sequences of vectors (where $d_0 = g_0$ are non-zero vectors) are as follows from the j^{th} step:

$$g_{j+1} - g_j = \lambda_j H d_j \tag{3.53}$$

Hence the optimally condition for the learning step λ_j derived from the orthogonal condition becomes (3.54), assuming that g_j and d_j are pairwise orthogonal and conjugate.

$$\lambda_j^* = \frac{-d_j^T g_j}{d_j^T H d_j} \tag{3.54}$$

If the weight space has dimension p then there can be only p linearly independent directions of vectors. Therefore, it is possible to represent any point as a linear combination of no more than p of the conjugate directions, and in particular if w^* is the sought location of the minimum error function, then there exists coefficients such that

$$w^* - w_0 = \sum_{j=0}^{p-1} \lambda_j^* d_j \tag{3.55}$$

If the error surface is quadratic with a positive definite Hessian then selecting H-conjugate search directions and learning steps from (3.54) guarantees a minimum of no more than p iterations. Conventional conjugate gradient algorithms use a line search to find the minimising step, and introducing scaling β_k into (3.54) gives

$$\beta_k = \frac{d_j^T H g_{j+1}}{d_j^T H d_j} \tag{3.56}$$

Induction can be established that this recursive definition of conjugate gradient search directions does not indeed yield a fully conjugate set when the error is quadratic, although the above equation is only defined when d_j and d_{j+1} are conjugate.

A version of the conjugate gradient algorithm that does not require line searches was developed by Moller and uses the finite difference method for estimating Hd_k and is demonstrated by Abraham (2003). It carries this out through monitoring the sign of the product $d_j^T Hd_j$, and defines δ as

$$\delta = d_j^T H d_j \tag{3.57}$$

Moller introduces two new variables, σ and $\overline{\sigma}$ to define an altered value of δ and $\overline{\delta}$. These variables are changed with ensuring that $\overline{\delta} > 0$. Although, this does not affect the error surface, and the Hessian with the quadratic approximation will still suggest that

there is a minimum along the search direction, producing a step size that shows good results in practice. $\bar{\delta}$ is defined as follows

$$\bar{\delta} = \delta + (\bar{\sigma} - \sigma) d_j^T d_j \tag{3.58}$$

The requirement for $\bar{\delta} > 0$ gives a condition for $\bar{\sigma}$:

$$\bar{\sigma} \approx \sigma - \frac{\sigma}{d_j^T d_j} \tag{3.59}$$

Moller then sets $\bar{\sigma} = 2\left(\sigma - \left(\delta / d_j^T d_j\right)\right)$ to satisfy (3.59) and so ensures $\bar{\delta} > 0$. Substituting this in (3.58) gives

$$\bar{\delta} = -\delta + \sigma d_j^T d_j = -d_j^T H d_j > 0 \tag{3.60}$$

An initial condition gives (Nabney, 2002):

$$\Delta_j = \frac{f(x_j) - f(x_j + \lambda_j d_j)}{f(x_j) - f_Q(x_j + \lambda_j d_j)} \tag{3.61}$$

where f_Q is the local quadratic approximation to f along d_j, given by

$$f_Q(x_j + \lambda_j d_j) = f(x_j) + \lambda_j d_j^T g_j + \frac{\lambda_j^2}{2} d_j^T H d_j \tag{2.62}$$

Simplifying (2.61) we obtain

$$\Delta_j = \frac{2\left(f(x_j) - f(x_j + \lambda_j d_j)\right)}{\lambda_j d_j^T d_j} \tag{3.63}$$

which can be calculated using only the gradient and no higher order derivatives. For potentially successful values see Nabney, 2002.

The variables or outputs $\mathbf{Y}$ of the function can be transformed by non-linear activation functions of the hidden layer. The attenuation of the output in this case is restricted to a tanh activation function. The outputs of the hidden units are therefore given by:

$$\mathbf{Y}_j = \tanh(\mathbf{X}_i) \tag{3.64}$$

The full feed forward expression from an unknown input vector becomes

$$\mathbf{Y}_1 = \left(\left(\tanh\left(\left(\mathbf{X}_1.\mathbf{w}_1\right)+\mathbf{b}_1\right)\right)*\left(\left(\mathbf{w}_2\right)+\mathbf{b}_2\right)\right) \tag{3.65}$$

Equation (3.65) also absorbs bias parameters into the weight matrices by introducing an extra hidden unit with a fixed value of +1, (Bishop 1995). The problem with any search method is the selection of an optimal number of weights and iterations required to map the data appropriately without over-fitting the data to measured input or output noise. An example of a one dimensional non-linear input to a one dimensional output is illustrated with a linear mapping using a pseudo linear inverse method, a non-linear over-fitted mapping using an MLP trained with an SVG and the actual clean system function. Noisy data points are collected for various outputs indicated as crosses in figure 3.37.

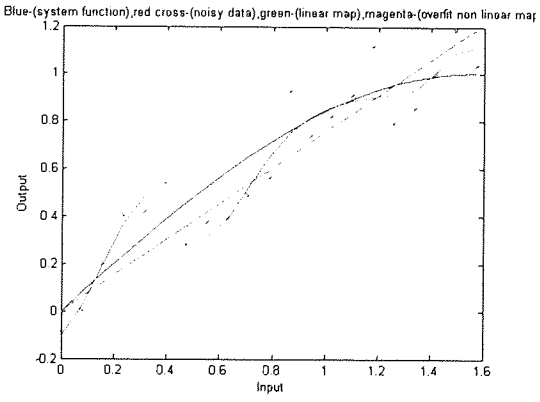

Figure 3.37 - An example of the problems associated with the various mapping functions. The blue curve is the actual system function. The red crosses are the collected noisy data points. The green line is the estimated function, given the noisy data points using a linear inverse method and the pink curved line is the predicted system function, given the noisy data points using an over-trained regressive MLP approach.

Figure 3.37 demonstrates a linear fit (green line) or line of best fit of the noisy input to output data (red crosses). A linear mapping in this case would be inappropriate to represent the correct mapping (blue curve). The non-linear mapping can be used to map the actual system curved response more accurately, however difficulties can arise from over-fitting the data to the system noise (magenta curve) which again would be inappropriate as a system mapping.

It is possible to analyse the network performance measures as a bench mark to optimise the network architecture as a result of associated noise. The training error function can be either a least squares or a canonical error representation. For a canonical error representation, assume that stochastic noise $\mathbf{e}_k$ is added to the deterministic function $\mathbf{y}_k(x;w)$ such that the target is equal to:

$$\mathbf{t}_k = \mathbf{y}_k(x;w) + \mathbf{e}_k \tag{3.66}$$

Equation (3.66) indicates that for each noise model associated with the target, it has a corresponding canonical error function, which represents the negative log likelihood of the data. From this it is possible to determine the training principal errors from the derived likelihood as:

$$L = p\left(t^1,\ldots,t^N \middle| x^1,\ldots,x^N\right)p\left(x^1,\ldots x^N\right) = \prod_{n=1}^{N} p\left(t^n \middle| x^n\right)p\left(x^n\right) \tag{3.67}$$

given that the conditional density is also given as:

$$p(t|x) = \prod_{k=1}^{c} p(t_k|x) \tag{3.68}$$

Equation (3.65) is given such that the target t may have several components and that each of the c outputs is independent. The developed cost or error function can therefore be

developed as a summation from (3.67) and (3.68) by minimising and taking the negative logs of both sides, hence maximising the evaluation of the likelihood:

$$E = -\log L = -\sum_{n=1}^{N} \log p\left(t^n \middle| x^n\right) - \sum_{n=1}^{N} \log p\left(x^n\right) \tag{3.69}$$

This performance measure can be used to interpret the error and convergence associated with the training set. Training optimisation can be performed on the basis of this method and through the use of validation data unknown to the model. The use of validation data can be used as a deterministic method to locate the optimal number of nodes and iterations to provide regularisation of the system function and prevent over-fitting.

In the determination of load magnitude the canonical training error and validation error of the MLP trained with an SCG is given after every epoch (50 learning iterations). The weight decay coefficient and number of hidden nodes is kept at a constant so that the minimal validation error can be recorded against the number of iterations, figure 3.38. The validation algorithm to determine the minimal error for early stopping is also shown in the right of the figure.

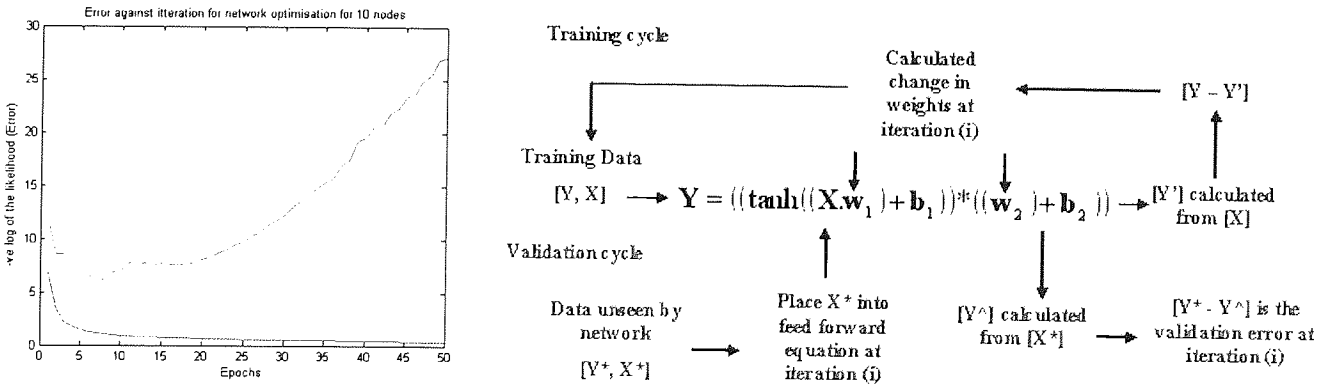

Figure 3.38 - MLP training error between input and output mappings. The red curve represents the error associated with the validation data during the training of the known data.

Figure 3.38 demonstrates the training convergence using an SCG or error between known input and output patterns (blue curve). The red curve represents the validation error associated with the training convergence. The calculation of the training error

[Y-Y'], and validation error [Y*-Y^], from the diagram is given after every epoch, where the selection of appropriate weightings is analysed. The unknown validation input pattern [X*] is fed forward through the network to give a predicted output [Y^], based upon the weightings [w_1, w_2] from the known input [X] and output [Y] training patterns. The difference between the predicted [Y^] and respective unknown validation output pattern [Y*] gives the validation error.

When the network starts to fit to the noise the resultant validation error (red curve) increases, such that the minimal validation error can be assumed to be a closer mapping of the true generalised function. The figure demonstrates that the minimal validation error is given as 8 epochs before the network starts to fit to the noise in the data, thus the network should only be trained for 400 iterations to prevent over-fitting.

This analysis of early stopping is repeated for a varying numbers of nodes and a constant weight decay coefficient. The minimum validation error for each number of nodes is recorded in each case. Plotting the minimal validation errors verses the node quantity can give an indication of the optimal number of nodes required. This is demonstrated in figure 3.39.

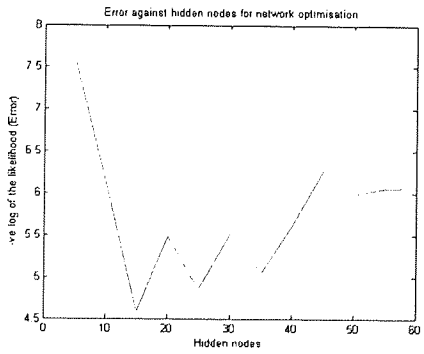

Figure 3.39 - Minimal validation errors for a varying number of nodes.

Figure 3.39 indicates that the minimum validation error lies somewhere between 10 and 30 nodes due to the dip in the validation error. The analysis must then be carried out all numbers of nodes between 10 and 30 to calculate the true minimum error. In this case the optimal number of nodes was found to be 19. The number of nodes is now maintained as

a constant and the weight decay coefficient is varied upon a logarithmic scale i.e. (0.01, 0.001 etc) to locate the optimal weight decay coefficient and iteration quantity for early stopping in relation to the minimum validation error. In this case the optimal weight decay coefficient was found to be $1x10^{-6}$ with an early stopping of 550 iterations. The example demonstrated is for a mapping between a vector voltage set and a vector output for load coordinates. Applying this method to demonstrate a visual representation similar to that in figure 3.40 gives a non-linear mapping from noisy input data as:

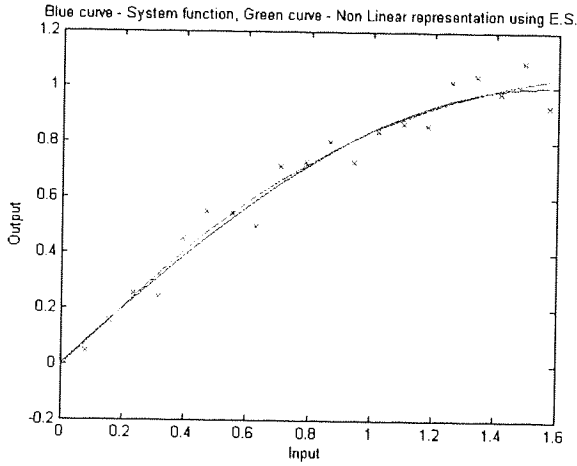

Figure 3.40 - Non-linear method with an early stopping criterion (green curve) mapping the true system function (blue curve) from noisy collected input data (red crosses).

It can be observed that the method of early stopping would be suitable to locate the system function accurately, even though the data may be subjected to external noise.

Due to the success of an MLP trained with an SCG and coupled with an early stopping criterion, it has been decided that this would be an acceptable approach, albeit that the given data set is large. This is such that the regularisation algorithm can perform successfully, due to small levels of uncertainty in the training data. Testing this approach the same data was computed for the load magnitude and position as with the linear interpretation method.

For the discrimination of **four load magnitudes** the same non normalised input and output patterns from the linear method were trained and regularised using this **MLP**

approach. Using the system with **linear sensing elements**, the optimal number of hidden nodes and weight decay coefficient was calculated as 57 and $1x10^{-9}$ respectively, with an early stopping of 2450 iterations, taken from 165 training patterns. The errors for the four load discrimination using an MLP gave: 0.46kg or 0.53% for load 1 at coordinate (20,41.5)cm, 0.37kg or 0.42% for load 2 at coordinate (20,27)cm, 0.56kg or 0.63% for load 3 at coordinate (60,41.5)cm and 0.44kg or 0.5% for load 4 at coordinate (60,27).

For the discrimination of the **four load magnitudes** using the **non-linear sensing elements** the results of the **regularised MLP** with the same non normalised data in the linear method gave optimised parameters of: 16 hidden nodes, a weight decay coefficient of $1x10^{-4}$ and an early stopping of 700 iterations from 154 training pattern gave: An error of 1.18kg or 1.44% for load 1, at coordinates (14.5,39)cm, the error for load 2 was 2.08kg or 2.54% at coordinates (64.5,39)cm, the error for load 3 was 1.11kg or 1.35% at coordinates (14.5,15)cm and the error for load 4 was 1.61kg or 1.97% at coordinates (64.5,15)cm.

3.5.7 Normalisation of the input patterns

Input patterns are normally scaled so that the magnitudes of the patterns are generally similar. This is so that the weightings in the model are generally similar, are of equal importance and so that the model weights can be initially randomised. Without normalisation, network training can get stuck in a local optimum because some of the weights are a very long way from their best values.

The normalisation procedure is based on a statistical scaling method that will transform the original data set into a normalised set in terms of a zero mean and unity variance. Each variable in the pattern is normalised independently from:

$$\mathbf{x}_i^n = \frac{\mathbf{x}_i - \bar{x}}{\sigma} \tag{3.67}$$

where subtracting the mean $\bar{x}$ from $\mathbf{x}_i$ gives a zero mean and division by the standard deviation σ of the set rescales the variable to have a variance of one, see (Nabney 2002).

This normalisation of the input patterns was performed using the same training patterns for both the system with the linear and non-linear sensing elements. This is to determine whether the use of this normalisation routine would strongly enhance the accuracy of the result.

3.5.8 Results and conclusions for regression models

For the system with ***linear sensing elements*** (OPB 704), the optimisation using normalisation and regularisation of the MLP architecture gave: 55 hidden nodes, a weight decay coefficient of $1x10^{-6}$ and an early stopping of 400 iterations.
The error associated with load 1 gave 0.74kg, or 0.86%,
load 2 gave 0.5kg, or 0.58%,
load 3 gave 0.49kg, or 0.56%,
and load 4 gave 0.44kg, or 0.51%.

For the system with ***non-linear sensing elements*** (SY-CR102), using normalisation and regularisation of the MLP gave optimised parameters of 30 nodes, a weight decay coefficient of $1x10^{-6}$, with an early stopping of 1150 iterations.
The error associated with load 1 gave 1.13kg, or 1.38%,
load 2 gave 2.23kg or 2.72%,
load 3 gave 0.81kg or 0.99%,
and load 4 gave 2.22kg, or 2.71%.

For the results of both processing methods see figure 3.41.

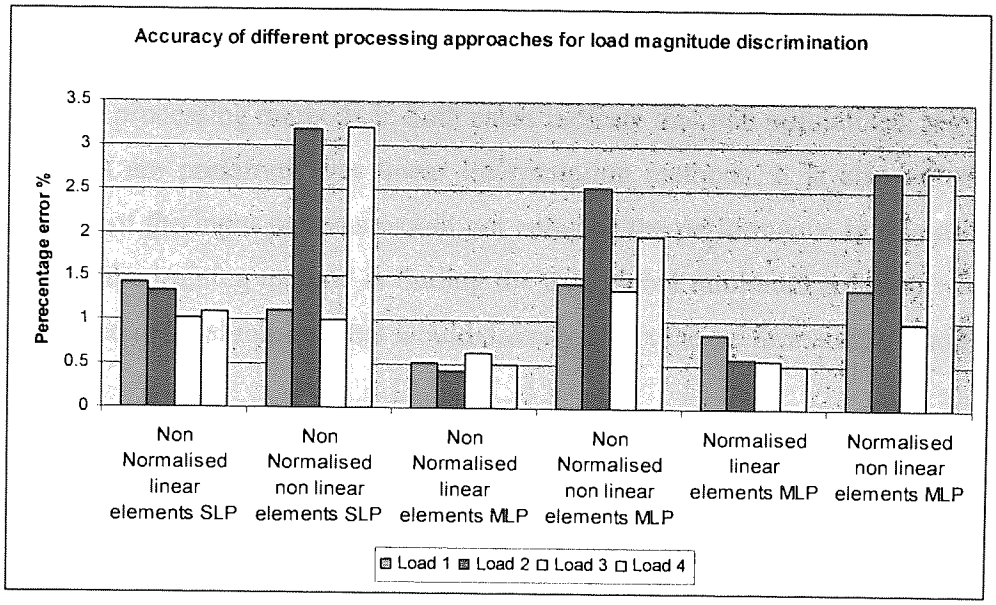

Figure 3.41 - Processing accuracies for the four loads on the surface for both linear (aluminium surface) and non-linear (steel surface) systems.

A selection of the appropriate processing and sensing method would have to be taken upon the general or averaged accuracies for the method. This would give a clear indication on the most appropriate method and is illustrated in figure 3.42.

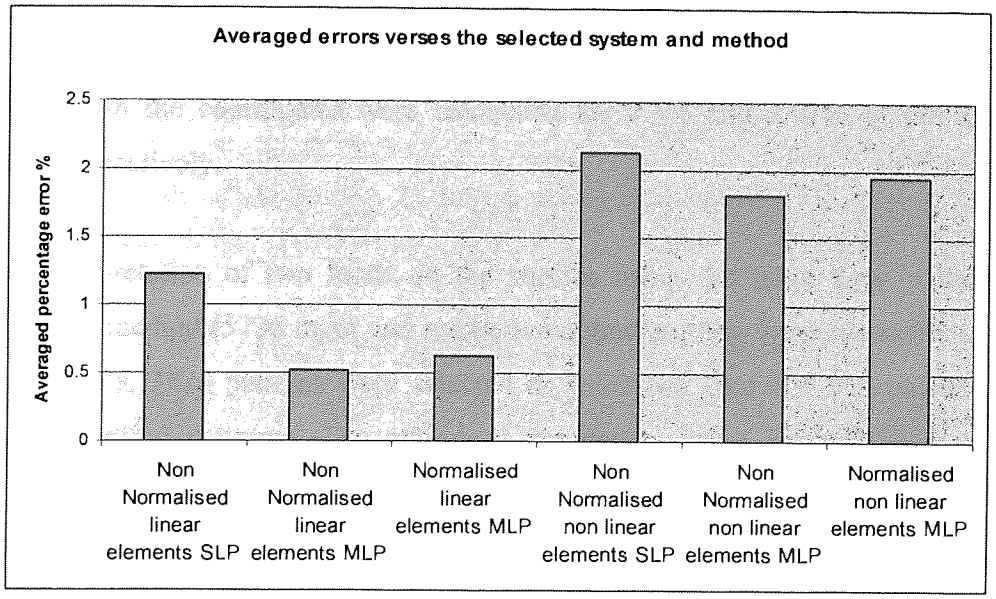

Figure 3.42 - Most appropriate system and processing method for load magnitude discrimination at four points on the surface.

From figure 3.42 it can be observed that a system with an aluminium surface with predominantly linear elements would perform better than a steel surface with non-linear elements. The processing methods in both cases indicate that non normalised, regularised MLP methods are preferred over linear interpretation methods. It is also noted that a normalisation of the input patterns would not enhance the performance in this case. This indicates that the training method is finding the true global minimum solution within the data as opposed to local minima that would directly affect the performance of the system.

Average errors of 0.52% for the aluminium surface with non-normalised linear sensing elements, also clearly lies within the initial specification of a 5% error allowance for the system. Similarly, an average error of 1.825% for the steel surface with non-normalised non-linear elements also lies within the specification, making both methods valid solutions for the requirements of the system.

Applying a regularised MLP method to interpret the loading coordinates of a 10kg point load from the same input data used in the linear interpretation method. From this 192 input samples were used as training patterns, 128 samples were used as validation patterns and 64 patterns were used as testing patterns optimised parameters of: 100 nodes, a weight decay coefficient of $1x10^{-7}$ and an early stopping of 25000 iterations. The errors associated with the coordinates were calculated as: 2.1% and 2.01% in the x and y directions respectively.

For the interpretation of two loads on the surface using the same data in the linear interpretation method (5736 input and respective output patterns were randomly selected as training data, 3824 patterns were selected as validation data and 912 patterns were selected as testing patterns). The optimised parameters using regularisation gave 77 nodes, a weight decay coefficient of $1x10^{-7}$ and an early stopping of 20000 iterations. From this the errors were derived as: 5.8% and 3.63% in the x and y direction for load 1. The errors for load 2 were also derived as: 6.67% and 4.59% in the x and y directions.

However such an evaluation also shows an averaged accuracy of 5.17% which is not far off the required accuracy requirement of 5% for the system, for feet positioning. To enhance accuracy further, it is possible to change the training structure. It can be assumed that the golfer stands directly in front of the ball during the golf stroke. If the feet are to move, then they will practically move symmetrically outwards or inwards about the head which is positioned in front of the ball. Thus the feet positioning distance from the head to the extent of the feet will be the same for the left and right feet, hence reducing network output dimensionality from four to two.

If the dimensionality of the position output is reduced to two then the results show an average positional accuracy of 2.055% which is well within the 5% requirement of the system. The comparison between linear and regularised non-linear methods for load position is shown in figure 3.43.

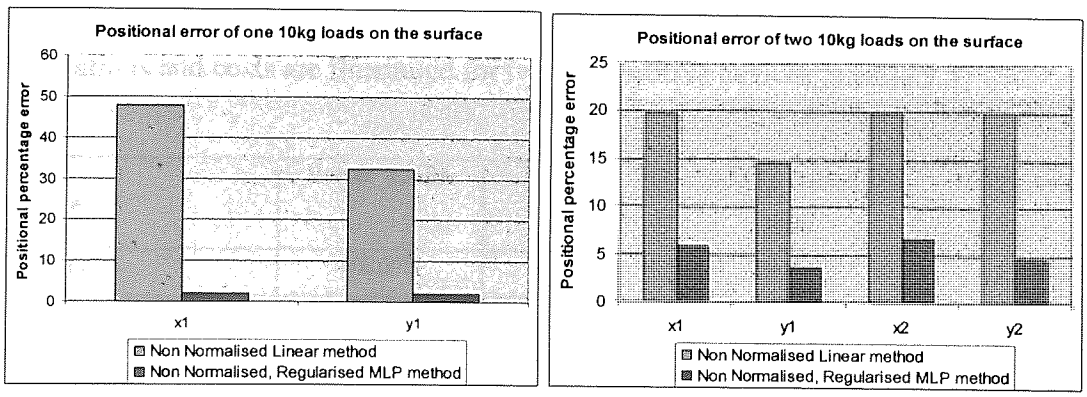

Figure 3.43 - Accuracy for a system with non-linear sensing elements for both the discrimination of one and two loads on the surface using two different processing approaches.

In figure 3.43 it can be observed that there is a large loss in accuracy when moving from a linear to a non-linear mapping of the input to the positional output. It also shows that a non-linear processor would be more suited in the discrimination of load position. This can be compared with the change in accuracy from a linear to a non-linear method in the description of load magnitude, which is very small in figure 3.42. This indicates that if the position of the load is fixed on the surface with changing magnitude then the system performs linearly even though the elements may behave in a non-linear manner as described earlier.

However, if the load is to be described as a position on the surface then the system or input data patterns is clearly non-linear in relation to the output patterns due to the large changes within the non-linear sensory response. This is indicated in figure 3.43 for the change in accuracies between linear and non-linear methods. Added to this the Navier evaluation of the loading position, upon the measured deflections clearly becomes a non-linear problem as in section 3.52. It predicted that non-linear mapping methods would be more accurate than linear methods, due the non-linear nature of the underlying system function and is supported by the results in figure 3.43.

These results can be compared, with that of competitive array measurement devices that can be bought 'off the shelf' direct from suppliers. Bertec offer a range of products to fulfil tactile sensing needs. The boards come in a range of sizes and the sensor elements can be spaced as close as 2mm apart. The board can be bought in sizes from a 4x4 to 64x64 array, and illustrates the loading profiles directly on to a screen in real time. Limitations and costs are illustrated for two competitive devices in table 3.3.

Feature	Bertec 4060A	Bertec 4060HT	AMTI OR6-5-2000	AMTI Acugait
Fz range	10000N	10000N	8918N	2590N
Fx, Fy range	5000N	5000N	4459N	431N
Size (mm)	400x600	400x600	463x508	500x500
Natural Freqency Hz	500	1400	500	150
Hysteresis	<±0.2%	<±0.2%	<±0.4%	<±0.4%
Mass	28kg	-	-	11.34kg
Resolution (mm)	0.1	0.1	0.75	-
Cost	£13137	£17338	-	-

Table 3.3 - Performance and data of competitive array-type force plates.

The figures in table 3.3 highlight the minimum resolution required in the position of the centre of pressure (and the cost). Unfortunately, there are no results for the accuracy of the predictions of load magnitude or position. However, this can be compared to an estimated resolution of the COP from the RFSES. This can be derived through an average

error calculation of the loading magnitudes in the x, and y directions, as a function of the distance between the feet on the surface.

Using the results from the MLP described earlier with linear elements, the estimated COP resolutions would give errors of 3.14mm in the x direction and 1.13mm in the y direction. This although not as accurate as the values in the table at a resolution of 0.1mm for the Bertec 4060A, and 0.75mm for the AMTI 0R6-5-2000, can still compete fairly well in terms of accuracy and at a fraction of the cost.

The RFSES has been developed to meet the demands of the specification, i.e. specific magnitude and position of the feet for example, whereas array systems are more generic solutions that have not specifically been designed for this application. Hence, the feedback to the golfer on the surface is more appropriate than that of an array system.

The array load table is rather overkill for the application in terms of the accuracy of measurement, which is really meaningless to the golfer on the surface. The above table also illustrates the results based upon surfaces slightly smaller than the RFSES, indicating that dimensions of the required size would be at an even greater cost than that shown.

It is to be concluded that the position of the golfer's feet on the surface is to be described first using a regularised MLP approach. Once the feet position have been described it is then possible to select an appropriate trained MLP for the respective feet position, to describe the magnitude of the loading at the feet during the golf swing. It is also noted that a 4mm steel surface will be selected due to the high repeatability of the surface and from the results indicated in figures 3.41-3.43. For supplementary pictures see Appendix C.3.

3.6 Other investigated applications using regression models

The application for this type of technology is wide in medical and sport based applications for diagnosis and therapy/improvement. The methods that have been proposed are to be used as supporting analysis for the RFSES and are: a sway table and a dynamic body support system.

3.6.1 Investigation of a novel-type sway table using regression and the RFSES

A sway table was developed using the RFSES for the analysis of human balance and typically measures the movements of the centre of gravity of a person. It is not possible to locate the centre of gravity accurately when using a visual system, whereas the force system is ideal for locating the centre of pressure (COP).

The results of experiments show that using a linear SLP model, the sample mean suggests that over 95% of the predictions can be estimated to within 1cm, with a standard deviation of 4.6mm. This was derived through the use of the aluminium surface described in Section 3.2, and linear sensing elements OBP 704 and algorithm in Section 3.5.3. Taking the magnitudes of the feet at four fixed standing positions, it was possible to calculate the location of the COP through triangulation, as the size and distance between loading points was known. From this the magnitude of movement from the mean position, the velocity, acceleration and frequency of sway in both x and y planes could be determined using an FFT to the derived position of the COP in the x and y directions.

An experiment was conducted that required a candidate to be spun around several times as to disorientate the subject. The sway and settling time of the candidate was investigated using this system and provides outputs such as the movement of the COP in the x and y positions as in figure 3.44.

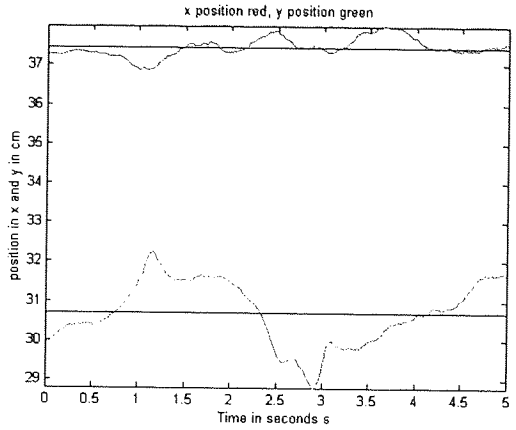

Figure 3.44 - Movement of COP sway in both the x and y directions over time. The straight black lines indicate the mean or settling position of the candidate

Figure 3.44 shows that the sway of the candidate is of greater magnitude in the y direction which is a forward and backward movement of the head, as opposed to a side to side movement in the x direction. Which is be expected after disorientation. Similarly the magnitude of movement can be also be derived over a period of time as in figure 3.45.

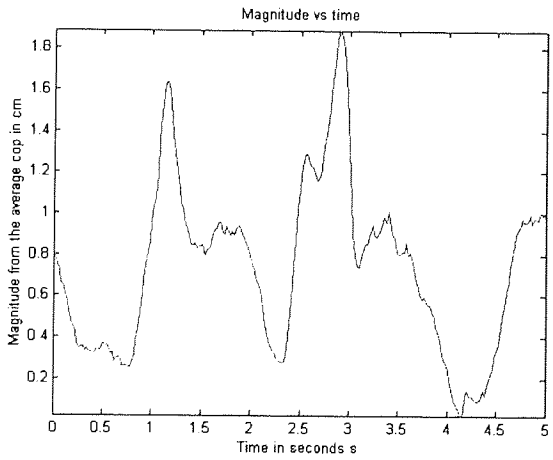

Figure 3.45 - Magnitude of the COP sway over a time period

The above figure shows useful feedback to determine the severity of sway, or unbalance. It shows that there is definitely an oscillatory motion suffered by the candidate, also giving the extents of the sway.

Similarly the velocity of movement over the time period can also be determined and is illustrated in figure 3.46.

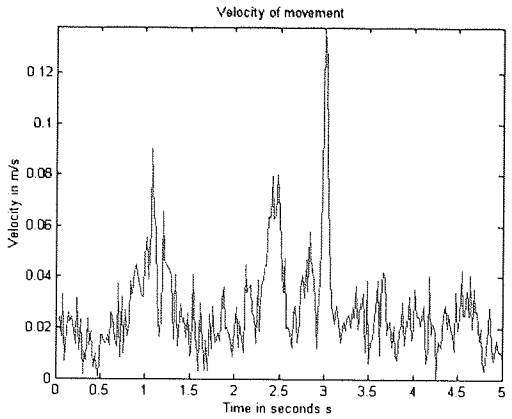

Figure 3.46 - Velocity of sway over the measured time period

In the case of figure 3.46 the analysis indicates that there is more or less a constant velocity of sway at around 0.02m/s and could therefore be indicative of the sway severity which can be monitored over a rehabilitation period. This can also be useful to numerically analyse the effect of a prescribed medication or treatment in the rehabilitation period.

The frequency of sway can also be indicative of the balancing condition, figure 3.47 shows that the frequency of sway in the y direction (sway to and fro from forwards to backwards) is about 0.8 Hertz using this RFSES. Thomas and Whitney (1959) say that the average elderly adult baseline sway frequency is 0.3Hz; however McNevin and Wulf (2002) found that young, healthy and physically active participants in their study had a baseline frequency of 1.5Hz and suggested that a high frequency sway indicates rapid corrections in the position of the centre of mass and therefore a healthy balance system.

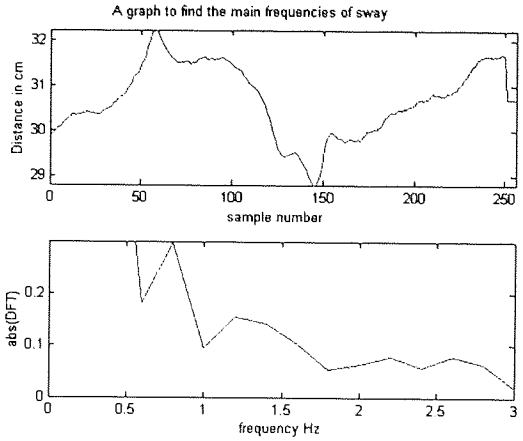

Figure 3.47 - Frequency of sway in the y direction with the candidates eyes open

An analysis was also carried out on the balance correction when spun around several times and with the candidates eyes closed to try and validate the claim by Edwards (1946). Edwards stated that the sway is attenuated by 50% with the eyes open. The average baseline amplitude of sway was attenuated by just over this 50% in the testing carried out. He also noted that the frequency of sway is reduced when the eyes are closed. An experiment carried out to validate these finding using the RFSES is demonstrated below.

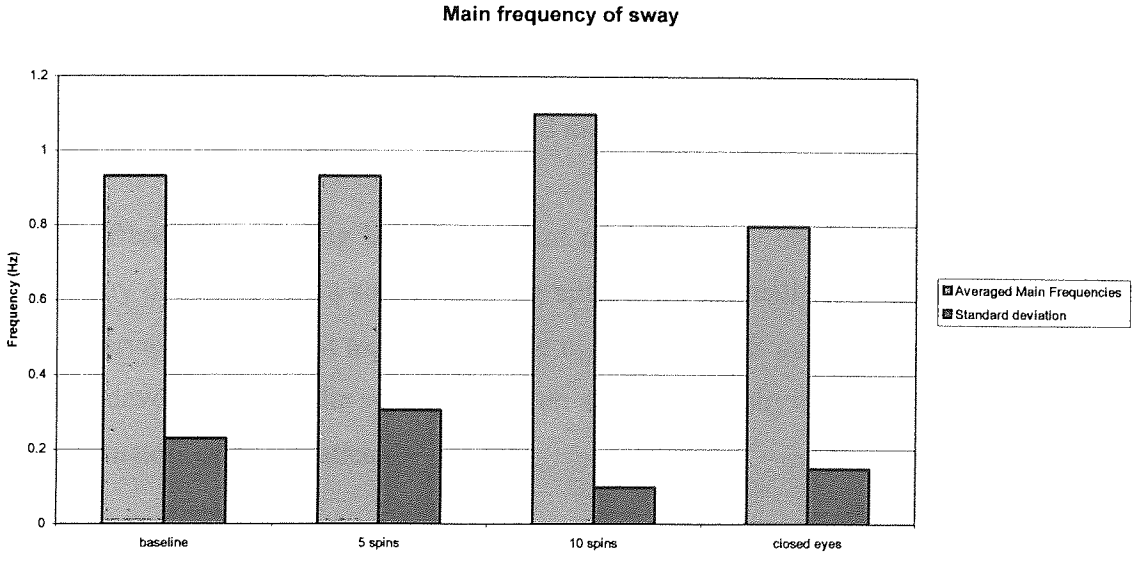

Figure 3.48 - How the principal frequencies change with respect to the eyes being open or closed following a disorientation of the body through spinning

It is observed in figure 3.48 that the frequency of sway is reduced when the eyes are closed and therefore validates Edwards' claim. This reduction in sway frequency signals a slower response to instability and can be attributed to the fact that one third of the available balance feedback systems are not in use. The above diagram also illustrates that the frequency of sway is increased as the level of disorientation is increased. This implies that higher frequent corrections are made by the balance system to compensate for higher levels of disorientation, thus reducing the stabilisation period required.

3.6.2 A novel-typed body support system using regression and the RFSES

A person who suffers a Spinal Cord Injury (SCI) will face many obstacles; one of the most common will be pressure sores which are difficult to treat. An SCI sufferer can typically be a paraplegic, or quadriplegic patient who has suffered irreversible damage to their spinal cord either through injury or illness.

When seated, the SCI sufferer who has lost the perception of pain in the skin can develop pressure sores on the contacting areas of the skin to the seat through a prolonged seating posture. These are generally formed when the blood flow is severely restricted to the skin, due to excess external pressure and can range from a slight blister to a potentially life threatening disorder effecting the skin and muscle layers down to the bone.

As SCI sufferers lose feeling below the point of their injury on their spinal cord, they have no way of telling that a sore is forming apart from manually looking at the skin on regular intervals. However it may be possible to apply RFSES integrated within a seat to prevent to development of the sores through an alarm or the physical moving of the body through actuators or pneumatics.

A RFSES with the methods and approaches described in Sections 3.2 – 3.5 can be used to interpret the loading distributions on the legs whilst seating, to determine the duration in the seating posture. The sensitivity of the surface, material and the effect of a changing

load distribution on the surface was calculated through the use of an extended evaluation of the Navier model expression 3.70, assuming loading distributions as:

(3.70)

$$w(x,y)=\frac{12(1-v^2)}{\pi^4.E.t^3}\sum_{a=1}^{\infty}\sum_{b=1}^{\infty}\left(\frac{\frac{16.P}{\pi^2.a.b.u.v}.\sin\left(\frac{a.\pi.g}{e}\right).\sin\left(\frac{b.\pi.h}{f}\right).\sin\left(\frac{a.\pi.u}{2e}\right).\sin\left(\frac{b.\pi.v}{2f}\right).\sin\left(\frac{a.\pi.x}{e}\right).\sin\left(\frac{b.\pi.y}{f}\right)}{\left(\frac{a^2}{e^2}+\frac{b^2}{f^2}\right)^2}\right)$$

Where w is the maximum deformation,

e = Width of surface in meters

f = Depth of surface in meters

g = horizontal distance of load from origin in meters

h = Vertical distance of load from origin in meters

v = Width of load area

u = Depth of load area

P = Load

Equation (3.70) can be evaluated for the changing deformation of the surface under applied load distributions of the legs for different seating postures. The physical seat dimensions were designed as to provide a seating width of the 95th percentile of males and a length of the 5th percentile of females, so that 95% of subjects could sit on the seat comfortably and was found to be 510mm by 465mm. The depth of the seat given as 30mm was designed to house the linear sensing elements (OPB 704) positioned using a GA along with their sensing range of 10mm and deformation of the surface required to be at around 6mm. For this an 8mm Perspex sheet was selected with a Young's Modulus of $1x10^{10}$ and Poisson's ratio of 0.7, to accommodate a seated loading distribution of 85kg.

The results of the equation with the desired parameters were use to give figure (3.49).

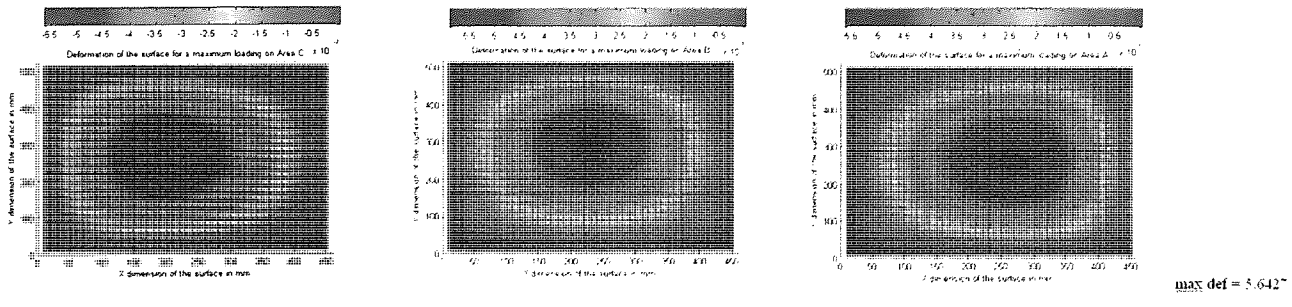

Figure 3.49 (left) - Deformation of the surface for an 85kg subject on the seating surface leaning to the left. (middle) - Surface deformation for a central seating posture. (right) - Deformation of the surface for a seating posture leaning to the right.

The diagrams illustrated in figure 3.49, shows that there are significant differences in the deformation of the surface subjected to a particular posture and postural change. From this it can be assumed that it is possible to use RFSES to infer the seating posture and load distribution on the surface.

The discrete COP on the surface was found to represent the seating posture through a representative SolidWorks™ model illustrated in figure 3.50. This illustrates that it is possible to determine the position of the COP and its magnitude of movement through the inference of the normal loads, such that the duration of the seating posture could be determined.

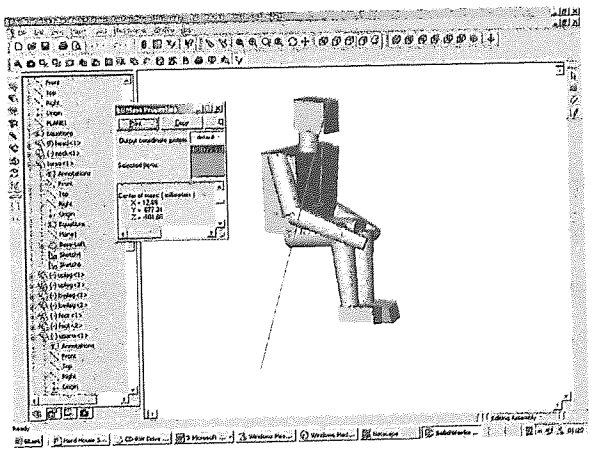

Figure 3.50 - Solid works representation of the body and movement of the COP for various seating postures.

The elements that were selected were nine linear reflective optical elements. This number was assumed to be at a number around an optimal of eight elements from figure 3.16. But a higher number of sensors were selected to see if it would enhance accuracy over eight elements. The sensing elements were applied in proximity to the surface and optimally positioned using the inverse Navier model with Genetic search algorithm, (the appliance

of such a technique is illustrated in Section 3.3.9.3). The design of the RFSES to infer seating posture and load distribution is illustrated in figure 3.51.

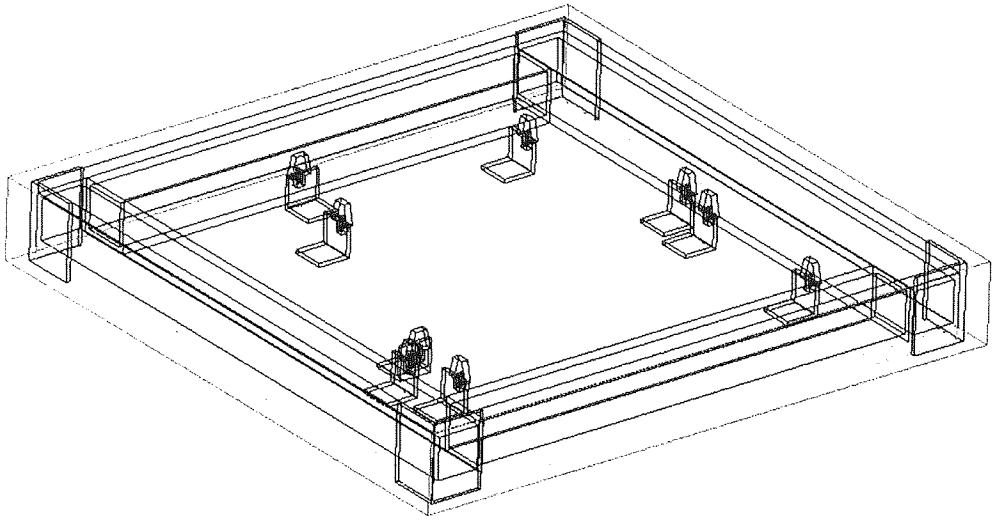

Figure 3.51 – Solid Works drawing of the seat with sensing elements.

The GA assumed that the main loading positions of the seating posture could be represented by 6 points (three along the length of each leg). This was assumed so that the GA could theoretically position the sensing elements around the main loading points of the legs whilst seating. The results of the GA are quite promising, locating themselves around the contours of the seating profile, which gives confidence to the enhanced system sensitivity.

Although point loading on weight hooks of radius 20mm, has been used as opposed to load distributions, and was carried out so that the theoretical mathematics and practical methods could be applied to the problem effectively. Taking point loading can be assumed to be a representation of distributive loading, although not exactly the same, the result of which, could still provide a generalised solution to the loading profile and movement. It is also important to be aware that such a generalised feedback would be an adequate tool to prevent DVT through seating.

Assuming that a regressive inference of the normal loads could be derived through, either a linear SLP or a regularised non-linear MLP model. Then the position of the COP on the surface can also be determined through a triangulation of the load magnitudes.

Initially an SLP method was used to infer the loading at the 6 key points on the surface given 201 training input patterns and gave an average error of load discrimination for 54 unknown input patterns of 4.04% with a standard deviation of 3.85kg for a total loading of 52kg on the surface.

A regularised MLP was also investigated using early stopping using the same training and test patterns as with the SLP method and it was found that the average error for the six load points was given as 4.75% with a standard deviation of 3.8kg.

This indicates that the system is predominantly linear due to the fact that better performances are achieved using the linear method, also supporting this the mathematical representation for the calculation of load magnitudes is also linear.
A similar experiment was carried out using non-linear reflective sensing elements (SY-CR104) and trained with 292 training patterns for various loading conditions at 4 load points on the surface.

It was found that an SLP model gave average loading errors of 1.89% from 58 unknown testing input patterns with a standard deviation of 6.6kg for a total loading on the surface of 61.6kg. Also a trained regressive regularised MLP gave average loading errors at the four points of 0.8% with a standard deviation of 6.69kg using the same data as with the SLP.

This shows that the system has now become predominantly non-linear due to the incorporation of non-linear elements, and the mathematical representation will also change into a non-linear solution.

Looking at the normal load distributions from the system with the linear elements the results can be displayed as a real time loading profile on the seat in figure 3.52 as:

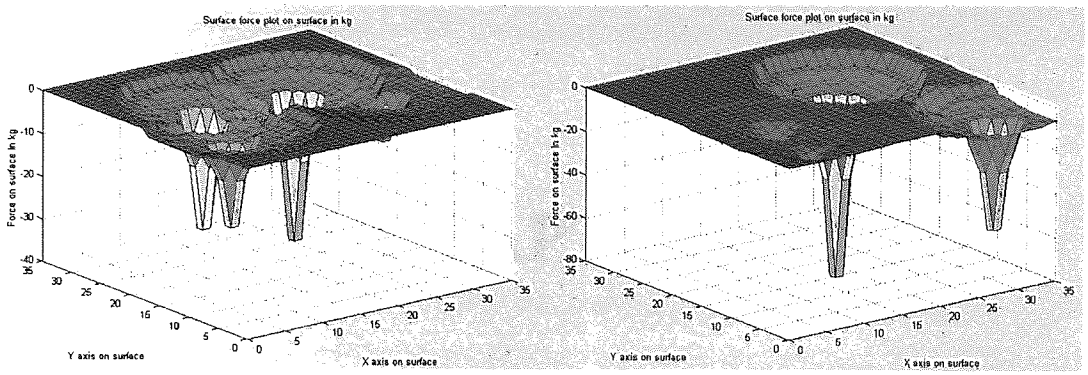

Figure 3.52 (left) - Candidate sitting to the rear of the seat. (right) - Candidate sitting with their posture to the right.

Using the most optimal system, i.e. the system with non-linear sensing elements and a regressive regularised MLP the COP could be calculated accurately and in real time. The accuracy of which in this case only has to be generally good. This is due to the fact that the system will only flag a change in posture when considerable movements are recorded in the movement of the COP and thus small errors in the COP will have little effect.

It has been shown that the appliance of such a RFSES has the ability to interpret the load distribution and the seating posture of the patient on the surface. This also comes with the added advantage of low complexity and cost, comparable to array approaches that can only give information regarding the load profile on the surface. See Tekscan (2000).

CHAPTER 4

Using RFSES and signal processing to describe movement on the surface through classification

This chapter illustrates a development of the research in Chapter 3, which applies time series methods to signals, so that inputs could be formulated to describe the loading conditions on the surface. From this it is possible to describe various movements, or information about the subject based upon the dynamic response of the surface in bending. For example the chapter illustrates a method for determining the height of a subject on a surface, through a simple dynamic activity on it. In this case the selected method gave an accuracy of 1.33cm of the subject's height.

The main section of the chapter illustrates methods for signal processing and a method for the classification of specific dynamic movements during the golf swing. This is such that the result can give a post-swing feedback on the basis of the classified result to improve swing performance. The proposed method is the first of its kind for classifying movements through force measurements of the feet only. For example, questions such as 'did the head move?' or 'did the knees bend?' have up to now, been answerable using vision systems only.

The results are based upon possible flaws during the backswing from the extracted transients, to examine the applied approach. The proposed methods indicate that 91.67% of unknown cases can be identified for a poor or good posture of the legs during the backswing. Also 95.83% of cases are classified correctly for the movement of the left foot off the surface during the backswing and 66.67% of cases are identified correctly for a poor or good orbit angle takeaway of the club during the backswing.

4.1 Digital filtering techniques

The purpose of filtering noise from a signal has to be more than just its appearance. In many cases, sensors with low levels of output amplitude such as strain or pressure sensors are more sensitive to any external noise. Small levels of external noise on the elements will be amplified for further processing and control of the system, such that the noise may appear as a real signal in terms of amplitude. If the processing algorithm is dependant upon clean, defined peaks and troughs in the time series as a control mechanism for decision-making, then it is important that the 'triggers' in the noise are eliminated. For example, when generating a stimulus on three pressure sensors, the impact of the stimulus, can cause noisy features in the captured transient. Such noise can confuse the signal processing algorithm in the characterisation of the captured transient, see figure 4.1.

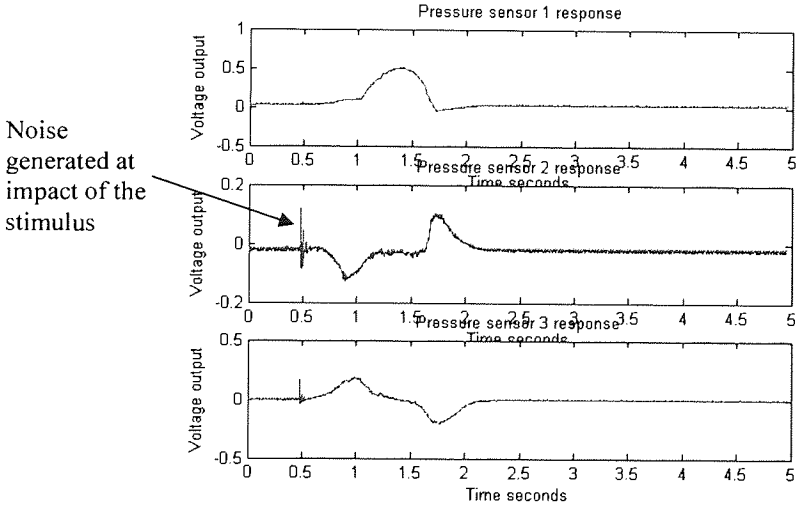

Figure 4.1 - Three pressure sensors stimulated by a loading condition after amplification. Note the magnitude of the noise at sensor two is greater than the peak transient magnitude.

There are two methods of noise elimination: analogue and digital filters. Analogue filters tend to be component driven, through the use of RC networks with comparators that can be developed as: analogue low, analogue high and analogue band pass filters. However, these types of techniques can be costly, so numeric and algorithmic techniques known as digital filters, can be drawn up to eliminate noise, without the use of any analogue components.

4.1.1 Using SVD as a filtering technique to eliminate noise

It is possible to use numerical PCA and SVD techniques to eliminate noise from the captured transient. This works through the manipulation and removal of various derived components in the signal. Fundamental components in the signal can be constructed and evaluated through the use of Singular Value Decomposition (SVD) or alternatively known as: Singular Spectrum Analysis (SSA) (Loskutov 2001), or Karhunen – Loeve Decomposition (KL) (Karhunen 1946 and Loeve 1955), or Empirical Orthogonal Functions (Broomhead, King 1986) for a presentation in the non-linear dynamics context.

SVD was first applied to square matrices in the 1870's by Beltram and Jordon (Klema 1980) and was developed for the extraction of quasi-periodic components from a time series. It was also shown that this method could be used for the improvement of a signal to noise ratio (Ghil 2000). SVD was also discovered to be an algorithm which can be applied in the forecasting of further dynamics of a series. However, the technique in this study will only be used for the suppression of noise in a time series, which is a very common use for SVD.

Assume **A** is an n by m matrix of real-valued data from a time series, with rank (*r*). A translation of the singular values can be determined from the data set **A**, using equation (4.7), whereby the singular value decomposition (SVD) of a square matrix can be viewed as a generalisation of the eigensystem of a square matrix. Setting the small singular values across the rank to zero, we can obtain matrix approximations whose rank equals the number of remaining singular values. By reducing the number of terms in the rank, good approximations of **A** can be developed, giving smoothing through the removal of signal noise.

The SVD technique is also directly related to Principal Component Analysis (PCA) technique. Principal components (PCs) are developed from an orthogonal linear transformation of the covariance matrix. In order to calculate these PCs it is necessary to

calculate the eigenvalues Λ and eigenvectors $\mathbf{V}$ of the data matrix $\mathbf{AA^T}$. The eigenvalues Λ of the data matrix $\mathbf{AA^T}$ can be derived from:

$$\Lambda = \mathbf{V}.(\mathbf{A}.\mathbf{A}^{\mathrm{T}})\mathbf{V}^{\mathrm{T}} \tag{4.1}$$

Equation (4.1) can then be rewritten in the form:

$$\Lambda = \mathbf{V}.\mathbf{A}.(\mathbf{A}.\mathbf{V})^{\mathrm{T}} \tag{4.2}$$

From the derivation of the eigenvectors the PCs can be derived from:

$$\mathbf{V}.\mathbf{A} = \mathbf{Z} \tag{4.3}$$

where $\mathbf{Z}$ is a matrix of PCs, thus from a substitution of (4.3) into (4.2) the result becomes:

$$\Lambda = (\mathbf{Z})(\mathbf{Z})^{\mathrm{T}} \tag{4.4}$$

Or simply the values of the PCs are calculated as the square root of the eigenvalues in 4.5, or these can be described as being singular values:

$$\Lambda = \mathbf{Z}^2 \Rightarrow \mathbf{Z} = \sqrt{\Lambda} \tag{4.5}$$

In PCA the resulting decomposition is used for the extraction of the most significant components and the truncation of random perturbations in the investigated series. The basic idea of filtration is to use a reconstruction of some of the PCs in the matrix **A**, but only the most significant ones. The significance of the PCs is usually determined by the value of their eigenvalues. The next stage is to reconstruct the time series using only the chosen eigenvectors. i.e. the reconstruction and approximation of the time series data matrix **A'** using only the significant eigenvectors as, Loskutov (2001):

$$\mathbf{A}'_{\mathrm{mxm}} = \mathbf{V}^{\mathrm{T}}_{\mathrm{r.x.m}}.\mathbf{V}_{\mathrm{r.x.m}}.\mathbf{A}_{\mathrm{m.x.m}} \tag{4.6}$$

where $\mathbf{V}_{\mathrm{r\ x\ m}}$ is a part of the eigenvector matrix corresponding to *r*, the first eigenvector values that have been selected in relation to the number of PCs are to be selected where *r*

< m. This PC filtration technique is based on and is almost the same as the SVD method which is defined as:

$$\mathbf{A} = \mathbf{U}\ \mathbf{\Sigma}\ \mathbf{V}^T \tag{4.7}$$

It is assumed that the data matrix is in a format of m > n. If m< n then the transpose of the data set $\mathbf{A}^T$ is used

U is an orthogonally rotated PCA consisting of regular eigenvectors columns of $\mathbf{AA}^T$.
$\mathbf{V}^T$ is also a unitary orthogonally rotated PCA consisting of eigenvectors of $\mathbf{A}^T\mathbf{A}$.
$\mathbf{\Sigma}$ is an (m x n) diagonal matrix with positive or non-zero elements called singular values, or alternatively the square root of the eigenvalues of matrix $\mathbf{AA}^T$, however this is only true if the mean is equal to zero.

SVD and PCA are similar methods and give similar outputs; however the PCA values and the singular values are not the same, although they follow the same characteristics across the rank. The difference is that in the PCA technique, the new filtered data matrix **A'** can be developed with the initial data set **A** and the selected eigenvectors in expression (4.5). However, a filtration using the SVD method requires both the **U** and **V** components, with only the selected number of singular values selected to be used in the filtration process by rank *(r)* in the diagonal of $\mathbf{\Sigma}$ from:

$$\mathbf{A}'_{nxm} = \mathbf{U}_{mxm}.\mathbf{\Sigma}_{nxm}.\mathbf{V}^T_{nxn} \tag{4.8}$$

4.1.2 Examination into the rank and working dimensions of data matrix A

The effectiveness of this SVD filtering technique can be related to the dimensions of the data matrix **A**. Assume that 1024 data samples have been taken from a theoretical random and periodic noisy sinusoidal series, which are sampled at a rate of 5Hz, and built into a 32x32 square matrix **A**. The values of the singular values across the rank in both cases are illustrated as red curves in figure 4.2.

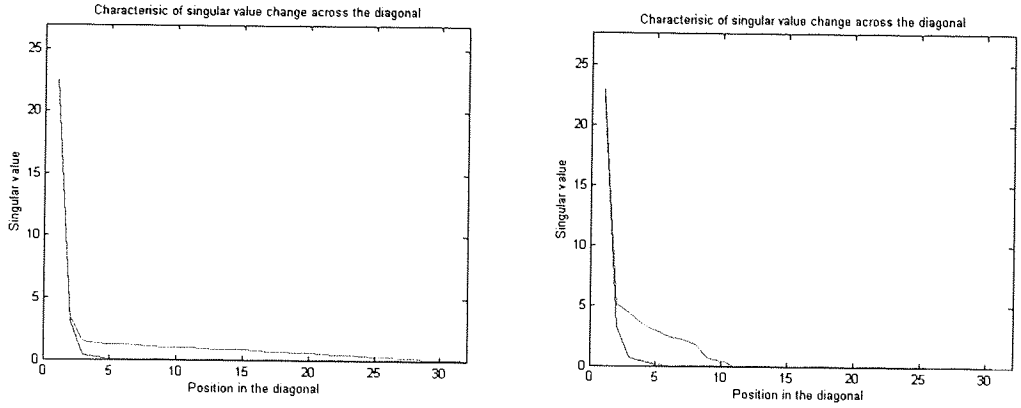

Figure 4.2 - Change in singular values for pre (red) and post. (blue) - Filtration for random noise (left) and periodic noise (right).

From figure 4.2 the red line indicates the magnitude of the singular values across the diagonal before a Butterworth filtration and the blue line is the changed singular values in the diagonal after filtration. It can be observed that the first two singular values remain with the same magnitude for pre and post filtration as these contribute most to the signal. Also, this is regardless of whether the signal has random or periodic noise associated with it.

The other singular values across the diagonal with low magnitude tend towards zero after filtration, as these are the noisy elements, thus proving the technique of the SVD filtration method. The Butterworth filtration method therefore indicates that first two values in the rank are the two components that contribute to the signal profile which filter on the basis of frequency only. It is therefore fair to suggest that setting all the values in the rank to zero after the second component on the rank, will give similar performance to that of Butterworth methods.

Therefore, assigning the rank *(r)* of singular values to be two in all cases, then the filtration results can be determined upon the elimination of all the other smaller components in the rank of Σ to zero.

It is then possible to translate the series into a matrix (**A**), in the order of 32x32, 64x16, 128x8, 256x4 and 512x2, and is shown in figure 4.3.

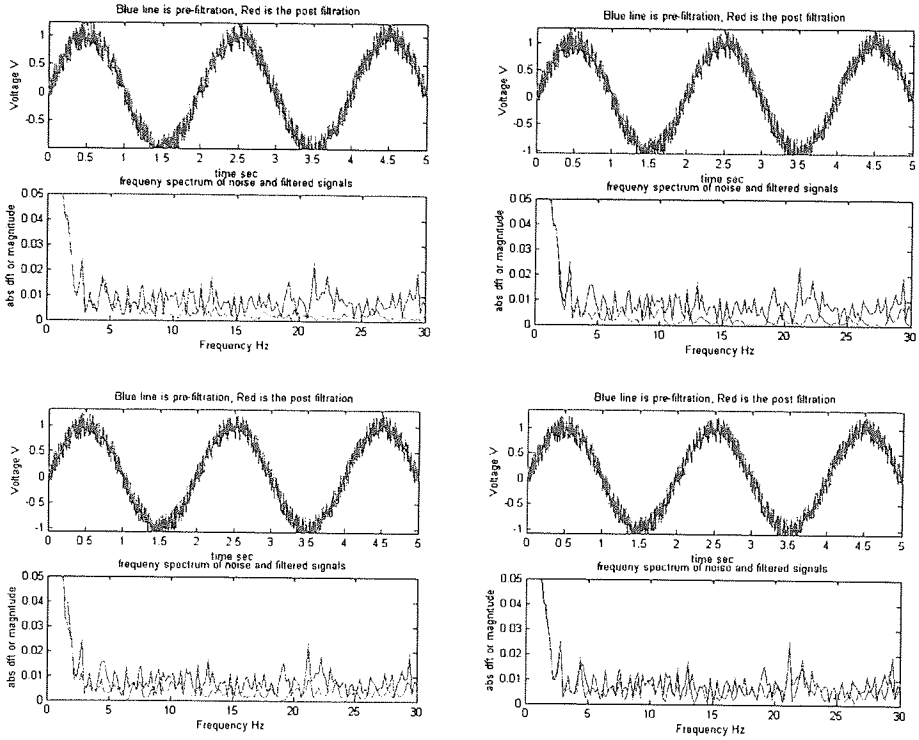

Figure 4.3 (top right) - SVD filtration in the time and frequency domain of a 32x32 data matrix, (top left) - SVD filtration of a 64x16 data matrix, (bottom left) - SVD filtration of the data matrix in a 128x8 format and, (bottom right) - SVD filtration of a data matrix with dimensions of 256x4.

Figure 4.3 are reconstructions of the filtered data matrix taking only the first two principal singular values and setting all of the other singular values to zero as described above. In the analysis of the data matrix with dimensions of (512x2), no filtration will take place if two singular values are kept to reconstruct the time series as only two singular values exist.

The success of the filtration was numerically evaluated by looking at the correlation between the clean input signal and the filtered response.

Correlation coefficients measure the degrees of association between two sets of data and have values which range between -1.0 and +1.0. A correlation coefficient of -1.0 indicates a perfectly negative or a linearly dependent relationship between two sets of data; a zero correlation coefficient indicates purely random behaviour (i.e., It means

simply that two things vary separately. That is, when the magnitudes of one thing are high; the other's magnitudes are sometimes high, and sometimes low, and can be described as being completely independent); and a +1.0 correlation coefficient indicates a perfectly positive linear relationship between the two sets of data. The correlation coefficients are based upon the cross-correlation between two normalized sequences of discrete length given as:

$$\mathbf{r}_{hx}(n) = \frac{1}{N}\sum_{i=0}^{N-1}\mathbf{h}(i)\mathbf{x}(i+n) \tag{4.9}$$

Expression (4.9) defines the cross-correlation between two normalised time series $\mathbf{h}(i)$ and $\mathbf{x}(i)$; however the incorporation of variable n, allows for flexibility in the calculation of the cross-correlation by searching for a similar time series out of phase with the template one. The maximum cross-correlation indicates the lag for the best linear correlation. If cross-correlation measures are to be computed between one sequence of data and a second sequence of data with different absolute values, then a further degree of normalisation is required. The cross-correlation coefficient is computed as:

$$\rho(n) = \frac{\frac{1}{N}\sum_{i=0}^{N-1}\mathbf{h}(i)\mathbf{x}(i+n)}{\frac{1}{N}\sqrt{\left[\sum_{i=0}^{N-1}\mathbf{h}^2(i)\sum_{i=0}^{N-1}\mathbf{x}^2\right]}} \tag{4.10}$$

The correlation coefficients from equation (4.10) are a measure of the strength of the linear relationship between two variables. The numerator expression represents the cross-correlation between the two series from equation (4.9) and the denominator term represents the normalisation of the cross correlation. Using this approach the similarity between the noisy to clean response and filtered to clean response can be determined. The evaluation is given in Table 4.1 for an SVD filtration of varying reconstruction dimensions of data matrix **A**. The noisy to clean signal correlation coefficient is initially calculated as: 0.9788, with a noise standard deviation of 0.1467.

SVD filtering: dimensions of **A**	Standard deviation Filtered-Clean	Filtered-Clean correlation	Reduction in standard deviation of noise	Improvement in correlation
32 x 32	0.0504	0.9975	0.0963	0.0187
64 x 16	0.0516	0.9974	0.0951	0.0186
128 x 8	0.0712	0.995	0.0755	0.0162
256 x 4	0.1065	0.9887	0.0402	0.0099
512 x 2	0.1467	0.9788	0	0

Table 4.1 - SVD filtration performance based upon the dimensions of the reconstruction matrix from the time series.

From the table it can be observed that a square matrix reconstruction **A** of the time series can be assumed to be optimal for filtration performance. However, if the square root of the number of elements in the time series is not an integer, then the length of the time series can be modified up to the next whole square, so that a square matrix can be reconstructed from the time series. This modification takes the form of padding or adding elements with the value of the mean of the magnitudes in the time sequence to the end of the series. The effect of padding will have no effect in the filtration process or in the evaluation of the large singular value components. This is because the padding elements have a constant mean and zero frequency. See Appendix D.1 for supplementary tests.

This method is robust as opposed to various other frequency dependent methods that filter out discrete frequencies. These types of approaches tend to keep noise in the signal that is of a similar frequency value to the input signal. Frequency dependent methods typically require a prior knowledge of the sampling rate, signal and noise frequencies to be able to function effectively. However, no such evaluation is required for the SVD method although the optimal number of singular values needs to be selected for the reconstruction of the series.

4.1.3 Defining the parameters of a low pass Butterworth frequency filter

Butterworth filters are well known and widely used for real time high and low pass filtering operations. Technically, Butterworth filters are designed in the analogue domain. However, a simplified process can be used for the digitisation of a Butterworth filter. Typically analogue frequency filter designs are carried out in the *(s)* plane in terms of a root locus plots with poles and zeros instead of in the *(z)* plane, which is the discrete dual of the Laplace transform for digital filters. The most successful approach is to take an analogue filter and translate it into an equivalent digital filter, essentially by mapping *H(s)* onto *H(z)*.

For example take an analogue 2nd order low pass Butterworth filter given in the *s* domain.

$$H(s) = K\frac{1}{(s-p_1)(s-p_2)} = \frac{r_1}{(s-p_1)} + \frac{r_2}{(s-p_2)} \tag{4.11}$$

Equation (4.11) represents the transform in the (s) domain which is also expressed as a set of partial fractions. Taking the i^{th} term, the inverse Laplace transform of equation (4.11) gives the impulse response *h(t)*:

$$h_i(t) = r_i e^{p_i t} \tag{4.12}$$

Sampling the impulse response at times $t = nT$, where $T = 2\pi\omega_s$ and ω_s is the sampling frequency from equation (4.11) and (4.12) gives:

$$h(nt) = K\left[r_1 e^{p_1 t} + r_2 e^{p_2 t}\right] \tag{4.13}$$

The z-transform of 4.13 is (4.14) below:

$H(z) = \sum_{n=0}^{\infty} h(nT)z^{-n}$ and in terms of expression (4.11): $H(z) = K\sum_{n=0}^{\infty}\left[r_1 e^{p_1 nT} + r_2 e^{p_2 nT}\right]$

Similarly a second method termed the bi-linear transform can be used to map the whole of the jω axis in the *(s)* plane onto the unit circle in the *(z)* plane. As before the whole of the left half plane (negative real plane) will be contained within the unit circle, ensuring that a stable analogue solution will give a stable digital solution.

The main difference is that this transformation cures the problem of aliasing associated with the impulse invariant method, by mapping all points in the *(s)* plane on to the *(z)* plane using the transformation:

$$s = k.\frac{z-1}{z+1} \tag{4.15}$$

Where k is given as:

$$k = \frac{2}{T_s} \tag{4.16}$$

Where in expression (4.16) the variables are defined as (T_s), which is the reciprocal of the sampling frequency and (ω_c) is the digital cut-off frequency in rad/s. However the problem with this transformation method is that of phase distortion more commonly known as frequency warping. It can be shown that the analogue and digital frequencies are related by the expression:

$$\omega_{\text{analogue}} = k\tan\left(\frac{\omega_{digital}T}{2}\right) \tag{4.17}$$

Thus the cut-off frequency characteristics in the analogue system needs to be pre warped through expression (4.17) prior to the transformation. In the case of a 2nd order lowpass analogue Butterworth filter in expression (4.18), the positions of the poles in the *–(s)* plane are given as: from Parks (1987):

$$p_i = -\sin(\theta_i) + j\cos(\theta_i) = e^{j\theta_i} \quad \text{and} \quad \theta_k = \frac{(2k+1)\pi}{2N} \tag{4.18}$$

Where N is the number of poles and k = 0, 1, 2 ... N-1. However the expression suggests that magnitude of the poles p_i, changes with regard to a change in the order of the filter, from the number of poles applied. Changing N as a function of the filter order will change the evaluation of θ_k, and hence p_i. Expression (4.18) can become:

$$H(s) = \frac{1}{\left(s + e^{j\pi/4}\right)\left(s + e^{-j\pi/4}\right)} = \frac{1}{s^2 + \sqrt{2}s + 1} \tag{4.19}$$

Expression (4.19) defines a low pass filter with a 3dB cut-off at 1 radian/s. Applying the warping digital frequency in (4.17) then resolving expressions (4.15), (4.16), (4.18) into (4.19) gives the expression for *H(s)*.

$$H(z) = K\left[\frac{r_1}{1 - e^{p_1 T} z^{-1}} + \frac{r_2}{1 - e^{p_2 T} z^{-1}}\right] \Rightarrow K\left[\frac{r_1 + r_2 - (r_1 e^{p_1 T} + r_2 e^{p_2 T}) z^{-1}}{1 - (e^{p_1 T} + e^{p_2 T}) z^{-1} + e^{(p_1 + p_2)T} z^{-2}}\right] \tag{4.20}$$

For a working example in the calculation of the filter coefficients see Appendix D.2.

This method of transformation generates a digital filter with impulse response identical to that of the analogue filter at the discrete instants $t = nT$; however, the sampling frequency affects the response of the discrete filter and will be subjected to aliasing as the digital filter is a sampled data system unlike the analogue filter.

Assuming that through the manipulation above the gain, numerator and denominator coefficients can be determined, the formulation is generally given in the form of:

$$H(z) = \frac{a_0 + a_1 z^{-1} + a_2 z^{-2} + \ldots a_n z^{-n}}{1 + b_1 z^{-1} + b_2 z^{-2} + \ldots b_n z^{-n}} \tag{4.21}$$

Effectively any order of filter can be used; however the order is selected upon the output characteristics required. A 4th order low pass filter has been selected due to the trade-off, between the start up duration, and the roll-off for noise attenuation.

High order filters, give better filtration performances for the removal of noise, however they can give poor start up problems in the filtered series. E.g. if a low sampling frequency is used (10-500Hz), then the settling time required for the series is greatly increased. As the series is of a finite length, and the start of the series is of some importance from the influencing stimulus, then relatively high order filters should not be used due to the start up condition.

Filters of low order such as one or two give fast responsive start up conditions; however retain features in the series that are of little importance in the series, such as low levels of external noise, or small levels of movement. An example illustrated in figure 4.4, shows an 85kg candidate standing on the 4mm steel platform, with one non-linear sensing element near the left heel recording the deformation of the surface. The data is captured at a sample rate of 20Hz, whilst the candidate lifts and drops the left heel on the surface.

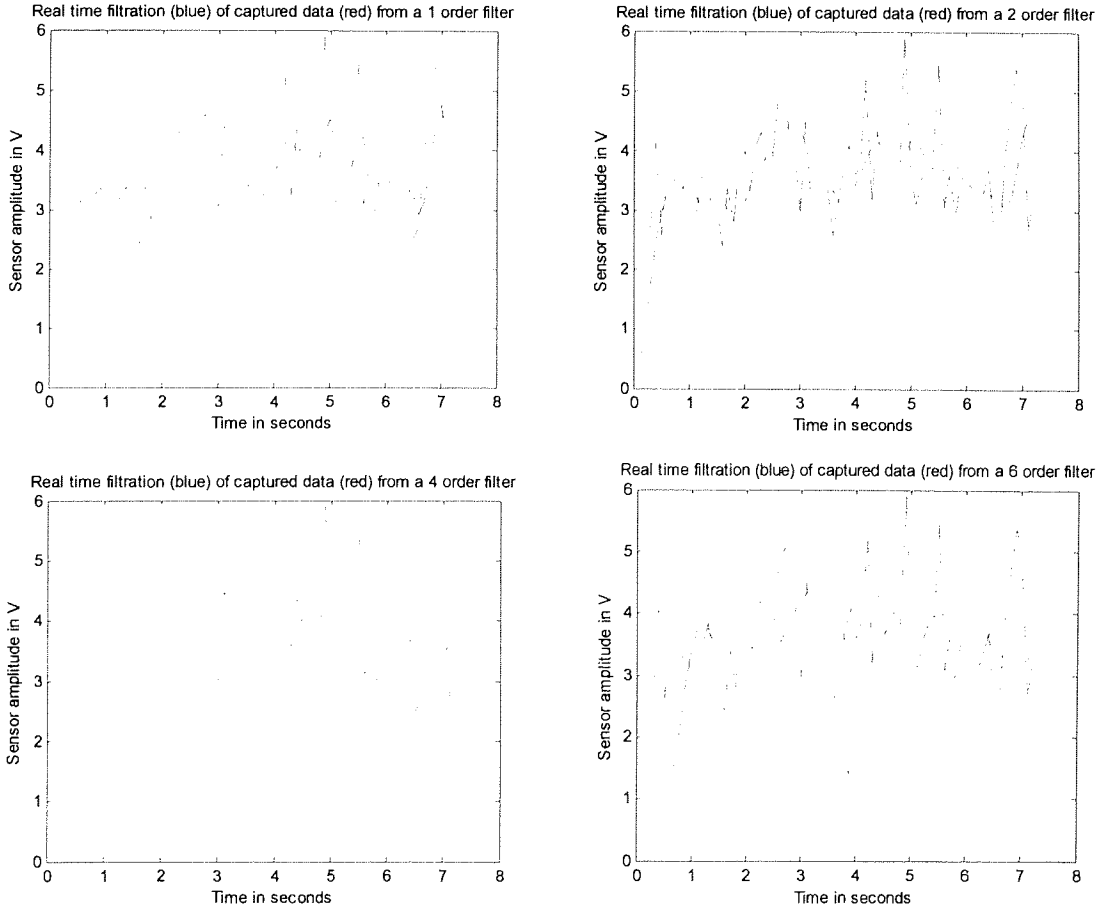

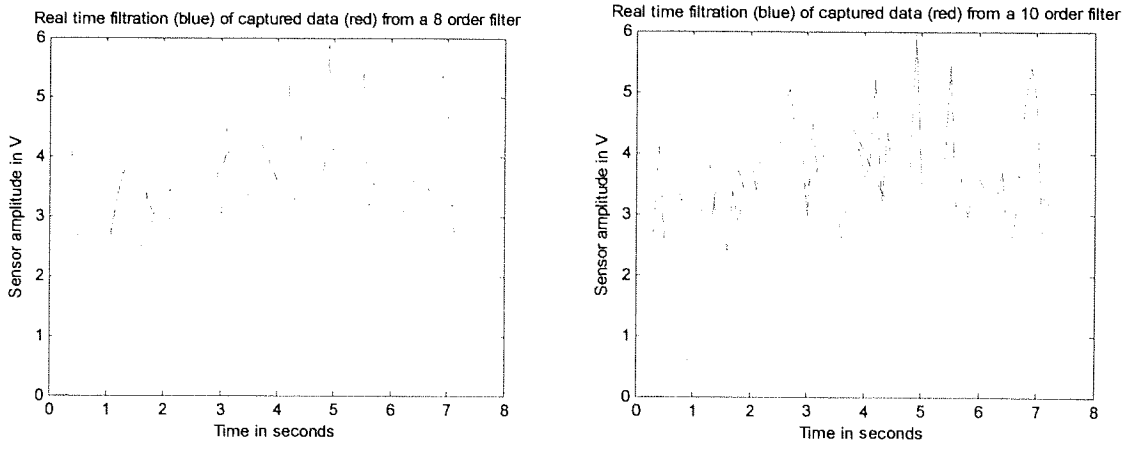

Figure 4.4 - Low-pass Butterworth filters performance against the order of the filter, during a candidate lifting and replacing their heel on the surface.

Figure 4.4 illustrates the effect of a changing order low-pass Butterworth filter. The lower orders show fast response rates but low forms of filtration smoothing of the noise in the system. High order filters show poor start up speeds, but good forms of generalisation and smoothing.

Any filter of about fourth order would be acceptable for the application and is compromises between the problems at the extremes. An evaluation of the coefficients of high order low-pass Butterworth filter are given in Appendix D.3.

4.1.4 Defining the feed forward filtered response through the z-transform and difference methods

Once the evaluations of the desired coefficients a and b have been formulated, then a feed forward method can be used to calculate the true output response at discrete values of $\mathbf{Y}(n)$. This is known as a direct form II transposed structure or alternatively as the difference method and can be derived from the canonical bi-quadratic section, shown diagrammatically, from (Oppenheim 1989).

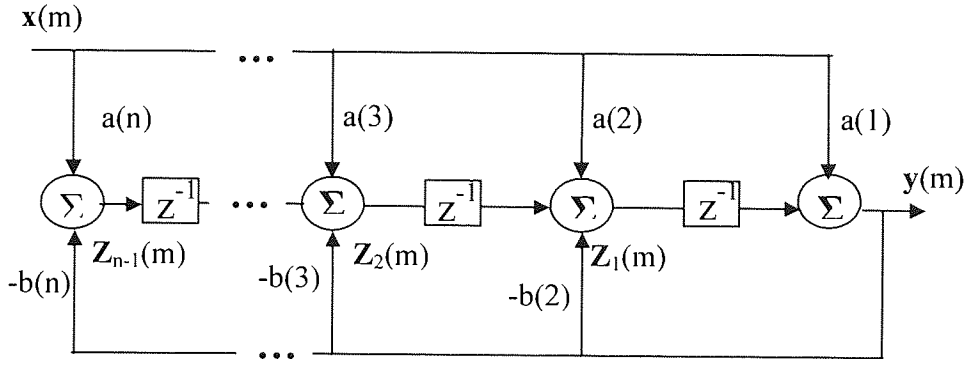

Figure 4.5 - A canonical bi-quadratic section for a common template $(n-1)^{th}$ order filter.

Figure 4.5 also represents the difference equations for sample (m) in the time domain as:

$$\begin{aligned} y(m) = {} & [x(m).\, a(1)] + [x(m-1).\, a(2)] + [x(m-2).\, a(3)] + \ldots [x(m-n-1).\, a(n)] \\ & - [y(m-1).\, b(2)] - [y(m-2).\, b(3)] - \ldots [y(m-n-1).\, b(n)] \end{aligned} \tag{4.22}$$

Going through the summation nodes in figure 4.5, from right to left for a sample at time m, the difference equations can be represented as, assuming that (n-1) is the filter order:

$$\begin{aligned} y(m) = {} & [x(m).a(1)] + [Z_1(m-1)] \\ Z_1(m) = {} & [x(m).a(2)] + [y(m).-b(2)] + [Z_2(m-1)] \\ & \vdots \\ Z_{n-2}(m) = {} & [x(m).a(n-1)] + [y(m).-b(n-1)] + [Z_{n-1}(m-1)] \\ Z_{n-1}(m) = {} & [x(m).a(n)] + [y(m).-b(n)] \end{aligned} \tag{4.23}$$

Applying z-transforms to (4.23) and solving for $Y(z)$, we get:

$$Y(z) = \left[\frac{a(1) + a(2)z^{-1} + \ldots + b(nb+1)z^{-nb}}{1 + b(2)z^{-2} + \ldots + a(na+1)z^{-na}} \right] X(z) \tag{4.24}$$

Equation (4.24) shows the standard transfer function of the filter defined in (4.21).

This proves that the difference method in the time domain is a valid solution. Using these algorithms it is possible to determine a filter with a desired frequency response. Using

these feed-forward methods it is possible to filter noisy data for the purpose of continuous static data. This method will therefore provide a real time smoothing of the digital input data before it is fed through the processing algorithm (section 3.5)

4.1.5 Analysis on the performance of the Butterworth algorithms for real data

Using the methods derived in (Sections 4.1.3 - 4.1.4) it is possible to develop a fourth order, real time, low pass Butterworth filter. Applying random and periodic noise to a clean signal, the clean signal is of high amplitude and can be viewed in the frequency spectrum between the value of 0 and 5Hz. The frequency cut-off has therefore been selected to attenuate at a value of 5Hz, such that all components greater than 5Hz are eliminated. Taking the sampling rate of 200Hz, the coefficients of a and b can be calculated and thus the feed forward algorithm gives the response of:

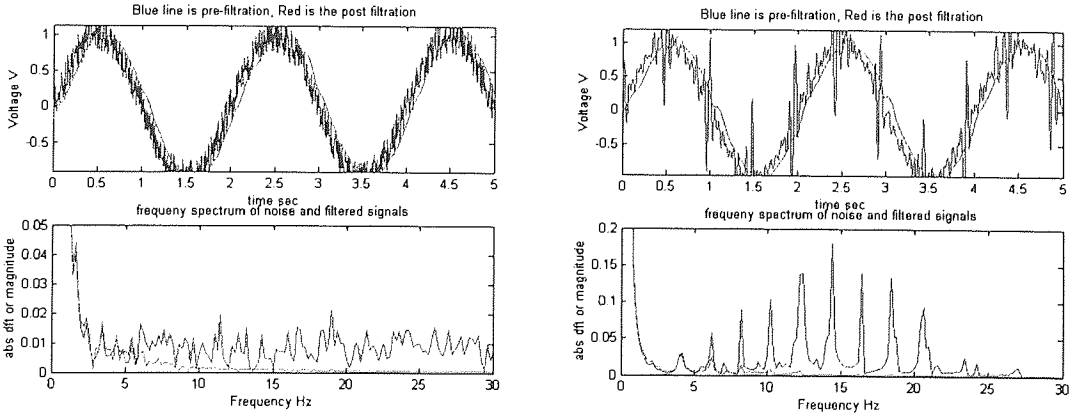

Figure 4.6 - (left) Response of the low pass Butterworth (red) for the filtration of random noise (blue) with a cut-off frequency of 5Hz in the time and frequency domain. (right) - A similar response for the elimination of periodic noise.

Figure 4.6 represents the time and frequency response (red curve) for the elimination of random and periodic noise, for frequencies above 5Hz. However, the response demonstrates a phase shift from the input, which is common in all digital filters.
The results of this analysis for the elimination of random noise are:

Correlation pre filtration: 0.9796
STD pre filtration is: 0.1435

Correlation post filtration: 0.9987
STD post filtration is: 0.0353

Correlation improvement: 1.912%
STD noise reduction: 75.4%

Similarly the results for periodic noise are:

Correlation pre filtration: 0.8849
STD pre filtration is: 0.3085

Correlation post filtration: 0.9981
STD post filtration is: 0.0431

Correlation improvement: 11.34%
STD noise reduction: 86.03%

Again this indicates that the performance of the filter is enhanced when exposed to periodic noise, as opposed to random noise. These results are also comparable with those of the SVD technique.

Finally real examples and comparisons of SVD and Butterworth methods are illustrated in Appendix D.4. It was found from analysis that the smaller components could be related to the noise and that the larger components could be related to the clean signal.

4.1.6 FFT-IFFT filtration method

The FFT-IFFT technique is a highly effective filtration technique, but it is not a real time method and its performance is dependant upon a pre-captured time series similar to the SVD method. This method is a frequency filtration approach, where the signal is converted back into the time domain, as in the Butterworth method, however the response is non-time shifted. The method is also similar to that of the band pass filter, with respect to the evaluation of the cut-off frequencies prior to filtration, which too is shifted in time.

Initially, the time series data is converted into the frequency domain through an FFT method. The frequencies that are to be rejected are set to zero and then the changed frequency spectrum is converted back into the time domain using an IFFT (Inverse Fast Fourier Transform) method. This method eliminates the roll-off problem associated with the band pass filters, so that the cut off frequency points and boundaries are purely quantised. Figure 4.7 demonstrates a plot of the frequency response of the noisy random noise across the full frequency spectrum, with its respective filtration response.

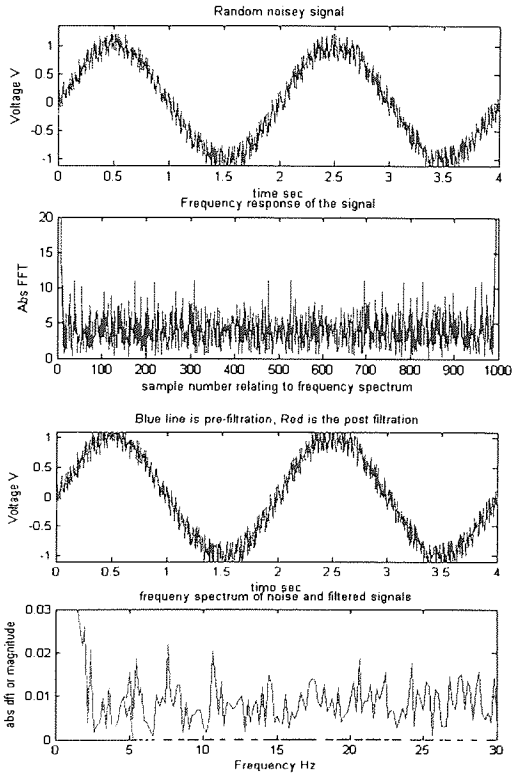

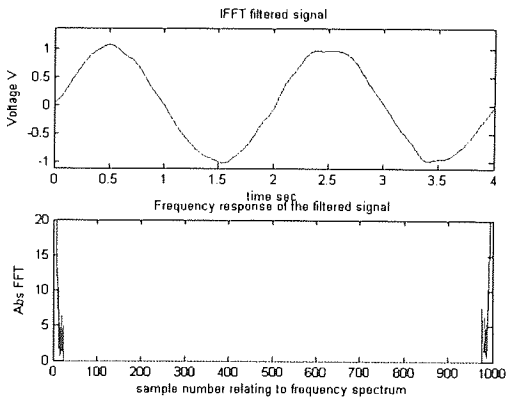

Figure 4.7 – (top left) Noisy input signal and frequency response.

(top right) - Mirrored frequencies that have been removed from the FFT and also demonstrates the filtered signal in the time domain from an IFFT of the filtered FFT.

(bottom left) - Difference between time and frequency plots from a cut-off at 5Hz for pre and post filtration.

The results of which show that in the elimination of random noise using an FFT-IFFT filter using the correlation coefficient method and standard deviation of this analysis is:

Correlation pre filtration: 0.9801

STD pre filtration is: 0.1419

Correlation post filtration: 0.9985

STD post filtration is: 0.0388

Correlation improvement: 1.84%

STD noise reduction: 72.66%

Similarly, the results for periodic noise are:

Correlation pre filtration: 0.9126
STD pre filtration is: 0.3120

Correlation post filtration: 0.9987
STD post filtration is: 0.0356

Correlation improvement: 8.62%
STD noise reduction: 88.56%

The FFT-IFFT method shows that again the performance is better for the elimination of random noise and also that the results are comparable with those of the Butterworth method. This is due to the fact that these two methods are both frequency cut-off methods, eliminating all noise above the 5Hz frequency.

4.2 The use of time series methods to characterise the collected filtered transients

Once the sensory responses have been filtered, it is possible to use gradient search techniques to capture a meaningful transient from the time series. We need to derive coefficients to characterise the profile of the relevant transient. One can use all of the discrete magnitudes in the time series as a describing feature. However, this will be at the expense of a large variable number of inputs applied to the classifying algorithm.

It is important that the number of inputs should be minimised so as to reduce the number of training patterns required for the algorithm to perform effectively. Typically, the number of training samples required for an effective neural approach is by rule of thumb: the number of inputs, multiplied by the number of hidden nodes, multiplied by 5 or 10 depending upon the training algorithm used. This is known as Widrow's rule, after Bernard Widrow. The multiplier depends on whether regularisation is used to control the network complexity. Thus, reducing the number of inputs will not only reduce the number of training samples required, but also reduce the computational time required to optimise and train the algorithm.

But a trade-off must occur, as it is important to attempt to maximise the number of characterising coefficients, as this tends to lead to greater network performances. In order to provide a short fixed length number of inputs that can describe the profile of a variable length transient, then various time series techniques can be applied to provide this function. This section will therefore discuss time series methods and techniques for an optimal representation to generate enhanced regression performances.

Time series introduce extra complications beyond the normal problems of other domains of intelligent data analysis. The obvious effect is that time introduces correlations between adjacent samples. Time introduces causality and hence an asymmetry and because of these effects normal methods developed for other domains do not apply directly without some modification.

Time series methods have been developed as an analysis tool for diverse domains. Financial markets wish to use yesterday's data to predict the data tomorrow. Medical analysis hopes to use existing recorded data to give medical responses in other circumstances that can be used as a diagnostic tool. These methods can also be used with meteorological recorded data as to predict the changing in weather patterns. All of these applications of time series analysis will in one way or another define one of two types of time series category, namely (a) deterministic and (b) stochastic models.

A deterministic system is generally a dynamic system that possesses initial and fixed states, with an established vector, state, or phase space, such that all future states can be determined. These systems are generally fully defined through a set of first-order ordinary differential equations or matrices which can be formulated from the laws of physics or accounting. The mathematical theory or ordinary differential equations ensures the existence and uniqueness of the trajectories if certain conditions are met (Kantz and Schreiber 1997). It is possible to determine whether the time series in question is deterministic or stochastic, from the evaluation of the error between the predicted evaluation $\hat{\mathbf{X}}_{t+k|t}$ and the actual measured value $\mathbf{X}_{t+k}$ of the modelled time series from:

$$\left|\hat{\mathbf{X}}_{t+k|t} - \mathbf{X}_{t+k}\right|^2 = \left|\mathbf{e}_{t+k}\right|^2 \tag{4.25}$$

If the squared error or squared error in prediction gives a value of zero then the system is predictable; however if this value is non zero then this defines a non-deterministic series.

If the parameters or states of the time series model are variable at various times in the series, then these are defined as non-deterministic or stochastic models (Kantz and Schreiber 1997). An approach used to handle these changing variables is the Markov processes with finite memory. A Markov model of order m defines the current state variables, represented by the values of the process during the last m time steps.

Alternatively, Wold (1938) proved that any time series can be expressed as a weighted linear combination of a deterministic and a non deterministic component. Assuming that a stationary time series $\mathbf{X}_t$ in time is non-deterministic, and that the mean of the series is equal to zero, this can be represented by:

$$\mathbf{X}_t = \mathbf{D}_t + \mathbf{e}_t + \sum_{j=1}^{\infty} \mathbf{g}_j \mathbf{e}_{t-j} \tag{4.26}$$

where $\mathbf{e}_t$ is a zero mean white Gaussian noise and $\mathbf{D}_t$ is the deterministic series. The stochastic part of the representation which is non predictable is given as a weighted sum of the noise terms, which is also useful in the prediction process, (Janacek 2001)

The prediction of the non-deterministic series $\hat{\mathbf{X}}_{t+k|t}$ can therefore be given as:

$$\hat{\mathbf{X}}_{t+k|t} = a_1 \mathbf{X}_t + a_2 \mathbf{X}_{t-1} + \ldots + a_m \mathbf{X}_{t-m} \tag{4.27}$$

However the stochastic model in expression (4.27) is assumed to be a linear predictor, which may have an infinite number of terms. The optimal number of terms used to define the model is dependant upon the minimum squared error of the prediction given by the expectation of expression (4.25). This is assumed that the model is a linear predictor and that the entire past from time t is available.

4.2.1 Characterisation of the time series

The mean and variance can easily be taken from a time series as indicators of the series; but do not give any information about the evolution of the series. Capturing the evolution of the series is an important feature in order to represent and regenerate the series from the characterising coefficients, which coefficients such as the mean and variance could not provide. Such evolutionary information can be obtained from the autocorrelations (AC) of the signal. Other such methods include: Auto Regressive (AR), Moving Average (MA), Discrete and Fast Fourier transforms (DFT and FFT), Feature Extractions (FE), Polynomial Fitting (PF), and SVD from the time series.

It is important to be aware that the captured data in this case is transient, and certain stationary time series methods will not be good indicators for the characterisation of transient data. Although, stationary methods can be used to characterise a transient if it split into various smaller sections. But this will be at the cost of added complexity and input dimensionality.

4.2.1.1 Characterisation using Auto Correlation

The autocorrelation is the correlation between the original series and a copy of the series displaced by k time points or k lags. The formulation of this autocorrelation expression is derived from that in (4.28) for a correlation between two time series and is given as:

$$\mathbf{r}_{xx}(n) = \frac{1}{N}\sum_{i=0}^{N-1}\mathbf{x}(i)\mathbf{x}(i+n) \tag{4.28}$$

The above expression will therefore give correlations relative to other points in the series and will hence give a normalised summation relative to the profile of the transient. It is therefore possible to apply the autocorrelation to develop characterising attributes of the time series for a predetermined lag k.

4.2.1.2 Characterisation using Auto Regressive models

If the time series is a stationary, non deterministic series as in equation (4.26), then for an autoregressive model the prediction at time t depends on previous values as suggested by expression (4.27) for an order of p with an associated zero mean Gaussian noise. Expression (4.29) can be written in the form of backshift operator B, assuming only a stochastic model as:

$$a(B)\mathbf{X}_t = \mathbf{e}_t \tag{4.29}$$

The polynomial $a(B)$, of order p is called the AR or autoregressive polynomial and is therefore defined from (4.26) & (4.27) as.

$$a(B) = 1 - a_1 B - a_2 B^2 - a_3 B^3 - \ldots - a_p B^p \tag{4.30}$$

In which the roots of the companion polynomial defined by the coefficients determine if the AR model is stationary. If the roots of the polynomial $a(\mathbf{X}_{t-1})$ lie within the unit circle then the series is stationary. This is understood from the fact that if $|a|$ is greater than 1 then equation (4.26) will give an infinite variance, suggesting that the series is non stationary or transient.

The estimation of the coefficients can be derived in a variety of ways, one of which is the Yule-Walker method. The method takes equation (4.30) and multiplies the terms by $\mathbf{X}_{t-k}$ such that the equation becomes:

$$E[\mathbf{X}_t \mathbf{X}_{t-k}] = E[a_1 \mathbf{X}_{t-1}\mathbf{X}_{t-k} + a_2 \mathbf{X}_{t-2}\mathbf{X}_{t-k} + \ldots + a_p \mathbf{X}_{t-p}\mathbf{X}_{t-k} + \mathbf{e}_t \mathbf{X}_{t-k}] \tag{4.31}$$

Taking expectation of equation (4.31) gives:

$$\gamma(k) = a_1\gamma(k-1) + a_2\gamma(k-2) + a_3\gamma(k-3) + \ldots + a_p\gamma(k-p) \tag{4.32}$$

This can be written in terms of the autocorrelations with lag k.

$$\rho(k) = a_1\rho(k-1) + a_2\rho(k-2) + a_3\rho(k-3) + \ldots + a_p\rho(k-p) \tag{4.33}$$

Equation (4.33) can therefore be written in matrix form for the autocorrelations using sequential lags from 1 to p as:

$$\begin{bmatrix} \rho(1) \\ \rho(2) \\ \vdots \\ \rho(p) \end{bmatrix} = \begin{bmatrix} 1 & \rho(1) & \rho(2) & \ldots & \rho(p-1) \\ \rho(1) & 1 & \rho(1) & \ldots & \rho(p-2) \\ \vdots & & & & \vdots \\ \rho(p-1) & \rho(p-2) & \rho(p-3) & & 1 \end{bmatrix} \cdot \begin{bmatrix} a_1 \\ a_2 \\ \vdots \\ a_p \end{bmatrix} \tag{4.34}$$

Equation (4.34) can now be solved for the values of the coefficients of $a_1 \ldots a_p$, through a square matrix inverse of the symmetric autocorrelations multiplied by the autocorrelations at sequential lags of k.

This evaluation of the AR model using the Yule Walker method defines the model coefficients through the summation of the autocorrelations of the series at various incremental lags. Alternatively the problem can also be solved using least squares, similar to the SLP approach in Section 3.6.4 for the full length time series as equation set:

$$\begin{aligned} \mathbf{X}_t &= a_1\mathbf{X}_{t-1} + a_2\mathbf{X}_{t-2} + a_3\mathbf{X}_{t-3} + \ldots + a_p\mathbf{X}_{t-p} \\ \mathbf{X}_{t-1} &= a_1\mathbf{X}_{t-2} + a_2\mathbf{X}_{t-3} + a_3\mathbf{X}_{t-4} + \ldots + a_p\mathbf{X}_{t-1-p} \\ &\vdots \\ \mathbf{X}_{t-k} &= a_1\mathbf{X}_{t-k-1} + a_2\mathbf{X}_{t-k-2} + a_3\mathbf{X}_{t-k-3} + \ldots + a_p\mathbf{X}_{t-k-p} \end{aligned} \tag{4.35}$$

The coefficients of equation (4.35) will therefore give the coefficients of the AR model of length p. The predicted value of the time series can therefore be related to the weighted sum of the coefficients and elements in the finite memory of the system; hence the derived coefficients will be responsive to the profile of the transient in question. It is important to determine the number of coefficients required to characterise the time series

effectively. This can be achieved through an analysis of the squared error between the actual and model prediction. The numbers of coefficients are increased until the analytical error is at a minimum thus describing the series most effectively. This can be described for an AR(q) model of varying coefficients for the collected time series shown in figure 4.8, using the least squares approach to determine the unknown coefficients a_p.

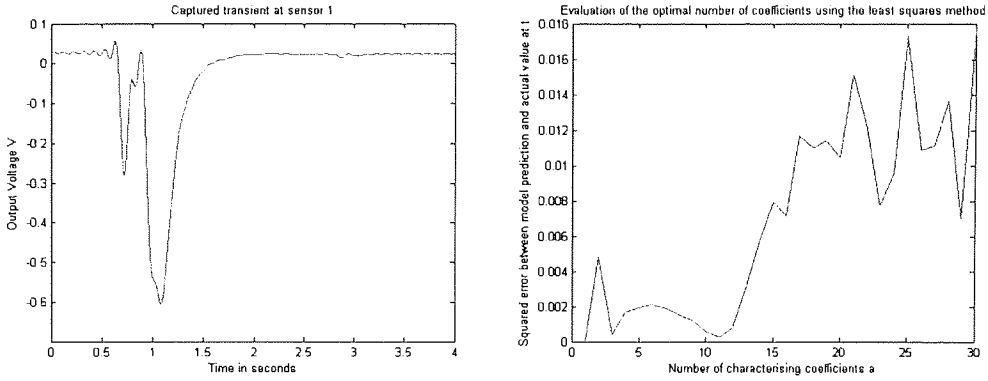

Figure 4.8 - Effect of changing the number
of charactering coefficients in the AR model (right) for the series on the left.

Figure 4.8 clearly shows the effect on the prediction error when the model is subjected to a high number of coefficients or over-fitting. From this it can be suggested that numbers of coefficients between 3 and 12 would be an adequate descriptor of the time series to be used as an input for a further describing regressive algorithm.

Furthermore the roots of the polynomial expression $a(B)$ in (4.30) for a 4th order AR model for the time series in figure 4.8 gives magnitude roots at 1.35, 1.07, 1.00, 1.00. This indicates that all of the magnitudes of the roots lie outside the unit circle and that the time series in question is transient. This also suggests that such regressive methods would only be suitable in the characterisation process if the transients are slit into smaller time windows.

4.2.1.3 Characterisation using MA and ARMA models

The moving average MA model can also be written as a sum of innovations for a time series and is given in the form:

$$\mathbf{X}_t = \mathbf{e}_t + b_1\mathbf{e}_{t-1} + b_2\mathbf{e}_{t-2} + ... + b_q\mathbf{e}_{t-q} \tag{4.36}$$

Where e_t is zero mean white noise called a moving average MA process of order q. It is also possible to incorporate a mean coefficient of the time series; however the time series is typically normalised so that the mean is reduced to zero. The series can again be expressed through the backshift operator from: $\mathbf{X}_t = b(B)\mathbf{e}_t$ to give the polynomial expression of order q as:

$$\mathbf{X}_t = \mathbf{e}_t + b_1\mathbf{e}_{t-1} + b_2\mathbf{e}_{t-2} + ... + b_q\mathbf{e}_{t-q} = \left(1 + b_1B + b_2B^2 + ... + b_qB^q\right)\mathbf{e}_t \tag{4.37}$$

Again the model coefficients can be solved using a least squares or Yule-Walker method. Once the coefficients have been determined then if the roots of the polynomial $b(B)$ lie outside the unit circle then the MA(q) process can be forecast, or this can be alternatively known as the invertibility condition.

By combining both the AR and MA models it is possible to generate a more general ARMA model in terms of the memory p and q can be expressed as:

$$\mathbf{X}_t = a_1\mathbf{X}_{t-1} + a_2\mathbf{X}_{t-2} + ... + a_p\mathbf{X}_{t-p} + \mathbf{e}_t + b_1\mathbf{e}_{t-1} + b_2\mathbf{e}_{t-2} + ... + b_q\mathbf{e}_{t-q} \tag{4.38}$$

Given the ARMA model it is possible to construct the autocorrelations and find the first few equations in the Yule-Walker set and hence determine the coefficients provided when the lags are small. If the lags are defined as large then the process is can be considered as a straight forward AR process.

4.2.1.4 Characterisation using DFT-FFT properties of the time series

Jean Baptiste Joseph Fourier (1768-1830) showed that periodic signals can be represented as weighted sums of harmonically-related sinusoids. Also non-repetitive or aperiodic signals can be considered as integrals of sinusoids which are not harmonically related. These two principles form the basis of the Fourier series and Fourier transform respectively. For discrete signals the Fourier transform can be expressed as a summation of exponential terms as opposed to integrals for continuous signals with sine and cosinusoids and is given in the discrete form of:

$$\mathbf{J}(w_j) = \frac{1}{\sqrt{N}} \sum_{t=0}^{N-1} \mathbf{X}_t e^{-iw_j t} \quad \text{for } w_j = 2/\pi j/Nj = 0,1,\ 2,\ \ldots,\ N-1 \tag{4.39}$$

In general the above DFT equation converts from a discrete time series into a comprehensive frequency spectrum. The inverse or reconstruction of the frequency spectrum into the time domain can also be defined as:

$$\mathbf{X}_t = \frac{1}{\sqrt{N}} \sum_{t=0}^{N-1} \mathbf{J}(w_j) e^{iwt} \tag{4.40}$$

Equations (4.39) and (4.40) are typically used as a method of smoothing and are explained in (Section 4.1.6), Janacek (2001). The DFT also has interesting properties that are directly related to a time series and can be used as characterising frequency attributes of the series. The DFT expression in (4.39) requires a computation of the frequency from a summation series of length N, where each term requires a calculation, which is computationally intensive. However Cooley and Tukey (1965) developed an enhanced method of the DFT so that time savings could be made in its calculation and is known as the FFT (Fast Fourier Transform). The method initially computes the spectrum and then obtains the autocorrelations from the basis that they are Fourier coefficients.

From the derivation of the FFT frequency series it is possible to locate the most prominent fundamental frequency and amplitude of the signal, as characterising attributes of the time series; however as with the mean and variance they take no account of local temporal structure, so that information about the series is lost.

4.2.1.5 Characterisation using derived polynomial coefficients of the time series

Alternatively it is possible to produce a polynomial that describes the time series. This will directly characterise the time series in both time and magnitude through a curve fitting process, similar to the methods applied for a regressive MLP. The polynomial of the series of order s is given by a non-linear expression as:

$$\mathbf{Y}_t = a_1 + a_2\mathbf{X}_t + a_3\mathbf{X}_t^2 + a_4\mathbf{X}_t^3 + \ldots a_s\mathbf{X}_t^s \tag{4.41}$$

The above expression can be described as a weighted non-linear sum of the time in the series with the addition of a starting constant when t = 0. This method can be related to that of an AR, MA model in some way, but does not encompass correlation through a memory in the series. For all observations in the series it is possible to develop an equation set and hence a representative matrix as:

$$\begin{bmatrix} \mathbf{Y}_1 \\ \mathbf{Y}_2 \\ : \\ \mathbf{Y}_N \end{bmatrix} = \begin{bmatrix} 1 & \mathbf{X}_1 & \mathbf{X}_1^2 & \mathbf{X}_1^3 & \ldots & \mathbf{X}_1^s \\ 1 & \mathbf{X}_2 & \mathbf{X}_2^2 & \mathbf{X}_2^3 & & \mathbf{X}_2^s \\ : & & & & & : \\ 1 & \mathbf{X}_N & \mathbf{X}_N^2 & \mathbf{X}_N^3 & \ldots & \mathbf{X}_N^s \end{bmatrix} \cdot \begin{bmatrix} a_1 \\ a_2 \\ a_3 \\ a_4 \\ : \\ a_{s+1} \end{bmatrix} \tag{4.42}$$

From this it is possible to derive the polynomial coefficients through a pseudo-inverse, or least squares approach. Again it is possible to define the optimal number of coefficients that characterise the series, through a minimisation of the error defined by:

$$\sum_{i=1}^{N}\left|\hat{\mathbf{Y}}_i-\mathbf{Y}_i\right|^2=\sum_{i=1}^{N}\mathbf{e}_i=e \tag{4.43}$$

In this case the optimal number of coefficients that characterise the series is demonstrated in figure 4.9 for a captured transient.

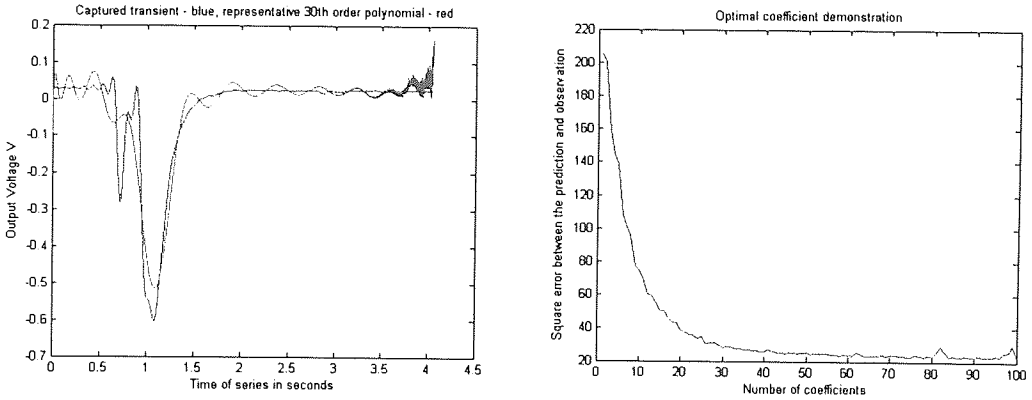

Figure 4.9 - (left) a representation of the polynomial fitting method for an evaluation of a 30^{th} order polynomial. (right) - The squared error between the predicted and captured series

The figure on the right shows the captured signal in blue. The red curve is a 30^{th} order polynomial representation of the blue signal, although it appears to be quite noisy. This is due to the fact that the polynomial is over defining, by being of such a high order.

However, this high order representation maps the blue signal more closely than any other smaller polynomial orders. This is demonstrated in the figure on the right hand side, which illustrates the error between the representation and the signal of varying polynomial orders. It shows that higher orders or numbers of coefficients are more representative of the signal in question.

Alternatively, a close mapping with a reduced total number of representing coefficients can be derived from a splitting of the time series into smaller sections, for example down into four equal window sizes. Using a polynomial representation of a lower order to define the transient in each of the windows will give a total lower number of characterising coefficients, from the complete transient. Such a derivation will give high

accuracies, similar to that of higher orders and also give a lower number of representing coefficients.

Although, the number of coefficients representing the series converges at around 30, it suggests that it is important to facilitate a high number of coefficients in the model; however this will come at the expense of high computation time and an increased number of inputs into the interpretation algorithm.

4.2.1.6 Characterisation using feature extraction from the time series

These methods are the most simplistic mathematical representations of a time series and the prominent features can be extracted directly from the time domain. They can be derived by simply looking at the time series, such as the magnitude of the greatest peak or trough and the time delay between peaks in the series. Other such features include the integral area under the transient, the gradients at certain points of the series, or the mean and standard deviation of the series. Such methods are computationally economic; however such methods do not give any information relating to the frequency or regression of the series.

For example, one feature is the integral of the transient divided by the triangulation integral between start and end points. This evaluation makes it possible to generate a value that is independent of the period of the summed transient, thus only the characteristic or shape of the transient is described as a proportional integral; albeit no information is held about the evolution of the transient in the extracted parameter. The formulation of this feature extraction is demonstrated in figure 4.10.

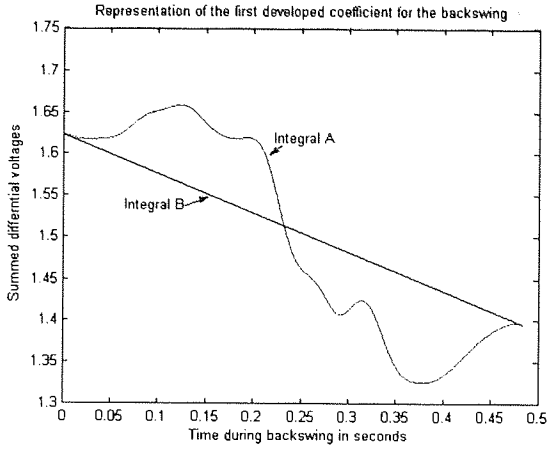

Figure 4.10 - Representation of the development of the feature extraction.

The above figure shows how the feature is derived from the series. Integral A is the magnitude area under the series over time. Integral B is the area under the line between the starting and end points. A division of the two integrals will give an evaluation of the gradient, and magnitude change throughout the evolution of the series. However, the derivation of the parameter it is highly dependant upon the starting and end points. If such points are prone to noise, then this may alter the magnitude of the parameter somewhat.

Other such features include: SVD (as in Section 4.1.1) that extracts the principal singular values that are characteristic of the series; the Instrumental Variable Autoregressive model (IVAR) that estimates the parameters of an AR process through a least squares approach from the form $A(q)\ \mathbf{y}(t) = \mathbf{v}(t)$, where $\mathbf{y}(t)$ expresses the time series, $A(q)$ is a polynomial representation of the auto-regressive series and $\mathbf{v}(t)$ is an arbitrary process assumed to be a moving average process of a selected order, Stoica (1985); and a partial-correlation representation which computes autoregressive models of successive orders of 1, 2,...s, by ordinary least squares and then evaluates the coefficients through retaining the last coefficient of each regression.

4.2.2 Regressive response to interpret the height of the subject on the surface

This section illustrates a simple example of the characterisation process, using extracted FFT's from a captured transient set it is possible to determine the height of a subject above a surface through an examination of the dynamic forces generating the transient set. This can be illustrated theoretically and examined practically, through the use of the frequency responses of the surface. For example; assume that the dynamic activity is to be a repetitive swinging motion of a golf club, from left to right, at a constant frequency, between two fixed points on the surface.

The amplitude of the fundamental frequencies will therefore, be dependent upon the subject's height above the surface. This is because the weight shift between the feet will change in relation to the subject's height. For example; as the height of the subject increases, the angle of swing between the two fixed points on the surface reduces, thus reducing in proportion of weight shift between the two feet. The magnitude of the amplitude must then be normalised by dividing by the subject's weight, so that the magnitude of the oscillations are independent of it, so that they purely represent the subject's height.

An example of this is shown in the captured oscillations of the surface, when swinging between two fixed points at a constant frequency of 0.75Hz, through the aid of a metronome. The surface used in this case was the wooden surface described in section (3.2.2), of dimensions 1000x419x18mm, with 8 linear sensing elements (OPB 704) equally pitched in a 4x2 matrix under the surface. Initially, the subject stands statically on the surface so that the RFSES can calculate the magnitude of the subject's weight for normalisation, using an MLP method discussed earlier in section (3.5.6).

The subject's heights were recorded and then were asked to swing the golf club for a fixed period of time, between the two fixed points on the surface, at the set frequency of the metronome. For example, the captured responses of the surface are represented in figure 4.6, for subjects with heights of 1.3m and 1.7m respectively.

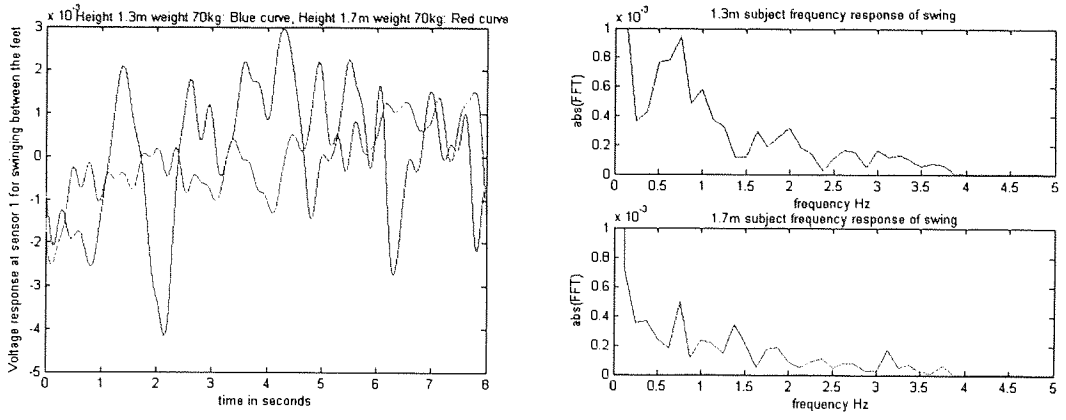

Figure 4.11a (left) - Captured transients of one of the sensing elements in proximity to the surface for subjects of 1.3m (blue curve) and 1.7m (red curve) respectively. (right) - Frequencies and amplitudes in the frequency spectrum for the two heights generated by an FFT of the captured transients in the left figure.

The above figure shows the relationship between the heights of the subjects and the recorded amplitudes. From this it is possible to determine the fundamental frequencies of the captured transients with the respective amplitudes through an FFT translation of the captured transient. As the amplitudes of the fundamental frequencies are representative of the subject's height then these are extracted from the FFT spectrum, using gradient search methods.

Extracting the amplitude of the fundamental frequency for all of the sensing elements in proximity to the surface, in this case eight, they are then divided by the calculated weight of the subject such that each profile is represented by a single vector of length 8. These evaluations are then to be used as the describing inputs to a secondary regressive regularised MLP, as to relate the describing amplitude input vector to the recorded subject's height.

For testing purposes a total of 38 subjects of different heights and weights were used to conduct the analysis. A regressive MLP algorithm was trained with a random 19 input and output patterns, with a further random 13 validating patterns. The optimisation gave a total of 12 hidden nodes, a weight decay coefficient of $1x10^{-9}$, with an early stopping of

50 iterations. The trained algorithm was then tested with a further 6 patterns unknown to the algorithm and the results show that the height of the subject could be calculated to within an average of 1.33cm of the subjects height, or alternatively at a prediction error of 8.89%, with a standard deviation of 2.14cm in figure 4.11b, although there are too few patterns to make this learning problem well-posed. (Full analysis see Appendix D.5)

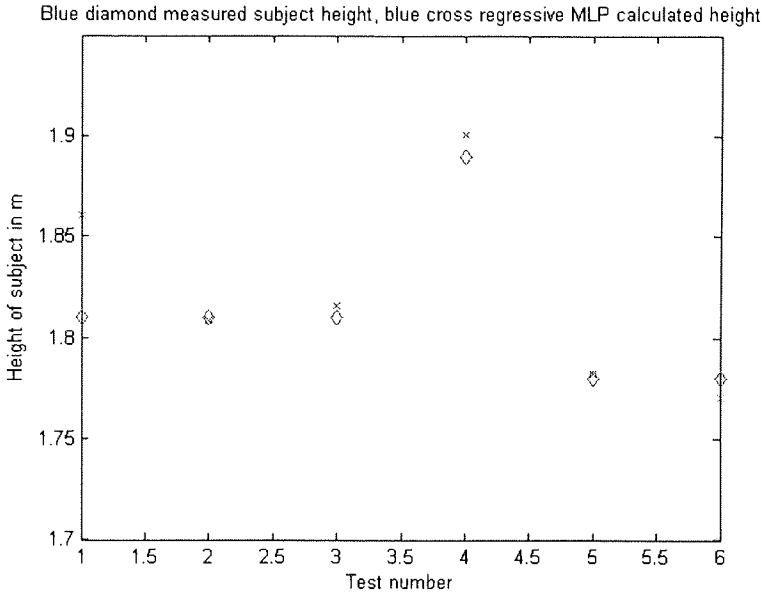

Figure 4.11b - Accuracy of the MLP for the unknown input patterns to determine the candidates height in m.

Although only small numbers of training patterns could be acquired, due to the number of possible candidates available, then this non-linear model may perform with enhanced results if more test subjects could be found. This would therefore give a better generalisation of the true mathematical relationship, between the swing amplitude and the subject's height. However, the method still shows good results even with small numbers of training patterns, and gives confidence of similar results, with larger volumes of training data. The determination of the height of a subject is a good parameter to know for the feedback of a text book golf swing. This is because the stance width should be shoulder width apart, which is in fact a function of the subject's height.

A good question that must be asked is 'How do different shaped people of different weights at similar height affect the results?' First of all, the subject's weight to their

height follows a normal distribution curve. This is such that most people are situated at or around the 50th percentile. Data at this point would be the ideal training data to use, as it generalises the majority of the population, which was used in the experiment above.

However, on the basis of using the non-linear algorithm with training data taken from the 50th percentile of subject's, then someone who is at the 95th percentile, i.e. someone who is overweight for their height would appear to be taller. This can be rectified through the addition of an extra input to the input pattern, such as the weight of the subject. This will enable the algorithm to distinguish between a variance across the distribution, through the use of the frequency amplitude and the weight as a separate entity.

The results illustrated above gives confidence that an extraction of coefficients from a characterisable surface response can be used to describe something useful about the subject, which is not in direct contact with the force surface. For example, in the classification of an incorrect movement this is not directly measurable from the surface.

4.3 Analysis of sensitivity of movement and surface response

It is important to be able to determine what types of movements or intricacies can give a characterisable surface response for sensory change and discrimination. This is so that it is possible to predict which movements can be classified successfully. For example, will the surface in question be sensitive enough to respond to a hand, or head movement etc? This can be computed theoretically for various movements, so that it is possible to predict which movements are possible to classify, as well as gain a general idea on the success rate of the possible classification.

Computers use digital techniques so it is important that the captured analogue signals are translated into digital ones. This conversion causes quantisation in both time and magnitude and form inaccuracies through the truncation and rounding process, to give a time and magnitude resolution.

The truncating operation is determined by the bit conversion of the ADC micro chip or circuit (Chapter 3.4). In this case the resolution of the device is 10bits and the sensory output range is 5V, thus the resolution of the device in this case is equivalent to: $5 / (2^{10}) = 4.9$ mV. Thus all voltage readings will be recorded in steps of this value, regardless of the actual analogue voltage. It is this resolution in the conversion from analogue to digital that gives rise to how sensitive the system is to the loading on the surface.

The first test is to investigate how far the Centre of Pressure (COP) can be moved before any of the sensory output values through the digital device read a step change of 4.9 mV. On this step change it can be assumed that the particular sensing element that has changed is sensitive to this movement of the COP, assuming that the COP for a body is at the centre of the surface and that the COP can be related to a specific dynamic movement.

For a theoretical evaluation it is assumed that all sensing elements under the surface are of equal distance from the surface at rest (5.5mm) and that all sensing elements possess the same characteristics. Initially, the deformations are calculated at each sensor point using the Navier model (3.22) and (3.23), under the influence of the COP at the centre for the designated mass of the body. Once the deformations have been calculated then these can be translated into analogue sensory voltage outputs from the representative sensory polynomial calibration (See figure 3.27 and expression 3.37).

Initially, the COP at the centre point is moved in steps, with a magnitude of 1mm from an angle of 0^0 until the digital value of any of the elements changes, either plus or minus the value of the resolution. At this point the threshold of movement away from the centre point is recorded. The process is reiterated for an angle change of 2 degrees up to an angle of 360^0.

Figure 4.12 represents the sensitivity of the sensing elements under the surface for various COP values ranging from 10 to 100kg. The circular configuration in the diagram represents the movement that the COP can make inside the circle without any of the sensor values changing digitally from the device.

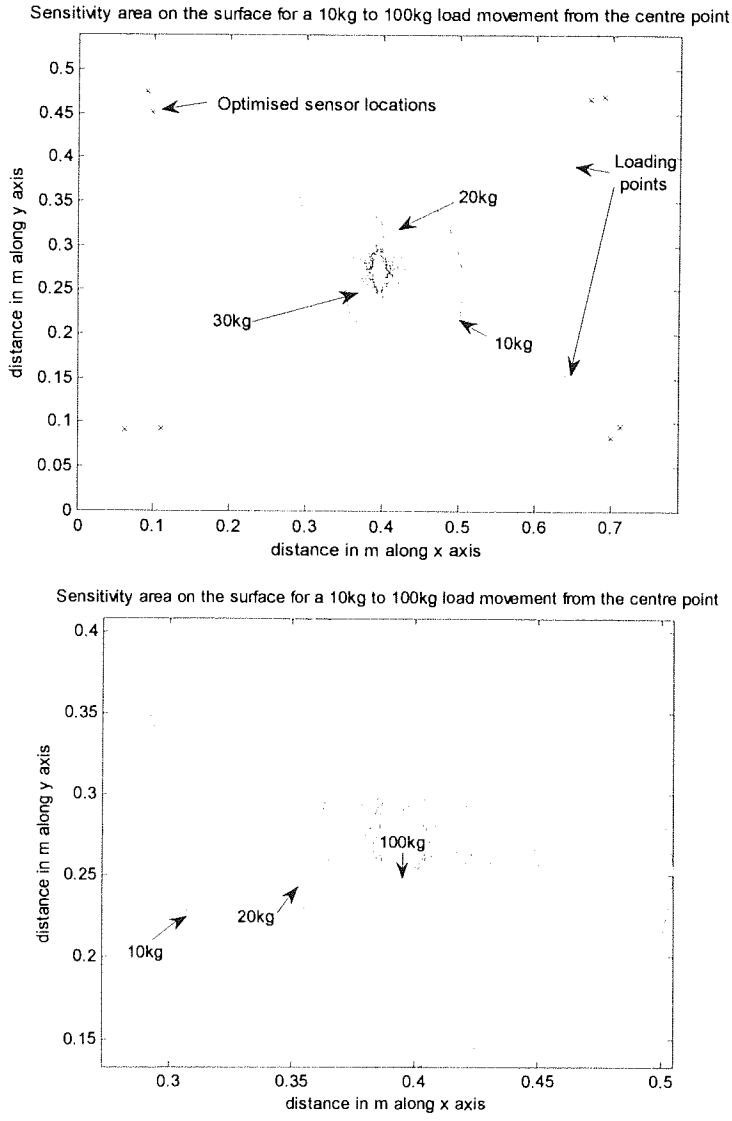

Figure 4.12 – (Top) Sensitivity of the surface and elements for a movement of a COP from the centre of the surface. The outer ring represents the sensitivity for a 10kg load on the surface and moving inwards is an incremental increase of load in steps to 10kg. The diamonds (◇) represent the positioning of the elements under the surface through the GA and (O) represents the loading points of the feet, see Section (3.3.9.3) and figure (3.23). The bottom figure is a closer view of the circle of sensitivity around the possible non sensitive movements of the load.

The deformation of the surface is said to be linear to the load, however the above diagram shows a non-linear increase in sensitivity to the applied load. This can be assumed to be the non-linear sensory response of the elements. The lower the magnitude of the load, then the less sensitive the element, due to the initial starting position on the curve that has a lower gradient value. A larger deformation is therefore required to change the sensory element output response by the resolution. However, the positioning, and range of the sensing elements has been designed to have a maximum sensitivity for loading conditions of the 50^{th} percentile, i.e. a loading of 74kg.

The diagram also shows symmetry and balanced sensitivity in the system, based upon the optimised sensing positions. However, this is only if the load magnitude is 20kg or greater, which can again be assumed to be due to the non-linear or low gradient curvature of the sensing elements at low deformations. This again shows encouraging results based upon the optimal sensing locations found by the GA.

4.4 Development of a representative model to determine the movement of the COP for various golf swing movements

To determine which movements the system should be sensitive to, a mathematical model representing the body in motion may be developed to infer parameters such as the movement of the COP and various other loading conditions. This is developed such that the movement of discrete activities are exact and repeatable for the development of the desired parameters.

Two classical ways of modelling a golf swing are: the double pendulum model by Lampsa (1975), Milburn (1982) and Cochran and Stobbs (1968), who modelled the body as a rigid frame, with a pendulum that was represented by a pivot at the shoulder joint and a hinge at the wrist. Consequently the path of the club for this model will be along the line of the stroke, with the club face being at right angles to the line of stroke. From this planar model it would be difficult to represent an inside to inside or inside to square

stroke used during a full golf swing, unless an additional variable perpendicular force is applied during the line of stroke.

This can also more commonly described as a three-link model described by Suzuki and Inooka (1998), Turner and Hillis (1999) and Rees Jones (2002) for the kinematics of the shoulders, arms and wrists during the golf swing. The model defines the geometry and kinematics of the players swing including joint reaction couples experienced when the joint limits are approached. The 3D model represented was set up for a computer based simulation of the dynamics of the golf swing, so that all of the possible spatial motions could exist. This enabled the user to vary the parameter sensitivity, such that the club head velocity, path and spatial orientation could be observed.

Secondly, a more appropriate rotation model can be used to represent the swing, (Brooks, 2002). The author suggests that the moving parts tend to turn around the spine, to give a rotation around the fixed axis. In the model the forces act on the moving body as to produce pure rotation about the fixed axis and that the axis may be horizontal or inclined, such that the moving body can follow circular paths about the body in 3D.

One step further than this is to develop a multiple link system that fully represents all of the possible degrees of freedom of the body, resulting in an even more representative model. The disadvantage of this would be that the development of such a system mathematically would be time consuming, complex and prone to human error due to the high number of Degrees of Freedom (DOF). However, it is possible to develop such a system using a computer package (SolidWorks^{TM}) similar to the one developed by Rees Jones using (MathCAD^{TM}). The advantage of such an approach allows for a more comprehensive model of the human body, with joint limitations and multiple DOF. Also it allows for a change in parameters, to what ever motion is required and it can calculate information regarding the state of the system, for example the movement of COM and COP on the surface during the swing.

The model parameters are based upon the 50th percentile of male adults (Pheasant 1998) for lumped mass body segments and are assembled to represent the stature of the human body. Figure 4.8 demonstrates the described assemblies for a three link model of the arm and of the leg, with connectivity to the torso.

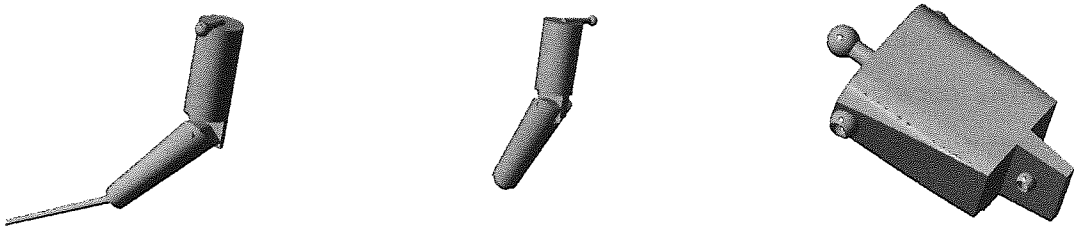

Figure 4.13 - Component linkages for the development of a realistic human mass model. (left) - A three link representation of the arm with a rotation ball joint at the shoulder, including joint movement limitation. (centre) - Linkage model of the leg with similar features to that of the arm including ball socket connectors. (right) - A rigid torso connector to bring all elements into communication.

The complete assembled model is demonstrated in figure 4.14 and demonstrates its function for the analysis of the golf swing.

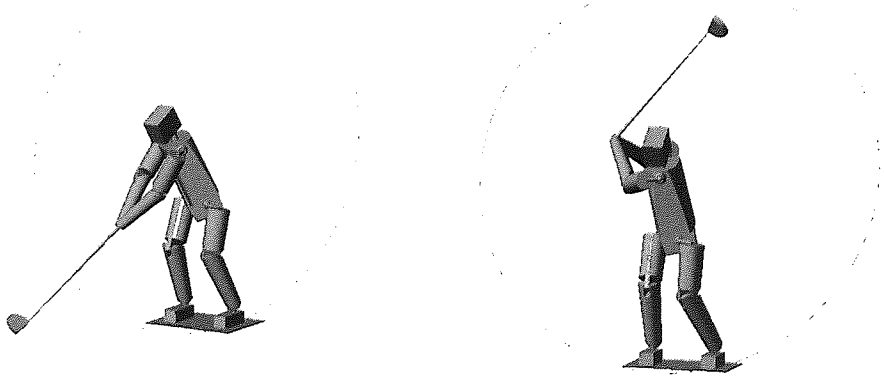

Figure 4.14 - The function of the proposed model used to represent the motion of the body during a golf swing.

4.5 Theoretical derivation of system sensitivity for various movements

The proposed system must be able to determine the efficacy of the golf swing. In order to describe this, it is possible to use the described model in Section 4.4 to define correct and incorrect dynamics on the surface using all of the possible DOF. Firstly, the model can describe what possible movements the system should be sensitive to, taken from the system resolution and secondly, the differentials of movement between swings. This should therefore indicate if various swings give large enough differences for the algorithm to interpret and classify.

In order to define which movements need to be classified, it is important to be aware of the most common flaws during the golf swing, in order for the system to interpret and give feedback upon the correctness of the movement. There are many possible common errors that can occur during the entire golf swing; however for the purpose of the analysis, only various flaws associated with the backswing will be investigated to test the proposed approach.

4.5.1 Problems associated with excessive head movement

Leadbetter (1993) suggests that excessive head movement is generally the effect of poor body rotation and movement of the spine. This head movement might be classified as being a combination of movement: 1) from side to side, 2) up and down, 3) toward and away from the ball-to-target line. Small movements of (1) and (2) are acceptable; but a large movement of class (3) results in a rocking of the weight distribution between the toes and the heels, giving rise to poor balance, resulting in shots being played from the toe or the heel of the club.

4.5.2 Problems associated with a flat laid-off backswing

Leadbetter also suggests that a problem can arise from which the angle the club takes during the backswing. An angle of backswing less than 60^0 from the ground is generally termed a 'flat laid-off backswing'. An ideal swing suggests that the club must be in balance so that it can work in harmony with the turning of the body. This can be generated by positioning the left elbow down towards the ground, so that it assists the upward movement of the club and counteracts any excess rotation of the left arm. Typically for a good backswing the club takes a backswing angle of around 75^0 relative to the ground as opposed to around 45^0 for a poor flat laid-off backswing.

A flat laid-off backswing generally gives poor balance from the fact that the swing plane can change dramatically between the mid-back to top swing. Figure 4.15 demonstrates these differences and illustrates the integration of such motion into the model for a correct and an incorrect orbit angle during the back swing.

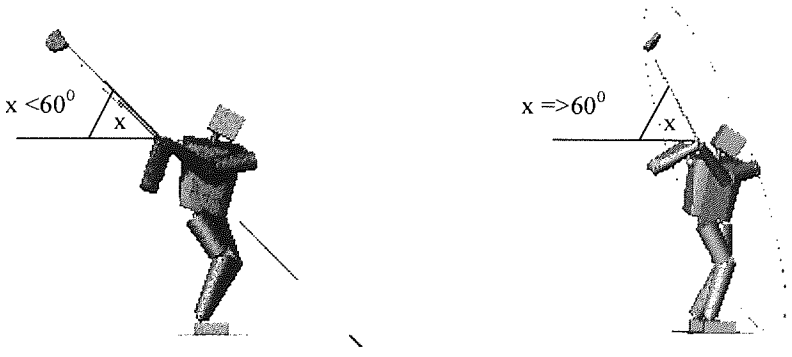

Figure 4.15 (left) - A flat laid backswing with an orbit angle of around 45^0 that is integrated within the model to demonstrate the dynamic movement of the body. (right) - A correct swing and orbit angle during the backswing that is also integrated into the model.

4.5.3 Problems associated with straight legs during the backswing

The greatest golf players have been less than average height (Leadbetter 1993). Longer limbs introduce a great deal of wasted motion, which inevitably leads to an inconsistent strike and poor shot pattern. In contrast, a short player with a much lower centre of gravity will benefit from a maximisation of swing leverage, a greater level of stability and hence more control during the stroke.

Better stability can be achieved through a widening of the stance and a flexing of the knees, thus resulting in a lower centre of gravity and better control during the stroke. This can also be simulated within the model and is illustrated in figure 4.16.

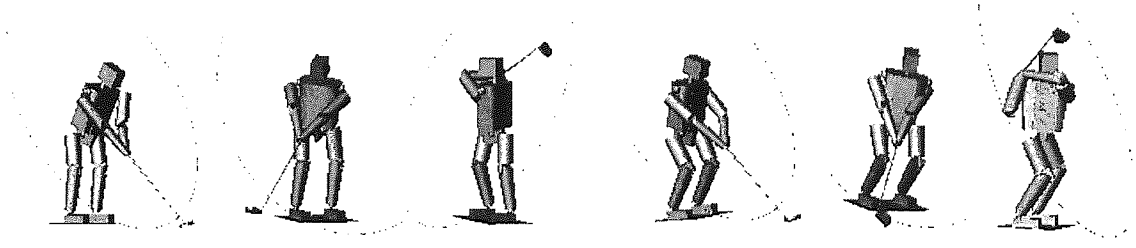

Figure 4.16 (left three figures) - Images for a swing adopting straight legs.
(right three figures) – Images for a correct backswing with flexed legs.

4.5.4 Problems associated through taking the leading heel of the surface during the backswing

Right handed golfers should keep the left foot planted during the backswing and create resistance to the coiling motion of the upper body. The purpose of the backswing is to create leverage and to achieve this it is important to create stability of the lower body during the swinging process. Ultimately, when swinging from top swing to follow through, the majority of the weight needs to be distributed through the left ankle, such that the left foot should remain fully planted on the surface.

Lifting the left heel off the ground during the backswing gives a change in height of the torso. Thus, to provide balance during the backswing, a straightening of the leading leg must result, which in turn forces the club to strike the ground just before hitting the ball.

From this it can be taken that the body or lower frame is a stabiliser for balance and control. Hence the left foot should remain planted during the backswing, although the foot can roll during the coiling of the body. This possible flaw can also be simulated within the model and is shown in figure 4.17.

Figure 4.17 - Problem of taking the left heel off the surface for a right handed golfer.

4.5.5 Derivation of the theoretical movement of the COP on the surface using the model to describe the system sensitivity for small movements

It is now possible to theoretically identify which of these movements 1) the system should be sensitive enough to, and 2) can be uniquely determined. Initially, an investigation of the theoretical movement of the COP on the surface should indicate which movements are sensitive to the system. In order to achieve this, the theoretical movement of the COP from the developed model can be compared with that of the circle of sensitivity described in (Section 4.3), for the weight of the model of 86kg. It can also be assumed that the COP at the initial balanced stance position can be translated to the centre point on the surface.

An examination of the movement of the COP on the surface from the model in conjunction with the derived circle of sensitivity should indicate the sensitivities of the surface for various movements. This illustration is shown in figure 4.18.

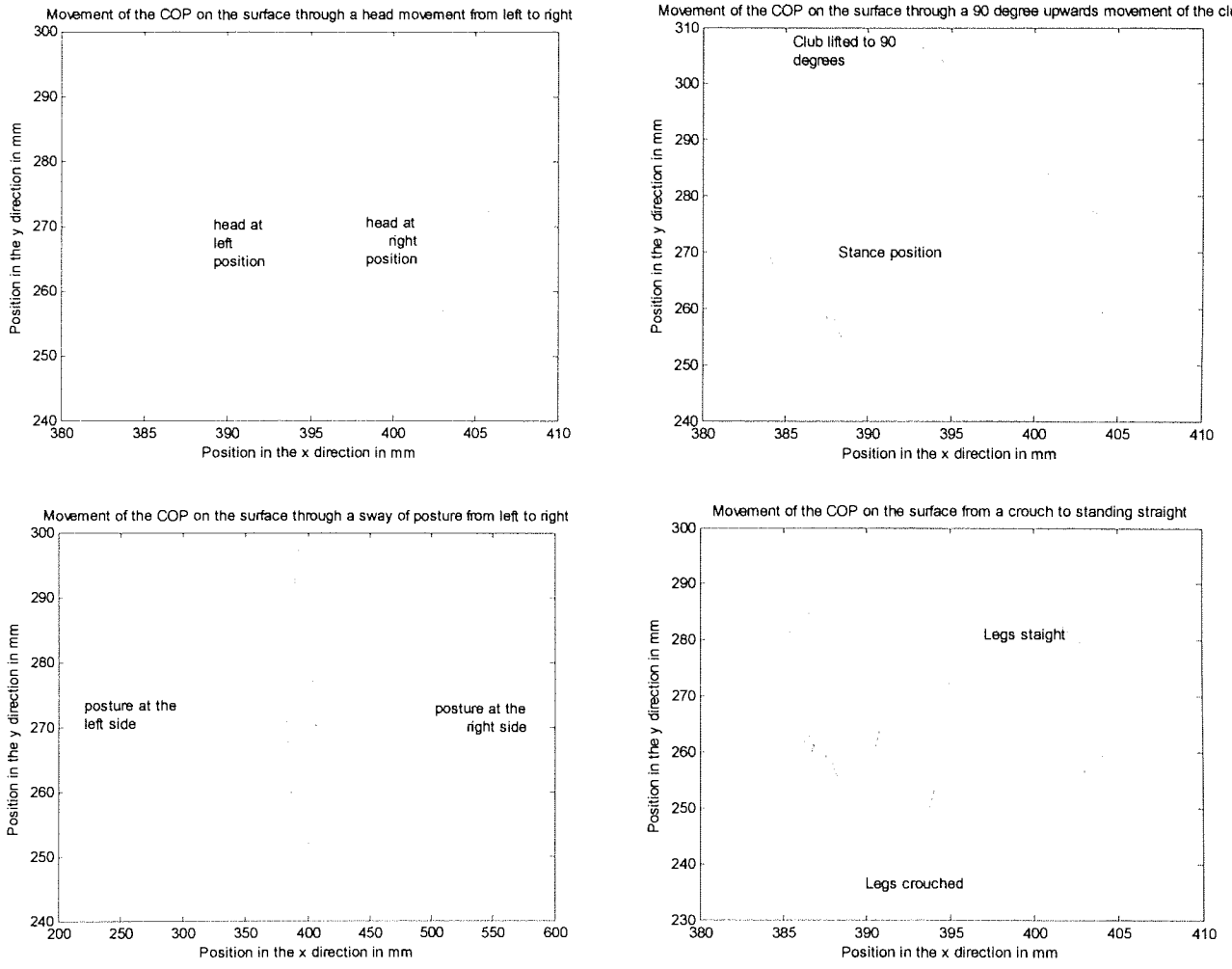

Figure 4.18 (top left) - Movement of the COP from a swing of the head from left to right on the surface in red. (top right) - The sensitivity of the surface for a lifting of the club off the surface to 90 degrees in front of the subject. (bottom left) - The sensitivity of the surface for a sway or weight shift from left to right. (bottom right) - The surface sensitivity from a crouched to standing position with the golf club where the resolution of the sensors is illustrated by the blue box in the diagrams.

This indicates that head movement lies within the resolution of the surface and hence will give no sensory response. The figures illustrates that the surface is sensitive to all other movements with the maximum being for a complete weight shift from left to right foot. This gives confidence that the surface will be sensitive to an incorrect club orbit, whether the foot comes off the surface and whether the knees are bent or straight.

It is important to be aware that the system will be more sensitive to the activities that are largely removed from the internal insensitive area. In this case it will be a sway, or foot movement off the surface. This is due to large changes of load condition on the surface throughout the activity, which induces large changes in voltage. The above diagrams also illustrate that, although a club angular movement, and crouched posture, will give a change in sensor reading, it will be less significant than of the sway or foot movement.

This scenario examined, illustrates the poorest sensitivities of the surface, which is ideal for carrying out a limitation analysis. This is due to the fact that the insensitive area was calculated from one point load moving from the centre of the plate, assumed to be for the movement of the COP as a generalisation of the activity. However; this will not be the case in the working solution, as we have four possible point loads, with the optimal positioning of these elements propagating towards the loading points. Close sensing proximity to the working load will therefore increase the sensitivity of the system.

Assuming a point load in the centre of the plate, then it is somewhat equal and distant from the most sensitive areas (optimised at the four loading points) and will be positioned at one of the most insensitive areas of the surface. The results illustrated above can be expected to be improved, if we examine the changes of the loading for various movements at the specific four loading points. This will also be in conjunction with four circles of insensitivity at the loading points, thus generating greater sensitivities of the system at the point loads as opposed to only one removed away from the four most sensitive points on the surface.

4.5.6 Derivation of the theoretical movement of the COP on the surface using the model to describe the differences between various backswings

As a result of the analysis in Section 4.5.5 the surface should be sensitive to all backswings to different degrees and can be assumed to be due to the large movements of the COP during the swing. It is this analysis that will define if there is enough variation in the movement of the COP in order to classify the swing.

The variations of the backswing have been defined being as one of eight possible combinations, as shown in Table 4.2:

Swing No.	Legs/knees flexed	Left heel planted	Correct orbit angle
1	Yes (1)	Yes (1)	Yes (1)
2	Yes (1)	Yes (1)	No (0)
3	Yes (1)	No (0)	No (0)
4	No (0)	No (0)	No (0)
5	No (0)	Yes (1)	Yes (1)
6	No (0)	No (0)	Yes (1)
7	No (0)	Yes (1)	No (0)
8	Yes (1)	No (0)	Yes (1)

Table 4.2 - Eight of the possible backswings investigating three possible flaws

Examine the movement of the COP from the central stance position at (0,0)mm for swings (1), (2), (5) and (8). These represent a perfect swing with no flaws (1), a perfect swing with an incorrect orbit angle (2), a perfect swing with the knees straight (5) and a perfect swing with the left foot being taken off the surface, during the backswing. These differences in classes or flaws have been modelled using the SolidWorks™ model to illustrate the movement of the COP for each class and are demonstrated in figure 4.19:

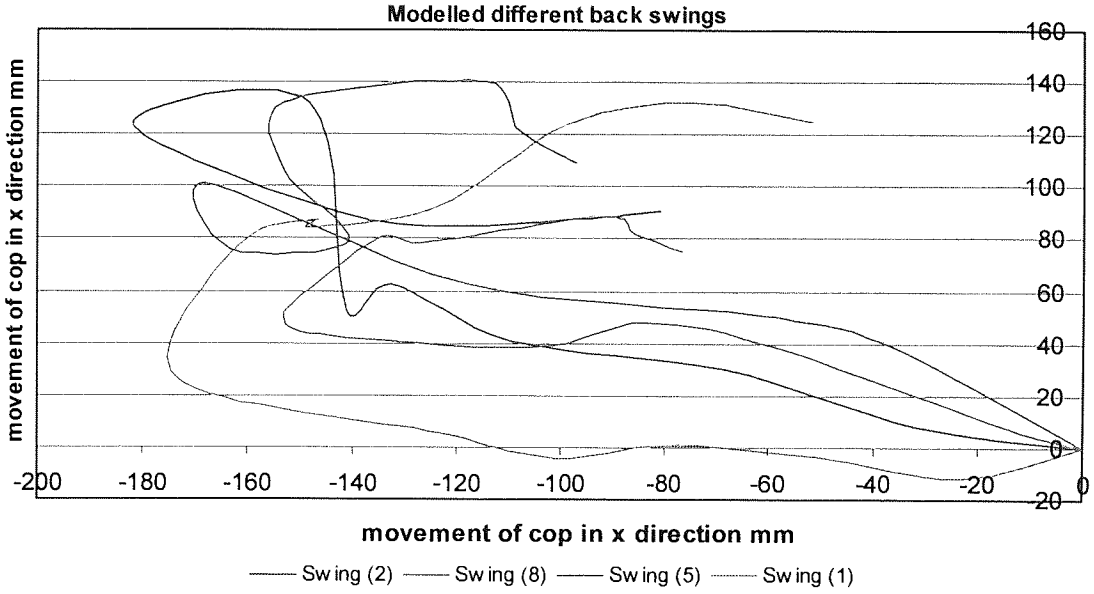

Figure 4.19 - Theoretical movement of the COP for various backswings using the SolidWorks™ modelling techniques.

The above figure illustrates that there are differences between the movements of the COP for various swings and this gives confidence of classifying various swings and transients practically.

4.6 The examination of practical data during the full drive swing

To generate real data for the practical movement of the body on the surface, a golf coach[1] was used to perform various golf swings. The experiment was carried out on the aluminium platform (Section 3.3.2), with 8 linear, equally pitched optical sensing elements, in a 4x2 matrix. The data was captured with a National Instruments USB DAQ PAD sampling at a rate of 1KHz, and subsequently filtered using a real time Butterworth method in Section 4.1.5. The captured transient patterns of the voltages during the swing were subsequently calibrated as in Section 3.5.1 and translated into load distributions and patterns at the feet. This was accomplished through the linear interpretation method described in Section 3.5.3 an example of loading and voltage transient patterns at the feet of the golf coach is demonstrated in figure 4.20, and Appendix D.6.

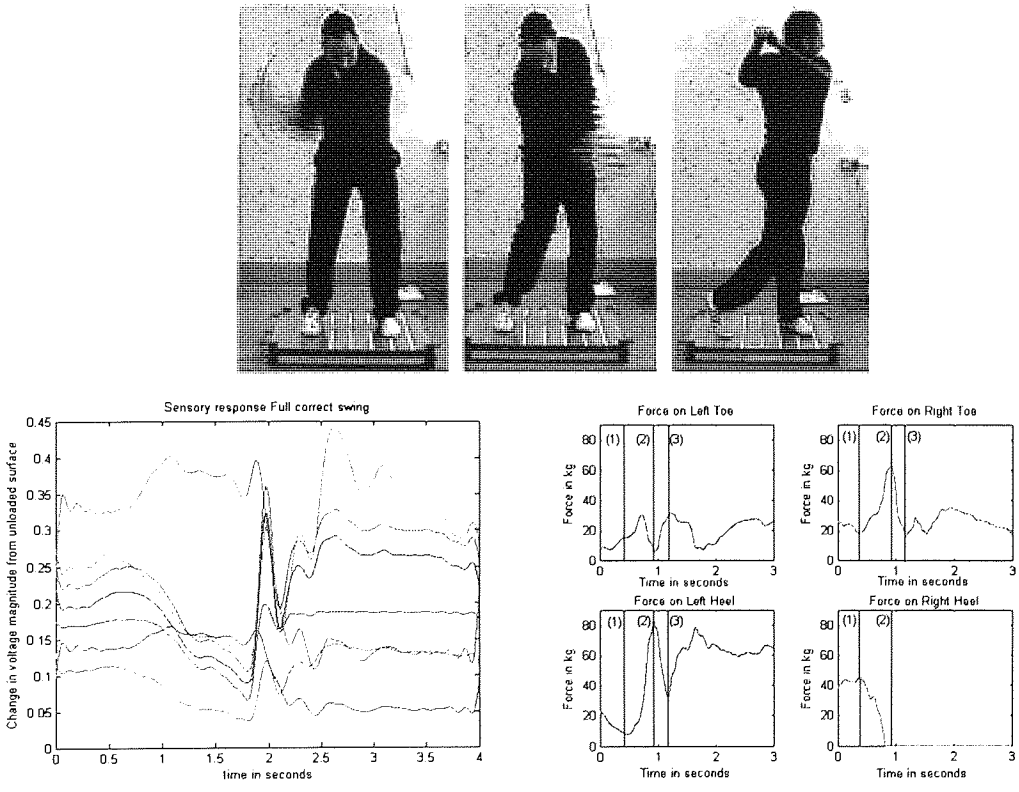

Figure 4.20 (top) - The image capture of a golf coach on the surface throughout a full drive swing. (bottom right) - Calculated foot force profile during the shot from the captured transients of the sensing elements in (bottom left) using a linear regression model, (Section 3.6.3)

[1] Golf Coach – Alistair Davies golf coach at the Belfry Golf Course UK

The figure illustrates a few key features; using video and force evidence it has been found that there are distinct points on the transient that can be related to key elements during the swing. The force profile shows that the load distribution is more or less balanced at the start of the swing at around t seconds (in the bottom left figure 1sec, 0 in bottom right). When the backswing is initiated, the forces on both of the planted feet remain balanced with a slight decrease in load on the left heel when the body and club are coiled into the top swing position at around t+0.4sec.

At this time the downswing (1) is initiated resulting in a large gradient change in the load distributions at the feet. The force of the body during the downswing is transferred from the right heel to the right toe, resulting in the right heel lifting off the surface at the point of impact (2) and observed in the above image, at t+1sec. Also during the downswing the generated dynamic forces can be observed up to the point of impact, of 153kg. The weight of the golfer on the surface was also measured at 86.5kg, which indicates that the forces generated during his swing are 1.77x that of the body weight, which is similar to the findings of (Kawashima 1987) who measured ground reaction forces of 160% for male adults.

At the point of impact (2) it can be observed that the majority of this dynamic force is exerted through the left heel and right toe, while the force on the left toe is reduced, which can be observed in the central image. This raises issues of the golfers balance at the point of impact, which he may need to address to enhance his performance further.

Following through to the top swing (3) the golf coach manages to equalise his load distribution on the three supporting points to enable an equal balance of weight.
However, it can be noted that a simple gradient search method can be used to locate these key points and times throughout the swing.

Compare these results with the findings of Robinson (1994), who used two force platforms, positioned one under each foot to generate the force profiles during the swing, the results of which are illustrated in figure 4.21.

Professional (Robinson 1994)

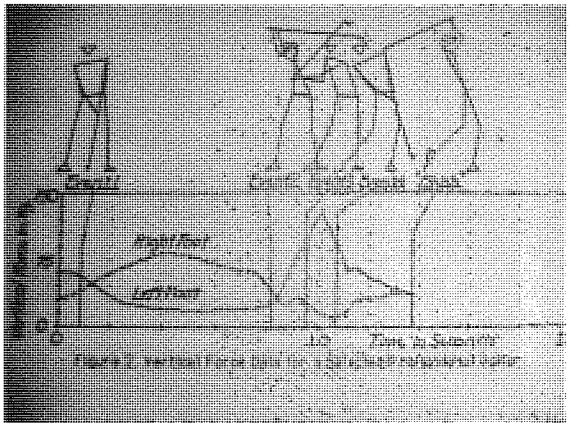

Amateur (Robinson 1994)

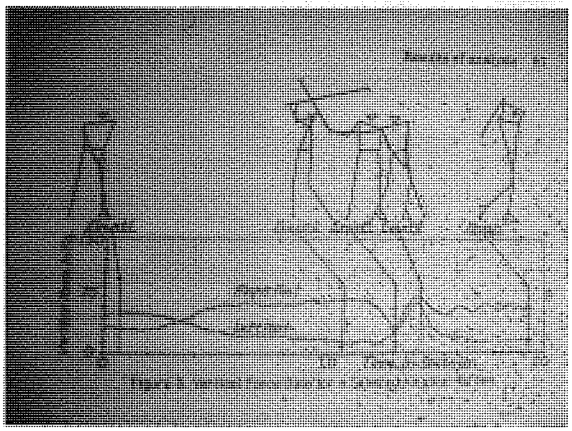

Data from the Golf Coach (Belfry)

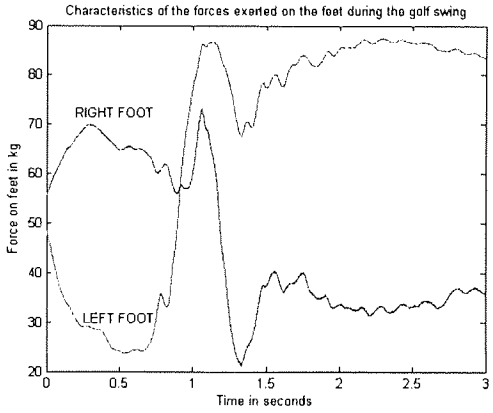

Figure 4.21 (top left) - The loading profile of the left and right feet for a professional golf player during a drive swing. (top right) - The loading profile of an amateur golf player during a drive swing. (bottom) - The loading profile at the feet of the golf coach on the surface.

The golf coach's loading profile at the feet is more similar to those of an amateur player. The results also give confidence that the magnitudes and characteristics of the loading at the feet from the RFSES are what would be expected of a full drive swing using the force plate approach. Also using only one RFSES, the loading profile of the heels and toes of both feet can be determined even if positioned anywhere on the surface. This can be compared with the force platform approach that would require several platforms to discretely calculate the summed magnitudes of the load distributions at specific locations. Alternatively complex image recognition techniques can be employed to the force platform data as to interpret the respective loading magnitudes at various locations under the feet.

Such derived force data can be used to give real time stance and post swing feedback, and is demonstrated in a pre-prototype programme in figure 4.22.

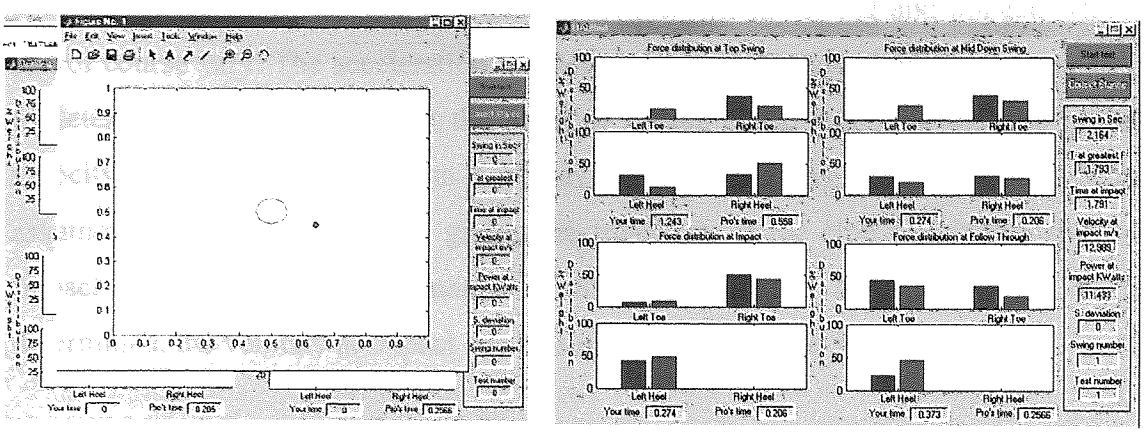

Figure 4.22 (left) - Golfer's centre of mass in relation to an ideal balance.
(right) - The comparison between the users swing and the golf coaches swing at different points during the swing, with additional variables about the swing given on the right hand side.

The figure on the left illustrates the centre of mass movement at the stance position. The COP is inferred through the derived forces from the MLP described, by taking the ratio of the forces between the left to right feet, so that the position of the COP in the x axis can be calculated. Similarly, the ratio between the forces on the heels to that on the toes can derive the COP in the y direction (shown as the small blue circle). The ideal balance at stance should possess equal load distribution between the toes and the heels and the left and right feet. For this, the ideal stance COP is illustrated as a red circle with a 10% tolerance limitation, for the user to adjust their balance.

The figure on the right illustrates the magnitudes of the loading at the feet at the key stages of the golf swing. The user's attempt is illustrated as the blue bars, and the golf coach's load distribution is illustrated as the red bars. This enables the user to think about the loading distribution at the feet, with the associated posture at the key points of the swing.

The variables illustrated indicate the time when the greatest forces are applied by the feet, thus relating to the greatest muscular activity during the swing. The time at impact was found to be when the force on the right toe peaks, see (figure 4.20 right). This can give indication to the peak muscular activity or effort during the swing, in relation to the point during the swing.

The velocity of the club head is computed using a constant speed of acceleration, and the distance the club head travels is also assumed to be constant. The variable

extracted from the data is the time period between the top swing and impact, which can of course vary. The acceleration is determined from the equation: $s = u\,t + \frac{1}{2}\,a\,t^2$, to determine the acceleration at the point of impact t, and assuming that the initial velocity u at top swing is equal to 0. The average length of the arm and club has been assumed to be at around 1.5m, giving the trajectory of the club from top swing to impact at an approximate distance of 6.12m. Once the acceleration has been determined, the velocity at impact can be simply calculated as: $v = u + a\,t$.

Once the impact velocity has been computed, it is then possible to determine the power applied by the muscles at impact from: $P = \frac{1}{2}\,m\,v^2$, where the mass used to create the power, is assumed to be equivalent to the difference between the summed forces at the feet at the stance position to the summed forces at impact.

The consistency variable is derived from group of golf swings. The standard deviation is taken from each load at the feet at the key positions. For example: the standard deviation is taken for the left toe forces for all swings at the top swing. This is repeated for all other feet forces, at all of the key positions. The variable is then simply determined from a summation of all of the standard deviations between swings. Alternatively, for such a parameter, the correlation coefficient between force transients could be taken as a similar output on swing consistency.

4.7 The examination of practical data during the backswing

A prototype of the commercial golf mat was used to capture real data throughout the different variations of golf swing. This comprised of the steel surface and structure in Section 3.2.2, with non-linear sensing elements in Section 3.3.8, positioned optimally in Section 3.3.9.3, captured at a rate of 1KHz using a serial ADC in Section 3.4, filtered post data capture, using an FFT-IFFT algorithm in Section 4.1.6. From the filtered transients, it is possible to break it up into discrete chronological components of the golf swing, so that the respective component can be fully examined and classified. The breakdown or windowing of the transient can either be determined through the derived force distributions in the right bottom of figure 4.20, or directly from the change in gradients of the transients (the left bottom of figure 4.20).

The direct transients are to be used to describe the movement on the surface as opposed to the derived force data. The reason for this is due to the fact that the derived force data from the transients has an error associated with it.

Examining the forces exerted on the feet theoretically and practically for the various classes of backswing, it is possible to determine if there is significant enough a difference between the forces exerted on the surface for various swings, to give a successful classification. Taking the practical captured transients and then developing the expected force distributions at the feet using a trained regularised MLP in Section 3.5.6, it is possible to compare this result with the modelled force distributions through triangulation of the calculated COP in Section 4.5.6. This is however assumed that all positions start with a balanced starting stance position in the centre of the plate. From this it should be possible to validate the accuracy of the model and to predict which classes of backswing are the most distinctive.

Initially, of the captured tests in the class, all the transients were windowed and then averaged to generate a mean swing transient set in the class, which can be assumed to be representative of the class. From this the mean force calculations at the feet are described for a swing of this type using an MLP approach. Figure 4.18 represents the expected forces at the feet for a practical backswing with both feet planted, a correct orbit angle and with the legs straight, i.e. swing (8). Also this is compared with that of the forces at the feet that the model suggests. For other results see Appendix D.7

Measured

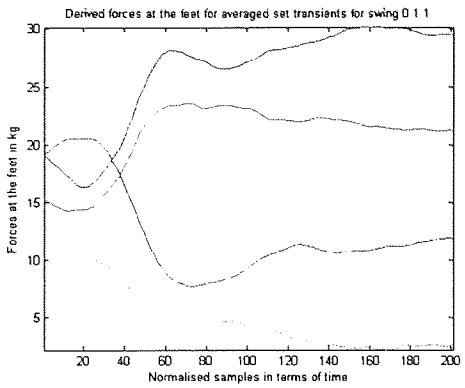

Modelled

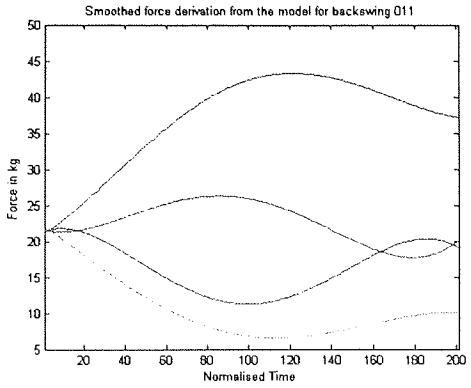

Figure 4.23 (left) - Forces expected at the feet for a practical swing of class (8). (right) - Forces at the feet of the model for a swing of class (8), where blue- right heel, red- right toe, green- left heel, cyan left toe.

These results therefore give confidence that the practical investigation coincides with that of the model and that the representation of the modelled COP suggests that classification between classes is possible, as uniqueness of the force distribution exists between classes.

4.8 Classification methodology for the inference of the kinematics of the body during the backswing

Eighteen tests for each individual class of backswing by the author (See Table 4.2) were captured from the surface for the process of the classification. It is important that the classification process should exist of as few describing classes as possible, as to enhance the system performance. For example, assuming that the classification process is between one of eight possible classes then a random selection process would give accuracies of only 12.5%. If on the other hand the classification process was only between two classes then a random process would give results of 50%.

Therefore, it is suggested that the problem is split down into various sub-classes, such that three classifying algorithms that are used to specifically define one flaw each, as opposed to only one network having to define all eight classifications. This will remove the complexity, and enhance the accuracy from one singular network. Also, as this approach is purely modular, then it is possible to add other networks to handle

other flaws, with the relevant training data. This will prevent the entire network from being retrained for any upgrades and amendments that may be required. The number of possible classes is therefore reduced from eight down to two. See figure 4.24 below.

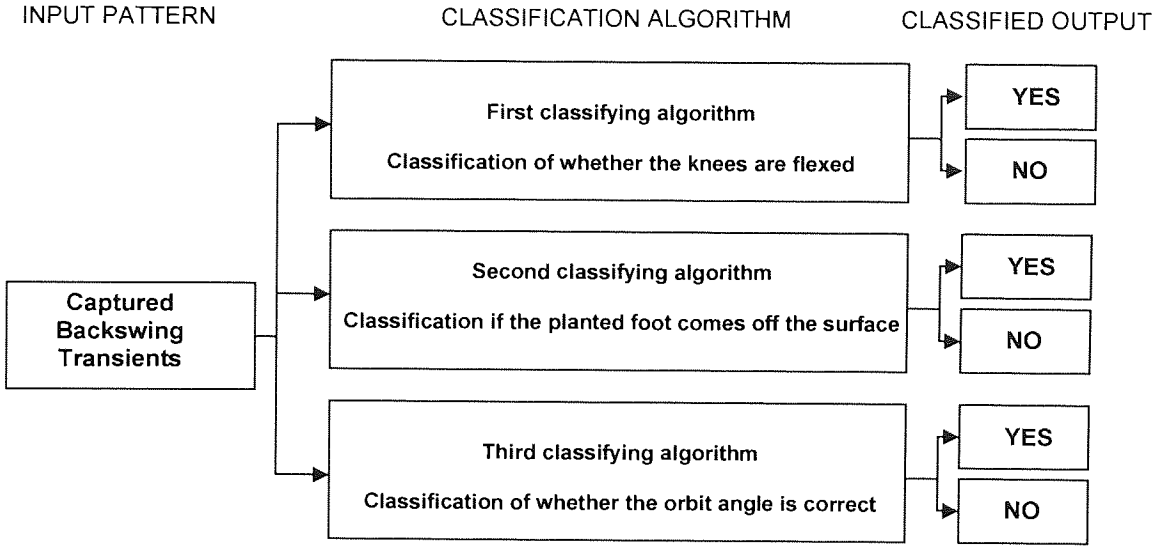

Figure 4.24 - Schematic of the proposed classification technique for various backswings.

Figure 4.24 shows that the same input pattern is given to three different classification algorithms, so that the performance of the classification is enhanced. A breakdown of the problem into two classes from eight also increases the number of possible input patterns in that class from 18 to 72. For example; this is as a result of a classification of all swings in the total data set that have the knees flexed verses all of the swings in the set without the knees flexed, regardless of what other motions are being performed during the backswing.

The above is also assumed that the raw transient input data is filtered using the FFT-IFFT method, discussed in Section 4.1.6 prior to characterisation, and then classification.

4.9 Development of an appropriate input pattern from the captured transient set

There are many ways of manipulating the captured filtered transients during the backswing to formulate the input pattern. The first of these is to use all of the eight captured transients as unique patterns to characterise the class of backswing. Using the time series analysis methods described in Section 4.6, it is possible to extract prominent features from the captured transients, to characterise them in the form of an input vector.

Secondly, the captured transient can be simply summed together to formulate one describing transient. The reason for this is so that the manipulation and characterisation of the transient would be more flexible, with respect to the dimensions of the characterising input vector and a reduction in the processing time required deriving the time series components for the characterisation.

As the positioning of the sensing elements under the surface are asymmetric, the addition of the signals together, will always give a unique new generalised transients, for what ever the activity occurs on the surface. If this method was used in a system, with symmetric sensing elements, then the generalised transient would be identical if the subject swayed to the left, to that if the subject swayed to the right, etc.

Thirdly, the captured transients can be normalised and summed together to generate one describing transient. The reason for a normalisation of each transient would be so that each transient possesses an equal contribution to the final derived summed transient. Only summing the transient also allows for the magnitudes of the transients to be fully represented.

Finally the transients can be evaluated through an averaging of the captured eight transients, to formulate a singular describing transient. The reason for this is that it is arguably more representative of the set of captured transients as opposed to a simple summation. The selection of the proposed method to develop the input pattern is entirely dependent upon how well the chosen algorithm performs. Thus, all approaches need to be investigated to determine the most appropriate method for algorithm performance. However, it is possible to apply a correlation analysis on the selected input to output pattern to give some indication on the most suitable input and characterisation method.

4.9.1 Characterisation using each unique transient to represent the input

Each of the captured transients, were characterised using various time series methods. (AC - Auto Correlation, AR - Auto Regressive model, ARMA - Auto Regressive Moving Average model, FE - Feature Extraction, IVAR - Instrumental Variable Auto Regressive model, PC - Partial Correlation, PF - Polynomial Fit, SVD - Singular Value Decomposition).

The characterising coefficients of the captured transients were examined against the output values relating to the input coefficients using the correlation coefficients as in Section 4.1.2. The input vector is assumed to be a singular dimensional series as is that of the output classification series. The two series are then correlated and the correlation coefficients are then used as a benchmark on how that specific input performs in relation to generating the output.

This is then repeated for all input coefficient values to give an idea of the most appropriate time series characterisation. For the purpose of the investigation, the analysis was carried out on all patterns with the legs bent or straight during the backswing (figure 4.18, Classification process 1).

These benchmarking methods do indicate how well linear or non-linear classification methods may perform. The correlation coefficient magnitude gives information upon the strength of association between two variables. The magnitude is the *effect size* for correlations. Typically, weak relationships are indicated by correlations <0.3, moderate relationships are indicated by correlations between 0.3 and 0.6, and strong relationships are indicated by correlations > 0.6 (Zizzi S, 2006).

If a relationship between two variables is "statistically significant" it means that the level of level of association is not due to chance, and that the significance level is based upon the magnitude of a correlation (effect size) and the sample size (n). If the sample size (n) is large then the correlation value is more statistically significant as opposed to a smaller sample of data.

Most correlation coefficients test only linear associations between two variables. However, there may be a non-linear relationship between two variables, which may lead to an inaccurate assessment of how the two variables are associated.

Finally, it is difficult for two variables to correlate if one or both measures aren't reliable, such as the ability to reproduce consistent results. Reliability amongst datasets can be interpreted on the same correlation coefficients as used earlier. The closer the correlation gets towards 1.0, the better the reliability of the measure. As a rule of thumb >0.9 is considered as very good repeatable data, >0.8, is considered as good, and >0.7 is considered as acceptable. (Zizzi S, 2006).

An example, of the benchmarking method: Assume a 3rd order polynomial expression can generate 3 coefficients to describe the generalised series for various swings (shown as values in the table). The correlation between the first describing coefficient values was correlated with the output class values. This data is taken for four transients captured, with the knees bent (class 1) and the knees straight (class 0).

Pattern number	First coefficient	Second coefficient	Third coefficient	Output Class
1	0.16	-1.5	2.7	1
2	0.25	-2.9	4.1	1
3	0.03	1.2	1.3	0
4	0.3	-1.7	2.9	1

Table 4.3 - Demonstrates the values of the orders of the input characterisation coefficients using a 3rd order polynomial fit, from the captured transient and the output class, for various back swings.

Using the example, the correlation coefficient between all of the first describing coefficient values and all of the recorded output classes (highlighted in red), in this case is equal to: 0.87. Similarly, the correlation coefficient between the second set of describing coefficients and the output class is equal to (-0.93) and then the third (0.84).

Taking the magnitude of the correlations and then taking an average of the correlation coefficients gives (0.88). Where this number is representative of how well all of the input data in the set correlates to that of the output class. This value will therefore give a clue on how well the chosen classification algorithm will perform with respect

to these selected inputs. The averages of the correlation coefficients are displayed in table 4.4, for different extracted input coefficients for whether the legs bent or straight.

Number of coefficients per element	Total number of coefficients in the input pattern	Average Correlation using AC	Average Correlation using AR	Average Correlation using ARMA	Average Correlation using FE	Average Correlation using IVAR	Average Correlation using PC	Average Correlation using PF	Average Correlation using SVD
1	8	0.113	0.322	0.078	0.056	0.121	0.316	0.078	0.132
2	16	0.108	0.322	0.242	0.153	0.121	0.214	0.146	0.155
3	24	0.104	0.291	0.183	0.153	0.084	0.238	0.075	0.151
4	32	0.099	0.355	0.159	0.154	0.086	0.264	0.109	0.154
5	40	0.095	0.382	0.301	0.151	0.075	0.289	0.097	0.166
6	48	0.091	0.32	0.069	0.144	0.067	0.307	0.096	0.167
7	56	0.086	0.23	0.1	0.151	0.075	0.316	0.15	0.15
8	64	0.082	0.186	0.07	0.154	0.073	0.313	0.087	0.137
9	72	0.08	0.147	0.07	-	0.067	0.296	0.076	0.139
10	80	0.078	0.132	0.112	-	0.067	0.283	0.078	0.141

Table 4.4 - How well the input patterns for various time series methods and components correlate with the output classification pattern.

Various time series approaches possess better correlations between the input and output patterns for varying numbers of extracted coefficients. In the main in can be observed that an extraction of one or between 4 to 7 coefficients for each one of the captured eight transients per swing would be most appropriate as a characterisation of the time series dependent upon the selected method. The best correlation shows a moderate data relationship with the value of 0.382 for five auto regressive coefficients per sensing element. Also a total of 144 data sets give indication on statistically good coefficient evaluations of the relationship between input and output patterns.

Examining the repeatability of the data within sets for five auto regressive coefficients per transient for the candidate with the knees bent gives an average correlation of 0.963, and for the knees being straight gives 0.982. This indicates that the selected input data for swing type for this category is very reliable and repeatable.

4.9.1.1 The use of *T*-tests to determine the difference between two population means

Examining the statistical significance between the means and variances in two datasets in the classes for example, can indicate how the classification algorithm is likely to perform. To determine this level of significance it is important to start off with an initial claim, also known as the null hypothesis, denoted by H_o. Alternatively a secondary claim can be made known as the alternative hypothesis H_a, whereby the null hypothesis is false. A statistical test is then used to prove or disprove the null hypothesis to determine the strength of the claim. See Devore J. L. (1991) Chapter 9.

Given that, $X_1, X_2, \ldots, X_m$ is a random sample population with mean μ_1 and estimated variance s_1^2. $Y_1, Y_2, \ldots, Y_n$ is a random sample population with mean μ_2 and estimated variance s_2^2, and X and Y are independent of one another.

The natural estimator of $\mu_1 - \mu_2$ is $\overline{X} - \overline{Y}$, the difference between the two sample means, such that the expression for the estimated standard deviation of $\overline{X} - \overline{Y}$ gives:

$$s_{\overline{X}-\overline{Y}} = \sqrt{\frac{s_1^2}{m} + \frac{s_2^2}{n}} \tag{4.44}$$

Because the population distributions are normal, both $\overline{X}$ and $\overline{Y}$ have normal distributions, implying that $\overline{X} - \overline{Y}$ is normally distributed, with expected value $\mu_1 - \mu_2$ and estimated standard deviation $s_{\overline{X}-\overline{Y}}$. Standardising $\overline{X} - \overline{Y}$ gives the standard normal variable:

$$T = \frac{\overline{X} - \overline{Y} - (\mu_1 - \mu_2)}{\sqrt{\frac{s_1^2}{m} + \frac{s_2^2}{n}}} \tag{4.45}$$

In a hypothesis testing problem, the null hypothesis H_o will state that $\mu_1 - \mu_2$ has a specific value. Denoting this value by Δ_o, the null hypothesis becomes:

H_o: $\mu_1 - \mu_2 = \Delta_o$. Often $\Delta_o = 0$, in which case H_o says that $\mu_1 = \mu_2$. A test statistic results from replacing $\mu_1 - \mu_2$ in (4.45) by the null value Δ_o.

Consider the alternative hypothesis H_a: $\mu_1 - \mu_2 > \Delta_o$. A value $\bar{x} - \bar{y}$ that considerably exceeds Δ_o (the expected value of $\overline{X} - \overline{Y}$ when H_o is true) provides evidence against H_o and for H_a. Such a value of $\bar{x} - \bar{y}$ corresponds to a positive and large value of T. Thus H_0 should be rejected in favour of H_a if T is greater than or equal to an appropriately chosen critical value. Because the test statistic T has a standard normal distribution when H_0 is true, the upper tailed region $T \geq T_\alpha$ gives a test with significance level α. Rejection regions for H_a: $\mu_1 - \mu_2 < \Delta_o$, and H_a: $\mu_1 - \mu_2 \neq \Delta_o$ that yield tests with desired significance level α are lower tailed and two tailed respectively.

Applying this theory to determine how similar the characterising coefficients are for whether the knees are bent or straight during the backswing, should provide a benchmarking tool to describe how the expected classification performance may be between the two classes.

Taking the 5th order AR characterising coefficients data for the first captured transient, illustrates how the data differs for the grouping of whether the knees are bent (m = 72) and straight (n = 72) during the backswing as in figure 4.25. Only looking at the first describing coefficient in the AR model, gives a mean of $\bar{x} = -1.407$ for the knees being bent during the backswing, and a mean of $\bar{y} = -1.512$ for the knees being straight during the backswing. Assuming that the two AR coefficient distributions are normal a calculation of the standard deviation of $s_1 = 0.27$, and $s_2 = 0.19$. Does the data indicate that the true average AR coefficient values μ_1 and μ_2 are different, taking the significance level $\alpha = 0.01$?

i) The parameter of interest is $\mu_1 - \mu_2$, the difference between the true average strengths for the two classifications.
ii) The null hypothesis is H_o: $\mu_1 - \mu_2 = 0$.
iii) The alternative hypothesis is H_a: $\mu_1 - \mu_2 \neq 0$; if H_a is true, then μ_1 and μ_2 are different.

iv) With $\Delta_o = 0$, then the test statistic value is

$$T = \frac{\bar{x} - \bar{y}}{\sqrt{\frac{s_1^2}{m} + \frac{s_2^2}{n}}}$$

v) The inequality in H_a implies that the test is two tailed. Taking an interpolation of the t distribution from (n = 72) from (chart: Devore J. L. 1991), for $\alpha = 0.01$, $\alpha/2 = 0.005$ and $t_{\alpha/2} = t_{0.005} = 2.65$. H_o will be rejected if $t \geq 2.65$ or if $t \leq -2.65$.

vi) Substituting m = 72, $\bar{x} = -1.407$, $s_1^2 = 0.073$, n = 72, $\bar{y} = -1.512$ and $s_2^2 = 0.035$ into the formula for T yields:

$$T = \frac{-1.512 - -1.407}{\sqrt{\frac{0.073}{72} + \frac{0.035}{72}}} = -2.7112$$

That is, the observed value of $\bar{x} - \bar{y}$ is more than three standard deviations above what would be expected were H_o true.

Since -2.7 < -2.65, the computed T does fall into the upper tail of the rejection region. H_o is therefore rejected at a level 0.01 in favour of the conclusion that $\mu_1 \neq \mu_2$. The sample data strongly suggests that the true average first AR coefficient values differ between whether the knees are bent or straight during the backswing.

In conclusion the T values for all of the 5 AR coefficients for the first captured transient gave:

1st AR coefficient: 2.7

2nd AR coefficient: -2.62

3rd AR coefficient: -2.433

4th AR coefficient: -2.93

5th AR coefficient: 2.78

The proof that all of these T values fall within the upper or lower tail rejection regions at either -2.65 or 2.65 apart from coefficient 2 and 3, indicating that in most cases $\mu_1 \neq \mu_2$. This highlights that there are definite differences in the signal characteristics between the two classes. The given T values illustrate that the strongest difference is

within the 4th AR coefficient from the first captured transient set, and is visually supported through a box and whisker diagram given in figure 4.25.

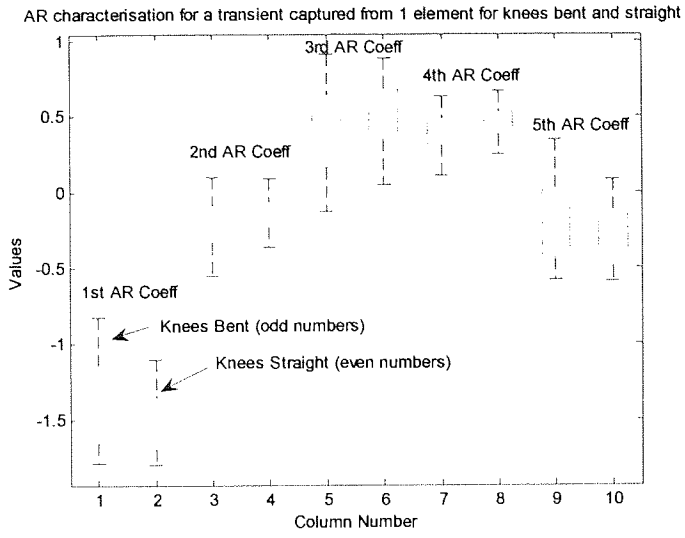

Figure 4.25 - Box and whisker plot for the classification between whether the legs are bent or straight during the backswing following a 5th Order AR characterisation from a windowed transient of the first sensing element.

The above plot shows show the data is separated between the two classes, using a 5th order AR model. It can be observed that the data between the classes, although different overlap somewhat. It therefore indicates that the success of the classification algorithm will not be 100%, due to the fact that the two classes are not discrete, using the AR characterisation.

Although the correlations in the table appear to be of a low quantity, this is purely dependent upon the linear correlation coefficient measurement used. However; this type of data used can still perform quite well with non-linear classification methods, as described earlier.

It may be possible to extract the most correlated individual coefficients out of the generated data set from one particular characterisation method and then mix them with other highly correlated components from different characterising approaches. This new developed vector will therefore possess a highly correlated input-to-output dataset. Testing these highly correlated mixed patterns, with different classification methods will test the theoretical argument. The performance of this approach is to be examined further in this chapter in Section 4.10.1.

4.9.2 Characterisation using a summation of all of the captured transients

The advantage of compounding the input transients into one singular transient is to enable a reduction in the number of inputs in the dataset. As with the approach in Section 4.9.1 the number of inputs can be as large as 64 components to fully describe the input. Alternatively, this approach will ultimately reduce the number of coefficients required to fully characterise the input and hence reduce the required processing time by a factor of eight. The method therefore develops one single transient through the addition of the magnitudes of the captured eight transients, at each captured point in time.

A similar examination of the correlation coefficients between the input and output patterns using this approach, will indicate the robustness of the input data in comparison to the method described in Section 4.9.1. The results are displayed in table 4.5.

Total number of coefficients in the input pattern	Average Correlation using AC	Average Correlation using AR	Average Correlation using ARMA	Average Correlation using FE	Average Correlation using IVAR	Average Correlation using PC	Average Correlation using PF	Average Correlation using SVD
1	0.042	-	0.311	0.459	-	0.337	0.307	0.286
2	0.038	0.244	0.239	0.383	0.054	0.293	0.171	0.147
3	0.034	0.332	0.204	0.296	0.125	0.302	0.311	0.135
4	0.031	0.356	0.183	0.275	0.056	0.312	0.096	0.167
5	0.027	0.378	0.403	0.302	0.073	0.323	0.342	0.175
6	0.023	0.341	0.030	0.313	0.071	0.333	0.121	0.177
7	0.020	0.294	0.086	0.287	0.114	0.344	0.271	0.178
8	0.019	0.259	0.065	0.273	0.076	0.351	0.196	0.175
9	0.020	0.188	0.109	-	0.079	0.3501	0.191	0.166
10	0.021	0.137	0.089	-	0.053	0.342	0.046	0.158

Table 4.5 - How the input elements correlate with the output pattern for various numbers of extracted coefficients, using several time series methods for summed transients.

The general average of all of the correlation coefficients is lower than that of table 4.4. I.e. the general average of all of the greatest correlations gives 0.298 in table 4.5, compared with 0.213 in table 4.4.

It is also to be noted that the greatest correlation evaluation in table 4.5 is 0.459, compared with only 0.382 in table 4.4. As a result of only being able to take one set of

coefficients to develop the input pattern, then the method of summing the input transients would be preferred to that of handling each of the eight transients separately, showing moderately correlating data between input-to-output patterns.

Analysing the data separation for the most correlating characterising coefficients from the summed transients, through the use of a T test similar to that in section 4.9.1.1 gave a value of 6.16. This high T value can be attributed to the small estimated variance in data within each class. Such a large distance is indicative of a better data separation between classes than that of the AR coefficient extraction. This is supported through the evaluation of the correlation coefficients and the box-whisker plot in figure 4.26, with respect of one feature extraction from the summed transient, see Section 4.2.1.6.

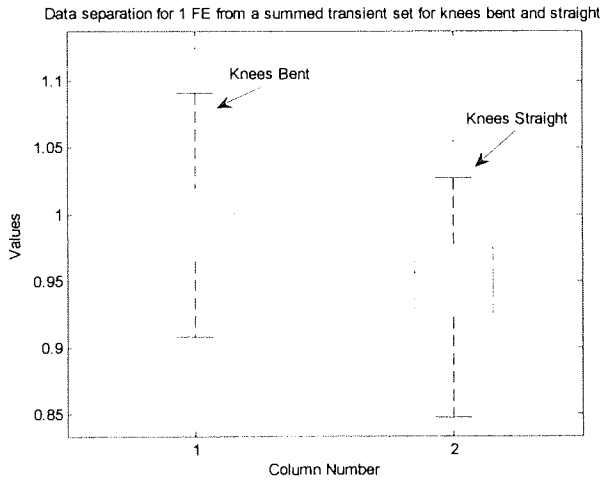

Figure 4.26 – Data separation between the two classes during the backswing, using only one extracted feature from the summed transient set of the eight elements.

The result in figure 4.26 supports the findings of the correlations given in tables 4.5, and 4.4. It is clear to see that the separation of data between classes in the above figure shows less overlap than that in figure 4.25, which are linearly related to the correlation measure. This separation demonstrates why there is a greater correlation between input-to-output patterns using this feature extraction, to that of a 5^{th} order AR extraction.

This type of feature extraction could indicate good linear classification performance to that of the 5^{th} order AR model; however it is difficult to determine how both types of characteristic extraction will perform using a non-linear classification method.

4.9.3 Characterisation using a normalised summation of all of the captured transients

Normalising the input transients and then summing, enables each transient to possess equal sensitivity and contribution to the final summed transient. By examining this approach it enables a derivation of the best method for manipulation and characterisation of the captured transients.

Applying the method of correlation it can be found how large an effect normalising the transients has, through a comparison of the results in table 4.5. The results from applying this approach are illustrated in table 4.6.

Total number of coefficients in the input pattern	Average Correlation using AC	Average Correlation using AR	Average Correlation using ARMA	Average Correlation using FE	Average Correlation using IVAR	Average Correlation using PC	Average Correlation using PF	Average Correlation using SVD
1	0.118	0.388	0.197	0.082	-	0.054	0.107	0.225
2	0.113	0.307	0.241	0.094	0.039	0.155	0.076	0.330
3	0.107	0.464	0.305	0.215	0.040	0.257	0.278	0.287
4	0.101	0.495	0.280	0.194	0.022	0.313	0.252	0.270
5	0.096	0.480	0.182	0.172	0.136	0.351	0.429	0.245
6	0.090	0.349	0.063	0.144	0.103	0.376	0.220	0.220
7	0.084	0.226	0.067	0.135	0.073	0.362	0.384	0.207
8	0.079	0.176	0.023	0.120	0.112	0.335	0.161	0.197
9	0.073	0.238	0.146	-	0.055	0.330	0.148	0.190
10	0.067	0.281	0.108	-	0.057	0.333	0.056	0.175

Table 4.6 - How the input elements correlate with the output pattern for various numbers of extracted coefficients, using several time series methods for normalised summed transients.

The maximum average correlation value is 0.495 and is the greatest value achieved using all other manipulations of the input transients. The average of all of the maximum averaged correlations for each characterising method using this approach, gives a value of 0.3. This can be compared with that of the previous manipulations and it suggests that a normalisation of the input data and then summing is more beneficial for enhanced correlation than handling each transient individually, or simply summing the transients directly. However, the impact of such a normalisation does have a beneficial effect, albeit small in comparison to handling a summed transient in relation to handling each transient individually.

Examining the separation of the most correlating data set using a box plot should indicate how the characterising data is separated through class type. It is predicted that it should be similar to that of the feature extraction method shown in figure 4.26. The reason for this is that correlation and separation are linear measures, and both are linearly related. A *T*-test was also conducted to illustrate the distance from two similar datasets as in section 4.9.1.1 from the normalised summed transient.

1st AR coefficient: 6.95

2nd AR coefficient: -7.1

3rd AR coefficient: -6.39

4th AR coefficient: 6.71

This illustrates that the distances are significant enough to illustrate that the sample means between the two classes are not equal, even at a value of $\alpha/2 = 0.0005$, where the critical value is calculated at 3.44 from the *T* distribution table. The distance evaluations also highlight that all extracted coefficients have similar data separations between classes, however showing alternative directions. This is also supported in figure 4.27.

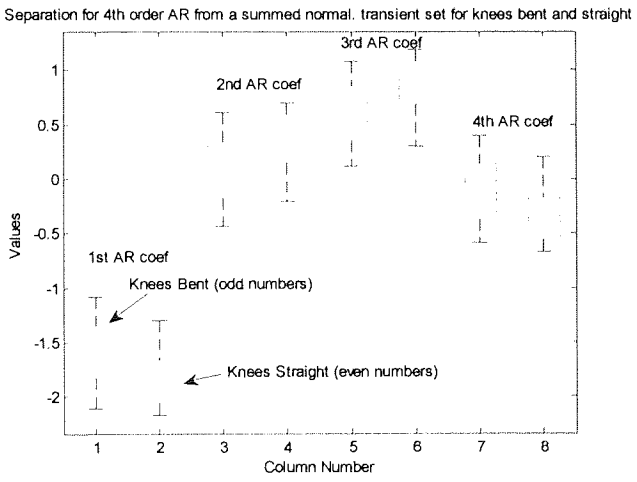

Figure 4.27 - Separation of data between classes for the knees bent or straight during the backswing, using a 4th order AR model extraction from a summed normalised transient.

As predicted the separation of the data is more visible than that of a poorer correlation as in figure 4.25. It illustrates that the separation is also similar to the data separation in figure 4.26, with similar correlation evaluation for input to output mapping. Again this type of separation shows some form of linear pattern, and indicates that a linear classification algorithm will perform better than a random guess of the class type.

4.9.4 Characterisation using a normalised average of all of the captured transients

It has been found that normalising the captured transients and combining the signal is the optimal data manipulation approach. However, it can be argued that combining the signals with a summation does not fully represent the magnitudes between the signals. It is therefore suggested that by taking the average of the combined signals, it is more representative of the group of captured filtered transients.

The correlation coefficients for a normalised averaged transient set were examined to determine whether or not an averaging of the transients has a large impact on how well the extracted coefficients correlate with the output pattern. The results of this experiment are contained in table 4.7.

Total number of coefficients in the input pattern	Average Correlation using AC	Average Correlation using AR	Average Correlation using ARMA	Average Correlation using FE	Average Correlation using IVAR	Average Correlation using PC	Average Correlation using PF	Average Correlation using SVD
1	0.009	0.393	0.142	0.160	-	0.178	0.295	0.301
2	0.011	0.337	0.159	0.228	0.149	0.215	0.180	0.301
3	0.018	0.458	0.248	0.289	0.098	0.295	0.325	0.252
4	0.027	0.497	0.222	0.228	0.130	0.344	0.236	0.238
5	0.036	0.473	0.229	0.192	0.086	0.376	0.421	0.222
6	0.045	0.328	0.032	0.214	0.068	0.395	0.247	0.206
7	0.054	0.212	0.093	0.195	0.059	0.370	0.385	0.194
8	0.063	0.172	0.051	0.180	0.065	0.333	0.150	0.186
9	0.072	0.237	0.141	-	0.038	0.327	0.201	0.180
10	0.081	0.276	0.092	-	0.076	0.328	0.053	0.200

Table 4.7 - How the extracted coefficients correlate with the output classification, assuming a normalised averaged transient from the captured transient set.

The results in table 4.7 indicate that the average of all of the greatest averaged correlations gives 0.297, which is similar to that of the normalised and non-normalised summed transients. However, the most important result is that the best correlation between inputs and output pattern is 0.497, using a 4^{th} order AR model. This indicates that the best correlation using this approach is slightly better than the best correlations from all of the other data manipulation approaches, also that the relationship between input to output patterns is moderate.

Again, evaluating using a *T*-test to determine how different the two classes of data are, the distances were evaluated as follows:

1st AR coefficient: 6.98

2nd AR coefficient: -7.09

3rd AR coefficient: -6.46

4th AR coefficient: 6.76

Again the evaluation shows a separation such that the null hypothesis is false, thus indicating that the two datasets are independently different and separable. The discrete values of the T-test are comparably similar to those of the 4th order AR model for the summed normalised transient, indicating that neither data manipulation method outperforms the other in terms of data separation, and hence possible classification.

Looking at the data separation amongst the extracted AR coefficients to define the class type is illustrated in figure 4.28, using a box-whisker plot also supporting the evaluations of the *T*-test.

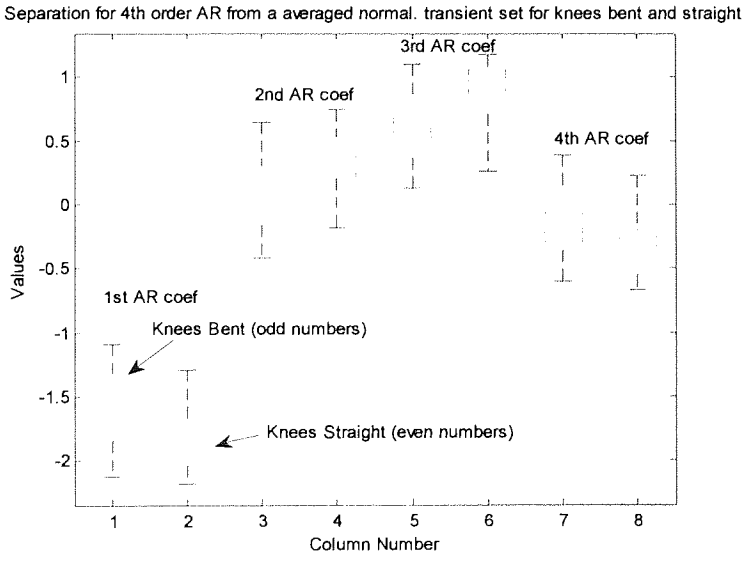

Figure 4.28 – Separation of the data within classes for a 4th order AR extraction from averaged normalised transients during the backswing.

It can be observed that the figure above and scale of it is somewhat similar to that in figure 4.27. The reason for this is due to the fact that the scaling of a normalised summation of transients gives similar characteristics as a normalised averaging of transients. Using an AR extraction, will give similar separations of data using the

same coefficient extraction method in either data manipulation technique. Although both manipulation methods are not identical, as correlations between patterns would be identical in tables 4.7 and 4.6, and can be assumed to be the scaling between the two manipulation methods.

On the whole, averaging the normalised transients does not make a significant difference to the result of the correlation between input and output patterns, as compared with other manipulations. This implies that either a non-normalised/normalised summed or normalised average of the transients could be used to generate better correlations between input and output patterns, compared with that of only handling each transient individually looking at the relationship correlations between input and output patterns.

4.10 Analysis into possible algorithms to provide the classification process

Many methods exist to formulate classification outputs relating to the input stimuli and the required output. These can be mathematical, linear, or non-linear. Inverse mathematical and linear evaluations tend to generate regressive output responses; however, these can be converted to generate classificatory outputs through the appliance of an additional algorithm to the regressive response.

There are many conventional methods that can be applied to generate classification outputs, such as: Single Layered Perceptron networks (SLP) or alternatively known as Generalised linear models (GLM), Multi Layered Perceptron (MLP) networks, or Bayesian techniques. However, the selection of such an algorithm is crucial to the application required.

4.10.1 Generalised Linear Models (GLM) or SLP methods

Single-layer networks implement the well known statistical techniques of linear regression and generalised linear models and can be applied to classification problems, (Nabney 2002) also (See Section 3.6.3 – 3.6.5). GLM models consist of a linear combination of the input variables, the coefficients which are the parameters of the model and an activation function approximate to the type of data being modelled.

The training algorithms used for these types of models consist of Iterated Re-weighted Least Squares (IRLS) approach to formulate a relationship between given input and output patterns. See Section 3.6.4 for SLP regressive training.

Resulting from the derived regressive output between input and output patterns, it is possible to generate a classificatory output response through the application of one of two possible activation functions, one of which is the logistic sigmoid function involving multiple independent attributes given in the form:

$$y_j = \frac{1}{1+e^{-a_j}} \tag{4.46}$$

where α_j represents the output from the SLP or MLP algorithm. This type of classification algorithm is designed to classify between one of two possible classes in the output vector i.e. if $\alpha_j < 0$ then the classification gives a value between $0 < y_j < 0.5$, or if $\alpha_j \geq 0$ then the classification gives a value between $0.5 < y_j < 1$. An example of this logistic classifying function is demonstrated through the classification of two classes from a generalised linear model by straight contours in figure 4.29, (Nabney 2002) with the Netlab toolbox: demnlab.

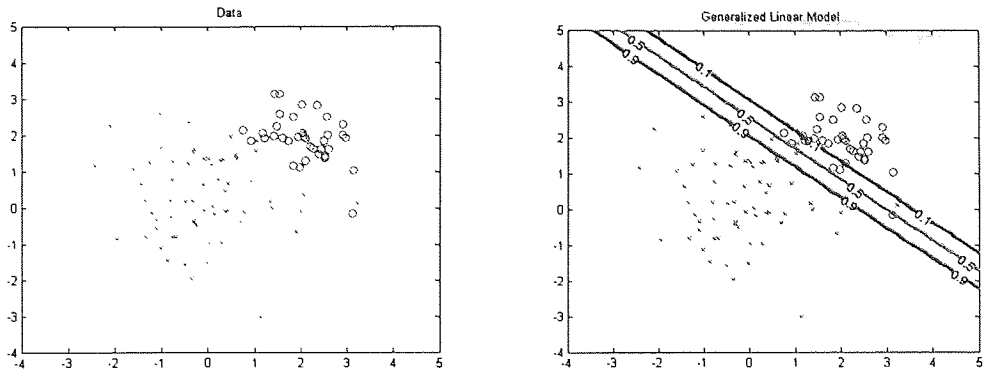

Figure 4.29 – (left) shows input data in two sets to be classified into either the first or second class. (right) shows the classification boundary provided by the GLM and logistic activation function for various decision boundaries at 0.1, 0.5 and 0.9

On classifying the output as either a 1 or a 0, the method allows for additional flexibility through the decision boundaries. Normally this would be set to 0.5, i.e. if y_j is greater than 0.5, then this would be rounded to the class 1, else this would be rounded to class 0. By incorporating a threshold parameter based upon the result of y_j then this allows for a biasing of the output, which could, when analysed enhance the system performance.

The second classifying function is generally the most common and is more commonly known as the softmax function. Its operation is somewhat similar to that of the logistic function with respect to the derived regressive response α_j to give classification y_j. It functions on the basis of a set of c mutually exclusive classes and is given in the form:

$$y_j = \frac{e^{a_j}}{\sum_{j'} a_{j'}} \tag{4.47}$$

This function can be used for multiple classifications from the regressive GLM and is demonstrated for the discrimination of three classes in two dimensional space illustrated in figure 4.30 (Nabney 2002), with the Netlab toolbox: demnlab.

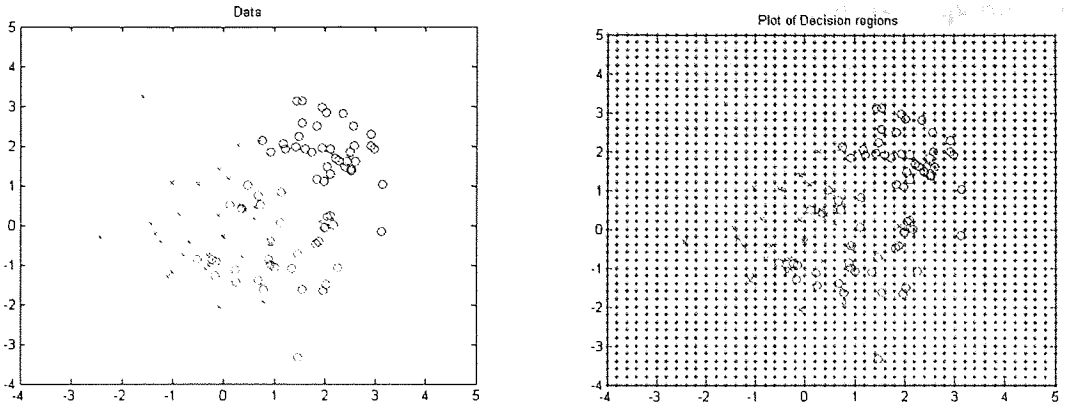

Figure 4.30 - illustrates the classification of three classes using the softmax function used from a regressive result obtained from the GLM

4.10.2 Classification using the result of MLP regressive methods

Classifications from figures 4.29 and 4.30 use the outputs of an SLP model. This is generated from logistic sigmoid activation and softmax functions (4.46) and (4.47) can also be applied to the regressive result of multi layered perceptron networks (MLP) to generate non-linear classifications due to the non-linear regressive output response from the correlation between input and output. These can be compared with linear boundary classifications using a GLM regressive approach.

Figure 4.31 illustrates the classification of two classes in a two dimensional space from non-linear decision boundaries. This is generated from a logistic sigmoid activation function coupled with the output response of an MLP. Taken from Nabney (2002) and the Netlab toolbox: demnlab.

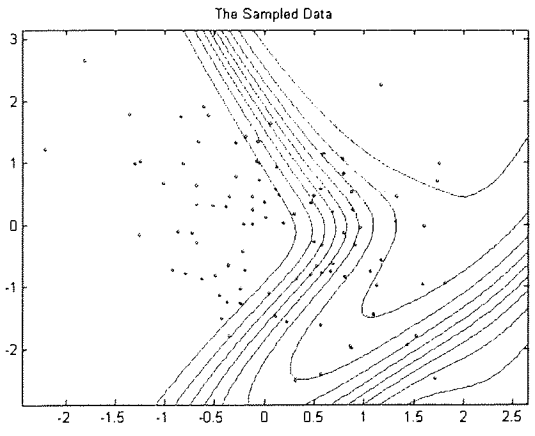

Figure 4.31 - shows the non-linear classification boundaries with different threshold decisions from a logistic activation function through an MLP regressive response

For the selection of an appropriate classification algorithm, it is important to determine the possible classifications of the input data. In all cases illustrated, the dimensions of the inputs have been two dimensional which is easy to visually generalise. However, if the input dimensionality is greater than three then such orders are difficult to plot on a maximum of 3 dimensions and visually perceive the class separation. Such high dimensional order is probable based upon the analysis of Section 4.9. From this, it would be difficult to strictly determine which approach would be optimal, thus both linear and non-linear classifications are to be analysed to determine the linearity of the dataset, accuracy and correlation.

4.10.3 Selection of the classification model through the handling of each individual transient

Analysing the actual system performance through handling each transient individually using a GLM and regularised MLP approach will give a true interpretation of the success of the input data manipulation technique.

An initial investigation was carried out on the best correlating input to output patterns from the respective characterisation technique (i.e. a 5^{th} order AR model for each transient, see Section 4.9.1). A GLM model was initially optimised using an (Iteratively Re-weighted Least Squares) IRLS training algorithm approach, with the decision boundary set at 0.5, and iterations stopped at 50. The approach gave accuracies of 75% for all unknown patterns, and 95.83% for all collected input patterns. An MLP was then trained with SCG using early stopping with a sigmoid logistic activation function to select between the two possible classes, (i.e. if the knees are flexed or not during the backswing). The optimal parameters were derived as possessing 6 nodes, a weight decay coefficient of $1x10^{-5}$ and an early stopping limit of 50 iterations, with accuracies of 62.5% for all unknown input patterns and 86.81% for all collected input patterns. This suggests that the linear model performs quite well in this case, with acceptable performances.

The reason why two performance indicators are illustrated is due to the fact that an analysis of the unknown input patterns is reflective of forthcoming patterns unseen by the algorithm, and is the leading benchmark measurement tool. But the analysis of all of the collected input patterns constructed from known trained, unseen test and validation patterns represents a greater range of possible inputs that may be observed by the system, although should only be used as a secondary measure if two classification methods, give similar unknown pattern accuracies.

The reason for such a large difference between the tests data measurements suggest that there could be a) too little data for the classification algorithms to interpret the underlying system function accurately, or b) that the input data of the test patterns is not very representative of the trained input patterns, or c) the trained and tested data could be effected by a high degree of noise and variation, see box plot in figure

(4.25), or d) due to the fact that when secondary flaws occur within the same class, but have with greater sensitivity than the one the extraction is looking for, may drown out the features that are important in the classification process, or be a combination of the four.

Table 4.4 in Section 4.9.1, illustrates that in general 5 extracted coefficients per transient gives optimal correlation performances between input characterisations and output classes. From this it is possible to extract the forty most correlating characterisations to define the eight captured transients. Again training with forty of the most correlating inputs using a GLM algorithm, gave accuracies of 70.83% for all unknown patterns, and 95.14% for all training patterns.

The MLP algorithm was then trained and gave optimal parameters of 15 nodes, a weight decay coefficient of $1x10^{-1}$ and an early stopping of 100 iterations, which gave classification accuracies of 62.5% for all unknown patterns and 86.11% for all collected patterns.

This indicates that the correlating coefficient theory performs fairly for the selecting of certain elements that could be used to perform with adequate results. Although the theory can give a general indication of which input features will give good performances, it can not be used to directly pin-point the inputs that should be adopted. This can be assumed to be due to the non-linear relations derived by the classification algorithm, which cannot be fully described by the linear correlating benchmarking system.

These results indicate that no one manipulation approach stands out more predominantly than any of the other methods. This can be assumed to be due to the non-linearity of the classification. Of the two manipulations demonstrated from the possible characterisations of the 8 sensing elements, all approaches show accuracies of around 62% for all unknown patterns using MLP and at around 72% for unknown patterns using the GLM method. This indicates how well the network and characterisation method will perform on new data presented to it.

Although the success of such an approach is quite poor in terms of a classification, various things could be used to enhance the classification performance. Such as: a) look at another variation of data manipulation of the captured transients, and characterisation method of the transient(s). Such as the methods discussed earlier and are described in Sections 4.10.3 – 4.10.5, b) eliminating the inaccuracies in human classification of the actual or degree of output class for a type of swing. This can be carried through the use of a vision system that can digitally measure the degree of movement, and hence select an appropriate class for the movement, which is more accurate than what a human perceives the class type to be, c) much more data can be collected within the various classes so as to generate a more accurate generalisation of the system function through MLP and GLM methods, although noise elimination within the data received by the algorithm as training or testing patterns is limited to low level noise elimination described in Section 4.1, d) alternative classification methods can be investigated, such as Bayesian techniques for example, which may be able to generalise more accurately but without the need for large samples of input data.

4.10.4 Selection of the classification model using a summed transient set

It has been found that a possible optimal approach of data manipulation, to classify whether the legs are bent or straight, is one which sums the captured transients and then characterises through taking one feature extraction (Table 4.5, Section 4.2.1.6).

Using 72 random patterns as inputs, a further 48 random patterns as validation patterns and 24 as unknown test patterns, a GLM was initially trained using IRLS with a decision boundary of 0.5. The algorithm gave a classification success rate of 79.17% for all unknown patterns and 70.83% for all of the collected input patterns, to determine whether the legs are bent or straight during the backswing.

A classifying MLP was then trained with a criterion of early stopping. The optimised parameters gave 40 hidden nodes, a weight decay coefficient of $1x10^{-5}$ and an early stopping of 50 iterations. The classification for all unknown patterns gave 79.17% and for all collected inputs a success rate of 70.83%. It has therefore been found that both

MLP and GLM models behave similarly, thus it can be suggested that some patterns can not be directly classified correctly as they overlap into the other class.

Selecting 8 of the most correlating inputs to output patterns (which is through taking 8 feature extractions from table 4.5), from all of the characterising coefficients may give an enhanced response. An optimised MLP was trained using this highly correlating data set giving 1 node, a weight decay coefficient of $1x10^{-1}$ and an early stopping of 50 iterations. The success of which was recorded at 70.83% for all unknown patterns and 75% for all input patterns. Similarly training with a GLM algorithm, gave results of 79.17% for all unknown patterns, and 71.53% for all input patterns. This also illustrates similar success rates for an extraction of one feature extraction to describe the transient using a GLM or MLP.

Examining the performance of the correlation indicators illustrated in table 4.5, for eight extracted coefficients from the summed transients, through a comparison of the classification algorithms performance is illustrated in table 4.8.

	Extraction of 8 AC coeff.	Extraction of 8 AR coeff.	Extraction of 8ARMA(4,4) coeff.	Extraction of 8 FE coeff.	Extraction of 8 IVAR coeff.	Extraction of 8 PC coeff.	Extraction of 8 PF coeff.	Extraction of 8 SVD coeff.
Correlation	0.019	0.259	0.065	0.273	0.076	0.351	0.196	0.175
MLP nodes	25	1	10	5	8	21	39	1
MLP weight decay coefficient	$1x10^{-3}$	$1x10^{-5}$	$1x10^{-5}$	$1x10^{-5}$	$1x10^{-6}$	$1x10^{-2}$	$1x10^{-1}$	$1x10^{-9}$
MLP early stopping	50	100	50	50	50	50	300	100
MLP for unknown patterns	58.33%	70.83%	54.17%	75%	50%	62.5%	83.33%	83.33%
MLP for all input patterns	63.89%	73.61%	65.28%	79.17%	60.42%	81.25%	82.64%	76.39%
GLM for unknown patterns	58.33%	58.33%	54.17%	79.17%	58.33%	62.5%	75%	87.5%
GLM for all input patterns	70.14%	68.75%	64.58%	71.53%	59.72%	70.83%	71.53%	71.53%

Table 4.8 - Success rates of the classification for both GLM and MLP logistic algorithms and comparison with the correlations between the inputs and output patterns.

From the results illustrated in table 4.8, it shows that there is a correlation between the system performance (in blue and red) and correlation magnitudes (in green). For average correlations less than 0.1 both algorithms perform quite poorly compared with those greater than 0.1. From this it can be suggested that the correlation analysis can not be used as a direct pin-point to the optimal input characterisation and classification of the transients; however it can be used to give a general idea on which characterisations may give optimal solutions and performance

Looking at the test set performance, neither model dominates the other. However, the best test set performance over all is from the GLM with 8^{th} order SVD coefficients as the input vector

4.10.5 Selection of the classification model using a normalised summed transient set

Taking the best correlating coefficients i.e. a 4^{th} order AR model of the summed normalised transient using an MLP classification approach with 38 nodes, a weight decay coefficient of $1x10^{-4}$, and an early stopping limit of 50 iterations. The results gave accuracies of 50% for all unknown patterns and 75% for all known patterns to interpret whether of not the knees were flexed during the backswing. Examining this performance against a GLM classification gave accuracies of 58.33% for all unknown patterns and 70.14% for all collected patterns, suggesting that a GLM method would be preferred in this case.

A similar analysis was carried out for an 8^{th} order extraction from the normalised summed transient. This was carried out in order to develop a robust comparison between different data manipulation methods from actual system performance measures, so that an optimal manipulation could be determined. The results are shown in table 4.9.

	Extraction of 8 AC coeff.	Extraction of 8 AR coeff.	Extraction of 8ARMA(4,4) coeff.	Extraction of 8 FE coeff.	Extraction of 8 IVAR coeff.	Extraction of 8 PC coeff.	Extraction of 8 PF coeff.	Extraction of 8 SVD coeff.
Correlation	0.079	0.176	0.023	0.120	0.112	0.335	0.161	0.197
MLP nodes	14	1	20	1	1	10	14	1
MLP weight decay coefficient	$1x10^{-5}$	$1x10^{-3}$	$1x10^{-6}$	$1x10^{-5}$	$1x10^{-4}$	$1x10^{-1}$	$1x10^{-4}$	$1x10^{-5}$
MLP early stopping	100	50	100	50	50	200	50	50
MLP for unknown patterns	50%	70.83%	62.5%	58.33%	62.5%	58.33%	70.83%	50%
MLP for all input patterns	69.44%	72.22%	72.22%	74.31%	61.81%	77.08%	71.53%	71.53%
GLM for unknown patterns	54.17%	70.83%	50%	66.67%	45.83%	70.83%	83.33%	62.5%
GLM for all input patterns	70.14%	68.06%	64.53%	71.53%	58.33%	71.53%	74.31%	71.53%

Table 4.9 - Classifying algorithms success rate from an 8^{th} order coefficient extraction. The input data for this analysis is a summed normalised transient during the backswing to interpret whether the knees are straight or flexed.

Observing the classifying algorithms' performance it is clear that normalising the transient and then summing is no more beneficial than simply summing the transients. In fact, through the operation of summation, the algorithm performs marginally better than that of the normalisation approach. The reason for this could be due to the fact that the magnitudes of each unique transient are of importance to the classifying algorithm in interpreting the class.

Secondly, the data also shows a good general correlation between network performance and the correlation of input to output patterns. Finally, it must also be acknowledged that the polynomial fitting method in both cases has been the optimal approach for algorithm success.

4.10.6 Selection of the classification model using a normalised averaged transient set

Examining the best average correlation characteristics (i.e. a 4th order AR model) between input characterisations and output patterns, through the examination of an MLP classification gave optimised parameters of 50 hidden nodes, a weight decay coefficient of $1x10^{-2}$ and an early stopping of 50 iterations. The success of the MLP gave accuracies of 45.83% for all unknown patterns and 74.31% for all collected input patterns. Using the GLM approach the success rates gave accuracies of 66.67% for all unknown input characterisations and 69.44% for all collected input patterns.

Extracting 8th order coefficients, examining the systems performance and comparing it with the other input data manipulation techniques, should be able to indicate the most optimal manipulation, with respect to other types of classification, for example if the orbit angle is correct or not.

The GLM and MLP classification performance with respect to a characterised normalised averaged transient set is illustrated in table 4.10.

	Extraction of 8 AC coeff.	Extraction of 8 AR coeff.	Extraction of 8ARMA(4,4) coeff.	Extraction of 8 FE coeff.	Extraction of 8 IVAR coeff.	Extraction of 8 PC coeff.	Extraction of 8 PF coeff.	Extraction of 8 SVD coeff.
Correlation	0.063	0.172	0.051	0.180	0.065	0.333	0.150	0.186
MLP nodes	55	1	5	6	17	1	25	6
MLP weight decay coefficient	$1x10^{-6}$	$1x10^{-7}$	$1x10^{-6}$	$1x10^{-9}$	$1x10^{-5}$	$1x10^{-1}$	$1x10^{-4}$	$1x10^{-4}$
MLP early stopping	100	350	100	50	100	100	50	50
MLP for unknown patterns	55.33%	62.5%	68.75%	70.83%	45.83%	75%	54.17%	54.17%
MLP for all input patterns	74.31%	75%	70.83%	76.39%	62.5%	77.78%	74.31%	83.33%
GLM for unknown patterns	54.17%	66.67%	75%	79.17%	45.83%	70.83%	87.5%	75%
GLM for all input patterns	72.22%	70.83%	70.14%	70.14%	54.17%	72.22%	76.39%	65.92%

Table 4.10 - GLM and MLP performances from an 8th order coefficient extraction from a normalised averaged transient to interpret whether the legs are flexed or straight.

Extracting the most correlating 8 coefficients between input and output patterns from the averaged normalised transient and applying an MLP classification algorithm gave 1 hidden node, a MLP weight decay coefficient of 1x10-1 and an early stopping of 50 iterations. The results of which gave accuracies of 83.33% for all unknown patterns and 79.86% for all collected input patterns. This suggests that the correlating method can give a general indication of which input features will give optimal solutions for classification performance. The GLM approach also gave accuracies of 75% for all unknown patterns and 77.08% for all collected input patterns.

It is to be noted that in general the MLP's average performance for all possible extracted coefficients is better using this data manipulation approach as opposed to other approaches for all possible input patterns. However, the best performance rate remains with the 8^{th} order polynomial fitting method from the summed transient set. It is also to be noted that the polynomial fitting method gives the greatest results using this data manipulation approach with a GLM algorithm.

A question that may be asked is 'Shouldn't the normalised summed, and normalised averaged transient sets give the same results?' Although, the transient characteristics are exactly the same, the scaling between the two sets is different by a factor of 8.

This difference in scaling is linear, but can cause the proportionality to be diluted, from the characterising coefficient extraction. Also a difference in scaling can cause the search directions to change during training in the classification process. Such dilutions of this linear scaling can cause different output results as illustrated from the results. This indicates that the two different approaches can be used as separate transient handling methods.

4.10.7 Conclusion on the selection of the most prominent data manipulation technique and classification algorithm for movement classifications

It has been found that any manipulation technique of the captured 8 transients has the potential to yield high classification rates. However, only one approach can be selected to give an optimal performance, which in this case is a summation of the eight captured transients. By formulating a simple summation of the transient, then this saves processor capacity and time for the formulation of the input vector.

The characterisation of the transients or developed transient can be examined through the correlation coefficients between input coefficients and output classification. The value of these coefficients can give a general indication of which input features will give a good classification performance; however they may not give the solution for an optimal characterisation and classification performance, although for optimal solutions the coefficient values remain large.

For the application of this type of classification with the quality of the captured inputs, both GLM and MLP approaches can be used to generate acceptable performances. The results indicate that the construction of the input to output data set is predominantly linear, thus either method can be used dependent upon the system accuracy.

Looking directly at the system accuracy for both measures, (i.e. unknown input patterns and all collected input patterns) need to be considered as a direct indicator to the performance of the characterisation method, as opposed to the correlation coefficients.

Manipulating the captured filtered transients through the different manipulation techniques, and characterising through the three prominent approaches for varying numbers of coefficients and then classifying using a GLM and MLP with early stopping gives results illustrated below.

4.11.1 Results for MLP and GLM classifications using a Partial Correlation characterisation for transient manipulation techniques to determine whether the legs are bent or straight during the backswing

PC interpretation of summed transient	2 inputs	3 inputs	4 inputs	5 inputs	6 inputs	7 inputs	8 inputs	9 inputs	10 inputs
GLM test - trained with validation + train	79.17	75	70.83	62.5	70.83	70.83	66.67	62.5	62.5
GLM all - trained with validation + train	68.06	67.36	66.67	65.28	68.75	71.53	69.44	70.83	70.14
MLP test - trained with train	62.5	62.5	75	75	75	66.67	62.5	62.5	70.83
MLP all - trained with train	75.69	69.44	80.56	73.61	73.61	80.56	81.25	77.78	75
Nodes for MLP from validation	47	1	18	1	1	2	21	20	1
Weight decay from validation for MLP 1*10^	-9	-6	-9	-1	-1	-2	-2	-2	-9
Iterations for early stopping for MLP from validation	50	350	50	150	150	50	50	50	50
MLP test - trained with validation + train	62.5	66.67	58.33	66.67	66.67	41.67	45.83	54.17	75
MLP all - trained with validation + train	79.86	70.14	84.72	72.92	73.61	74.31	86.81	88.19	79.17

Table 4.11 - Classification performances for a discrimination of whether the legs are bent or straight using a Partial Correlation characterisation from a summed transient.

PC interpretation of summed normalised transient	2 inputs	3 inputs	4 inputs	5 inputs	6 inputs	7 inputs	8 inputs	9 inputs	10 inputs
GLM test - trained with validation + train	70.83	58.33	62.5	70.83	75	75	75	70.83	70.83
GLM all - trained with validation + train	66.67	66.67	69.44	71.53	72.92	75	75	75.69	75
MLP test - trained with train	66.67	54.17	70.83	58.33	66.67	75	58.333	70.83	62.5
MLP all - trained with train	70.14	73.61	73.61	79.86	77.78	79.86	77.083	72.22	77.08
Nodes for MLP from validation	53	10	3	60	34	2	10	1	2
Weight decay from validation for MLP 1*10^	-5	-3	-1	-5	-3	-1	-1	-1	-1
Iterations for early stopping for MLP from validation	50	50	50	50	50	50	200	50	50
MLP test – trained with validation + train	58.33	58.33	58.33	62.5	62.5	66.67	66.67	70.83	62.5
MLP all - trained with validation + train	68.75	78.47	74.31	82.64	85.42	73.61	94.44	74.31	81.25

Table 4.12 - Classification performances for a discrimination of whether the legs are bent or straight using a Partial Correlation characterisation from a summed normalised transient.

PC interpretation of averaged norm transient	2 inputs	3 inputs	4 inputs	5 inputs	6 inputs	7 inputs	8 inputs	9 inputs	10 inputs
GLM test - trained with validation + train	75	62.5	58.33	70.83	70.83	75	75	75	66.67
GLM all - trained with validation + train	70.14	68.75	68.75	69.44	72.22	73.611	74.31	73.61	72.22
MLP test - trained with train	58.33	70.83	70.83	70.83	66.67	58.33	75	54.17	70.83
MLP all - trained with train	63.89	76.39	81.25	82.64	79.17	81.25	77.78	79.86	76.39
Nodes for MLP from validation	35	3	6	15	57	15	1	30	1
Weight decay from validation for MLP 1*10^	-5	-5	-1	-5	-9	-2	-1	-1	-1
Iterations for early stopping for MLP from validation	50	50	50	50	50	50	100	100	50
MLP test - trained with validation + train	66.67	70.83	70.83	54.17	45.83	62.5	75	62.5	70.83
MLP all - trained with validation + train	74.31	75.64	84.03	84.72	82.64	83.33	76.39	93.75	75.69

Table 4.13 - Classification performances for a discrimination of whether the legs are bent or straight using a Partial Correlation characterisation from an averaged normalised transient.

4.11.2 Results for MLP and GLM classifications using a polynomial fitting characterisation for transient manipulation techniques to determine whether the legs are bent or straight during the backswing

PF interpretation of summed transient	2 inputs	3 inputs	4 inputs	5 inputs	6 inputs	7 inputs	8 inputs	9 inputs	10 inputs
GLM test - trained with validation + train	75	75	75	75	66.67	70.83	70.83	66.67	62.5
GLM all - trained with validation + train	65.92	68.06	70.83	70.83	69.44	68.75	72.92	72.92	70.83
MLP test - trained with train	58.33	70.83	70.83	70.83	75	45.83	83.33	70.83	70.83
MLP all - trained with train	70.83	73.61	72.92	69.44	72.22	72.92	82.639	72.22	72.22
Nodes for MLP from validation	55	50	10	1	10	14	39	1	2
Weight decay from validation for MLP 1*10^	-5	-9	-2	-1	-9	-8	-1	-9	-1
Iterations for early stopping for MLP from validation	50	50	50	100	50	50	300	150	50
MLP test - trained with validation + train	58.33	66.67	66.67	66.67	66.67	50	66.67	58.33	58.33
MLP all - trained with validation + train	74.31	81.25	76.39	65.97	76.39	75	89.58	70.14	67.36

Table 4.14 - Classification performances for a discrimination of whether the legs are bent or straight using a Polynomial Fitting characterisation from a summed transient.

PF interpretation of summed normalised transient	2 inputs	3 inputs	4 inputs	5 inputs	6 inputs	7 inputs	8 inputs	9 inputs	10 inputs
GLM test - trained with validation + train	62.5	70.83	79.17	87.5	83.33	79.17	83.33	91.67	79.17
GLM all - trained with validation + train	58.33	60.42	70.83	74.31	77.08	75	75.69	83.33	79.17
MLP test - trained with train	58.33	62.5	75	54.17	75	70.83	70.833	75	62.5
MLP all - trained with train	58.33	73.61	75.69	73.61	79.17	84.03	77.083	73.61	81.25
Nodes for MLP from validation	1	3	1	50	40	33	14	2	50
Weight decay from validation for MLP 1*10^	-4	-5	-7	-2	-3	-9	-4	-2	-5
Iterations for early stopping for MLP from validation	50	500	50	50	50	50	50	50	50
MLP test - trained with validation + train	70.83	66.67	70.83	70.83	70.83	75	75	62.5	75
MLP all - trained with validation + train	63.89	68.06	73.61	81.25	79.17	85.42	88.19	70.83	87.5

Table 4.15 - Classification performances for a discrimination of whether the legs are bent or straight using a Polynomial Fitting characterisation from a summed normalised transient. The blue figures represent the optimal performance from the examined algorithm.

PF interpretation of averaged norm transient	2 inputs	3 inputs	4 inputs	5 inputs	6 inputs	7 inputs	8 inputs	9 inputs	10 inputs
GLM test - trained with validation + train	75	75	87.5	87.5	79.17	91.67	91.67	87.5	91.67
GLM all - trained with validation + train	70.14	65.28	77.08	77.08	76.39	77.78	77.08	79.17	80.56
MLP test - trained with train	70.83	62.5	75	62.5	70.83	79.17	54.167	66.67	66.67
MLP all - trained with train	70.83	72.22	79.86	71.53	83.33	75.69	74.306	73.61	76.39
Nodes for MLP from validation	60	57	2	1	6	3	25	10	55
Weight decay from validation for MLP 1*10^	-1	-6	-2	-8	-9	-3	-4	-3	-3
Iterations for early stopping for MLP from validation	50	50	100	500	100	50	50	50	50
MLP test - trained with validation + train	62.5	75	75	62.5	70.83	70.83	70.83	58.33	66.67
MLP all - trained with validation + train	70.83	76.39	79.86	71.53	81.94	75	84.72	70.83	79.86

Table 4.16 - Classification performances for a discrimination of whether the legs are bent or straight using a Polynomial Fitting characterisation from an averaged normalised transient.

4.11.3 Results for MLP and GLM classifications using an SVD characterisation for transient manipulation techniques to determine whether the legs are bent or straight during the backswing

SVD interpretation of summed transient	2 inputs	3 inputs	4 inputs	5 inputs	6 inputs	7 inputs	8 inputs	9 inputs	10 inputs
GLM test - trained with validation + train	70.83	75	79.17	79.17	79.17	83.33	83.33	79.17	83.33
GLM all - trained with validation + train	63.89	64.58	70.83	67.36	68.06	68.06	68.06	68.75	70.83
MLP test - trained with train	66.67	58.33	75	87.5	62.5	79.17	83.33	79.17	83.33
MLP all - trained with train	65.97	77.78	70.83	70.83	79.86	72.92	76.39	70.14	75
Nodes for MLP from validation	1	65	1	1	30	1	1	1	2
Weight decay from validation for MLP 1*10^	-1	-4	-5	-4	-1	-5	-9	-4	-3
Iterations for early stopping for MLP from validation	50	50	50	50	100	50	100	50	50
MLP test - trained with validation + train	58.33	70.83	70.83	70.83	75	70.83	75	79.17	75
MLP all - trained with validation + train	64.58	84.72	68.75	70.83	95.83	72.92	73.61	72.22	75

Table 4.17 - Classification performances for a discrimination of whether the legs are bent or straight using a SVD characterisation from a summed transient.

SVD interpretation of summed norm transient	2 inputs	3 inputs	4 inputs	5 inputs	6 inputs	7 inputs	8 inputs	9 inputs	10 inputs
GLM test - trained with validation + train	66.67	66.67	66.67	66.67	66.67	66.67	66.67	70.83	58.33
GLM all – trained with validation + train	69.44	69.44	68.75	70.83	70.14	69.44	70.14	72.22	70.83
MLP test - trained with train	70.83	66.67	58.33	58.33	58.33	54.17	50	62.5	66.67
MLP all – trained with train	75.69	72.92	81.94	84.72	86.81	85.42	71.53	75	84.03
Nodes for MLP from validation	28	1	15	21	20	12	1	1	26
Weight decay from validation for MLP 1*10^	-6	-1	-1	-1	-2	-3	-5	-9	-1
Iterations for early stopping for MLP from validation	100	450	250	100	100	50	50	50	300
MLP test - trained with validation + train	70.83	66.67	70.83	58.33	62.5	45.83	50	66.67	58.33
MLP all – trained with validation + train	83.33	69.44	95.14	93.06	93.75	90.28	71.53	76.39	93.06

Table 4.18 - Classification performances for a discrimination of whether the legs are bent or straight using a SVD characterisation from a summed normalised transient.

SVD interpretation of averaged norm transient	2 inputs	3 inputs	4 inputs	5 inputs	6 inputs	7 inputs	8 inputs	9 inputs	10 inputs
GLM test - trained with val+train	58.33	54.17	58.33	62.5	62.5	70.83	70.83	54.17	66.67
GLM all – trained with val+train	65.28	63.89	63.19	63.89	67.36	68.06	69.44	68.06	67.36
MLP test - trained with train	62.5	58.33	50	41.67	50	45.83	54.17	45.83	62.5
MLP all – trained with train	71.53	76.39	75.69	81.25	81.94	81.94	83.33	82.64	78.47
Nodes for MLP from val	59	40	5	48	6	30	6	15	5
Weight decay from val for MLP 1*10^	-6	-9	-2	-1	-1	-1	-4	-1	-6
Iterations for early stopping for MLP from val	50	50	50	300	250	200	50	150	50
MLP test - trained with val+train	58.33	66.67	45.83	45.83	54.17	45.83	54.17	54.17	58.33
MLP all – trained with val+train	70.14	82.64	76.39	90.97	88.89	90.97	87.5	92.36	85.42

Table 4.19 - Classification performances for a discrimination of whether the legs are bent or straight using a SVD characterisation from an averaged normalised transient.

The above tables represent the classification performances for the three predominant characterisations. The GLM performances are illustrated in green for both unknown input patterns and all of the patterns respectively, trained with the validation and

training data. The results in black illustrate the results for a trained MLP optimised using the validation data. The results in red illustrate the performances of the MLP trained with the optimised parameters using both the trained and validation data. The reason why training results are illustrated is so that it can be used as a secondary measure. This secondary measurement will only be used if two or more methods show similar results for the unknown data accuracies.

The results show that the optimal characterisation gives a success rate of 91.67% for unknown patterns given to the GLM algorithm to classify whether the legs are bent or straight, using a 9^{th} order polynomial fitting algorithm from a summed normalised transient.

Looking at the performances from both methods, it can be seen that the GLM classification method out performs the MLP algorithm in classifying the presented input vector of different quality. It is therefore fair to suggest that the GLM algorithm will again outperform the MLP in classifying the flaws of different quantity. This indicates that linear classification is more suited to this type of mapping to non-linear methods.

GLM methods have also been selected as the classification algorithm due to the fact that the input data patterns are identical to the previous classification, although the output pattern will change slightly. Thus the previous results indicate the support for a GLM approach.

4.11.4 Results for GLM classifications using the three main prominent characterisations on the various transient manipulation techniques for a classification on whether the planted foot comes off the surface or not

PC interpretation of summed transient	2 inputs	3 inputs	4 inputs	5 inputs	6 inputs	7 inputs	8 inputs	9 inputs	10 inputs
GLM test - trained with validation + train	75	75	66.67	66.67	70.83	70.83	70.83	70.83	70.83
GLM all - trained with validation + train	81.94	84.72	83.33	84.03	85.42	85.42	85.42	84.72	84.72

PC interpretation of summed norm transient	2 inputs	3 inputs	4 inputs	5 inputs	6 inputs	7 inputs	8 inputs	9 inputs	10 inputs
GLM test - trained with validation + train	62.5	66.67	62.5	62.5	62.5	66.67	66.67	66.67	66.67
GLM all - trained with validation + train	70.14	82.64	79.86	78.47	79.17	79.17	79.17	81.25	81.25

PC interpretation of averaged norm transient	2 inputs	3 inputs	4 inputs	5 inputs	6 inputs	7 inputs	8 inputs	9 inputs	10 inputs
GLM test - trained with validation + train	54.17	66.67	66.67	62.5	62.5	62.5	58.33	62.5	58.33
GLM all - trained with validation + train	68.06	81.25	81.94	78.47	78.47	79.86	79.17	79.86	80.56

PF interpretation of summed transient	2 inputs	3 inputs	4 inputs	5 inputs	6 inputs	7 inputs	8 inputs	9 inputs	10 inputs
GLM test - trained with validation + train	95.83	91.67	95.83	95.83	87.5	95.83	87.5	87.5	83.33
GLM all - trained with validation + train	86.11	85.42	86.81	88.19	87.5	88.89	88.19	89.58	90.28

PF interpretation of summed norm transient	2 inputs	3 inputs	4 inputs	5 inputs	6 inputs	7 inputs	8 inputs	9 inputs	10 inputs
GLM test - trained with validation + train	66.67	58.33	62.5	62.5	75	75	79.17	83.33	79.17
GLM all - trained with validation + train	59.03	69.44	66.67	71.53	79.86	78.47	84.72	86.11	84.72

PF interpretation of averaged norm transient	2 inputs	3 inputs	4 inputs	5 inputs	6 inputs	7 inputs	8 inputs	9 inputs	10 inputs
GLM test - trained with validation + train	41.67	50	54.17	62.5	66.67	70.83	79.17	75	83.33
GLM all - trained with validation + train	50	69.44	63.19	69.44	79.86	77.78	84.72	86.11	88.19

SVD interpretation of summed transient	2 inputs	3 inputs	4 inputs	5 inputs	6 inputs	7 inputs	8 inputs	9 inputs	10 inputs
GLM test - trained with validation + train	91.67	87.5	87.5	83.33	83.33	91.67	91.67	87.5	83.33
GLM all - trained with validation + train	92.36	92.36	92.75	92.36	92.36	93.75	93.75	93.75	95.14

SVD interpretation of summed norm transient	2 inputs	3 inputs	4 inputs	5 inputs	6 inputs	7 inputs	8 inputs	9 inputs	10 inputs
GLM test - trained with validation + train	54.17	62.5	62.5	58.33	87.5	91.67	91.67	91.67	91.67
GLM all - trained with validation + train	66.67	70.83	72.22	70.83	87.5	90.28	90.97	90.97	92.36

SVD interpretation of averaged norm transient	2 inputs	3 inputs	4 inputs	5 inputs	6 inputs	7 inputs	8 inputs	9 inputs	10 inputs
GLM test - trained with validation + train	54.17	62.5	62.5	62.5	75	79.17	75	75	75
GLM all - trained with validation + train	69.44	71.53	72.22	70.14	82.64	89.58	87.5	87.5	83.33

Table 4.20 - GLM classification to interpret whether the foot remains planted on the surface for various data manipulation techniques and the prominent characterisation methods.

The results illustrated in the above table show that a 7^{th} order polynomial method is the most suitable method for classification of the presented data manipulated as a summed transient set. Accuracies show system performance of 95.83% to classify whether the foot comes off the surface during the back swing. This indicates that this type of classification has far more dominant input characteristics as opposed to the previous classification flaw. This is to be expected due to the large quantity of load

shift for the foot leaving the surface. However, using direct force magnitude data instead of this classification approach, will predict whether the foot comes off the surface or not 100% of the time, by simply looking at the loading conditions on the right heel throughout the swing. This will be the preferred method used in the commercial system; however, the research demonstrates the capabilities of this approach for something that cannot be determined through other direct force means.

4.11.5 Results for GLM classifications using the three main prominent characterisations on the various transient manipulation techniques for a classification on whether the orbit angle is correct or not

PC interpretation of summed transient	2 inputs	3 inputs	4 inputs	5 inputs	6 inputs	7 inputs	8 inputs	9 inputs	10 inputs
GLM test - trained with validation + train	62.5	41.67	41.67	58.33	58.33	62.5	50	58.33	54.17
GLM all - trained with validation + train	52.78	51.39	49.31	58.33	65.97	63.89	61.81	61.11	62.5

PC interpretation of summed norm transient	2 inputs	3 inputs	4 inputs	5 inputs	6 inputs	7 inputs	8 inputs	9 inputs	10 inputs
GLM test - trained with validation + train	54.17	58.33	58.33	54.17	54.17	54.17	54.17	50	50
GLM all - trained with validation + train	52.78	54.86	61.11	61.11	60.42	61.11	63.89	62.5	63.19

PC interpretation of averaged norm transient	2 inputs	3 inputs	4 inputs	5 inputs	6 inputs	7 inputs	8 inputs	9 inputs	10 inputs
GLM test - trained with validation + train	45.83	50	54.17	41.67	33.33	37.5	45.83	41.67	45.83
GLM all - trained with validation + train	51.39	54.86	57.64	56.94	56.25	59.72	59.03	59.03	57.64

PF interpretation of summed transient	2 inputs	3 inputs	4 inputs	5 inputs	6 inputs	7 inputs	8 inputs	9 inputs	10 inputs
GLM test - trained with validation + train	50	54.17	50	50	50	41.67	50	45.83	37.5
GLM all - trained with validation + train	53.47	52.08	52.78	55.56	58.33	59.72	61.81	62.5	65.97

PF interpretation of summed norm transient	2 inputs	3 inputs	4 inputs	5 inputs	6 inputs	7 inputs	8 inputs	9 inputs	10 inputs
GLM test - trained with validation + train	45.83	50	66.67	50	66.67	62.5	62.5	54.17	54.17
GLM all - trained with validation + train	50	61.81	66.67	56.25	63.19	61.11	59.03	56.25	61.81

PF interpretation of averaged norm transient	2 inputs	3 inputs	4 inputs	5 inputs	6 inputs	7 inputs	8 inputs	9 inputs	10 inputs
GLM test - trained with validation + train	50	62.5	62.5	58.33	62.5	54.17	66.67	54.17	62.5
GLM all - trained with validation + train	53.47	65.97	65.28	61.11	60.42	59.03	59.03	62.5	69.44

SVD interpretation of summed transient	2 inputs	3 inputs	4 inputs	5 inputs	6 inputs	7 inputs	8 inputs	9 inputs	10 inputs
GLM test - trained with validation + train	37.5	45.83	41.67	41.67	41.67	50	58.33	58.33	58.33
GLM all - trained with validation + train	52.08	52.77	51.39	52.08	49.31	54.86	59.72	59.72	59.03

SVD interpretation of summed norm transient	2 inputs	3 inputs	4 inputs	5 inputs	6 inputs	7 inputs	8 inputs	9 inputs	10 inputs
GLM test - trained with validation + train	58.33	54.17	54.17	58.33	58.33	58.33	50	50	58.33
GLM all - trained with validation + train	59.72	61.81	60.42	67.36	65.97	65.28	63.19	63.19	65.28

SVD interpretation of averaged norm transient	2 inputs	3 inputs	4 inputs	5 inputs	6 inputs	7 inputs	8 inputs	9 inputs	10 inputs
GLM test - trained with validation + train	54.17	54.17	54.17	54.17	54.17	62.5	54.17	54.17	50
GLM all - trained with validation + train	58.33	59.03	59.72	59.03	59.72	61.81	65.97	66.67	62.5

Table 4.21 - GLM classification method for various data manipulation techniques and characterisation coefficients to interpret whether or not the orbit angle is correct during the backswing.

The results in Table 4.21 shows that the optimal classifying approach for the correct orbit angle is a 4^{th} order polynomial fitting characterisation of a summed normalised transient giving a classification accuracy of 66.67%.

It is also important to be aware that the polynomial fitting algorithm is the most effective method in characterising any form of input pattern. This is supported by its consistent performance over all examinations, added to this through the delivery of the greatest classification performances for all of the flaws examined.

These results show that the most sensitive movement on the surface is whether or not the planted foot comes off the surface during the backswing and the least sensitive is that of the correct orbit angle. The reason why this is so is due to the fact the angle of the club has very low influence over the loading variances on the feet, and hence can be drowned out through more dominant loading conditions from other flaws. This can be supported with that of the model and the analysis of the real data using the taxonomy of the input data.

Taking the average of all of the normalised summed captured transients in one class, should give the mean transient response for that particular class. This can also be generated from the model for a particular class, through a determination of the expected loads and sensory voltages at the discrete points under the surface, through the use of the calibration polynomial and the Navier model of deformation.

Examining the differences between an ideal backswing and a swing with one error, should indicate the effect of that error on the input transients. The magnitude of the difference should then indicate the resultant sensitivity of that particular error. This is demonstrated in figure 4.32.

Measured average transients in the class Modelled transients in the class

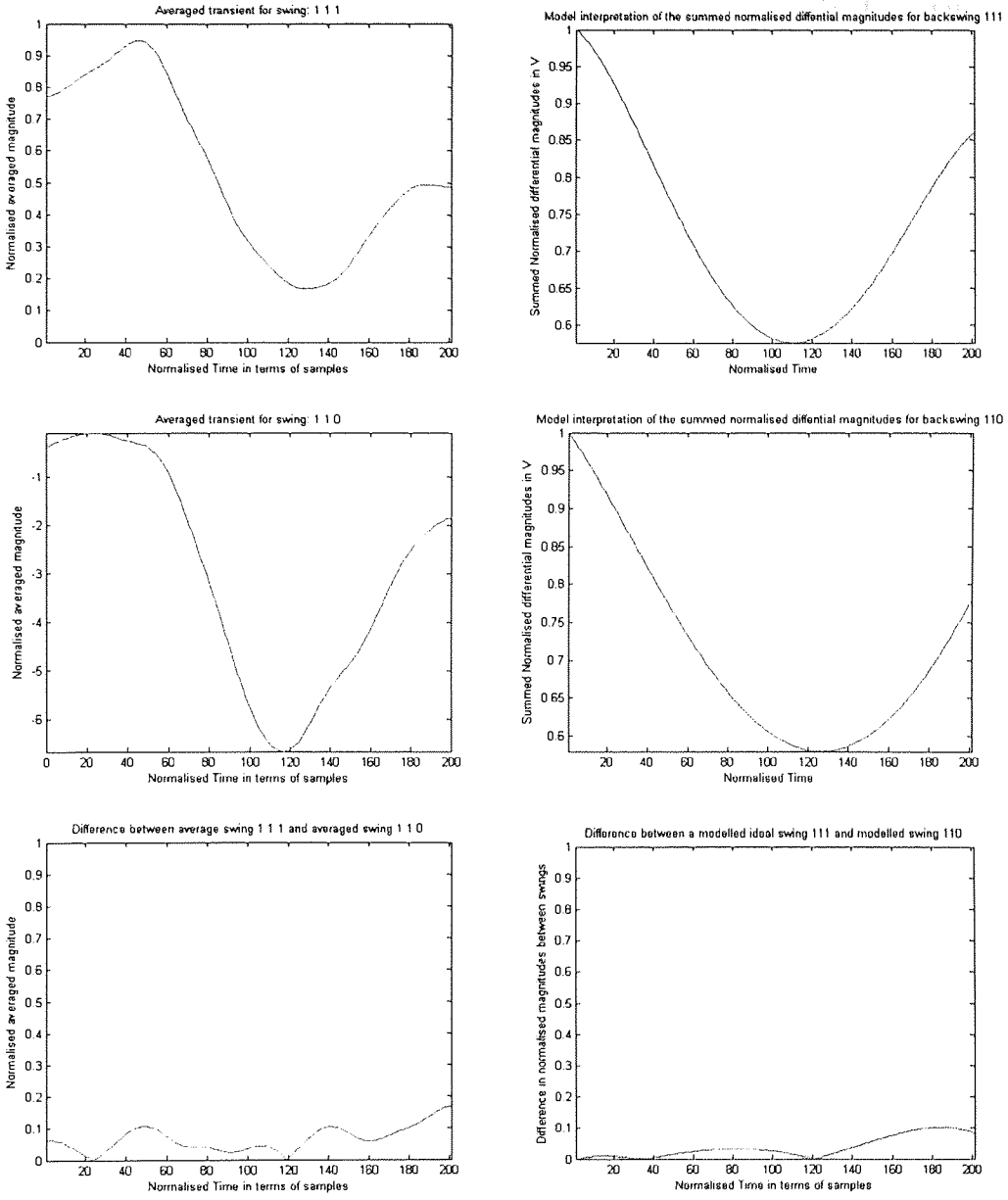

Figure 4.32 (top left) - Averaged ideal backswing (111) from the normalised summed transients from the real data. (top right) - Summed normalised transients that the model predicts. (middle left) - Averaged normalised summed transient for a swing with an incorrect orbit (110). (middle right) - Summed normalised transient set from the model. (bottom left) - Difference between an ideal swing and one with an incorrect orbit from the real data. (bottom right) - Difference between an ideal swing and a swing with an incorrect orbit from the model.

It shows that the figures on the right of the model are similar to those of the real data on the left. For all other taxonomies see Appendix D.8. The differences between the ideal swing 111 and a swing with an incorrect orbit 110 gives an integral of the

difference from the real transients of: 12.92. Similarly the model suggests an integral of the difference of: 7.3. From this analysis it was found that: (Codes from table 4.2)

Order the model suggests for sensitivity from lowest to highest:
011 legs straight 3.7
110 orbit angle incorrect 7.3
101 foot off the surface 10.4

Order the real data suggests for sensitivity from lowest to highest:
110 orbit angle incorrect 12.9
011 legs straight 23.8
101 foot off the surface 24.2

Order the classification algorithm interprets the sensitivity of the movement
110 orbit angle incorrect 66.67% for unknown patterns, 66.67% for all patterns
011 legs straight 91.67% for unknown patterns, 83.33% for all patterns
101 foot off the surface 95.83% for unknown patterns, 88.89% for all patterns

This shows that the taxonomy of the real data is descriptive of the success rate of the movement class. This indicates that this approach can be used as an initial investigation into the sensitivities of various movements for various other aspects of the golf swing, assuming that real data has been captured.

It has been shown that it is possible to discriminate between various movements on the surface, through an examination of the captured transients. This indicates that this method can determine meaningful movements on the surface without the use of a vision system and without the use of human prognosis or complex image recognition techniques.

Vision systems, are well known as accurate systems for the measurement of human body movement. The Vicon system is one of the world's most accurate vision measurement systems, and can measure human movement at a reflective marker up to a maximum error of 1mm. However, such a system can cost up to £10k for each

camera used, (typically this will be from a minimum of 3), with a dedicated signal conditioning unit and processor hardware costing in the region of £5k.

Although the RFSES with associated method described can not classify movements up to these levels of accuracy, it is still quite effective at classifying different bold movements. This is in fact more useful for this application, as a classification of movement is more meaningful than a complex movement profile, with thousands of measurements to digest to determine what needs to be done to enhance performance.

It has also been found that that a coupling of the transients through a summation or averaging of normalised or non-normalised transients is optimal for system performance and processor capacity. It has also been determined that the most effective way of handling various classifications of the swing is to classify each possible error in the swing individually and to assign an optimal characterisation and classification algorithm to it.

The characterisation of the combined transient is more representative through means of SVD, Polynomial Fitting and Partial Correlation, than any other time series describing method and thus giving greater classification performances. For the examination of various other flaws or movements in the swing these characterisation methods need to be investigated for various numbers of extracted coefficients.

The MLP or GLM approach can be used as means for classification from the characterisation, with the GLM model outperforming the MLP method. Once an MLP has been trained using early stopping, the algorithm can also be tested through the use of the optimal derived parameters, from the validation data and trained using both the validation and training set to determine whether or not this enhances the overall system performance. The GLM approach is a useful algorithm to determine what the optimal characterisation and number of coefficients is, due to the fact that the training of the GLM algorithm is far quicker that that of the MLP with early stopping. This supports the exploration of which are the most predictive features, which can then be used for the MLP.

CHAPTER 5

Discussion, conclusion and further work

This chapter reviews the main functions and methods required to develop a golf driving mat that can interpret the loading distribution at the feet and to classify various movements on the surface. This chapter is to also investigate the way forward for more complex operations using this technology.

5.1 Review of the main functions of this technology for a golf driving mat

For the design of the golf mat the surface and structure must have dimensions equal to or be greater than 510mm for a shoulder width and 285mm for a foot size taken from the anthropometrics of the body. Also for a standard commercial golf mat the dimensions must not exceed (1380x1380)mm. Also there are limitations on the thickness which needs to be no greater than 20mm. This has to include the sensing elements in their operating range, the base and the surface itself. For this the surface is suspended above the base by 10mm by a steel frame of 30x10mm to increase the damping of the system. An aluminium surface of dimensions (850x600x6)mm was selected to produce maximum repeatability and to withstand the maximum loading of 150kg to allow for peak forces during the golf swing.

The sensing elements that have been selected are non-linear reflective optical sensors that can be integrated within the limitations of the surface and structure. They fulfil the required criteria compared with other possible elements. The optimal number of sensor elements has found to be 8. The research has also shown that high system accuracies can be achieved through the use of this few sensing points. The position of the elements has been determined by an inverse solution to the Navier model and genetic search algorithm to interpret positions of elements with equal sensitivity.

The data acquisition device is to be integrated within the surface consisting of an 8 channel device with a 10 bit resolution and sampling frequency of 1kHz with a USB digital communication bus.

It has been found that an MLP with early stopping is an optimal regressive method to interpret the position of the load on the surface. This will be for the interpretation of the feet position on the surface at the stance position. Once the position of the feet has

been calculated, it is then possible to interpret the load magnitude at the toes and heels of the feet at the set positions. This is optimally accomplished through the use of a regularised regressive MLP, as the preferred method over a linear approach.

The results for both the position and magnitude of the stimuli indicate that such a system can compete fairly well with other commercial devices (see end of section in 3.5.8). However, it has been shown that these systems have the ability to generate loading evaluations at various parts of the feet on the same surface, where competitive devices would require two or more systems or processing capability to provide a similar function.

On the basis of novelty, this research demonstrates methods applied to RFSES that can determine attributes of the loading conditions that other force systems can not. For example the system can determine the height of the subject or the type of upper body movement on the surface through the analysis of the weight distribution and weight shift at the feet through time.

The research also demonstrates that the degree of sensitivity of movement on the surface that can be described through the use of the model, or through the use of the taxonomy between the transients of the flaw to those without that particular flaw. This should illustrate which flaws are possible to classify and those which aren't.

This classification function arises from an analysis of the evolution of the transients through time, when affected by the changing foot loads on the surface. This evolution holds information relating to the type of motion on the surface that can be represented by various coefficients through the use of time series methods. It has been found that a collection of the transients through the means of summation is the most effective approach for accuracy and a reduction in the dimension of input pattern and processing time.

It has also been found that optimal classification performances can be derived through a break down of the problem into various characterisation and classification algorithms with respect to each particular flaw as opposed to only one algorithm to solve for every possible classification.

The best representations of the time series have been found to be Polynomial Fitting methods when coupled with possible classification algorithms. For regressive system responses, the regularised MLP approach was found to be the most effective. For classification outputs, it was found that either regularised MLP or GLM methods would give acceptable results. In order to locate optimal characterisations it was found that the GLM approach would be most suited to reduce the training time required using a regularised MLP.

In hindsight, on completion of the research, it was noted that Bayesian techniques can be applied to MLP networks. MLP methods can be applied to all the required generalisations in the research provided that the size of the dataset is large enough. It is generally agreed that unregularised MLP networks should be trained with at least 5-10 times as many patterns as weights (approximately the number of inputs times the number of hidden units times the number of outputs).

The number of training patterns that could be captured during the research was limited due to the time taken and subject's effort to record specific human movements for large datasets. For example, in the prediction of the height of a subject on the surface, 38 different subjects were used to collect the training pattern set. Gathering sufficient quantities of data to reliably train an MLP would be an enormous task.

Early stopping was used to regularise the MLP networks on the small training datasets used. However, given that sometimes there were more weights than training patterns, many of the results for the MLP were flawed.

If this research was to be replicated for such cases, Bayesian techniques can be applied to MLP approaches, as Bayesian techniques give better generalisations regardless of the uncertainty in the training dataset, and also can generalise without the use of early stopping rules.

At the outset we hoped to classify various movements on the surface and to avoid the need for a costly vision system. We found that it is possible to classify various movements on the surface with accuracies in the region of 90%. Such a system can give automated instantaneous feedbacks on the possible flaws during the swing that

vision systems may not be able to provide. The system is easily moved and complex optics and conditioning hardware does not need to be set up. For other applications researched and using the discussed methods see Appendix E.1-E3.

5.2 Other applications that now can be investigated using dynamic sensing

The illustrated methods in this research have shown that it possible to provide a wider range of applications, for example in the analysis of gait or running performance on a treadmill. The movements of the body on the surface on a treadmill would result in the moving of the loading coordinates and a changing of the loading magnitudes a category [8] activity (see Chapter 1.4).

Using the methods described in Chapters 3, 4 and 5 it is therefore possible to analyse the transients of the elements under the surface to determine, or classify between various types of gait or running posture. As movement on a treadmill is cyclic it is possible to window the meaningful transients between the start and end of the cycle and then analyse this window, using the predominant characterisation methods described. A classification or regressive response about the movement or loading condition can then be described, assuming that the movement or loading has a significant effect on the transients that would fundamentally change the characterisation vector. This would provide a self contained system that could indicate the underlying problems relating to the gait of the patient or athlete that the naked eye could fail to see.

To provide a similar function using conventional means a load platform would be required to interpret the complex loading profiles on the surface, that would then need to be analysed further by the operator. For the type of upper body movement or gait a video or motion tracking system with complex data recognition software would then be required in a darkened room to classify the type of movement.

Finally, the methods and techniques described in the thesis can be used to weigh items on conveyor belts in the manufacturing industry. A typical problem in the canning industry is to weigh tin lids while they move along a conveyor belt. A substrate or

glue is placed on the lid so that it can be bonded to the outside of the tin; however there is no conventional way of describing the quantity of substrate on the lid. Typical methods that have been examined are vision systems, but these methods cannot weigh or determine the quantity of substrate on the tin lid. Array-type tactile methods have been applied but these cannot determine the load on various tin lids as they are moving along the belt.

The methods described make it possible to develop a system or technique to interpret the fixed loading magnitudes moving along the surface using dynamic sensing, through an analysis of the transients in the time domain. It is also possible to combine the function of an array sensor with these characterisation, classification and regressive functions to provide a more robust and accurate system; however this would come at a greater cost to that of the RFSES.

References

Abdel-Aziz Y.I. and Karara H.M. (1971). Direct linear transformation from comparitor coordinates in object-space coordinates in close range photogrammetry. Proceedings from ASPUI Symposium on close-range photogrammetry, Am soc Photogrammetry, pp. 1-19.

Abernethy B, Neal R.J., Moran M.J. (1990). Expert-novice differences in muscle activity during the golf swing. Science and Golf (Edited by A.J. Cochran). London: E & FN Spon. pp. 54-60.

Abraham A. (2003). Meta learning evolutionary artificial neural networks. Neurocomputing. Vol. 56 (2004), pp. 1-38

Ando S., Shinoda H., Yonenaga A., Terao J. (2001). Ultrasonic six axis deformation sensing. IEEE Transactions on ultrasonics, ferroelectrics and frequency control. Vol. 48, no. 4, pp. 1031-1045.

Banim R.S., Brett P.N., Tierney M.J. and Hinds M. (2003). Application of inverse methods to temperature measurement in internal mixers. Proceedings of the Institution of Mechanical Engineers, Vol. 217, Part E: J. Process Mechanical Engineering, pp. 295-306.

Barber J. (Dec 1978), Jerry Barber explains his unorthodox swing theories, Golf Digest, Vol. 29, no. 12, pp. 131-137.

Barrentine S.W., Fleisig G.S. and Johnson H. (1994). Ground reaction forces and torques of professional and amateur golfers. Science and Golf II: Proceedings of the World Scientific Congress of Golf, held at the University of St. Andrews, Scotland, (Edited by M.R. Farrally and A.J Cochran), pp. 33-39.

Begej S. (1988). Planar and finger shaped tactile sensors for robotic applications. Journal of Robotics and Automation. Vol. 4, no. 5, pp. 472-484.

Bishop, C.M. 1995. Neural networks for pattern recognition. Oxford University Press.

Brett P.N., Li Z. (2000). A tactile sensing surface for artificial neural network based automatic recognition of the contact force position. Proceedings of the Institution of Mechanical Engineers, Part I (Journal of Systems and Control Engineering), Vol. 214, no. I3, pp. 207-15.

Brooks R.J. (2002). Is it a Pendulum, is it a Plane? Mathematical models of putting. Chapter 12, Science and Golf IV: Proceedings of the World Scientific Congress in Golf, held at the University of St. Andrews, Scotland, July 2002, pp. 127-141.

Broomhead, D., King G.P. (1986). Extracting qualitative dynamics from experimental data. Physica D, Vol. 20, pp. 217.

Brown D., Best R., Ball K., Dowlan S. (2002). Age, centre of pressure and clubhead speed in golf. Science and Golf IV: Proceedings of the World Scientific Congress of Golf, held at the University of St. Andrews, Scotland, July 2002, (edited by M.R. Farrally and A.J Cochran), pp. 28-34.

Brugler J.S., Meindl J.D., Plummer J.D., Salisbury P.J., Young W.T. (1969). Integrated electronics for a reading aid for the blind. IEEE J Solid-State Circuits, Vol. SC-4, no. 6, pp. 304-12.

Budney D.R., Bellow D.G. (1990). Evaluation of golf club control by grip pressure measurement. Science and Golf (Edited by A.J. Cochran), pp. 30-35, London: E&FN Spon.

Burden A.M., Grimshaw P.N., Wallace E.S. (1998). Hip and shoulder rotations during the golf swing of sub-10 handicap players. Journal of Sports Sciences, Vol. 16, pp. 165-176.

Cameron A, Daniel R, Durrant-Whyte H. (1988). Touch and motion. IEEE 1988, pp. 1062-1067.

Canepa G, Petrigliano R, Campanella M, De Rossi D. (1998). Detection of incipient object slippage by skin like sensing and neural network processing. IEEE Transactions on systems, man and cybernetics part B cybernetics, Vol. 28, no. 3, pp. 348-356.

Carlsoo S. (1967). A kinetic analysis of the golf swing. J. Sports Med. Phys. Fitness, Vol. 7, pp. 76-82.

Checinski SS, Agrawal AK (1985). Magnetoelastic tactile sensor. Robot Sensors, Tactile Transducers, pp. 229-235.

Chen Z.H., Luo R.C. (1998). Design and implementation of capacitive proximity sensor using microelectomechanical systems technology. IEEE Transactions on Industrial Electronics, Vol. 45, no. 6, pp. 886-894.

Cochran A., Stobbs J. (1968). The search for the perfect swing. Philadelphia, J.B. Lippincott Co.

Cooley J., Tukey J. (1965). An algorithm for the machine calculation of complex Fourier series, Math Comp Vol. 19, pp. 297-301.

Cooper J.M., Bates B.T., Bedi J, Scheuchenzuber J. (1974). Kinematic and kinetic analysis of the golf swing, in Biomechanics IV, University Park Press, Balimore, pp. 298-305.

Cooper M.A.J., Mather J.S.B. (1994). Categorisation of golf swings. Science and Golf II: Proceedings of the World Scientific Congress of Golf, held at the University of St. Andrews, Scotland, (Edited by M.R. Farrally and A.J Cochran), pp. 65-70.

Crosnier J.J. (1985). Grasping systems with tactile sense using optical fibres. Robot Sensors, Tactile Transducers, pp. 209-217.

Dargahi J. (1998). Surface texture measurement by combining signals from two sensing elements of a piezoelectric tactile sensor. Proceedings of SPIE – The International Society for Optical Engineering, Vol. 3376, pp. 122-128.

Dargahi J. (2000). A piezoelectric tactile sensor with three sensing elements for robotic, endoscopic and prosthetic applications. Sensors and Actuators A: Physical, Vol. 80, no. 1, pp. 23-30.

Devore J.L. (1991). Probability and Statistics for Engineering and the Sciences. Third Edition, Publisher Duxbury, Chapter 9, pp. 326-329

Dujardin F.H., Ertaud J.Y., Aucouturier, T, Nguen J, Thomine J.M. (1997). Smoothing technique using Fourier transforms applied to stereometric data obtained from optoelectronic recordings of human gait. Human Movement Science, Vol. 16, pp. 275-282.

Edwards A. (1946). Body sway and vision. Journal of Experimental Psychology, no. 36, pp. 526-535.

Eghtedari F, Morgan C. (1989). A novel tactile sensor for robot applications. Robotica, Vol. 7, pp. 289-295.

Engel J., Chen J., Chang L. (2003). Development of polyimide flexible tactile sensor skin. Journal of Micromechanics and microengineering, Vol. 13 no. 3, May 2003, pp. 359-366.

Fairweather M.M. (2002). A critical examination of motor control and transfer issues in putting. Science and Golf IV: Proceedings of the World Scientific Congress of Golf, held at the University of St. Andrews, Scotland, July 2002, (edited by M.R. Farrally and A.J Cochran), pp. 100-112.

Fischer H, Trapp R (1996). Tactile optical sensor for use in minimal invasive surgery. Health care in the information age, IOS Press and Ohmsha, Chapter 68, pp. 623-629.

Fiorillo A.S. (1997). A piezoresistive tactile sensor. IEEE Transactions on Instrumentation and Measurement, Vol. 46, no. 1, pp. 15-17.

Ghil M., Allen R.M., Dettinger M.D. Ide K., Kondrashov D., Mann M.E., Robertson A., Saunders A., Tian Y., Varadi F. and Yiou P. (2000). Advanced spectral methods for climatic time series. Rev. Geophys.

Guadagnoli, M., Holcomb W., (2002). The efficacy of video feedback for learning the golf swing, Science and Golf IV: Proceedings of the World Scientific Congress of Golf, held at the University of St. Andrews, Scotland, July 2002, (edited by M.R. Farrally and A.J Cochran), pp. 142-150.

Harris G.F., Abu-Faraj Z.U., Wertsch J.J., Abler J.H., Vengsarkar A.S. (1995). Holter type system for study of plantar foot pressures. Biomedical Engineering applications, Basis Communications, Vol. 7, no. 4, pp. 409-415.

Harrison A.J., Atkins R.M. Scott H.J.F (1994). A simple device for measurement of load-bearing forces during walking. Proceedings of the Institution of Mechanical Engineers, Part H (Journal of Engineering in Medicine), Vol. 208, no. H3, pp. 159-162.

Hillis D.W. (1982). High resolution imaging touch sensor. International Journal of Robotics Research, Vol. 1, no. 2, pp. 33-44.

Hosea T.M., Gatt C.J., Galli K.M., Langrana N.A., Zawadsky J.P. (1990). Biomechanical analysis of the golfer's back. Science and Golf (Edited by A.J. Cochran), (London: E - FN Spon) pp. 43-48.

Howard L., Stone J., Fu J., (2001). Real time displacements with Fabry-Perot cavity and a diode laser. Journal of the International Societies for Precision Engineering and Nanotechnology, Vol 25, pp. 321-335.

Hughes W.F. (1979). An introduction to viscous flow. McGraw-Hill, pp.22.

Janacek G. (2001). Practical Time series. Arnold texts in statistics. pp. 33-47, 106-110.

Jayawant B.V., Onori M.A., Watson J.D.McK. (1985). Robot tactile sensing: A new array sensor. Robot Sensors, Tactile Array sensors, pp. 199-205.

Johnson, J.B., Huffman T.R. (1974). Tactile prosthetic device for the denervated hand. Annales de l'Association Internationale pour le Calcul Analogique, pp. 9-10.

Kantz H., Schreiber T., (1997). Non-linear time series analysis. Cambridge Non-linear Science Series 7. pp. 29-32, 202-206.

Kapit W. Macey R.I., Meisam E. (2000). Functional Organization of the nervous system. The Physiology coloring book 2nd Edition 2000, pp. 82-113.

Karhunen K. (1946). Zur Spektraltheorie stochastischer Prozesse. Ann. Acad. Sci. Fennicae, (A)I, no. 34.

Kawahima K. (1987). The biomechanics of golf swing: a Practical application to golf swing by weight transfer loci. Japanese Journal of Golf Science 1(1), pp. 34-40.

King A.A., White R.M. (1985). Tactile sensing array based on forming and detecting an optical image. Sensors and Actuators, Vol. 8 pp. 49-63.

Kinoshita, G. (1983). Multifunctional tactile sensors with multielements for fingers. Proceedings of the 1983 International Conference on Advanced Robotics, Vol. 1, pp. 195-202.

Kinoshita, G. (1984). Tactile sensor with Hall IC. Transactions of the Society of Instrument and Control Engineers, Vol. 20, no. 2, Feb. 1984, pp. 181-183.

Klema V.C. and Laub A.J. (1980). The singular value decomposition: its computation and some applications. IEEE Transactions on Automation and Control, Vol. AC-25, pp. 164-176.

Koenig G., Tamres M., Mann R.W. (1994) The biomechanics of the shoe-ground interaction in golf. Science and Golf II: Proceedings of the World Scientific Congress

of Golf, held at the University of St. Andrews, Scotland, (Edited by M.R. Farrally and A.J Cochran), pp. 40-45.

Komatsubara M., Yasui M., Shinoda, H. ando, S. (1993). A study on ultrasonic emission tactile sensor. SICE '93. Proceedings of the 32nd SICE Annual Conference. International Session (IEEE Cat. No.93 TH 0575-1), pp. 1313-1316.

Lampsa M.A. (1975). Maximising distance of the golf drive: An Optimal Control Study. Transactions of the ASME, December 1975, pp. 362-367.

Larcombe, M.H.E. (1981). Carbon fibre tactile sensors. Proceedings of the 1st International Conference on Robot Vision and Sensory Controls, pp. 273-276.

Lawrence T.L., Schmidt R.N. (1997). Wireless in-shoe force system (for motor prosthesis). Proceedings of the 19th Annual International Conference of the IEEE Engineering in Medicine and Biology Society. `Magnificent Milestones and Emerging Opportunities in Medical Engineering', Vol. 5, pt. 5, pp. 2238-2241.

Leadbetter D. (1993). David Leadbetter's Faults and Fixes with John Huggan. Harper Collins Publishers Inc.

Leaver S.O., McCarthy J.M., Bobrow J.E. (1988). The design and control of a robot finger for tactile sensing. Journal of Robotic Systems, Vol. 5, no. 6, pp. 567-581.

Leung A., Payandeh S. (1996). Application of adaptive neural network to localization of objects using pressure array transducer. Robotica, Vol. 14, no. Pt4, pp. 407-414.

Liqun D., Guiryong K., Arai F., Fukuda T., Itoigawa K., Tukahara Y. (2003). Structure design of micro touch sensor array. Sensors and actuators A (Physical), Vol. A107, no. 1, Oct 2003, pp. 7-13.

Loeve M. (1955). Probability theory. Van Nostrand, Princeton, N.J. USA.

Loskutov A., Istomin I., Kotlyarov O. (2001). Data analysis: Generalisations of the local approximation method by singular spectrum analysis. v1. pp. 1-12.

Lowe B., Fairweather I.H. (1994). Centrifugal force and the planar golf swing. Science and Golf II: Proceedings of the World Scientific Congress of Golf, held at the University of St. Andrews, Scotland, (Edited by M.R. Farrally and A.J Cochran), pp. 59-64.

Maalej N., Webster J.G. (1988). A miniature electrooptical force transducer. IEEE Transactions on biomedical engineering, Vol. 35, no. 2, pp. 93-97.

Mayol-Cuevas, W.W., Juarez-Guerrero, J., Munoz-Gutierrez, S. (1998). Proceedings of the IEEE International Conference on Systems, Man and Cybernetics. Vol. 5, pp. 4246-4250.

McLaughlin P.A. and Best R.J. (1994), Three-dimensional kinematic analysis of the golf swing. Science and Golf II: Proceedings of the World Scientific Congress of Golf, held at the University of St. Andrews, Scotland, (Edited by M.R. Farrally and A.J Cochran), pp. 91-96.

McNevin N. H, Wulf G (2002). Attentional focus on supra-postural tasks affects postural control. Human Movement Science, no. 21, pp. 187-202.

Milburn P.D. (1982). Summation of segmental velocities in the golf swing. Medicine and Science in Sports and Exercise. Vol. 14, no. 1, pp.60-64.

Moore E. H. (1920). On the reciprocal of the general algebraic matrix. Bulletin American Mathematical Society, no. 26, pp. 394-395.

Moss Salentijn L (1992). The human tactile system, Advanced tactile sensing for Robotics, World scientific series in robotics and Automated systems - Vol. 5, Chapter 7, pp. 123-150.

Mott D.H., Lee M.H., Nicholls H.R. (1986). An experimental very high resolution tactile sensor array. Robot sensors, Vol. 2. pp 179-188.

Munger B. L., Ide C. (1988). The structure and function of cutaneous sensory receptors. Arch Histol Cytol, Vol. 51, pp. 1-34.

Nabney I.T. (2002). Algorithms for pattern recognition. Published by Springer-Verlag London Berlin Heidelberg. With the use of: Netlab demnlab.

Navier C.L.M.H (1823). Bulletin de la societé philomathhique de Paris, no. 75, 1823.

Nesbit S.M., Cole J.S., Hartzell, T.A., Oglesby K.A. Radich A.F. (1994). Dynamic model and computer simulation of a golf swing. Science and Golf II: Proceedings of the World Scientific Congress of Golf, held at the University of St. Andrews, Scotland, (Edited by M.R. Farrally and A.J Cochran), pp. 71-76.

Okuda I., Armstrong C.W. (2002). Biomechanical analysis of professional golfer's swing: Hidemichi Tanaka. Science and Golf IV: Proceedings of the World Scientific Congress of Golf (edited by M.R. Farrally and A.J Cochran), pp. 18-27.

Oppenheim, A.V., & Schafer, R.W. (1989). Discrete time signal processing. Englewood Cliffs, NJ: Prentice Hall. pp. 311-312.

Pacini F. (1835). In: Kowalzik R, Hermann B, Biedermann H et al (1996). Two-point discrimination of vibratory perception of the sole of the human foot. Foot and ankle international – Vol. 17, no. 10, pp. 629-634.

Parks T. W., Burrus C. S. (1987), Digital filter design, New York: John Wiley and Sons, Inc., pp. 168.

Peine W.J., Son J.S., Howe R.D. (1994). A palpation system for artery localization in laparoscopic surgery. Proceeding of the First International Symposium on Medical Robotics and Computer Assisted Surgery, pp. 250-253.

Penny J.E.T., Lindfield G., (2000). Numerical methods using matlab. Second Edition. Publisher: Prentice Hall, pp 317.

Penrose R. (1955). A generalized inverse for matrices. Proceedings of the Cambridge Philosophy Society, no. 51, pp. 406-413.

Pforringer W., Rosemeyer B (1987). The golf shoe. In Segesser B (ed): The Shoe in Sport. Chicago, Yearbook Medical Publishers, pp. 121-128.

Pietrocarlo, T A (1996). Foot and ankle considerations in golf. Clinics in Sports Medicine, Vol. 15, Issue 1, January 1996, pp. 129-146.

Pink M., Jobe FW., Perry J. (1985). Electromyographic analysis of the shoulder during the golf swing. International Journal of Sport Biomechanics. Vol. 1, no.3, pp. 221-232.

Pirolo D.G., Kolesar E.S. (1989). Piezoelectric polymer tactile sensor arrays for robotics. Proceedings IEEE National Aerospace and Electronics conference, pp. 1130-1135.

Plander I. (1987). Trends in the development of sensor systems and their use in some technological areas. Robotics, Vol. 3, no. 2, June 1987, pp. 157-165.

Potts A.D. (2002). Putting alignment in golf: A laser based evaluation. Chapter 10, Science and Golf IV: Proceedings of the World Scientific Congress in Golf, held at the University of St. Andrews, Scotland, July 2002, pp. 142-150.

Rebman J., Morris K.A. (1985). A tactile sensor with electooptical transduction. Robot Sensors, Tactile Array Sensors, pp. 145-155.

Rees Jones J. (2002). A spatial model of the rigid-body club swing. Chapter 1. Science and Golf IV: Proceedings of the World Scientific Congress in Golf, held at the University of St. Andrews, Scotland, July 2002, pp. 3-17.

Relmer E.M., Danisch L. (1999). Pressure sensor based on illumination of a deformable integrating cavity. United States Patent, Canadian Space Agency, Patent Number 5,917,180.

Richards J., Farrell J., Kent J., Kraft R. (1985). Weight transfer patterns during the golf swing. Research Quarterly, Vol. 56, pp. 361-365.

Rittler C. (1988). Chapter 14. Sensor application to the peripheral neuropathy of the foot. In Tactile sensors for robotics and medicine, Webster, J.G. pp. 281-298.

Robinson R.L. (1994). A study of the correlation between swing characteristics and club head velocity. Science and Golf II: Proceedings of the World Scientific Congress of Golf, held at the University of St. Andrews, Scotland, (Edited by M.R. Farrally and A.J Cochran), pp. 84-90.

Russell A.R. (1990). Tactile sensing of 3-dimensional surface features. Robotica, Vol. 8, no. APR, pp. 111-115.

Russell, A.R., Parkinson S. (1993). Sensing surface shape by touch. Proceedings - IEEE International Conference on Robotics and Automation, Vol. 1, pp. 423-428.

Schoenwald, Jeffrey S.Thiele, Alfred W., Gjellum, David E. (1987). Novel fibre optic tactile array sensor. Proceedings of SPIE - The International Society for Optical Engineering, Vol. 718, pp. 148-152.

Shinoda, H. ando S. (1994). Ultrasonic emission tactile sensor for contact localization and characterization. Proceedings - IEEE International Conference on Robotics and Automation, no. 3, pp. 2536-2543.

Shippen J. (2002). The calculation of a lumped-mass model from acceleration and force-plate data. Proceedings of the Institute of Mechanical Engineers, Vol. 216. Part H:J Engineering in Medicine. pp. 333-340.

Slater-Hammel A.T. (1948). Action current study of concentration movement relationships in the golf stroke. Research Quarterly Vol. 19, pp. 164-177.

Spencer, R. M. (1984). Tactile sensing in flexible manufacturing cells. National Conference Publication - Institution of Engineers, Australia, no. 84/5 pp. 118-122.

Stoica, P. et al., Optimal instrumental variable estimates of the AR-parameters of an ARMA process, IEEE Trans. Autom. Control, Vol. AC-30, 1985, pp. 1066-1074.

Stone R.S.W., Brett P.N(1996). A sensing technique for the measurement of tactile forces in the gripping of dough-like materials. ImechE Part B, Journal of Engineering Manufacture 1996, Vol. 210, pp. 261-269.

Stone R.S.W. (1997). PhD Thesis, A distributive tactile sensing technique for soft deformable contact. The University of Aston, UK, 1997.

Suzuki S., Inooka H. (1998). A new golf-swing robot model utilising shaft elasticity. Journal of Sound and Vibration. Vol. 217, no. 1, pp 17-31.

Tanie K, Komoriya K, Kaneko M, Tachi S, Fujikawa A. (1985). A high resolution tactile sensor. Robot Sensors, Tactile Array Sensors, pp. 189-198.

Thomas D. P., Whitney R. J. (1959). Postural movements during normal standing in man. Journal of anatomy, no. 93, pp. 524-539.

Timoshenko S., Woinowsky-Krieger S. (1959). Theory of plates and shells. Engineering Societies Monographs. Second Edition McGraw-Hill, pp. 47-111.

Tongpadungrod P. (2002). PhD Thesis. Characteristics of distributive tactile sensing Systems. The University of Bristol, 2002.

Toski B., Flick J. (1978). How to become a complete golfer, Golf Digest Publication.

Turner A.B, Hillis N.J. (1999). A three link mathematical model of the golf swing. Science and Golf III: Proceedings of the World Scientific Congress in Golf. pp. 3-12.

Vater A. (1741) In: Kowalzik R, Hermann B, Biedermann H et al (1996). Two-point discrimination of vibratory perception of the sole of the human foot. Foot and ankle international – Vol. 17, no. 10, pp. 629-634.

Wallace E.S., Graham D., Bleakley E.W. (1990). Foot-to-ground pressure patterns during the golf drive: a case study involving a low handicap player and a high handicap player. Science and Golf (Edited by A.J. Cochran).

Wallace E.S., Grimshaw P.N., Ashford R.L. (1994). Discrete pressure profiles of the feet and weight transfer patterns during the golf swing. Science and Golf II: Proceedings of the World Scientific Congress of Golf, held at the University of St. Andrews, Scotland, (Edited by M.R. Farrally and A.J Cochran), pp. 26-32.

Weinstein S. (1968). Intensive and extensive aspects of tactile sensitivity as a function of body part, sex and laterality, In *The Skin Senses*, ed, Kenshalo D.R., Charles C. T, Springfield, II, 1968, pp. 185-222.

Williams K.R., Cavanagh P.R. (1983). The mechanics of foot action during the golf swing and implications for shoe design. Medicine and Science in Sports and Exercise, Vol. 15, pp. 247-255.

Worth A.J., Spencer R.R. (1989). A neural network for tactile sensing: The Hertzian contact problem. Proceedings of the International Joint Conference on Neural Networks, June (Washington D.C.), Vol. 1, pp. 267-274.

Wyburn G.M. (1960). The nervous system, An outline of the structure and function of the human nervous system and sense organs, Academic press, 1960, Chapter 2, pp. 16-49.

Yoshinobu M., Christos E., Constantinou, Sadao O. (2004). Micro-mechanical sensing platform for the characterization of the elastic properties of the ovum via uniaxial measurement. Journal of Biomechanics, Vol. 37, no. 1, pp. 67-72.

Yuji J., Shida K. (2000). A new multifunctional tactile sensing technique by selective data processing. IEEE Transactions on instrumentation and measurement. Vol. 49, no. 5, pp. 1091-1094.

Web Addresses of various competitive systems:
http://www.tekscan.com, June (2003)
Computerized analysis Golf Adventure (1998).
www.golfadventure.com/analyse/anglais/a_analyse1.htm
http://faculty.washington.edu/chudler/receptor.html, August (2002)
http://www.visualsunlimited.com, March (2004)

Zizzi S, Spring 2006, West Virginia University:
http://www.wvu.edu/~physed/sportpsych/zizzi/r.pdf

APPENDIX A

Supplementary notes for Chapter 1

A.1 Singular and dual video methods of biomechanical movement and movements of clubs

Video footage of dynamic behaviour can be used in the post analysis of data capture, to determine various characteristics and parameters from the swing. This can be used specifically as a training or practicing aid or more commonly as evidence to support other time-dependent measured parameters. Guadagnoli (2002) carried out studies on the basis of the efficacy of video feedback for the learning of a golf swing. The study was designed to test the efficacy of video instruction relative to verbal and self-guided instruction. His results concluded that video analysis is an effective means of practice but the improved performance such as consistency and shot distance may take time to develop.

Similarly a system by the Computerised analysis golf adventure (1998) takes two-dimensional video footage parallel to the line of swing for further analysis through an image-processing package. The image program superimposes a simple frame built up of straight lines to reconstruct the skeleton of the body. This characterisation of the golf swing from the video shot can then simply be superimposed over a proportional elite golfers swing frame of reference. The differences between dynamics can then easily be observed, to provide anecdotal feedback. However the effectiveness of this technique is debated.

Video footage is the most conventional method used for motion tracking coupled with 3-d motion analysis techniques to formulate kinematic parameters of the activity, such as anatomical point x, y and z coordinates. From this it is possible to calculate the body segments and centre of mass coordinates. An example of this application is one by McLaughlin and Best (1994), Lowe (1994), Fairweather (2002), Burden (1998) and Cooper (1994) who used two synchronised S-VHS video cameras positioned normal to each other with the focus as the golf player on the surface. All swings were then analysed using a motion analyser program to reconstruct digitised points imaged into the video from the two cameras views to 3-d coordinates using a direct linear transformation method such as Abdel-Aziz and Karara (1971).

A.2 Evaluation of the biomechanics of bodies using laser based systems

Conventionally laser based systems are well-documented and researched systems that are used to track and monitor moving points in space. These systems are mainly used to monitor the performance of activities in the sports industry. Primarily these systems are used in the analysis of the golf swing. This is due to the complexity of the activity that is to be monitored, as the activity is relatively stationary in comparison to activities that cover large sensing ranges, such as running based sports.

The main drawback with laser-based systems is that the accuracy of results can be affected by daylight impinging on the sensing elements and can distort the true value of the measurement. Secondly the person is expected to wear a body suit or parts of a suit with reflective markers to be able to record the measured movement. This can limit the mobility and flexibility of the subject and confines activities mainly to indoor laboratories which places the subject in an environment different from their usual one, which can affect performance.

An example of such a device is in the analysis between swing characteristics and club head velocity Robinson (1994), who used a swing analyser coupled with a four synchronised video cameras to record images required for the 3-d video data. A tent provided shade for the motion tracking system that requires an overhead collimated light source to operate. This collimated light source is the fundamental difference between a normal camera system and a motion tracking system. These motion-tracking systems are mainly hybrid developments from multi-camera systems and follow a similar measurement and analysis process. However the initial video measuring technique used two cameras to triangulate the position in 3-d space, but most tracking systems today can use as many as twelve cameras. Examples of such systems are ones used by Hosea (1990), Nesbit (1994) and Barrentine (1994) who used 4 cameras respectively with reflective markers placed on the body, club shaft and ball as to capture data into the video processor. The point coordinates are then digitised using a direct linear transformation method, which can then generate outputs such as three-dimensional stick figures for further quantification.

Other laser-based methods have been documented for the use in the analysis of the alignment during the putting swing, Potts (2002). The investigation quantified putting alignment using a laser light source embedded into the heel of the putter so that the laser diode module projected at right angles to the face of the putter. A 3V battery power source for the laser was located within the shaft of the putter. Alignment was quantified when the laser light source impinged on to a graduated score board located behind the ball. The graduated score board was videotaped continuously throughout testing. However the acceleration and velocity of the club head cannot be measured using this single laser approach.

A.3 Evaluation of forces imposed on the club

The evaluation of grip pressure can be considered as an important factor in the mechanics of the golf swing, as some instructors comment that students have little feel for the golf swing because their grip is too tight. Toski and Flick (1978) presume that when grip pressure is at a minimum the muscles are at ease enhancing the feel for striking the ball. Yet others claim a firm grip is essential and key to club control Barber (1978). Budney (1990) investigates whether golfers should apply light or firm grip pressure and the impulse times on the each hand when the ball is hit with the club. In order to carry out this analysis three pressure transducers were placed at various locations on the club that relate to key grip pressure points on the hands. The transducers consisted of simply supported beams on which metal foil electrical resistance strain gauges bonded to the bottom surface.

Centripetal forces on the club have also been investigated by Lowe (1994) who used linear displacement transducers integrated on the shaft. Radial displacements of the L.D.T. were outputted as electrical signals proportional to the distance moved to analyse the relative mass displacements along the shaft throughout the swing.

A.4 Evaluation of electromyography and myoelectric voltages from the body

Muscle groups that are activated during the golf swing have also been analysed through the use of electromyography EMG. This type of analysis is for two main points; the first is to understand which muscles contribute to the swing and secondly to find out which muscle activity may lead to injury. The first work carried out using EMG was performed on 'good' golfers by Slater-Hammel (1948), who found that the contraction movement coordination of muscle groups for individuals was extremely consistent, but with variation between subjects. Pink, et al. (1985) described a manual muscle test for various muscle groups as a percentage of maximal muscular activity in skilled golfers using surface electrodes. Okuda (2002) examined selected biomechanical factors associated with successful long driving with an individual with small body mass. He concluded that a pattern of muscle activation is consistent with a movement sequence of proximal to distal segments for a successful swing. He also concluded that the initiation of hip rotation must be performed before the club reaches the back swing for a successful swing. Hosea (1990) investigated muscular activity for amateurs compared with that of professional players. Firstly he reported much higher EMG activity as a percentage of a maximal voluntary contraction in the amateurs with less variability in the professionals. He also calculated peak shear, bending, torque and compression in the lumbar spine in relation to the EMG activity and concluded that they all were much greater in amateurs than in professionals, where only the peak compression load was greatest.

EMG activation has also been investigated for different shots using selected clubs, by Abernathy (1990) and Bechler (1995), who concluded that relative timing is a variable feature of control at the electromyographic level.

APPENDIX B

Supplementary notes for Chapter 2

B.1 A detailed description of the receptors in the human sensing system

Tactile sensing is the process of determining physical properties and events through contact with objects in the world. There are five main sensing modalities-sight, sound, smell, taste and touch. Most of these systems have been investigated and described as mechanical systems such as computer vision systems for the process of sight, audio systems for the replication of sound such as speech recognition systems, electronic noses are readily available for the detection of a range of molecules for the process of smell and chemical tests can be implemented to replicate the sensation of taste. However it is the sensation of touch that has been neglected over the years and research in this area is nowhere near as large in volume as the other sensing modalities.

The reason for this is due to the fact that the sensation of touch can not be described as a localised organ, such as sight or sound and is distributed and diffuse over a wide area within the skin. Thus the creation of an artificial tactile skin is much more complex than the development of discrete sensing devices. This is due to the number of sensations that it can describe such as detection of shape, texture, friction, force, pain, temperature and many other related properties.

Tactile sensing is therefore difficult to imitate, unlike sight and sound that are well defined physical quantities and the capture of such data is a solved problem in these areas. That is why vision research, for example, is only concerned with images and interpretation and not so much with the development of new cameras and optics. However tactile sensing systems are not even at this point and are still concerned with the fundamentals of coherent data capture.

If it is possible to develop a mechanical tactile system that can represent a physiological nervous system closely then this system would be able to perform any of the tactile sensations and functions that a human cerebral cortex could decode. However the system in question is only required to analyse a tactile sensation through either static or dynamic loading condition and would vastly reduce the complexity of the replication. Only looking at the physiological touch sensation, it is possible to

replicate various functions accurately. The receptors and the surface of the physiological system are shown in figure B.1.

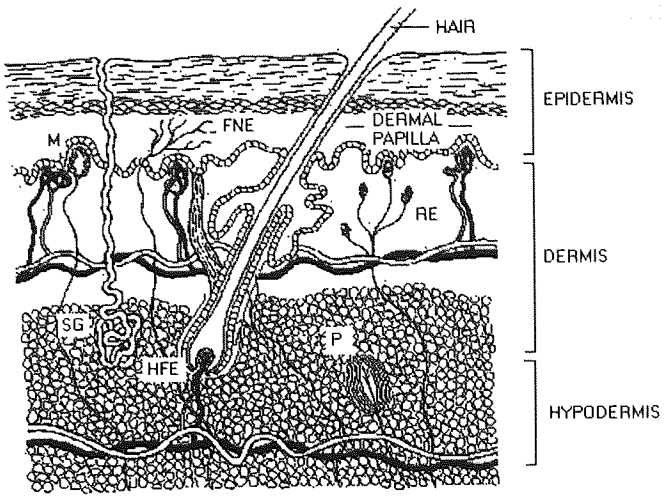

Figure B.1 - Anatomical construction of the skin. This figure indicates the various glands, sensory receptors and location in the structure. (Faculty of Education at Washington University)

The dimensions of the skin layers in figure B.1 for glabrous skin has an epidermal layer of about 1.5 mm in thickness and a dermis of about 3 mm. Hairy skin has an epidermal layer of 0.07 mm in thickness and a dermis of about 1-2 mm. The diagram above can describe a glabrous or hairy section of skin. The anatomical positions of the glands and receptor terminals are indicated in the figure as: [P] Pacinian corpuscle, which responds to vibration and is most sensitive in the 150-300Hz range and is located in the deep layers of the dermis in both hairy and glabrous skin. The [HFE] Hair Follicle Receptor, is integrated within the piloneural complex on the hair follicle Munger and Ide (1988), As many as three hundred groups of hair follicles may be supplied by one nerve fibre and are stimulated by pressure as distinct from light touch. [SG] Sweat gland can be located at regular intervals along the protruding ridges of the dermis. The [RE] Ruffini Ending responds to pressure on the skin. The [M] Meissner's corpuscles respond to vibration and are most sensitive in the ranges of 20-40Hz and are located just below the dermal papilla layer. [FNE] Free nerve endings, different types of free nerve endings that respond to mechanical, thermal or noxious stimulation.

There are only three sensory modalities apparent in the skin; temperature from thermoreceptors, pressure from mechanoreceptors and pain from nociceptors. Each modality has its own low-threshold sensory nerve terminal and nerve fibre pathway to

the brain so that information regarding the quality and type of particular stimuli does not get mixed with other types of stimuli. The pressure sensation in the skin is the modality that will be examined more closely as it can be associated with vibration (i.e. changing pressure), touch and tactile stimuli. One such somatic receptor that is receptive to pressure and change in pressure is the Pacinian corpuscle x15 shown in figure B.2, courtesy of Visuals Unlimited.

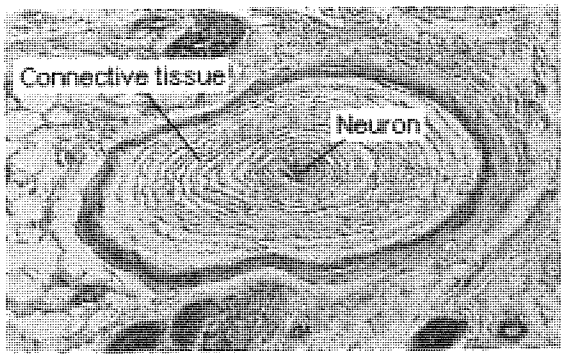

Figure B.2 - Pacinian receptor corpuscle. (Visuals Unlimited)

The above diagram shows a Pacinian corpuscle which is a sensory receptor for crude touch. These receptors are the largest and least numerous of all mechanoreceptors and were first described by Vater (1741) and later by Pacini (1840), from whom the name is derived. The dimensions of the corpuscle can be up to 3mm in length and 2mm in width and the inner neuron is formed by 30-60 concentric layers of closely packed cellular lamellae of Schwann cells. The connective tissue of the viscous gel filled capsule is less compact than the inner core and is composed of 20-70 concentric cellular lamellae of perineural cells. Exteroceptive mechanical pressure applied to the skin surface indent the skin, resulting in stimulation of the Pacinian corpuscle lying in the hypodermal layer.

Since this is deep within the skin then only strong pressure stimuli, causing sufficiently deep indentation can activate them. Thus Pacinian corpuscles are pressure sensors and the action potential is released within the corpuscles upon the distributed pressure and release of the stimuli. This excitation and release of a stimulus allows the corpuscle to detect changes in pressures and detect vibration from its ability to rapidly adapt to applied pressures.

APPENDIX C

Further results and analysis for Chapter 3

C.1 The differential equation for the deflection of a surface

Described here is the derivation of Navier's model for the deformation of thin plates. Initially it must be assumed that the load acting on a plate is normal to its surface and that the deflections are small in relation to the thickness of the plate. This condition can be rigorously satisfied only if the middle surface of the bent plate is a developable surface. The expression for small deflections comparable to the surface thickness gives an approximate expression used for the curvature of the material. This can be proved in:

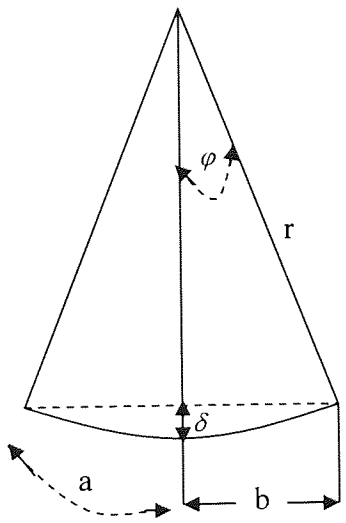

Figure C.1 - Change in surface strain on the surface.

$$\varphi = \frac{a}{r} \text{ and } b = r.\sin\varphi \tag{3.1}$$

It can be seen that the assumed bending of the plate will imply a compressive strain in the middle of the surface in the circumferential direction. The magnitude of this strain on the surface can therefore be calculated as from (C.1):

$$\varepsilon = \frac{a-b}{a} = \frac{r\varphi - r.\sin\varphi}{r\varphi} \tag{3.2}$$

and for small deflections we can assume that:

$$\sin\varphi = \varphi - \frac{\varphi^3}{6} \tag{3.3}$$

which substituted into (3.2) gives: $\varepsilon = \frac{\varphi^2}{6}$ (3.4)

To represent this strain as a function of the maximum deflection δ, we observe that:

$\delta = r(1-\cos\varphi) \approx \frac{r\varphi^2}{2}$, Hence $\varphi^2 = \frac{2\delta}{r}$ and substituting into (3.4) we obtain: $\varepsilon = \frac{\delta}{3r}$ (3.5)

where ε is the maximal strain at a maximal deformation. If a plate is bent to a non-developable surface the middle surface undergoes some stretching during bending and the theory of pure bending will be accurate enough only if the strain in the middle surface is small in comparison with the maximum bending strain = h/2r - (3.6), where h is the thickness of the surface. From this it can be found that the maximum allowable deformation for the calculation of the surface must be equal or less than 1.5 times the thickness of the surface thickness from:

$$\frac{\delta}{3r} = \frac{h}{2r} \Rightarrow \delta = \frac{3}{2}h \tag{3.7}$$

At the boundary the plate is simply supported through forces normal to the edge and is free to move at the edges. From this we can assume that any strain in the middle of the plate during bending is neglected. Assume a plate in the diagram below with the load distributed over the upper surface of the plate denoted with a magnitude of q, so that the load is acting on the element q dx dy, given that M is the moment of rotation and Q is the shearing force.

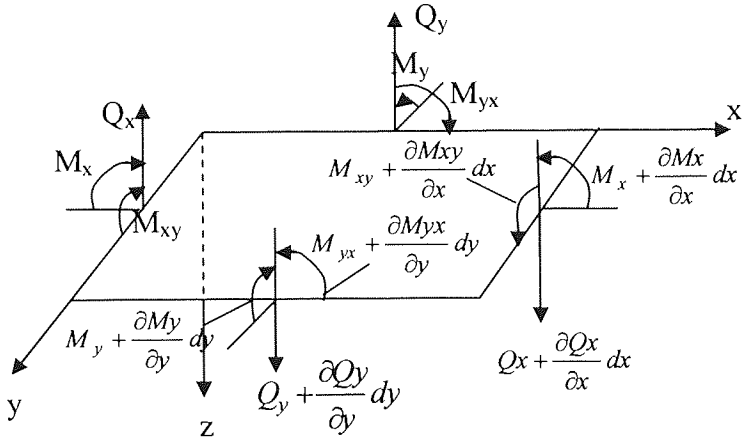

Figure C.2 - Forces and Moments expressions acting on both x and y planes on a rectangular plate.

Projecting all the forces acting on the element onto the z axis we obtain the following equation of equilibrium from Timeshenko (1959) :

$$\frac{\partial Q_x}{\partial x} dxdy + \frac{\partial Q_y}{\partial y} dydx + qdxdy = 0 \text{, where } \frac{\partial Q_x}{\partial x} + \frac{\partial Q_y}{\partial y} + q = 0 \tag{3.8}$$

Taking moments of all the forces acting on the element with respect to the x axis, we obtain the equation of equilibrium.

$$\frac{\partial M_{xy}}{\partial x} dxdy - \frac{\partial M_y}{\partial y} dydx + Q_y dxdy = 0 \tag{3.9}$$

Breaking expression (3.9) down into components of x and y we achieve:

$$\frac{\partial M_{xy}}{\partial x} - \frac{\partial M_y}{\partial y} + Q_y = 0 \text{ in respect of the x axis and} \tag{3.10}$$

$$\frac{\partial M_{yx}}{\partial y} + \frac{\partial M_x}{\partial x} - Q_x = 0 \text{ for moments in the y axis} \tag{3.11}$$

Since there are no forces in the x and y direction and no moments in the z direction then the shearing forces Q_x and Q_y can be eliminated from expression (3.8) through a substitution of (3.10) and (3.11) into equation (3.8) so the expression now becomes:

$$\frac{\partial^2 M_x}{\partial x^2} + \frac{\partial^2 M_{yx}}{\partial x \partial y} + \frac{\partial^2 M_y}{\partial y^2} - \frac{\partial^2 M_{xy}}{\partial x \partial y} = -q \tag{3.12}$$

Also this can be simplified due to the virtue that $M_{yx} = - M_{xy}$, (Moments about the axis from figure C.2). The expression now becomes:

$$\frac{\partial^2 M_x}{\partial x^2} + \frac{\partial^2 M_y}{\partial y^2} - 2\frac{\partial^2 M_{xy}}{\partial x \partial y} = -q \tag{3.13}$$

The moments (M_x and M_y) in x, y and xy directions, the bending stress D, and the Poisson's ratio given as v, gives:

$$M_x = D\left(\frac{1}{r_x} + v\frac{1}{r_y}\right) = -D\left(\frac{\partial^2 w}{\partial x^2} + v\frac{\partial^2 w}{dy^2}\right) \text{ for the moment in the x plane and}$$

$$M_y = D\left(\frac{1}{r_y} + v\frac{1}{r_x}\right) = -D\left(\frac{\partial^2 w}{\partial y^2} + v\frac{\partial^2 w}{dx^2}\right) \text{ for the moment in the y plane and the expression}$$

The twisting moment in the xy direction is:

$$M_{xy} = -\int_{-h/2}^{h/2} \tau_{xy} z.dz = \frac{Gh^3}{6}\frac{\partial^2 w}{\partial x \partial y} = D(1-v)\frac{\partial^2 w}{\partial x \partial y}$$

Substituting these moment expressions into equation (3.13) and simplifying we get:

$$\frac{\partial^4 w}{\partial x^4}+\frac{\partial^4 w}{\partial y^4}+2\frac{\partial^4 w}{\partial x^2 \partial y^2}=\frac{q}{D} \tag{3.14}$$

Assuming that the plate is rectangular and is simply supported around the edges then the loading on the plate can be described as:

$q = q_0 \sin\frac{\pi x}{e}.\sin\frac{\pi y}{f}$, where q_0 represents the intensity of the load, e and f represents the length and width of the rectangular plate respectively. Therefore through substitution equation (3.14) then becomes:

$$\frac{\partial^4 w}{\partial x^4}+\frac{\partial^4 w}{\partial y^4}+2\frac{\partial^4 w}{\partial x^2 \partial y^2}=\frac{q_o}{D}\sin\frac{\pi x}{e}.\sin\frac{\pi y}{f} \tag{3.15}$$

and satisfying the boundary conditions where:

w, M_x, M_y, $\frac{\partial^2 w}{\partial x^2}$ and $\frac{\partial^2 w}{\partial y^2}$ = 0, for either x, y = 0, or x = e and y = f.

Solving for the deflection w as a function of x and y, i.e. $w = f(x,y)$. The function can therefore be expressed in the form of a double trigonometric series.

$$f(x,y)=\sum_{a=1}^{\infty}\sum_{b=1}^{\infty}k_{ab}\sin\frac{a\pi x}{e}.\sin\frac{b\pi y}{f} \tag{3.16}$$

To calculate the coefficient $k_{a'b'}$ of this series it is important to multiply both sides of equation (3.16) by $\sin(b'\pi y/f)dy$ and integrate from 0 to f to give for the y axis:

$\int_0^f \sin\left(\frac{b.\pi.y}{f}\right).\sin\left(\frac{b'.\pi.y}{f}\right)dy = 0$, when $b \neq b'$ and

$\int_0^f \sin\left(\frac{b.\pi.y}{f}\right).\sin\left(\frac{b'.\pi.y}{f}\right)dy = \frac{f}{2}$, when $b = b'$ so that the expression (3.16) becomes:

$$\int_0^f f(x,y)\sin\left(\frac{b'.\pi.y}{f}\right)dy=\frac{f}{2}\sum_{b=1}^{\infty}k_{ab'}\sin\left(\frac{b.\pi.y}{e}\right) \tag{3.17}$$

Multiplying by sin(a' πx/e)dx and integrating from 0 to e with respect to the x axis, the full expression becomes:

$$\int_0^e \int_0^f f(x,y).\sin\left(\frac{a'\pi.x}{e}\right).\sin\left(\frac{b'\pi.y}{f}\right)dydx = \frac{e.f}{4}.k_{a'b'} \tag{3.18}$$

Performing the integration indicated in expression (3.18), through a summation of partial sinusoid loadings for a given load distribution for a given point of interest *f(x,y)*. The total deflection can be obtained by adding in the bending stiffness of the surface to the double trigonometric series to give:

$$w = \frac{1}{\pi^4 D}\sum_{a=1}^{\infty}\sum_{b=1}^{\infty}\frac{k_{ab}}{\left(\frac{a^2}{e^2}+\frac{b^2}{f^2}\right)^2}.\sin\left(\frac{a.\pi.x}{e}\right).\sin\left(\frac{b.\pi.y}{f}\right) \tag{3.19}$$

Dividing each term of the double trigonometric series through by a function of a and b squared allows for a convergence of the series. This occurs through the addition of smaller components or steps in the deformation to give greater accuracy or result. As the number of selected harmonics in the x and y directions (i.e. a and b), increase as does the number of terms in the series, hence the greater the number of decimal places the result will give.

From this formula we can obtain the expression to find the coefficients of k_{ab} to give

$$k_{ab} = \frac{4q_0}{e.f}\int_0^e \int_0^f \sin\left(\frac{a.\pi.x}{e}\right).\sin\left(\frac{b.\pi.y}{f}\right)dxdy = \frac{16q_0}{\pi^2 a.b} \tag{3.20}$$

Applying a load of magnitude W at the coordinates of g and h, an expression k_{ab} can be derived from expression (3.20) as:

$$k_{ab} = \frac{4W}{e.f}\sin\left(\frac{a.\pi.x}{e}\right).\sin\left(\frac{b.\pi.y}{f}\right) \tag{3.21}$$

From expression (3.20) it can be observed that the integral is set over a specific singular point, thus x and y variables tend to g and h respectively, however the parameters of the integral can be extended to formulate the coefficients of k_{ab} as a load distribution over a desired rectangular area in the x y plane (3.21). Substituting expression (3.21) into (3.19) the complete expression becomes:

$$w(x,y)=\frac{4W}{\pi^4 e.f.D}\sum_{a=1}^{\infty}\sum_{b=1}^{\infty}\frac{\sin\left(\frac{a.\pi.g}{e}\right).\sin\left(\frac{b.\pi.h}{f}\right)}{\left(\frac{a^2}{e^2}+\frac{b^2}{f^2}\right)^2}.\sin\left(\frac{a.\pi.x}{e}\right).\sin\left(\frac{b.\pi.y}{f}\right) \tag{3.22}$$

where D and can be obtained through an integration of the bending moments to give:

$$D=\frac{t^3 E}{12\left(1-\nu^2\right)} \tag{3.23}$$

C.2 Pictures of the golf mat with the sensing technology

The picture top left illustrates the sensing elements positioned under the surface with a copper power bus supplying all of the elements. The picture on the top right shows the finished version of the golf driving mat with the steel surface and sensing elements integrated within the mat.

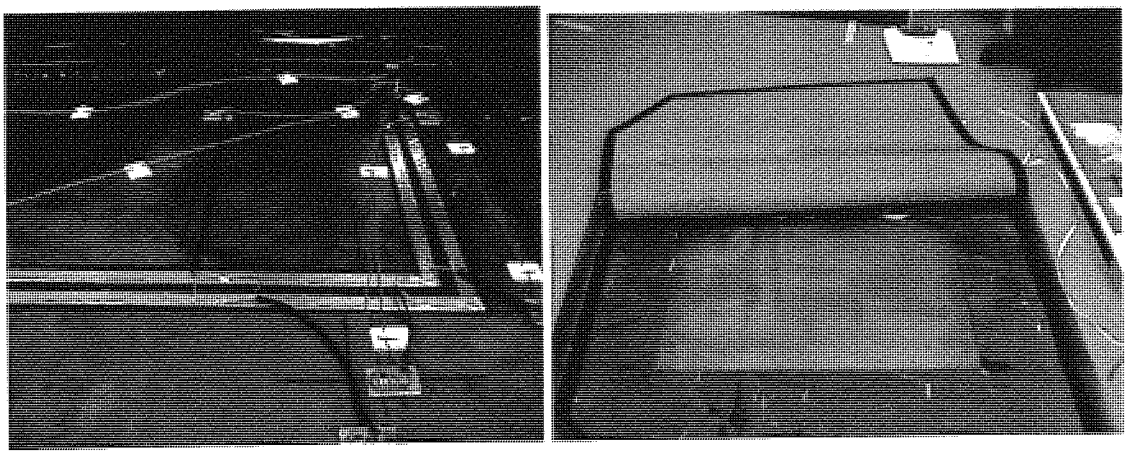

Figure C.3 - Pre-prototype of the golf driving mat. (left) - Sensor configuration under the surface. (right) - Configuration of the golf mat within side the driving mat.

The next development of the golf mat will consist of a flexible circuit, or four main PCB's each handling two sensing elements at the optimal positions. This will also have an integrated USB ADC circuit that are to be connected to the sensory PCB's with ZIF and ribbon cables.

The golf mat will also consist of two platforms, integrated within the surface. One will be trained for the left handed golfer and the second one facing the left hand platform will be for the right handed player. This will provide a reduction in complexity within the training algorithm to distinguish between the two types of player, allowing the orientation of the feet to be always placed in the trained directions on the surface. This will also allow for high accuracies, as illustrated in section 3.5.

APPENDIX D

Supplementary notes for Chapter 4

D.1 Detailed analysis of the SVD filtration method

A theoretical sinusoidal input given in the form: $signal = m.\sin(2\pi f.t)$, where the magnitude of the input signal m = 1, the input frequency f = 0.5Hz and the duration of the given time series is T = 5 s.

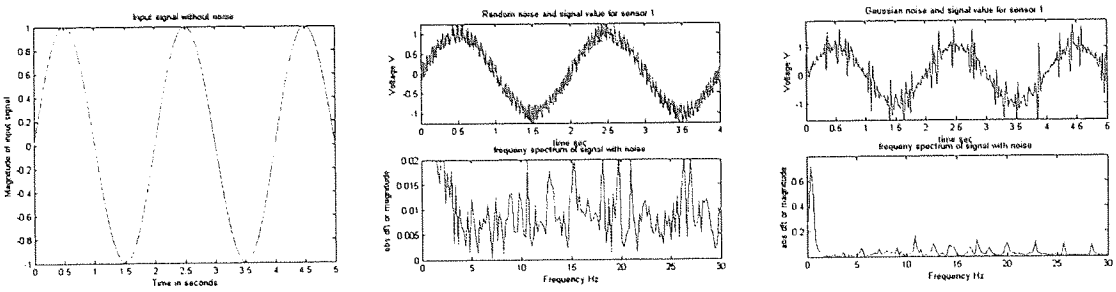

Figure D.1 - (left) Theoretical clean input with an amplitude of 1 and frequency of 0.5Hz. (centre) Clean signal with an additive random noise with a signal to noise ratio of 0.5 and resulting frequency response. (right) Clean signal with added periodic noise and resultant frequency response.

The data in the above figures are to be used for theoretical filtration purposes. Firstly, the noise frequencies in the signal are demonstrated using a Fast Fourier Transform for a pre filtration analysis.

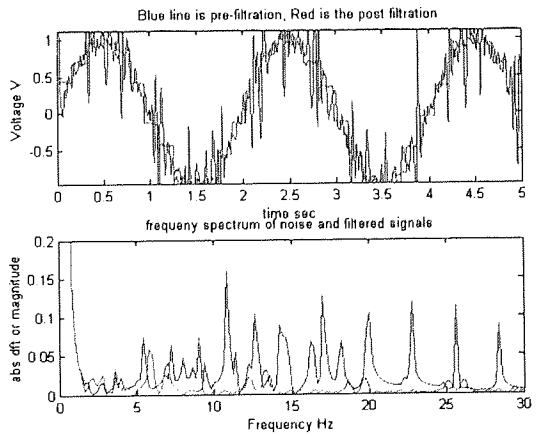

Figure D.2 - Red filtered response in time (top) and frequency (bottom) using the SVD filtration method using the first two principal SV's, the blue curve is noisy signal.

From this it can be determined that the SVD technique is a feasible method to eliminate noise. However the indicators of the correlation coefficients show that the SVD filtering method performs better in eliminating periodic noise which is more common in the real world, as opposed to random noise. The benefit of this type of filtration method is that it is non frequency dependent. Noise is generally considered

to contribute to the smaller singular values and hence these are eliminated regardless of its frequency component.

D.2 Detailed analysis of the Butterworth filtration method

Given that the Butterworth filtration function is written as H*(s)*, the mapping function $z = e^{sT}$, or alternatively in the frequency domain as $z = e^{jwT}$, where T is the sampling period, maps points in the *(s)* plane into the *(z)* plane. Points in the left of the *(s)* plane (stability region) are transformed to points that lie within the unit circle in the *(z)* plane which define the coefficients of the filter.

Once the zeros and poles of the analogue filter have been defined it is possible to use an impulse invariant method to provide the translation from the Laplace domain *(s)* into a z-transform. Assuming a 2nd order low pass Butterworth filter represented by two poles *(p)* gives the analogue response in the Laplace domain as:

$$H(s) = K\frac{1}{(s-p_1)(s-p_2)} = \frac{r_1}{(s-p_1)} + \frac{r_2}{(s-p_2)} \qquad \text{(D.1)}$$

For example we require a cut-off at 5Hz, i.e. $\omega_c = 2\pi.\ 5$, with a sampling frequency of 30Hz, i.e. $\omega_s = 2\pi.\ 30$ and defining the pre-warp desired cut-off frequency as $\omega_p = k.\tan\left(\frac{2\pi.5}{2.30}\right) = k.\tan\left(\frac{\pi}{6}\right) = \frac{k}{\sqrt{3}}$ and replacing s by s/ω_p and substituting in (D.1) gives: $H(s) = \frac{1}{3(s/k)^2 + \sqrt{6}(s/k)+1}$ and applying the transform from (D.1) gives:

$$H(z) = \frac{1}{3\left(\frac{z-1}{z+1}\right)^2 + \sqrt{6}\left(\frac{z-1}{z+1}\right)+1} = H(z) = \frac{z^2+2z+1}{\left(4+\sqrt{6}\right)z^2 - 4z + 4 - \sqrt{6}} \qquad \text{(D.2)}$$

Dividing through by z^2, gives:

$$H(z) = \frac{1+2z^{-1}+z^{-2}}{\left(4+\sqrt{6}\right)-4z^{-1}+\left(4-\sqrt{6}\right)z^{-2}} = \frac{1}{\left(4+\sqrt{6}\right)}\left[\frac{1+2z^{-1}+z^{-2}}{1-\frac{4}{\left(4+\sqrt{6}\right)}z^{-1}+\frac{\left(4-\sqrt{6}\right)}{\left(4+\sqrt{6}\right)}z^{-2}}\right] \quad \text{(D.3)}$$

$$K = \frac{1}{\left(4+\sqrt{6}\right)},\ a_0 = 1,\ a_1 = 2,\ a_2 = 1,\ b_1 = -\frac{4}{\left(4+\sqrt{6}\right)},\ b_2 = \frac{\left(4-\sqrt{6}\right)}{\left(4+\sqrt{6}\right)} \quad \text{(D.4)}$$

D.3 Evaluation of the numerator and denominator coefficients for a 4th order Butterworth filter

The given expressions have been taken from a standard relationship for N = 4 order filter, however the coefficients of (a) and (b) in the expression are given as standard derived coefficients for a 4th order expression as:

The numerator coefficients are given as: And Denominator coefficients of:

$$b_0 = \frac{\omega_c^4}{k^4 + \alpha\omega_c k^3 + \beta\omega_c^2 k^2 + \alpha\omega_c^3 k + \omega_c^4} \qquad a_0 = 1$$

$$b_1 = \frac{4\omega_c^4}{k^4 + \alpha\omega_c k^3 + \beta\omega_c^2 k^2 + \alpha\omega_c^3 k + \omega_c^4} \qquad a_1 = \frac{-4k^4 - 2\alpha\omega_c k^3 + 2\alpha\omega_c k^3 + 4\omega_c^4}{k^4 + \alpha\omega_c k^3 + \beta\omega_c^2 k^2 + \alpha\omega_c^3 k + \omega_c^4}$$

$$b_2 = \frac{6\omega_c^4}{k^4 + \alpha\omega_c k^3 + \beta\omega_c^2 k^2 + \alpha\omega_c^3 k + \omega_c^4} \qquad a_2 = \frac{6k^4 - 2\beta\omega_c^2 k^2 + 6\omega_c^4}{k^4 + \alpha\omega_c k^3 + \beta\omega_c^2 k^2 + \alpha\omega_c^3 k + \omega_c^4}$$

$$b_3 = \frac{4\omega_c^4}{k^4 + \alpha\omega_c k^3 + \beta\omega_c^2 k^2 + \alpha\omega_c^3 k + \omega_c^4} \qquad a_3 = \frac{-4k^4 + 2\alpha\omega_c k^3 - 2\alpha\omega_c k^3 + 4\omega_c^4}{k^4 + \alpha\omega_c k^3 + \beta\omega_c^2 k^2 + \alpha\omega_c^3 k + \omega_c^4}$$

$$b_4 = \frac{\omega_c^4}{k^4 + \alpha\omega_c k^3 + \beta\omega_c^2 k^2 + \alpha\omega_c^3 k + \omega_c^4} \qquad a_4 = \frac{k^4 - \alpha\omega_c k^3 + \beta\omega_c^2 k^2 - \alpha\omega_c^3 k + \omega_c^4}{k^4 + \alpha\omega_c k^3 + \beta\omega_c^2 k^2 + \alpha\omega_c^3 k + \omega_c^4}$$

$$\alpha = 2\left[\cos\left(\frac{\pi}{8}\right) + \cos\left(\frac{3\pi}{8}\right)\right],$$
$$\text{and} \qquad \beta = 2\left[1 + 2\cos\left(\frac{\pi}{8}\right)\cos\left(\frac{3\pi}{8}\right)\right] \qquad \text{(D.5)}$$

D.4 Comparison between Butterworth and SVD filtration techniques

A final quantitative analysis can be carried out to determine how the singular values change in the diagonal in relation to Butterworth filtration. In theory the large components that contribute most to the signal should be unaffected and the smaller components that contribute to noise should be eliminated. This technique is to be used to prove the theory that the smaller components specifically relate to noise and that the large components relate to the clean signal.

To carry out this analysis the singular values are initially calculated from a square matrix reconstruction of the dataset before filtration. The data set is then filtered using a low pass Butterworth with a cut-off frequency at 5Hz and then the singular values are then re-calculated on the filtered time series data through a square matrix reconstruction. Note: the values change dramatically at the value of two, illustrating that the first two values are complementary to the signal and the remaining proportionally smaller singular values can be assumed to noise in the signal

Putting this filtration method into practice to eliminate noise from the captured time series is represented in figure D.5.

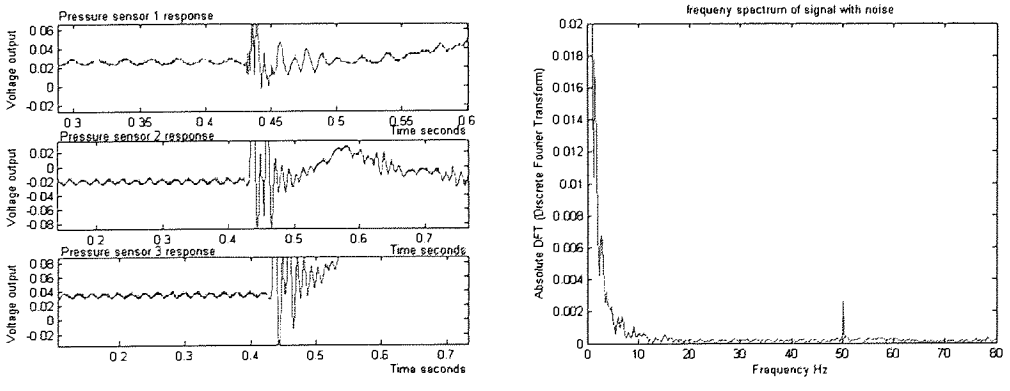

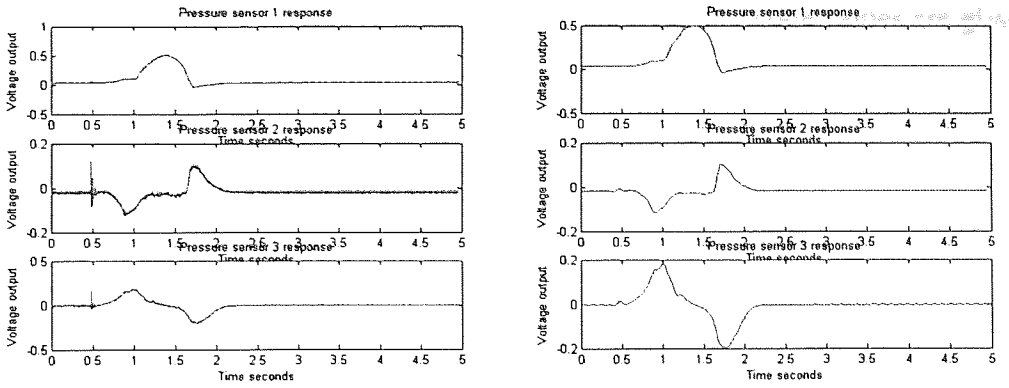

Figure D.3 (top left) - Magnified impression of the captured noisy transients. (top right) Frequency response of the first transient, indicating the fundamental noisy frequency at 50Hz. (bottom left) - Full noisy captured transient. (bottom right) - Result after a FFT-IFFT filtration of frequencies greater than 10Hz.

The results indicated in figure D.3, are quite interesting. The top right figure shows a frequency spike at 50Hz, which is indicative of the external AC noise in the transformer being transferred through the DC supply into the sensor and through the amplifier. The FFT-IFFT method shows that such a technique can be used (bottom right) for the filtration of real captured noise in the system.

D.5 Training of a regressive MLP using early stopping to interpret the height of a subject on the surface subject to a dynamic movement

Regularisation training for a regressive MLP for height discrimination using early stopping gives an optimal number of nodes as:

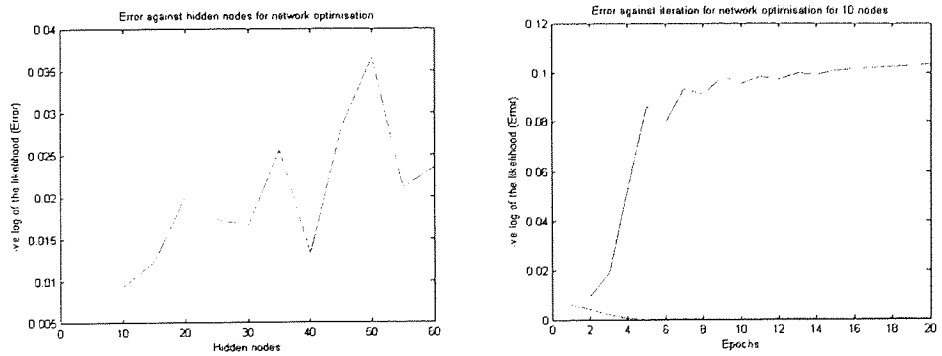

Figure D.4 - Canonical error for various nodes in the architecture of an MLP for the inference of a subject's height. (right) - Validation error in red changing with respect to the training optimisation in blue.

The specific optimal errors from the validation data for various node values are given:

Nodes	Epochs	Error
5.0000	1.0000	0.0110
10.0000	2.0000	0.0092
15.0000	2.0000	0.0122
20.0000	1.0000	0.0200
25.0000	1.0000	0.0173
30.0000	1.0000	0.0165
35.0000	1.0000	0.0257
40.0000	1.0000	0.0131
45.0000	1.0000	0.0281
50.0000	1.0000	0.0366
55.0000	1.0000	0.0210
60.0000	1.0000	0.0235

Looking specifically around the 10 node point gives:

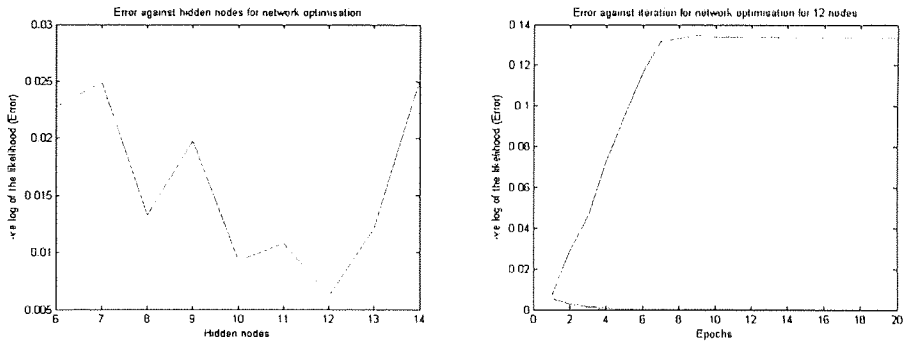

Figure D.5 - Canonical error for nodes between 6 and 14 in the architecture of an MLP for the inference of a subject's height. (right) - Validation error in red changing with respect to the training optimisation in blue

Nodes	Epochs	Error
6.0000	1.0000	0.0227
7.0000	1.0000	0.0248
8.0000	1.0000	0.0132
9.0000	1.0000	0.0198
10.0000	2.0000	0.0092
11.0000	1.0000	0.0108
12.0000	1.0000	0.0062
13.0000	1.0000	0.0121
14.0000	1.0000	0.0252

Examining the value of the learning step at 12 nodes gives

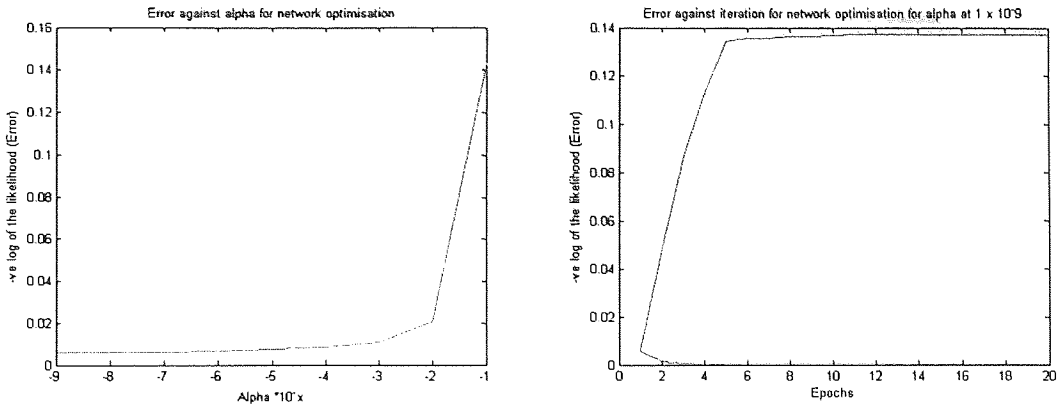

Figure D.6 - Canonical error for learning steps in the order of $1x10^{-1}$ to $1x10^{-9}$ in the architecture of an MLP for the inference of a subject's height. (right) - Validation error in red changing with respect to the training optimisation in blue.

weight decay $1x10^n$	Epochs	Error
-1.0000	6.0000	0.1436
-2.0000	5.0000	0.0202
-3.0000	1.0000	0.0108
-4.0000	1.0000	0.0080
-5.0000	1.0000	0.0072
-6.0000	1.0000	0.0062
-7.0000	1.0000	0.0061
-8.0000	1.0000	0.0060
-9.0000	1.0000	0.0060

The optimised parameters of which gave 12 nodes, a learning step of $1x10^{-9}$ and an early stopping of 50 iterations (1 epoch). Testing with unknown patterns to the MLP gave: 0.0133m average error or 8.8882%.

D.6 Illustration of the captured transients for a full golf swing

Below is a representation of the captured filtered transients for a full golf swing. It is to be noted that the peaks and troughs of the transients indicate the key points in the swing that can be used to segregate the transient into chronological stages.

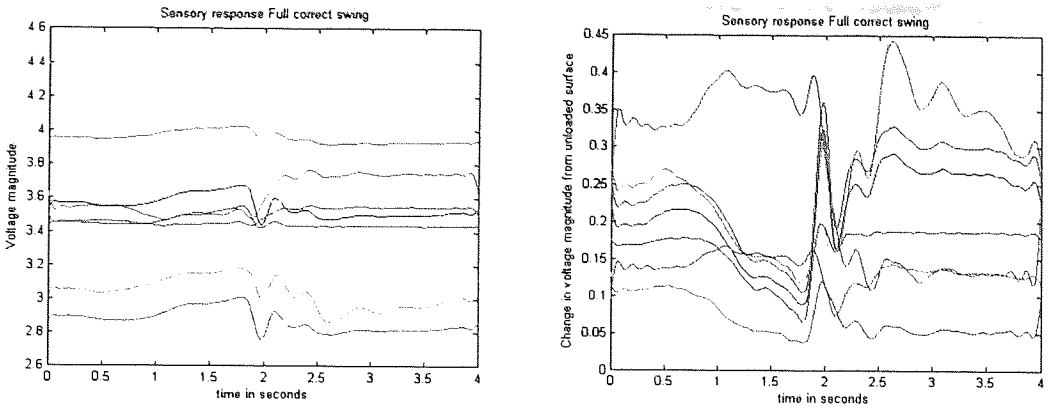

Figure D.7 (left) - Captured transients from a full correct golf swing. (right) - The differential voltages derived from the figure on the left from the initial voltages when the surface is unloaded.

D.7 Similarities between the model and the practical data for the derivation of foot force data

This section describes how various golf backswings with errors are illustrated through the use of the model and from the averaged data set from the captured transients. The interpretation of load magnitude at the four points of the feet from the movement of the COP is derived through a triangulation, assuming that the feet are fixed, for an error free backswing 111, and smoothing of the model forces gives:

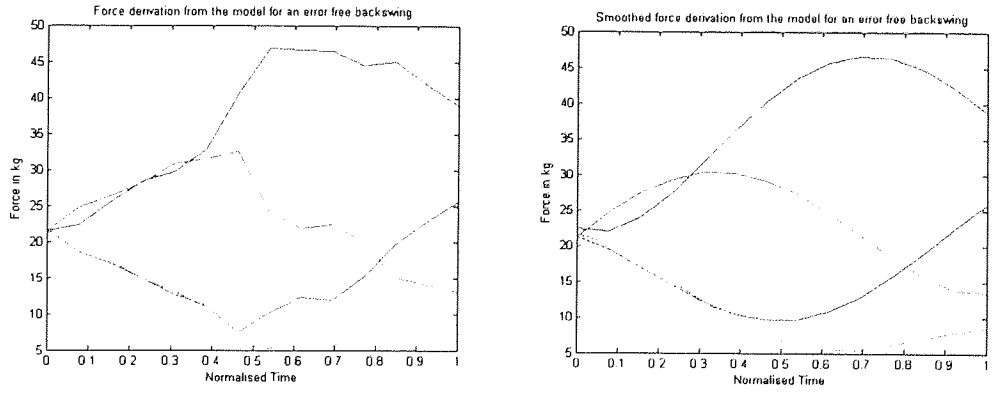

Figure D.8 - is a representation of the modelled forces at the feet for an ideal backswing 111

The average sensory transients from the data set for swing 111 are illustrated in the left plot in D.8 which has been calculated from the linear inverse multiplication method of the differentials to give the forces from the averaged ideal swing sensory transients. However the load on the surface of the candidate was 70kg at rest, as opposed to 86kg that the model suggests, however it is the characteristics of the transients that is of most interest.

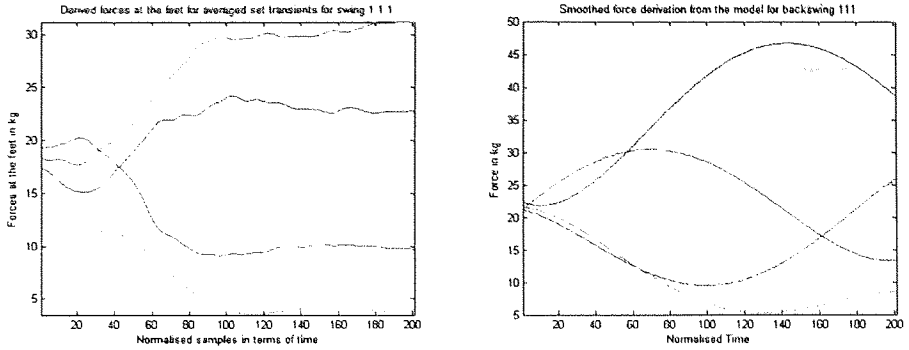

Figure D.9 - A comparison between the model (the right figure) and the practical data (the left figure) is given in the above for an ideal backswing 111.

Similarly the forces can be examined for a correct backswing with an incorrect orbit 110

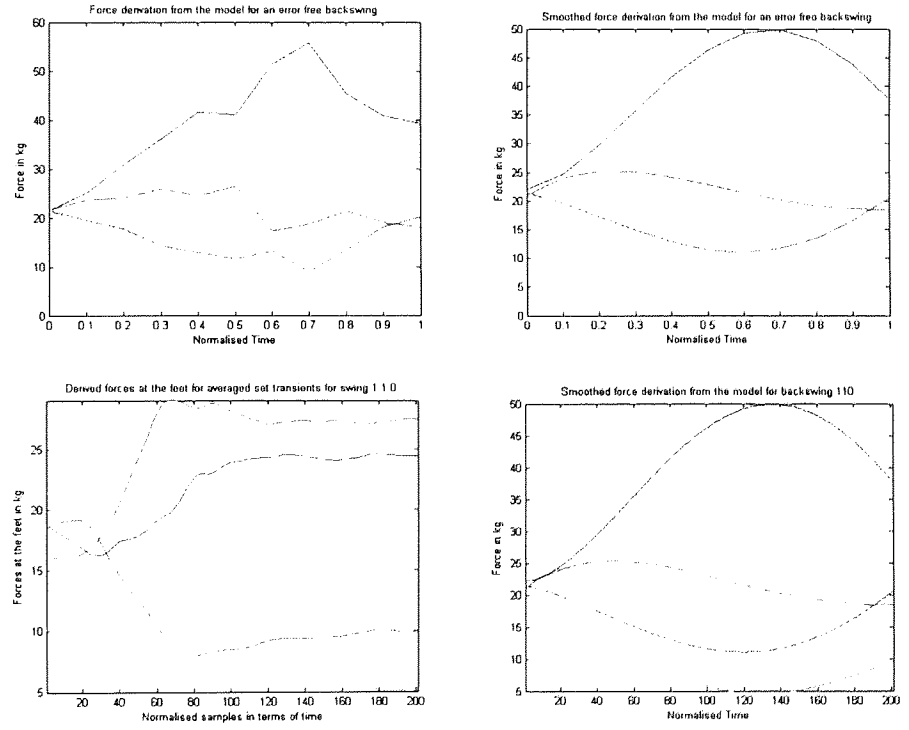

Figure D.10 - A comparison between the model (both top and bottom right) and the practical data (bottom left) for a correct backswing with an incorrect orbit 110.

Similarly for a correct backswing with foot off 101

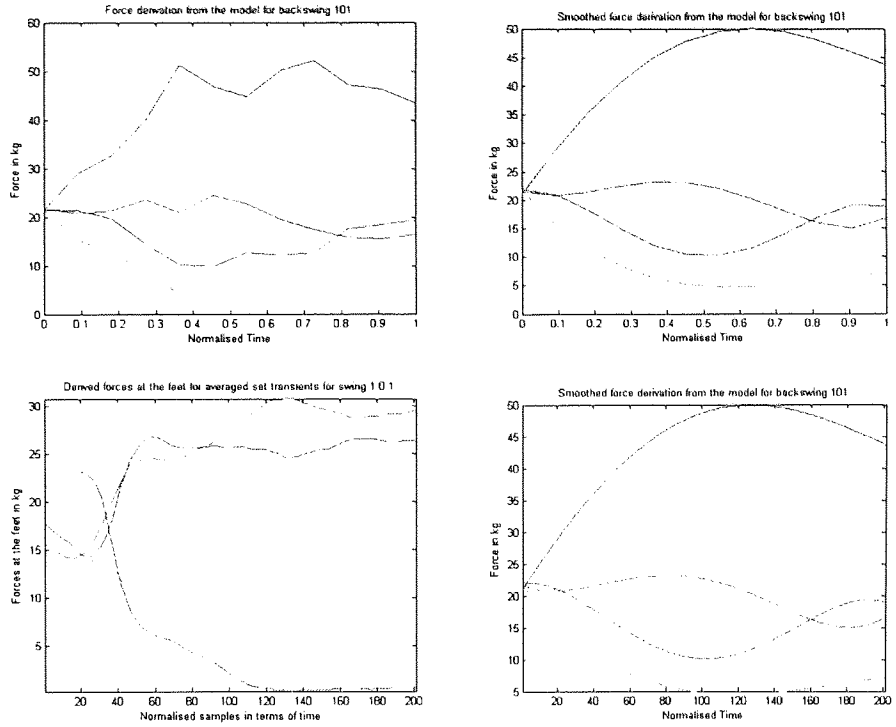

Figure D.11 - A comparison between the model (both top and bottom right) and the practical data (bottom left) for a correct backswing with the planted foot being taken from the surface 101.

And again for a correct backswing with the legs straight 011

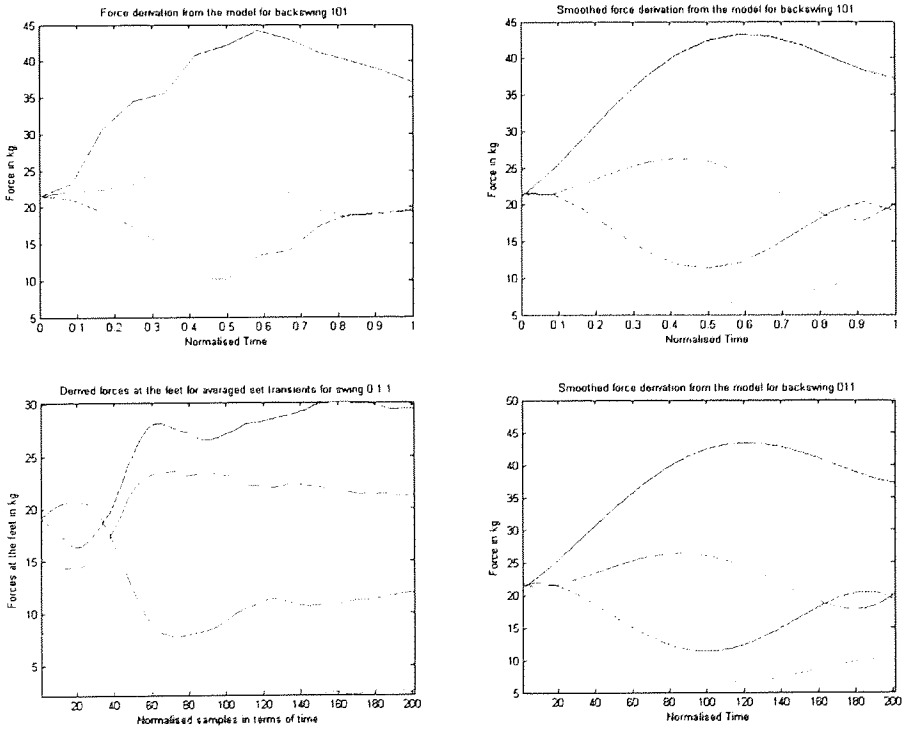

Figure D.12 - A comparison between the model (both top and bottom right) and the practical data (bottom left) for a correct backswing with the legs straight during the swing 011.

D.8 Taxonomy of the movement on the surface for the practical and modelled data

Differences between averaged ideal back swing with averaged non-ideal swings.

The transient expected from an averaged ideal swing using real data is given on the left, with that of the model on the right.

Measured

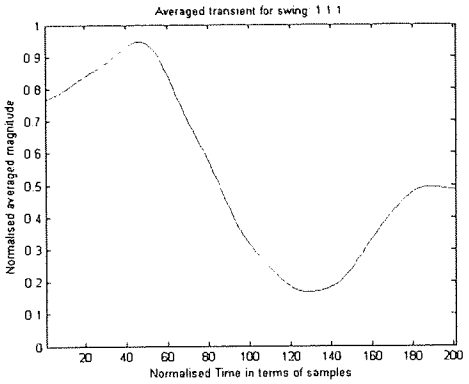

Modelled

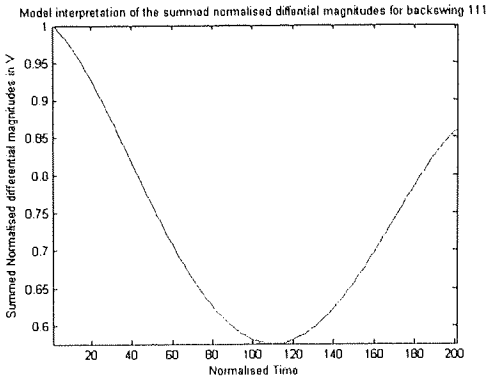

Figure D.13 - Difference from the practically captured normalised summed transients, with those that the model suggests for an ideal backswing 111.

111-011:Integral of differential: 23.76, Integral of differential model: 3.70

Measured

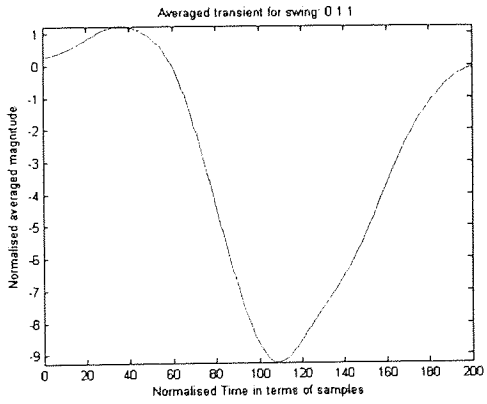

Modelled

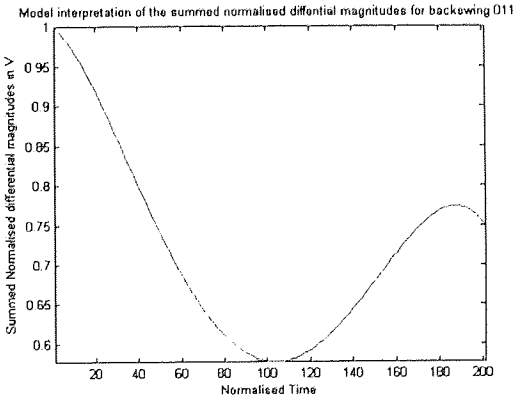

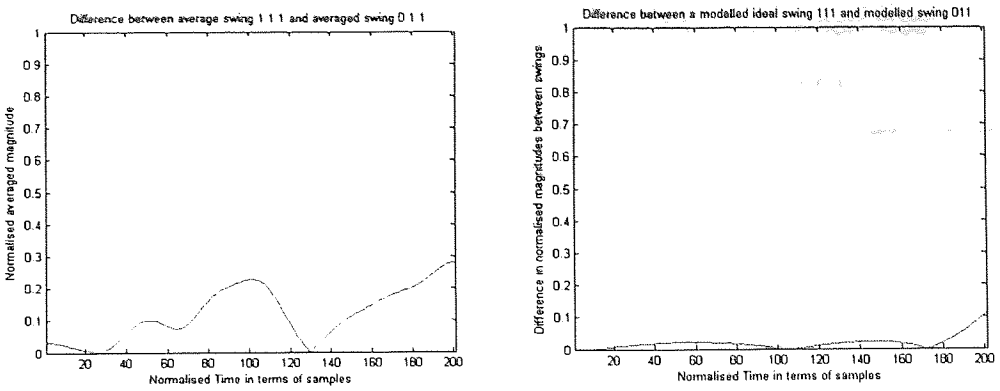

Figure D.14 - Difference from the practically captured normalised summed transients, with those that the model suggests for an ideal backswing with straight legs 011. (bottom) - Difference from the ideal swing 111 for both the practical and the model.

111-101:Integral of differential: 24.16, Integral of differential model: 10.39

Measured Modelled

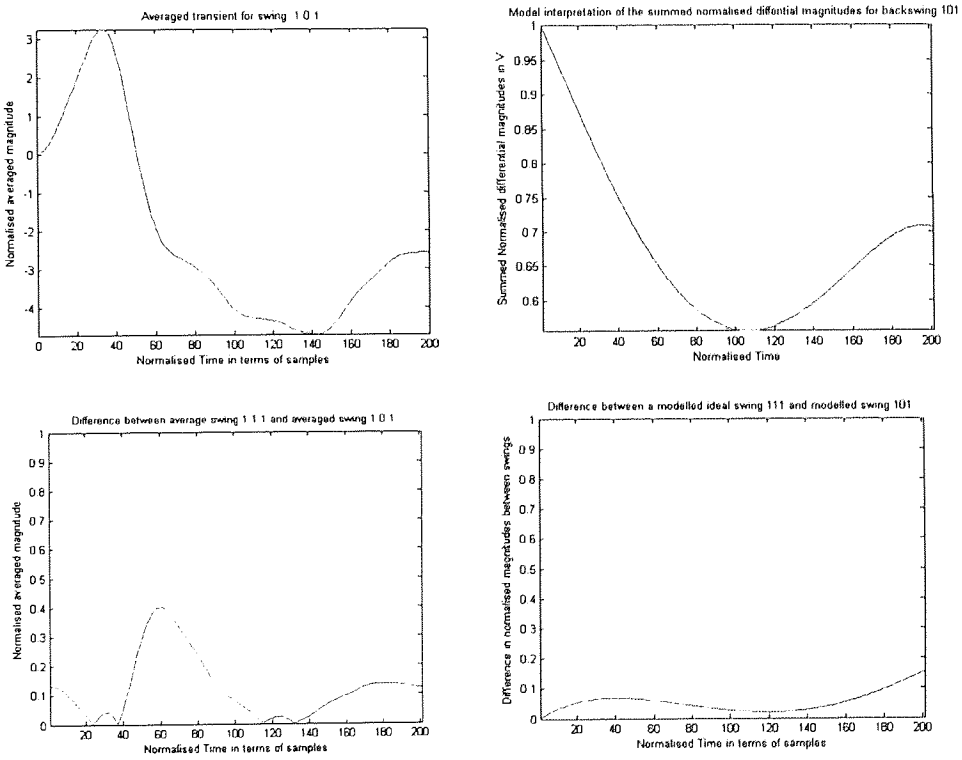

Figure D.15 - Difference from the practically captured normalised summed transients, with those that the model suggests for an ideal backswing with the planted foot coming off the surface 101. (bottom) - Difference from the ideal swing 111 for both the practical and the model.

111-110:Integral of differential: 12.92, Integral of differential model: 7.30

Measured

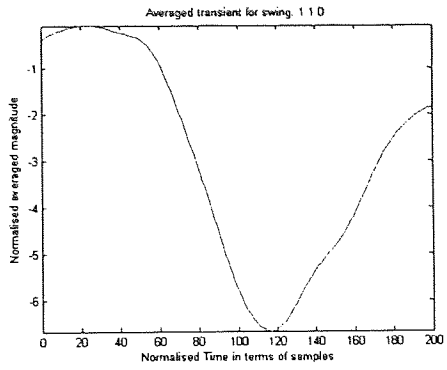

Modelled

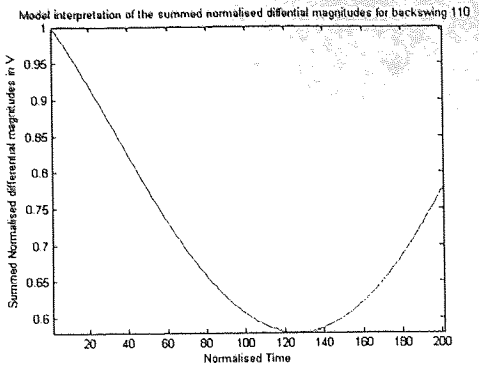

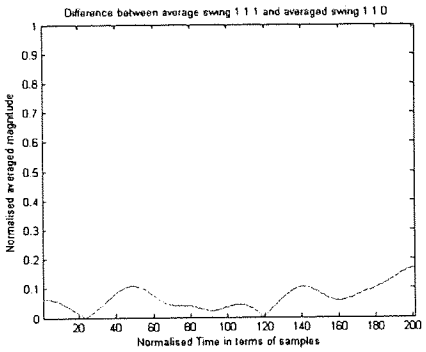

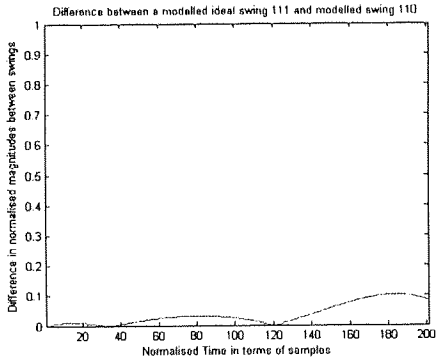

Figure D.16 - Difference from the practically captured normalised summed transients, with those that the model suggests for an ideal backswing with an incorrect orbit angle 110. (bottom) - Difference from the ideal swing 111 for both the practical and the model.